Reliability analysis in orientation estimation for indoor positioning

Andreas Ettlinger

Dissertation zur Erlangung des akademischen Grades
Doktor der technischen Wissenschaften (Dr.techn.)

Department für Geodäsie und Geoinformation
Fakultät für Mathematik und Geoinformation
Technische Universität Wien

Abstract

The research done in the course of this thesis is located in several scientific fields. On the one hand, this thesis contains methodological advancements in the field of parameter estimation methods, statistical tests and reliability. On the other hand, algorithms specific to pedestrian indoor positioning and especially orientation estimation are developed. Nevertheless, it is possible to transfer these concepts to other fields of research and applications.

The progress in parameter estimation methods is related to the Gauss-Helmert model (GHM), which consists of general condition equations, implicitly containing the parameters or states to be estimated as well as the observations. The measures of inner reliability are derived in the GHM and are generalized, such that they can be used for any kind of systematic deviation parameterized in the observation model. The minimum detectable bias (MDB) and the correlation coefficients between test statistics are identified to be sufficient in order to assess inner reliability. Through a proper analysis of the least-square adjustment (LSA) solutions in the GHM and the corresponding statistical tests, main factors influencing the inner reliability measures are identified. The findings with regard to inner reliability in LSA are consequently transferred to the extended Kalman filter (EKF). The GHM is also applied to the EKF. In the common formulation of the EKF, the system equation unambiguously determines the state vector and the measurement equation exhibits the Gauss-Markov model. Both of the prementioned aspects are not mandatory in the newly formulated EKF update equations. Espically the possibility to use redundant condition equations in the system equation enables the fusion of information from multiple sub-systems in an overall EKF.

Two algorithms are introduced in this thesis, which can be used in indoor positioning applications. On the example of orientation estimation in pedestrian indoor positioning with smartphones, the approach of using an overdetermined system equation in the EKF is applied. It is shown, that this approach leads to a higher precision of the estimated states and improved inner reliability. The approach of fusing the information from multiple pedestrians leads to lower MDBs and greatly reduced correlation coefficients between the corresponding test statistics. The findings regarding inner reliability act as guideline for the development of another algorithm for orientation determination based on the accelerometer, gyroscope and magnetometer contained in a smartphone. Together with some heuristics, an algorithm is introduced, which exhibits robustness to magnetic anomalies affecting the smartphones's magnetometer. The proposed approach is tested in small scale experiments with high accuracy ground truth data. It is compared to three other algorithms introduced in related publications regarding orientation estimation in indoor positioning and outperforms them by at least 40%.

Contents

1 Introduction

Many applications require a proper location information of pedestrians in buildings. When guiding pedestrians to certain locations [29, 132, 136] or gaining insights about pedestrian behavior in buildungs [82, 123, 76][B5], it is necessary to estimate the position as well as attitude and velocity. As nearly all people carry smartphones, which contain multiple sensors providing position information, it is the commonly used device to accomplish these tasks. The lack of accurate global navigation satellite system (GNSS) positions in buildings due to GNSS signal degradation, requires the use of other smartphone sensors for positioning. There are indoor positioning approaches using GNSS in the outdoor-indoor transition [62, 198] or high-sensitivity GNSS [155, 99], but the major effort in research and development for indoor positioning is on other techniques.

Pedestrian dead reckoning (PDR) relies on the self-contained inertial measurement unit (IMU), composed of an accelerometer and a gyroscope and is widely used in different combinations with other approaches for the positioning. It provides relative position information, by detecting steps of the user carrying the smartphone and propagating the orientation of the phone as well as the user heading [183]. PDR suffers from drift effects due to summing up orientation and position changes leading to an increase of the errors with time [70]. That's the reason, why PDR is commonly combined with absolute positioning techniques such as Wi-Fi lateration [146, 197] or fingerprinting [80, 64][B2]. Wi-Fi positions exhibit a measurement noise of several meters [77, 146]. In order to increase the precision, Wi-Fi positions are fused with the short-time stable PDR. This leads to a smoother Wi-Fi position and in return, the absolute information from Wi-Fi stabilizes the PDR outcome [26, 140]. Absolute position can be also derived from other radio signals [3]. Another source of information is the building plan, which can help to stabilize PDR [102] or can further refine the PDR-Wi-Fi fusion [131, 120]. Both approaches, the radio positioning as well as map-matching based on building plans, require additional hardware infrustructure or external information. Beside the IMU, there are other self-contained sensors which can be used for the fusion with PDR. The barometer provides information about the height which is mainly used for floor detection [130, 30] and the smartphone camera also provides relative information about position and orientation [148, 143]. Big potential for indoor positioning is upcoming now with LiDAR, which is integrated only in a few smartphone models until now [161, 19]. The magnetometer senses the magnetic flux density of the earth magnetic field and can be used to compute the heading with respect to the magnetic north direction [83] pp. 147 ff. It provides absolute information on the heading and it is therefore commonly fused with the IMU which is also known as magnetic, angular rate and gravity (MARG) sensor array. The magnetometer's main drawback is, that it cannot distinguish between the earth magnetic field and other ambient magnetic fields produced either from the carrier platform or the environment [37, 144, 86]. [115] provide an overview on magnetometer integration approaches for navigation applications and calibration procedures to mitigate systematic deviations. Ambient magnetic fields or magnetic anomalies must not necessarily be disadvantageous as they can be used in the fingerprinting approach for indoor positioning [111, 17][B1] or in other applications like airborne navigation [15, 14].

Herein, only the computation of the absolute 3D orientation of the smartphone is considered based on the integration of IMU and magnetometer. The focus on the orientation arises due to the chosen sensors (accelerometer, gyroscope and magnetometer), which do not provide an overdetermination for the translation or velocity. Orientation determination with the prementioned sensors is a challenging task in indoor environments, especially with low-cost devices such as smartphones. Thus, the aim of this thesis is, to provide algorithmic developments, which support the mitigation of systematic deviations in a MARG sensor array affecting the device or platform orientation. On the one hand, the novel approaches

with strong focus on detectability of systematic deviations presented herein, may be interesting for developers looking for robust estimation procedures in indoor positioning. This work contains methodological concepts which can be integrated to extend existing algorithms but also an stand-alone algorithm to reliably fuse the observations from MARG sensor arrays. On the other hand, the research on the mathematical methods behind these approaches (i.e. parameter estimation and statistical testing of computed quantities), are useful for different scientific disciplines. The further developments in observation models and sequential estimation, extend the methodological base in parameter estimation problems indepently from the specific application. Scientists and developers with an interest in this field of research, can find new concepts herein, supporting their work and raise new research questions.

The methodological progress in parameter estimation is narrowed down to the extended Kalman filter (EKF). The functional model of the EKF is extended to the Gauss-Helmert model (GHM) which allows the use of condition equations implicitly containing the parameters and observations. This leads to EKF-update equations which are very similar to the ones formulated in the common Gauss-Markov model (GMM), enabling the use of overdetermined system or state propagation equations. Overdetermination in the prediction step of the EKF means, that the overall system which the EKF describes, consists of multiple sub-systems each having its own process of state-propagation. It may be possible to solve this in the common EKF structure but the introduction of an overdetermined system equation enables a higher flexibility in the formulation of the functional model. The fusion of multiple sub-systems sharing common states in one EKF is a novel approach which has been developed in the course of this thesis. This methodological advancement is applicable to any field of research which is based on estimating time-varying parameters or states.

Inner reliability and its corresponding measures are a common analysis tool in geodetic applications and especially in the field of engineering geodesy. As it is possible to derive the EKF from least-squares adjustment (LSA), the theory of reliability can be used to analyze if unmodeled systematic deviations are present in the observations (inner reliability) and, if so, to quantify their influence on the estimated parameters (outer reliability). Herein, the inner reliability measures and corresponding test statistics are derived for the GHM and are consequently further applied to the results of the EKF based on the GHM. Emphasis is on the analysis of the extended or more general measures of inner reliability (in contrast to the common approach of data snooping) such as statistical tests and corresponding minimum detectable bias (MDB) as well as their correlation coefficients. As inner reliability is mainly based on one-dimensional biases in the scientific literature, this thesis also aims to generalize the MDB and correlation coefficients of test statistics to any kind of multi dimensional systematic deviations. The structure of the resulting equations in the GHM are very similar to the results in the GMM. Nevertheless, drawing conclusions about improving the measures of inner reliability is more difficult. The reason is, that the observations do not represent the equations of the functional model as in the GMM. Instead, the condition equations to compute the misclosures implicitly contain the parameters and the observations, leading to an additional aspect to be considered in reliability analysis.

Based on the methodological advancements, two novel algorithms specific to orientation determination are introduced. First, data from multiple pedestrians walking the same trajectory are fused within one EKF which estimates the orientation parameters. This necessitates the use of an overdetermined system equation in the EKF where the pedestrians represent the sub-systems. The algorithm is analyzed on a conceptual base herein but it exhibits promising properties, such as a more reliable detection of systematic deviations in the MARG sensor array and higher precision of the estimated states. The second algorithm is developed based on the findings of the analysis of inner reliability and contains heuristic elements. Separating the inclination and heading computation and using an EKF with a reformulated

magnetometer observation model to suppress the influence of magnetic anomalies are its main concepts. This algorithm has been applied to small-scale experiments and exhibits an improved performance in these cases, compared to other established algorithms from relevant publications on pedestrian indoor positioning.

This thesis is structured as follows. In section 2, the scientific context of the provided work is outlined. Section 3 contains the theoretic foundations which are necessary for the presentation of the published research and further considerations. The main outcomes of the articles which have been published in the course of this research are presented in section 4 and the articles itself are attached in appendix A. Publication [A1] (section 4.1) elaborates on the derivation of the EKF in the GHM, using an overdetermined system equation to improve inner reliablity in indoor orientation estimation. In publication [A2] (section 4.2), the analysis of inner reliability in the GHM is deepened and publication [A3] (section 4.3) outlines an algorithm for robust heading determination by mitigating magnetic anomalies. The aim of section 5 is, to merge the insights from the published research. A thorough derivation of inner reliability in the GHM and also for the EKF is provided in section 5.1. The numeric example in section 5.2 concludes the further developments by showing the advantages of the algorithmic developments based on the inner reliability measures.

2   Scientific context

The reseach and findings of this thesis are categorized into pure mathematical or statistical aspects and specific applications to orientation determination for indoor positioning. The next sub-sections follow this rationale, where gaps between published literature and needed solutions are identified to motivate the developments of this thesis. In section 2.1, sequential parameter estimation based on the extended Kalman filter (EKF) and the Gauss-Helmert model (GHM) with the corresponding statistical tests are outlined. Further research is necessary in several aspects of this topic in order to enable the reliable estimation of the orientation in indoor positioning. Multiple linked systems have to be fused in one EKF to enhance the detection of systematic deviations leading to the mandatory usage of the GHM. Scientific literature lacks a thorough derivation of the test statistics which describe inner reliability in the GHM and also multi-dimensional statistical tests have to be considered.

The basic ideas of the developed algorithms for orientation determination in indoor positioning are twofold: on the one hand fusing the information of multiple pedestrians (which applies to the field of crowd sourcing and collaborative navigation) and on the other hand using the measures from inner reliability as guidelines for the EKF model design. Section 2.2, points out, that algorithms using these principles are rare in scientific literature.

2.1   Reliability in parameter estimation methods

In this thesis, special emphasis is on the GHM as it enables the connection of parameters and observations in any kind of nonlinear condition equations in the functional model of an estimator based on least-squares adjustment (LSA). It is possible to derive the update equations of the EKF in the context of LSA [150] and therefore, they can be also represented in the GHM. The first part of the methodological advancements in section 2.1.1 is on the formulation of the EKF in the GHM. It especially elaborates on the necessity to use these equations to represent multiple subsystems. The second methodological aspect is about statistical hypothesis testing in LSA and EKF leading to the concept of reliability, which is not a unique term in statistics. Herein, reliability means the ability to detect and identify systematic deviations with a certain probability (inner reliability) and quantifying their influence on estimated quantities (outer reliability) when using parameter estimation methods [164] pp. 74. Contrary to that, is the reliability engineering which aim is to describe the durability and security of systems [199, 200] or [55] pp. 745 ff. In section 2.1.2, the literature about geodetic reliability is screened which shows, that this concept is not directly introduced for the GHM.

2.1.1   EKF in the GHM and distributed systems

The EKF is the nonlinear extension of the Kalman filter which is first introduced by [81] and its measurement equation usually exhibits the structure of the GMM, i.e it is possible to compute the observations from the quantities in the state vector. Thus, the filter innovation are represented by the predicted residuals which are directly available from the difference of the actual observations and computed observations using the predicted state [39] pp. 102 or [163] pp. 214. Herein, the GHM is used in the measurement equation which first appears in [160]. This EKF formulation is then used e.g. in the self-calibration of stereocameras [23, 24] or in the georeferencing of laserscanner-based multi-sensor systems [174] and unmanned aerial system [13]. [173] extend the GHM-EKF by including nonlinear state constraints. In [58] pp. 302 ff., it is shown, that the GHM is also necessary in the standard formulation of the EKF to derive the residuals and redundancy numbers for the observation groups or random quantities in the

system equation. Total least-squares (TLS), which is a possible solution algorithm for errors-in-variables (EIV) models, is a special case of the nonlinear GHM, which is shown in [135] on the example of similarity transformation. The total LSA can be transferred to the EKF, as e.g. shown in [153, 126, 127]. [49] derive an optimal filtering solution for EIV models with the minimal variance criterion.

The crowd-sourcing approach for orientation determination in indoor positioning (section 2.2.1) requires the consideration of EKF-variants which are able to handle the information from multiple systems. Each considered entity (e.g. pedestrians in the context of indoor positioning) represents such a system, which in sum describe an overall system to be monitored (e.g. all pedestrians moving inside a building). The systems composing the overall system are commonly known as agents in literature and herein they are called subsystems from here on. In order to fuse the information from multiple subsystems the distributed or decentralized Kalman filter (DKF) and its variants are commonly used [128, 169]. A special case is, that systems are based upon each other which is called cascaded subsystems and the cascaded Kalman filter can be used to solve such state estimation problems [108]. Another variant of a DKF is the federated Kalman filter, where the subsystems are evaluated by an EKF. These results are fused in a centralized algorithm (information fusion) and the knowledge gain is distributed back to the subsystems (information distribution) [122]. [57, 186] use the federated Kalman filter for indoor localization of mobile robots. [32] uses a weighted robust DKF for sensor systems to determine the components of auto-correlated and cross-correlated noises. DKFs are also used for collaborative localization and navigation. [185] derives a message passing DKF and applies it to a multi-agent system, where the individual agent observations correspond to odometry and landmark coordinates. Random sample consesus can be used in conjunction with DKFs to detect faulty subsystems [149]. In collaborative localization also centralized Kalman filters are used which process all observations from the multiple subsystems in the measurement equation to estimate common states [27, 178].

The problem appears, when the subsystems compose the system equation (i.e. control input quantities from multiple subsystems) of a centralized EKF. In this case, the system equation is overdetermined which is not covered in the literature. In this thesis this gap is closed, by using the GHM to derive the EKF update equations for such cases.

2.1.2   Reliability in the GHM

Geodetic reliability is based on the research of Baarda [5, 6]. Baarda's investigations about statistical tests in geodetic networks contain many aspects of today's perspective on reliability, such as the separation into inner and outer reliability, derivation of the minimum detectable bias (MDB) and also the consideration of separability of multiple alternative hypothesis. These concepts are an indispensible part of quality control in geodetic applications such as geodetic networks [192, 61, 28, 110], laserscanning applications [93, 72], computer vision and photogrammetry [34, 21]. The statistical tests to identify or locate erroneous observations based on the observation residuals are extended and adapted to different cases such as correlated observations [71] pp. 192, n-dimensional outliers [96] and a-posteriori variance factor [139] leading to different test distributions. N-dimensional outliers necessitate the further development of the MDB because only in the 1-dimensional case it is a scalar value. Otherwise it is a vector with an infinite number of solutions describing a n-dimensional shape, such as an ellipse for 2D coordinate observations or an ellipsoid for 3D observations (known as threshold-ellipse or threshold-ellipsoid) as e.g. outlined in [71] pp. 296 ff. [87, 192] show a derivation of n-dimensional MDBs. Another extension to statistical tests is shown in [105], who derive more powerful statistical tests based on the generalized chi-square distribution. The Type III error due to multiple alternative hypothesis (i.e. choosing the wrong alternative hypothesis) [56], is early adapted by [34], who extended it to multiple n-dimensional

alternative hypothesis. It is mainly influenced by the correlation coefficient of test statistics which can be described as the cosine of the angle between two vectors describing two 1-dimensional test statistics or the maximum eigenvalue of a matrix relating the column spaces of two n-dimensional test statistics. Further research on this topic is done by [188], who introduces upper bounds for the type I, type II and type III error in the 1-dimensional case. [142, 187, 68] extended the MDB by considering the type III error (i.e. separability), leading to another measure which equals the MDB only in the optimal case (i.e. zero correlation). Otherwise it is higher, depending on the correlation coefficient of the used test statistics. Further development of reliability theory is also done in the case of correlated observations [141] or singular variance-covariance matrices (VCM) [177].

In many references, it is assumed, that observations are affected by outliers in contrary to systematic deviations concerned in this contribution. [107] outlines, that outliers (or gross errors) are stochastic quantities, but they can be treated as deterministic biases (i.e. systematic deviations) which leads to the mean shift model. Reliability theory belongs to this type of approaches, because the shift of the test distribution by the non-centrality parameter (which is the basic assumption, see section 3.1.3) is nothing else but a mean shift. Another mean shift approach which deals with outliers is e.g. shown in [92]. The alternative is to use variance inflation approaches, where the outliers are modeled as stochastic quantities. [94, 91, 95] estimate weights for observations within the expectation maximization method to downweight outlying observations (i.e. increase the variance of such observations). A comparison between the variance inflation model and the mean shift model is outlined in [106]. Variance inflation is closely related to rboust estimation, which is based on influence functions, describing the influence of one additional observation on a statistic with corresponding underlying distribution [52] pp. 41 ff. Robust estimation goes back to [67, 51], who introduced robust M-estimators. The classical minimization of squared errors leads to unbounded influence functions and therefore to non-robust estimators, but they show other optimality properties, i.e. minimum variance and unbiasedness. The most basic and most famous robust estimator is the median, which tolerates up to $49.\dot{9}$ % of erroneous observations. Robust estimation is also used in recent years in different types of geodetic networks [50, 85, 193]. The least median square algorithm [147], can be seen also as a robust estimator (in fact it is also introduced as such) due to the usage of the minimization of the median of the sum of squared residuals. But it is also a combinatorial method (because of the necessity of building sub-groups of observations and compare these estimation results), which is another approach of dealing with outliers. Other combinatorial methods are the maximum subsample method [134], the information criterion [107] or to use sub-groups of observations which are compared by using statistical tests [8, 12]. Baysian statistics are not treated herein. Nevertheless, the same approaches, statistical tests [41], robust estimation [90] pp. 99 ff. or variance inflation [48], are used. Statistical tests [166, 150] and reliability [175, 176][B4] are also applied in the EKF and their applications are outlined in the next section. There are also many variants of robust EKFs, e.g. based on the M-estimator [88, 125] or the H-infinity filter (estimator derived from using the H_∞-norm) [73] or [159] pp. 333 ff.

Reliability theory is developed mainly in the GMM. [35] states on pp. 166, that outliers in the observations can be reduced to outliers in the constraints and can be treated in the same way as in the GMM. [98] derived the statistical tests for additional parameters in the GHM but doesn't extend the results to inner reliability. Thus, the derivation of the reliability theory in the GHM and possible additional considerations for implicit functional models are a major motivation of this work.

2.2   Systematic deviations in navigation applications

There are different approaches to handle or treat systematic deviations in sensors for navigation applications, including smartphone sensors for orientation determination. Figure 1 serves as guideline for this section and shows two possibilities to categorize these approaches. One way to categorize is, at which point in the process of localization the treatment of systematic deviations is done. The other way of categorization is the methodological approach on how the systematic deviations are computed or treated. Both point of views are concisely outlined in the next paragraphs. Figure 1 indicates, that the following considerations are narrowed down to the detection of systematic deviations in inrun applications. The two algorithms developed herein are assigned to this field of research.
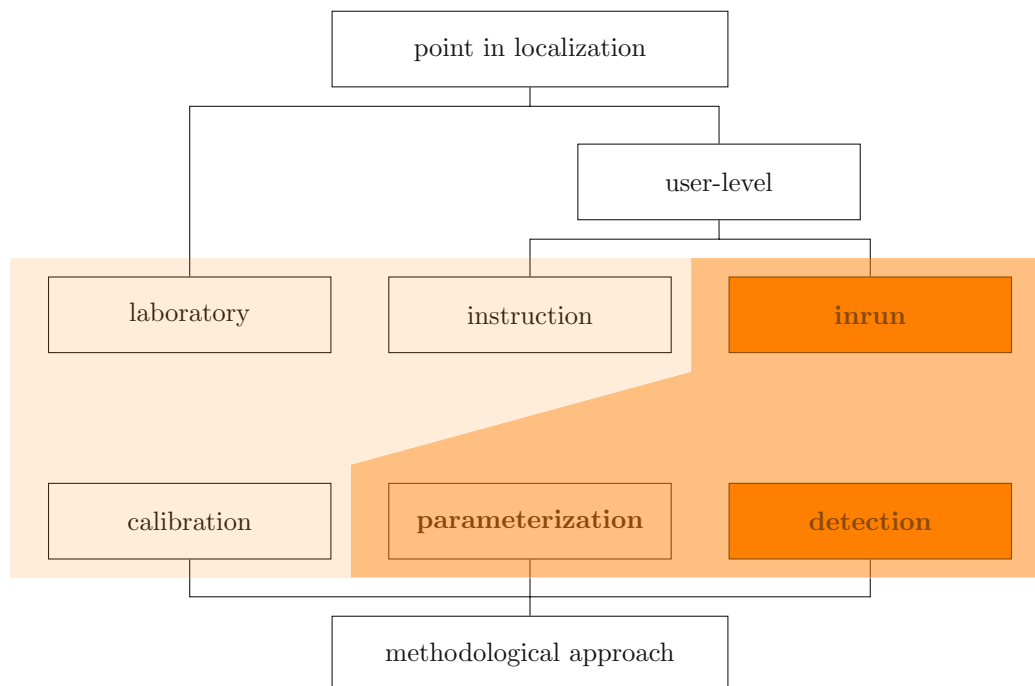

Figure 1: Treatment of systematic deviations in navigation applications. The focus is on the detection of systematic deviations in inrun methods herein.

Regarding the point in localization, where systematic deviations are determined, there are two subcategories: Under laboratory conditions with special equipment [168] pp. 219 ff. or at the time of intended usage of the sensors. The second case is the treatment at user-level, which can be further split into instruction-based methods and inrun methods [129]. In the instruction-based methods, the sensors have to undergo special movements or maneuvers prior to the localization process, which enables the computation of systematic deviations. In smartphone applications, the ellipsoid-fitting method is commonly used for the calibration of the magnetometer [37, 144, 172, 86, 118]. With the constraint, that the magnetometer observations ideally are located on a sphere with known radius, i.e. the known value of the magnitude of the earth magnetic field (EMF), it is possible to determine the sensor and platform errors. [115] give an overview on magnetometer calibration but the presence of magnetic anomalies requires the use of inrun methods, where systematic deviations are treated beside the computation of the quantities which are necessary for the current navigation application. Section 2.2.2 further elaborates on inrun methods to detect magnetic anomalies in indoor positioning.

Regarding the methodological approach of computing systematic deviations, three sub-categories are considered (figure 1). Calibration means, to determine values representing the systematic deviations in separate routines and use these values in the subsequent localization algorithm. This approach is already covered by the laboratory calibration and instruction-based methods in the previous paragraph and is not in the scope of this work.

Parameterization in inrun methods subsumes the approaches, where quantities are included in the set of parameters to be estimated, which account for the influence of systematic deviations. [137, 121] directly integrate biases for the accelerometer and gyroscope in the state vector in the coupling of GNSS/INS coupling. This is also done in the fusion of IMU and magnetometer to compute orientation (e.g. estimation of accelerometer and gyroscope biases [38, 54, 114], magnetometer errors [22, 170, 53]) or in indoor positioning in genaral [191]. In such applications, observability and estimability measures are used to assess if these biases (or in general any state in the state vector) can be reasonably estimated [63, 133, 158]. In observability, one analyzes, if the initial state vector can be unambiguously determined from a given batch of observations [75, 182]. Estimability is defined differently and it says, that a state is estimable if its variance at a certain timestamp is lower than the initial variance [7]. Still both concepts are connected, as stated in [43] and estimability is sometimes also called stochastic observability [45] pp. 104-105. [154] show how to model outliers in total Kalman filtering by additionally estimating them beside the actual quantities of interest. An inrun approach based on cascaded EKF to treat biases is shown in [11].

In the detection approach of figure 1, the presence of systematic deviations in the sensor observations is determined and if necessary appropriate actions are performed to mitigate them. Detection, identification and adaption (DIA) is commonly used and relies on the statistical tests from reliability theory [166, 150]. In GNSS positioning, it is better known as receiver autonomous integrity monitoring (RAIM) used to locate faulty satellite observations [162, 101] and is also extended to DIA by excluding or isolating them [181, 180]. RAIM is usually based on the computed residuals which especially helps to improve the accuracy in harsh environments, such as urban canyons and buildings [100, 109]. Another RAIM approach is the solution separation, which is a combinatorial approach based on different subsets of satellite observations [78, 79]. An overview on RAIM and further aspects in GNSS integrity is e.g. shown in [25]. The approach of DIA is also implemented in the coupling of GNSS and inertial navigation system (INS) for detecting unmodeled deviations [40, 74] and spoofing [84]. The GNSS/INS coupling provides similar advantages as the fusion of Wi-Fi positioning with INS in indoor applications. The GNSS positions help to stabilize the INS drift and the INS solution is used to propagate the position and orientation in the time between GNSS observations and when it is not available.

Contributions, which use the classical concept of DIA in indoor navigation applications are rare. DIA and integrity monitoring is e.g. used in the positioining with bluetooth [189] or in the fusion of Wi-Fi fingerprinting with PDR in an unscented Kalman filter [190]. In indoor applications, it is more common to use robust approaches for treating outliers but also hardware failures [103]. The term robust does not necessarily mean to perform a robust estimation method but can also mean that an indoor positioning system works in challenging environments and heterogeneous scenarios [184]. The most common approach to reduce the influence of outliers or systematic deviations in indoor positioning is, to analyze the sensor observations and check if they meet certain conditions. [36, 66] weight the rssi observations by signal analysis to exclude observations which are likely subject to non-line-of-sight (NLOS) conditions. Set-membership is e.g. used for fault detection in indoor localization of robots [2].

The development of the two novel algorithms in this thesis is based on adjusting the functional model of an EKF, such that inner reliability measures are improved (i.e. increasing the performance of the detection and identification of systematic deviations). The following subsections outline the literature being the

basis for the adjustments in the functional model. Section 2.2.1, elaborates on crowd sourcing to motivate the introduction of the algorithm which is based on fusing the information from multiple pedestrians. Section 2.2.2 focuses on inrun-approaches to detect systematic deviations in the magnetometer as this is the most critical sensor for orientation determination in indoor positioning. It is shown, that the there is the potential to design an algorithm based on statstical tests for magnetic anomaly mitigation which is closely related to inner reliability.

2.2.1 Crowd sourcing in indoor positioning

The progress in smartphone technology and Internet of Things (IoT), enables the collection of data from many pedestrians which is called crowd sourcing. Crowd sourcing is mostly used to collect radio signals (e.g. Wi-Fi or Bluetooth Low Energy) to create radio maps for indoor positioning which are the basis for different fingerprinting methods [47]. A trend in current literature is to refine this approach by using methods from machine learning and deep learning [18, 157, 156]. It is also common to collect PDR trajectories computed for each pedestrian and use these data to create the radio maps [46, 117, 196, 194]. Another variant is to use crowd sourced radio signals as landmarks and recursively support the online PDR solution and improve the landmark coordinates [179]. Ambient magnetic fields must not necessarily be disadvantageous as they can be used as location-specific features in the magnetometer data. [116] use crowd sourced magnetometer data to improve the creation of radio maps and [4] generate magnetic field maps for fingerprinting. Beside radio maps it is also possible to derive floor plans [112] or use the crowd sourced data to predict pedestrian motion in a building [119][B5]. [195] exploits the turn behavior of pedestrians on specific points in the building to aid the PDR heading computation.

There is no literature about using the smartphone sensor observations from multiple pedestrians in real-time or postprocessing to compute the corresponding trajectories. Simultaneous localization and mapping (SLAM) for multiple robots [16, 167] as well as the robotic applications in section 2.1.1 could be also applied to the pedestrian case. Buildings commonly exhibit a very constrained motion pattern of pedestrians especially in corridors. The idea is to use the data from pedestrians walking e.g. in a corridor and evaluate these data in one EKF. This requires the temporal as well as spatial synchronization of the crowd sourced observations, which is not considered herein. The focus is on the development of an EKF which is capable of fusing multi-pedestrians smartphone sensor observations in order to improve the inner reliability and therefore the estimation of orientation.

2.2.2 Detection of magnetic anomalies in indoor positioning

A common approach is to fuse the gyroscope, accelerometer and magnetometer (i.e. the MARG sensors) in an extended Kalman filter (EKF) to estimate the smartphone orientation [38, 54][B3]. The critical point in these approaches is, that magnetic anomalies also influence the inclination component of orientation (roll φ and pitch θ angles in Euler angle parameterization). [124, 171] try to avoid this by using complementary filters where the change in the inclination is computed from accelerometer and the change in the heading component of orientation (the yaw angle ψ in Euler angle parameterization) is computed from the magnetometer. A possibility for mitigation is, to use the known quantities of the EMF to determine if magnetic anomalies are present. There are many variants in the literature, exploiting this information: [20] use this knowledge to compute adaptive variances for the magnetometer observations. [145, 104] only perform the EKF update if certain conditions are kept, such as the deviation of the magnitude of the magneotometer observations and the known magnitude of the EMF being beyond a preset threshold. [1] use statistical tests as detectors for perturbations in the magnetometer observations. A

fuzzy infrerence system rule set takes the output of the statistical tests and determines the mean value as well as the standard deviation of the heading deviation. Another approach is to parameterize the systematic deviations in an EKF (i.e. include them in the state vector). It is not common to estimate each type of systematic deviation separately in the EKF but to subsume them in a bias and an affine transformation parameterized with a symmetric matrix [144, 86]. [22] includes this bias and the elements of the symmetric matrix in the state vector of an EKF and an unscented Kalman filter. [53] additionally integrate the EMF in the sensor frame to the state vector and propagates it with the gyroscope observations.

From this recherche it becomes apparent, that inner reliability could be a promising approach to detect the presence of systematic deviations in order to improve orientation estimation algorithms. Especially, the magnetometer is subject to multiple sources of deviation and therefore, the measures from inner reliability will be used to develop an EKF which robustly determines the smartphone orientation. In publication [A3], the focus is on the performance with respect to heading accuracy. Section 5 extends this research by analyzing additionally the inner reliability measures of this algorithm.

3   Theoretic foundations

3.1   Parameter estimation and reliability

3.1.1   LSA in the GHM

In the GHM, the functional model consists of condition equations $\mathbf{f}(\mathbf{l}, \mathbf{x}) = \mathbf{0} \in \mathbb{R}^{b \times 1}$ implicitly containing the observations $\mathbf{l} \in \mathbb{R}^{n \times 1}$ and parameters $\mathbf{x} \in \mathbb{R}^{u \times 1}$, where the more common "Gauss-Markov" model (GMM) is just a special case of. $\mathbf{l}$ is derived or available from measurements and therefore, it is treated as a random quantity. It is split into a deterministic part (for now the expectation $E\{\}$) and a random part

$$\mathbf{l} = E\{\mathbf{l}\} - \mathbf{v}, \ \ \mathbf{v} \sim N(\mathbf{0}, \mathbf{\Sigma}_{\text{ll}}), \tag{1}$$

in which the residuals $\mathbf{v} \in \mathbb{R}^{n \times 1}$ represent the randomness of the observations which are assumed to be Gaussian or normally distributed. $\mathbf{0}$ corresponds to the first moment of the distribution (i.e. the expectation) and $\mathbf{\Sigma}_{\text{ll}}$ is the Variance-Covariance matrix (VCM) and describes the second moment (i.e. the dispersion). The parameters $\mathbf{x}$ are assumed to be non-random respectively deterministic. The estimated parameters $\hat{\mathbf{x}}$ (the hat sign "ˆ" will be used throughout this thesis to mark estimated quantities) are random because of using the random observations for estimation.

As indicated above, $\mathbf{l}$ and $\mathbf{x}$ have to equate the functional model to result in the zero-vector. In general only special sets of these quantities fulfill this condition. Obviously, the theoretic true quantities $\tilde{\mathbf{l}} = \mathbf{l} + \tilde{\mathbf{v}}$ and $\tilde{\mathbf{x}}$ have to fulfill $\mathbf{f}(\tilde{\mathbf{l}}, \tilde{\mathbf{x}}) = \mathbf{0}$. In reality, these quantities are not available, which necessitates the use of the estimated quantities

$$
\begin{aligned}
\mathbf{f}(\hat{\mathbf{l}}, \hat{\mathbf{x}}) = \mathbf{f}(\mathbf{l} + \hat{\mathbf{v}}, \hat{\mathbf{x}}) &= \mathbf{0} \\
\mathbf{f}(\mathbf{l} + \hat{\mathbf{v}}^{(i)}, \hat{\mathbf{x}}^{(i)}) &\approx \mathbf{f}(\mathbf{l} + \hat{\mathbf{v}}^{(i-1)}, \hat{\mathbf{x}}^{(i-1)}) + \frac{\partial \mathbf{f}}{\partial \hat{\mathbf{v}}^{(i)}}\big|_{\mathbf{l} + \hat{\mathbf{v}}^{(i-1)}, \hat{\mathbf{x}}^{(i-1)}} (\hat{\mathbf{v}}^{(i)} - \hat{\mathbf{v}}^{(i-1)}) \\
&\quad + \frac{\partial \mathbf{f}}{\partial \hat{\mathbf{x}}^{(i)}}\big|_{\mathbf{l} + \hat{\mathbf{v}}^{(i-1)}, \hat{\mathbf{x}}^{(i-1)}} (\hat{\mathbf{x}}^{(i)} - \hat{\mathbf{x}}^{(i-1)}) \\
&\approx \mathbf{f}(\mathbf{l} + \hat{\mathbf{v}}^{(i-1)}, \hat{\mathbf{x}}^{(i-1)}) - \mathbf{B}^{(i)}\hat{\mathbf{v}}^{(i-1)} + \mathbf{B}^{(i)}\hat{\mathbf{v}}^{(i)} + \mathbf{A}^{(i)}(\hat{\mathbf{x}}^{(i)} - \hat{\mathbf{x}}^{(i-1)}) \\
&\approx \mathbf{w}^{(i)} + \mathbf{B}^{(i)}\hat{\mathbf{v}}^{(i)} + \mathbf{A}^{(i)}d\hat{\mathbf{x}}^{(i)}
\end{aligned}
\tag{2}
$$

where the linearization with Taylor series expansion corresponds to the equality constraint of Lagrange optimization (e.g. [10] page 67 ff.), which is used to compute $\hat{\mathbf{x}}$ and $\hat{\mathbf{v}}$. Due to the linearization, the estimated quantities from iteration step $i - 1$ are used as development point in the subsequent iteration step. $\mathbf{w}^{(i)} \in \mathbb{R}^{b \times 1}$ is the misclosure vector, $\mathbf{B}^{(i)} \in \mathbb{R}^{b \times n}$ is the observation matrix and $\mathbf{A}^{(i)} \in \mathbb{R}^{b \times u}$ is the design matrix. For the sake of readability, the iteration superscripts are omitted from here on. The squared and weighted sum of residuals $\hat{\mathbf{v}}^T \mathbf{Q}_{\text{ll}}^{-1} \hat{\mathbf{v}}$ corresponds to the main condition of Lagrange optimization which should be minimized. $\mathbf{Q}_{\text{ll}}$ is the cofactor matrix, which results when extracting the a priori variance of unit weight or variance factor σ_0^2 from the VCM of the observations $\mathbf{\Sigma}_{\text{ll}} = \sigma_0^2 \mathbf{Q}_{\text{ll}}$. The solutions of $\hat{\mathbf{x}}$ and $\hat{\mathbf{v}}$ (with corresponding cofactor matrices) in the GHM are

$$\mathbf{Q}_{ww} = \mathbf{B}\mathbf{Q}_{ll}\mathbf{B}^T$$
$$\mathbf{Q}_{\hat{x}\hat{x}} = (\mathbf{A}^T\mathbf{Q}_{ww}^{-1}\mathbf{A})^{-1}$$
$$\mathbf{A}^+ = \mathbf{Q}_{\hat{x}\hat{x}}\mathbf{A}^T\mathbf{Q}_{ww}^{-1}$$
$$\mathbf{B}^+ = \mathbf{Q}_{ll}\mathbf{B}^T\mathbf{Q}_{ww}^{-1} \tag{3}$$
$$d\hat{\mathbf{x}} = -\mathbf{A}^+\mathbf{w}$$
$$\mathbf{Q}_{\hat{v}\hat{v}} = \mathbf{B}^+(\mathbf{Q}_{ww} - \mathbf{A}\mathbf{Q}_{\hat{x}\hat{x}}\mathbf{A}^T)(\mathbf{B}^+)^T$$
$$\hat{\mathbf{v}} = -\mathbf{B}^+(\mathbf{I} - \mathbf{A}\mathbf{A}^+)\mathbf{w},$$

where $\mathbf{A}^+$ and $\mathbf{B}^+$ are the pseudo-inverses of $\mathbf{A}$ and $\mathbf{B}$ (see e.g. [89] pp. 57 for their properties). The details on these derivations can be found e.g. in [35] pp. 164 ff. or [58] pp. 187 ff.

3.1.2 EKF

Herein, the EKF quantities and equations are outlined in the LSA notation to connect the statistical tests from LSA and reliability theory (section 3.1.3) to the EKF. The propagation model $\mathbf{f}_{\bar{x}} \in \mathbb{R}^{u \times 1}$ is also known as system equation (k indicates the epochs) which provides the predicted state vector $\bar{\mathbf{x}}_k$

$$\bar{\mathbf{x}}_k = \mathbf{f}_{\bar{x}}(\hat{\mathbf{x}}_{k-1}, \boldsymbol{v}_{k|k-1}, \boldsymbol{\zeta}_{k|k-1}) \tag{4}$$

including three input quantities, the previously estimated state $\hat{\mathbf{x}}_{k-1}$, the system control $\boldsymbol{v}_{k|k-1} \in \mathbb{R}^{n_v \times 1}$ and the system noise $\boldsymbol{\zeta}_{k|k-1} \in \mathbb{R}^{n_\zeta \times 1}$. The system equation is the time-discrete solution of a system of partial differential equations (i.e. time-continuous description of the state propagation) [44] pp. 31 ff., [31] pp. 125 ff. $\boldsymbol{v}_{k|k-1}$ and $\boldsymbol{\zeta}_{k|k-1}$ are quantities which describe the deterministic and stochastic propagation respectively of the state from epoch $k-1$ to epoch k and both are treated as random variables. $\boldsymbol{\zeta}_{k|k-1}$ subsumes the imperfections of the propagation model, which are assumed to be Gaussian distributed with zero-mean $\boldsymbol{\zeta}_{k|k-1} \sim N(\mathbf{0}, \boldsymbol{\Sigma}_{\zeta\zeta})$. The system control quantities $\boldsymbol{v}_{k|k-1} = E\{\boldsymbol{v}_{k|k-1}\} - \mathbf{v}_{v,k|k-1}$ are modeled in a similar way as the observations in section 3.1.1. Thus, they consist of a deterministic part (i.e. the expectation $E\{\boldsymbol{v}_{k|k-1}\}$) and a random part $\mathbf{v}_{v,k|k-1} \sim N(\mathbf{0}, \boldsymbol{\Sigma}_{vv})$. The VCM of $\bar{\mathbf{x}}_k$ is computed with variance propagation and the assumption, that $\hat{\mathbf{x}}_{k-1}$, $\boldsymbol{v}_{k|k-1}$ and $\boldsymbol{\zeta}_{k|k-1}$ are uncorrelated [163] pp. 216

$$\boldsymbol{\Sigma}_{\bar{x}\bar{x},k} = \mathbf{B}_s\boldsymbol{\Sigma}_{ll,s}\mathbf{B}_s^T = \begin{bmatrix} \mathbf{T}_{k|k-1} & \mathbf{Y}_{k|k-1} & \mathbf{Z}_{k|k-1} \end{bmatrix} \begin{bmatrix} \boldsymbol{\Sigma}_{\hat{x}\hat{x},k-1} & \mathbf{0} & \mathbf{0} \\ \mathbf{0} & \boldsymbol{\Sigma}_{vv,k|k-1} & \mathbf{0} \\ \mathbf{0} & \mathbf{0} & \boldsymbol{\Sigma}_{\zeta\zeta,k|k-1} \end{bmatrix} \begin{bmatrix} \mathbf{T}_{k|k-1}^T \\ \mathbf{Y}_{k|k-1}^T \\ \mathbf{Z}_{k|k-1}^T \end{bmatrix}$$

$$= \mathbf{T}_{k|k-1}\boldsymbol{\Sigma}_{\hat{x}\hat{x},k-1}\mathbf{T}_{k|k-1}^T + \mathbf{Y}_{k|k-1}\boldsymbol{\Sigma}_{vv,k|k-1}\mathbf{Y}_{k|k-1}^T + \mathbf{Z}_{k|k-1}\boldsymbol{\Sigma}_{\zeta\zeta,k|k-1}\mathbf{Z}_{k|k-1}^T$$

$$\mathbf{T}_{k|k-1} = \frac{\partial\mathbf{f}_{\bar{x}}}{\partial\hat{\mathbf{x}}_{k-1}}\big|_{\hat{\mathbf{x}}_{k-1},\boldsymbol{v}_{k|k-1},\boldsymbol{\zeta}_{k|k-1}} \tag{5}$$

$$\mathbf{Y}_{k|k-1} = \frac{\partial\mathbf{f}_{\bar{x}}}{\partial\boldsymbol{v}_{k|k-1}}\big|_{\hat{\mathbf{x}}_{k-1},\boldsymbol{v}_{k|k-1},\boldsymbol{\zeta}_{k|k-1}}$$

$$\mathbf{Z}_{k|k-1} = \frac{\partial\mathbf{f}_{\bar{x}}}{\partial\boldsymbol{\zeta}_{k|k-1}}\big|_{\hat{\mathbf{x}}_{k-1},\boldsymbol{v}_{k|k-1},\boldsymbol{\zeta}_{k|k-1}}.$$

As it is more common in literature to use the VCMs for the EKF equations, this notation is also

applied herein. The index s indicates quantities which belong to the system equation and therefore, $\mathbf{B}_s$ contains the Jacobian matrices and $\boldsymbol{\Sigma}_{\mathrm{ll},s}$ the VCMs of the random quantities appearing in the state propagation process. The observations $\mathbf{l}_{m,k}$ at epoch k are used to update or correct $\bar{\mathbf{x}}_k$. The equations $\mathbf{f}_m \in \mathbb{R}^{n_m \times 1}$ which link $\mathbf{l}_{m,k}$ and $\hat{\mathbf{x}}_k$ are called measurement equation

$$\mathbf{w}_{m,k} = \mathbf{l}_{m,k} - \mathbf{f}_m(\bar{\mathbf{x}}_k), \tag{6}$$

where $\mathbf{w}_{m,k} \in \mathbb{R}^{b_m \times 1}$ is called the filter innovation (in contrast to the misclosure vector in section 3.1.1) and $\bar{\mathbf{x}}_k$ is used as approximate solution (i.e. linearization point) for $\hat{\mathbf{x}}_k$. The update equations are (see e.g. [39] pp. 107 ff. or [159] pp. 121 ff.)

$$
\begin{aligned}
\mathbf{A}_{m,k} &= \frac{\partial \mathbf{f}_m}{\partial \hat{\mathbf{x}}_k}|_{\bar{\mathbf{x}}_k} \\
\boldsymbol{\Sigma}_{\mathrm{ww},m,k} &= \boldsymbol{\Sigma}_{\mathrm{ll},m,k} + \mathbf{A}_{m,k}\boldsymbol{\Sigma}_{\bar{\mathbf{x}}\bar{\mathbf{x}},k}\mathbf{A}_{m,k}^T \\
\mathbf{K}_{m,k} &= \boldsymbol{\Sigma}_{\bar{\mathbf{x}}\bar{\mathbf{x}},k}\mathbf{A}_{m,k}^T\boldsymbol{\Sigma}_{\mathrm{ww},m,k}^{-1} \\
\boldsymbol{\Sigma}_{\hat{\mathbf{x}}\hat{\mathbf{x}},k} &= (\mathbf{I} - \mathbf{K}_{m,k}\mathbf{A}_{m,k})\boldsymbol{\Sigma}_{\bar{\mathbf{x}}\bar{\mathbf{x}},k} \\
\hat{\mathbf{x}}_k &= \bar{\mathbf{x}}_k + \mathbf{K}_{m,k}\mathbf{w}_k.
\end{aligned}
\tag{7}
$$

The index m marks all quantities belonging to the measurement equation. The index k marking the current epoch, is omitted from here on for the sake of better readability. Thus, only the previously estimated state $\hat{\mathbf{x}}_{k-1}$ and its VCM exhibit a time index in the context of the EKF for the rest of this work.

3.1.3 Inner reliability

The validity of the assumptions in the functional model in (2), the stochastic model assumptions in $\boldsymbol{\Sigma}_{\mathrm{ll}}$ and the corresponding solutions of LSA (fifth and seventh equation in (3)) have to be controlled given the observed values in $\mathbf{l}$. These equations represent the null hypothesis H_0 which is accepted or rejected based on statistical tests. The only assumption, which one can control, is the zero-mean of the expectation value of the residuals (1). This leads to the global test [165] pp. 90 ff.

$$
T_G = \hat{\mathbf{v}}^T \boldsymbol{\Sigma}_{\mathrm{ll}}^{-1} \hat{\mathbf{v}} \begin{cases} H_0: \ T_G \leq T_{G,c}(\alpha) \rightarrow T_G \sim \chi_r^2 \\ H_A: \ T_G > T_{G,c}(\alpha) \rightarrow T_G \sim \chi_{r,\lambda_G}^2 \end{cases}
\tag{8}
$$

which uses the chi-square distribution χ^2 as test distribution. If the test value T_G is not significant (i.e. less or equal than the critical value $T_{G,c}(\alpha)$, where α is the type I error or significance number), there is no reason to reject H_0. In this case the test value follows a central χ_r^2-distribution with $r = b - u$ degrees of freedom. Otherwise, it follows a non-central χ^2-distribution with additional non-centrality parameter λ_G. The global test just detects discrepancies in the model assumptions of H_0, the localization of sources for the discrepancies has to be done in a subsequent procedure. The reason for the rejection of H_0 in the global test can be either an insufficient stochastic model $\boldsymbol{\Sigma}_{\mathrm{ll}}$ or unmodeled effects in the functional model (2). Throughout this thesis, it will be assumed, that the reasons are unmodeled effects and especially systematic deviations in the observations.

Systematic deviations in the observations, are introduced by extension of (1)

$$\mathbf{l} = E\{\mathbf{l}\} + \mathbf{C}\boldsymbol{\nabla} - \mathbf{v} \tag{9}$$

with a deterministic vector $\boldsymbol{\nabla} \in \mathbb{R}^{u_\nabla \times 1}$ and known coefficient matrix $\mathbf{C} \in \mathbb{R}^{n \times u_\nabla}$ [164] pp. 57 ff. $\boldsymbol{\nabla}$ is included in the functional model of an GMM in the overall parameter vector $\hat{\mathbf{x}}_O = [\hat{\mathbf{x}}_A, \hat{\boldsymbol{\nabla}}]^T$, where the original parameters $\hat{\mathbf{x}}$ are numerically not equal anymore to $\hat{\mathbf{x}}_A$ due to the incorporation of $\hat{\boldsymbol{\nabla}}$. [71] pp. 184 ff. show the detailed derivation of the extended functional model in the GMM and the a brief summary of the solutions is

$$
\begin{aligned}
\mathbf{Q}_{\hat{\nabla}\hat{\nabla}} &= (\mathbf{C}^T \mathbf{Q}_{\mathrm{ll}}^{-1} \mathbf{Q}_{\hat{v}\hat{v}} \mathbf{Q}_{\mathrm{ll}}^{-1} \mathbf{C})^{-1} \\
d\hat{\boldsymbol{\nabla}} &= \mathbf{Q}_{\hat{\nabla}\hat{\nabla}} \mathbf{C}^T \mathbf{Q}_{\mathrm{ll}}^{-1} \hat{\mathbf{v}} \\
d\hat{\mathbf{x}}_A &= d\hat{\mathbf{x}} - \mathbf{Q}_{\hat{x}\hat{x}} \mathbf{A}^T \mathbf{Q}_{\mathrm{ll}}^{-1} \mathbf{C} d\hat{\boldsymbol{\nabla}} \\
\mathbf{Q}_{\hat{x}\hat{x},A} &= \mathbf{Q}_{\hat{x}\hat{x}} + \mathbf{A}^+ \mathbf{Q}_{\hat{\nabla}\hat{\nabla}} (\mathbf{A}^+)^T \\
\hat{\mathbf{v}}_A &= \hat{\mathbf{v}} - \mathbf{Q}_{\hat{v}\hat{v}} \mathbf{Q}_{\mathrm{ll}}^{-1} \mathbf{C} d\hat{\boldsymbol{\nabla}} \\
\mathbf{Q}_{\hat{v}\hat{v},A} &= \mathbf{Q}_{\hat{v}\hat{v}} - \mathbf{Q}_{\hat{v}\hat{v}} \mathbf{Q}_{\mathrm{ll}}^{-1} \mathbf{C} \mathbf{Q}_{\hat{\nabla}\hat{\nabla}} \mathbf{C}^T \mathbf{Q}_{\mathrm{ll}}^{-1} \mathbf{Q}_{\hat{v}\hat{v}},
\end{aligned}
\tag{10}
$$

where again the cofactor matrices are used for the computation of the estimated quantities (contrary to the other equations of the test statistics where it is necessary to use the VCMs). Quantities without the index A belong to the H_0 model, as this is the originally evaluated and tested model in (8). Consequently, the inclusion of $\hat{\boldsymbol{\nabla}}$ leads to the model of the alternative hypothesis H_A (with corresponding quantities marked with index A). The advantage of this procedure is, that all quantities from H_A can be computed from the quantities of H_0 without the need of an additional estimation step. The derivation of the global test in H_A

$$T_{G,A} = \hat{\mathbf{v}}_A^T \boldsymbol{\Sigma}_{\mathrm{ll}}^{-1} \hat{\mathbf{v}}_A = \hat{\mathbf{v}}^T \boldsymbol{\Sigma}_{\mathrm{ll}}^{-1} \hat{\mathbf{v}} - d\hat{\boldsymbol{\nabla}}^T \boldsymbol{\Sigma}_{\hat{\nabla}\hat{\nabla}}^{-1} d\hat{\boldsymbol{\nabla}} \tag{11}$$

shows, that in the case, that $\hat{\boldsymbol{\nabla}}$ equals the unmodeled systematic deviations, the term $d\hat{\boldsymbol{\nabla}}^T \boldsymbol{\Sigma}_{\hat{\nabla}\hat{\nabla}}^{-1} d\hat{\boldsymbol{\nabla}}$ equals the non-centrality parameter in (8). Thus, one can directly use the statistical test (also called local test)

$$T_A = d\hat{\boldsymbol{\nabla}}^T \boldsymbol{\Sigma}_{\hat{\nabla}\hat{\nabla}}^{-1} d\hat{\boldsymbol{\nabla}} \begin{cases} H_0 : \ T_A \leq T_{A,c}(\alpha) \rightarrow T_A \sim \chi_{u_\nabla}^2 \\ H_A : \ T_A > T_{A,c}(\alpha) \rightarrow T_A \sim \chi_{u_\nabla, \lambda_A}^2 \end{cases} \tag{12}$$

to check if $\hat{\boldsymbol{\nabla}}$ is the reason for rejection of H_0 in the global test (i.e. a possible sysematic deviation in the observation vector). The statistical tests (8), (11) and (12) are only valid when σ_0^2 is used in the computation of the VCMs from the corresponding cofactor matrices. Using the estimated or aposteriori variance factor $\hat{\sigma}_0^2 = \hat{\mathbf{v}}^T \mathbf{Q}_{\mathrm{ll}}^{-1} \hat{\mathbf{v}}/r$, leads to other underlying distributions, which are e.g. shown in [71] pp. 182 ff. or [139].

In real applications, multiple local tests $T_{A,i}, \ i = 1, ..., n_A$ are performed to identify the reason for the discrepancy in the global test. This has two main implications. First, one cannot use α in (12) as this results in different sensitivities of T_G and $T_{A,i}$ for a certain choice of $\hat{\boldsymbol{\nabla}}_i$. A common choice to overcome this issue is to use the Bonferroni correction $\alpha_A = \alpha/n_A$ [107]. There are also other approaches, in which for each $T_{A,i}$ a corresponding $\alpha_{A,i}$ is computed, leading to a lower type II error β of the testing procedure [60, 9]. The second implication of multiple local tests is, that one has to choose among all significant $T_{A,i}$.

There is a probability of choosing the wrong $H_{A,i}$ and this probability is already introduced in section 2.1.2 as type III error γ [56] pp. 13 ff. For u_∇-dimensional $\hat{\boldsymbol{\nabla}}$ an approach of assessing the type III error is shown in [33] and more literature is available for the 1-dimensional case [188, 187, 142, 68].

The type II error β corresponds to the probability of erroneously rejecting H_A (and implicitly adopting H_0) in (8). It is a preset value and an important quantity for the computation of the MDB

$$d\hat{\nabla}_{0,i} = \sqrt{\frac{\lambda_{A,\chi^2}(\alpha_A, \beta, u_\nabla = 1)}{\mathbf{c}_i^T \boldsymbol{\Sigma}_{\mathrm{ll}}^{-1} \boldsymbol{\Sigma}_{\hat{v}\hat{v}} \boldsymbol{\Sigma}_{\mathrm{ll}}^{-1} \mathbf{c}_i}} \tag{13}$$

where the vector $\mathbf{c}_i$ results from the consideration of only one-dimensional $d\hat{\nabla}_{0,i}$. The computation of $\lambda_{A,\chi^2}(\alpha_A, \beta, 1)$ is e.g. described in [164] pp. 66. (13) is just the rearrangement of (12) in the one-dimensional case and replacing $T_{A,i}$ with the non centrality parameter. The MDB is the main quantity for the assessment of inner reliability and it is the threshold, systematic deviations or outliers have to exceed, such that they can be detected with a preset probability of $1 - \beta$ (i.e. the power of a statistical test) given the type I error α_A. It is also defined for the u_∇-dimensional case [87, 192], which will be also treated herein in section 5.1. The special case of setting $\mathbf{c}_i^T = [0, ..., 1, ..., 0]$ with only the entry at position i leads to the approach of data snooping [165] pp. 103 ff. It is one of the most frequently used testing procedures in geodetic applications. The redundancy numbers r_{ii} being the main diagonal elements of the redundancy matrix

$$\mathbf{R} = \mathbf{Q}_{\hat{v}\hat{v}} \mathbf{Q}_{\mathrm{ll}}^{-1} \tag{14}$$

are also commonly used measures for the assessment of controllability and localization of outliers in single observations.

3.2   Orientation estimation for indoor positioning

3.2.1   Coordinate frames

The aim of orientation determination is to align the smartphone body frame (B-frame) with the navigation frame (N-frame). The local-level frame (L-frame) is an intermediate frame which results, when the z-axis of the B-frame is aligned with the z-axis of the N-frame (from which it only differs by a rotation around the z-axis). All frames are right handed and the rotation angles (i.e. the Euler angles φ, θ and ψ) are counted positive along the short rotation of the x- into the y-axis, the y-axis into the z-axis and the z-axis into the x-axis. The x-axis of the N-frame is aligned with geographic north, the z-axis with the direction of the gravity vector and the y-axis completes the frame by pointing into the east direction. The used coordinate frames are summarized in figure 2 and are adopted from [45] pp. 23 ff.
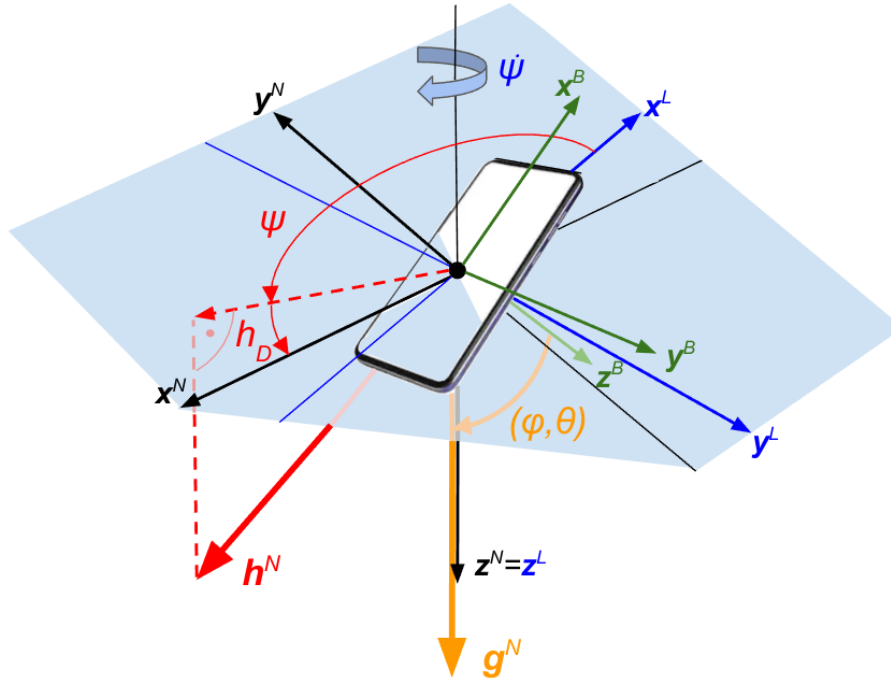
Figure 2: Frames for orientation determination.

The Euler angles are already mentioned which represent one way to parameterize the orientation. Each angle performs the rotation around its corresponding axis and the full rotation from the N-frame into the B-frame (and vice versa) is done with the rotation matrices

$$
\begin{aligned}
\mathbf{R}_N^B &= \mathbf{R}_x(\varphi)\mathbf{R}_y(\theta)\mathbf{R}_z(\psi) \\
\mathbf{R}_B^N &= \mathbf{R}_z(-\psi)\mathbf{R}_y(-\theta)\mathbf{R}_x(-\varphi) \\
&= \mathbf{R}_z^T(\psi)\mathbf{R}_y^T(\theta)\mathbf{R}_x^T(\varphi) \\
\mathbf{R}_x(\varphi) &= \begin{bmatrix} 1 & 0 & 0 \\ 0 & \cos\varphi & -\sin\varphi \\ 0 & \sin\varphi & \cos\varphi \end{bmatrix} \\
\mathbf{R}_y(\theta) &= \begin{bmatrix} \cos\theta & 0 & \sin\theta \\ 0 & 1 & 0 \\ -\sin\theta & 0 & \cos\theta \end{bmatrix} \\
\mathbf{R}_z(\psi) &= \begin{bmatrix} \cos\psi & -\sin\psi & 0 \\ \sin\psi & \cos\psi & 0 \\ 0 & 0 & 1 \end{bmatrix}.
\end{aligned}
\tag{15}
$$

The Euler angles can be determined when sensing the gravity vector $\mathbf{g}^N$ with the accelerometer and the earth magnetic field $\mathbf{h}^N$ with the magnetometer. Both quantities are known and the numeric value for $\mathbf{g}^N = [0.0, 0.0, 9.81]^T$ $[m/s^2]$ which is accurate enough provided that a low-cost accelerometer is used. The EMF values $[20.9, 0.0, 44.3]^T$ $[\mu T]$ are available in a coordinate frame which x-axis is aligned with the magnetic north pole (z-axis is the same as in the N-frame). In order to derive $\mathbf{h}^N$, these values have

to be rotated into the N-frame by using the magnetic declination $\mathbf{R}_z(h_D = 4.99°)$ (according to figure 2). The numeric values are derived from an earth magnetic field model for Vienna, Austria[1]. One decimal is also accurate enough considering a standard deviation of the magnetometer noise of $0.5 - 3.0\ \mu T$

3.2.2 Sensor observation models

In the static and noise-free case, the accelerometer provides the gravity vector in the B-frame $\mathbf{g}^B = \mathbf{R}_x(\varphi)\mathbf{R}_y(\theta)\mathbf{g}^N$, and the roll angle φ and the pitch angle θ (i.e. the inclination angles) are computed with

$$
\varphi = \arctan \frac{-g_y^B}{g_z^B}
$$
$$
\theta = \arctan \frac{g_x^B}{g_y^B \cdot \sin\varphi + g_z^B \cdot \cos\varphi}.
$$
(16)

With known inclination angles, the yaw angle ψ is derived in the same manner. In the non-perturbated and noise-free case, the magnetometer provides $\mathbf{h}^B = \mathbf{R}_N^B \mathbf{h}^N$, which is rearranged $\mathbf{h}^L = \mathbf{R}_y(-\theta)\mathbf{R}_x(-\varphi)\mathbf{h}^B = \mathbf{R}_z(\psi)\mathbf{h}^N$ such that

$$
\psi = \arctan \frac{h_y^L}{h_x^L}.
$$
(17)

A more detailed derivation of these equations can be found e.g. in [138].

The gyroscope provides the rate of change of the B-frame from epoch $k-1$ to k, which is expressed as angular velocities around the B-frame axes. According to [168] pp. 42, the angular velocities of the Euler angles are computed with

$$
\dot\varphi = (\omega_y^B \cdot \sin\varphi + \omega_z^B \cdot \cos\varphi)\tan\theta + \omega_x^B
$$
$$
\dot\theta = \omega_y^B \cos\varphi - \omega_z^B \sin\varphi
$$
$$
\dot\psi = \frac{1}{\cos\theta}(\omega_y^B \cdot \sin\varphi + \omega_z^B \cdot \cos\varphi).
$$
(18)

When using the Euler angle paremeterization, the gimbal lock problem has to be considered. It appears when the pitch angle takes the value of $\pm 90°$. In this case, there is an infinite number of combinations of φ and ψ, describing the same rotation from the N-frame into the B-frame (and vice versa). Mathematically, this appears as divisions by zero in (16) and (18). The orientation quaternion is a parameterization which doesn't exhibit this behavior. The computation of the orientation quaternion from accelerometer and magnetometer is e.g. shown in [171] and the propagation with the gyroscope as well as the conversions to Euler angles and rotation matrix elements can be found in [97] pp. 264 ff. and pp. 167 ff.

As mentioned, the equations to derive orientation information from accelerometer, magnetometer and gyroscope are only valid in the case of a static sensor, no noise and no systematic deviations. In reality, each sensor observation contains a number of systematic deviations and the sensor noise ϵ_i which is always treated as Gaussian distributed with zero-mean. The observation models for accelerometer and gyroscope are

---

[1]ngdc.noaa.gov/geomag/calculators/magcalc.shtml?model=igrf#igrfwmm, retrieved 03.08.2022

$$\mathbf{a}^B = \mathbf{R}_N^B \mathbf{g}^N + \boldsymbol{\delta}_a^B + \boldsymbol{\epsilon}_a$$
$$\boldsymbol{\omega}^B = \mathbf{R}_N^B \boldsymbol{\omega}_{ie}^N + \boldsymbol{\delta}_\omega^B + \boldsymbol{\epsilon}_\omega,$$

(19)

where $\boldsymbol{\delta}_a^B$ and $\boldsymbol{\delta}_\omega^B$ are the bias vectors. Herein, they are treated as deterministic quantities but it is also common to model them stochastically (especially when they are included in the state vector), e.g. as first-order Gauss-Markov process [31] pp. 355 ff. $\boldsymbol{\omega}_{ie}^N$ is the earth rotation in the B-frame which can be neglected (i.e. set to zero) as this quantity can only be reasonably determined with exhaustive calibration, careful alignment and a static sensor with very long observation duration [69]. When these sensors are carried by pedestrians, additional effects appear in (19). For the accelerometer, these accelerations due to user motion show a periodic pattern and can be modeled as additional states [151, 65] or they can be mitigated by fusing accelerometer and gyroscope to propagate the gravity vector in the B-frame $\mathbf{g}^B$ [152]. The magnetometer is subject to multiple systematic deviations [86, 144] and the full observation model is

$$\mathbf{m}^B = (\mathbf{I} + \boldsymbol{\Delta}_{sn})[(\mathbf{I} + \boldsymbol{\Delta}_{si})\mathbf{R}_N^B(\mathbf{h}^N + \boldsymbol{\delta}_a^N) + \boldsymbol{\delta}_{hi}^B] + \boldsymbol{\delta}_b^B + \boldsymbol{\epsilon}_m,$$

(20)

where $\boldsymbol{\Delta}_{sn}$ and $\boldsymbol{\Delta}_{si}$ are matrices to account for the sensor scale plus non orthogonality as well as soft-iron influences (magnetization due to earth magnetic field of components on the sensor platform which are fixed with respect to the magnetometer). $\boldsymbol{\delta}_{hi}^B$ is the hard iron bias, which subsumes the magnetic flux density due to magnetic components on the sensor platform (also fixed with respect to the magnetometer). $\boldsymbol{\delta}_a^N$ represents magnetic anomalies in the sensor's environment and $\boldsymbol{\delta}_b^B$ is the sensor bias of the magnetometer. The magnetometer observation model (20) corresponds to the one used in [45] pp. 221 with the difference, that also sensor scale and non orthogonality $(\mathbf{I} + \boldsymbol{\Delta}_{sn})$ is considered.

4   Publications and main results

In this section, the main outcomes of the publications [A1], [A2] and [A3] are outlined which build the core of this thesis. [A1] contains the derivations of the EKF in the GHM with a focus on an overdetermined system equation. Thus, it is possible to fuse the smartphone sensor observations from multiple pedestrians heading into the same direction within one EKF, which is conceptually implemented in this publication. Additionally, inner reliability is assessed, based on the redundancy numbers (14) in [A1]. [A2] contains further analysis of inner reliability in the GHM. On the one hand, the different measures for the assessment of inner reliability are outlined and on the other hand, the main factors which influence these measures are identified. Numerical examples of plane fitting and yaw computation with multiple static magnetometers are evaluated to strengthen the theoretic considerations. In [A3], an algorithm is designed for orientation determination with a MARG sensor array which can be used in real scenarios. Implicitly, the design of this algorithm is guided by the aim of improving inner reliability. Together with some heuristics, this algorithm exhibits robustness to magnetic anomalies and outperforms other algorithms from relevant publications in a small-scale pedestrian indoor positioning experiment.

Beside the three main publications, also other work has been published in the course of this thesis, which is partially closely related to the topics covered herein. [B1] elaborate on the absolute positioning in indoor environments using Wi-Fi, RFID and ambient magnetic fields. In [B2], further indoor positioning experiments are performed with regard to RFID. Publication [B3] can be seen as the starting point of this thesis. An EKF for indoor orientation estimation with a MARG sensor array is presented with a focus on statistical tests on the filter innovation to detect turns and suppress the influence of systematic deviations. In [B4], the redundancy numbers for the individual sensor observations are derived and analyzed - for the same implementation of the EKF as in [B3] - by using the GHM. The analysis of building utilization with a mobility graph is the focus of [B5]. [B6] use the robot operating system (ROS) in different applications of engineering geodesy to point out its advantages.

The next three subsections contain the main ideas and outcomes of the main publications. The publications itself are included in appendix A.

4.1   Publication A1

The motivation of [A1] are the results from [B3], where systematic effects appear in the determined smartphone orientation. An EKF with Euler angles used as direct observations has been applied in [B3] which leads to the problem, that inner reliability cannot be directly analyzed for the smartphone observations (i.e. gyroscope, accelerometer and magnetometer). Thus, the EKF update equations are derived in the GHM and overdetermination in the system equation is considered in [A1].

The overall functional model of the EKF in the GHM consists in a first step of the state propagation model $\mathbf{f}_{\bar{\mathbf{x}}}$ as introduced in (4) and the observation model $\mathbf{f}_m$ implicitly containing $\hat{\mathbf{x}}$ and $\mathbf{l}_m$ (i.e. the functional model of the GHM (2)). In order to consider the overdetermination of the system equation, another function vector $\mathbf{f}_s^* \in \mathbb{R}^{b_s^* \times 1}$ is included in the overall functional model

$$\mathbf{0} = \begin{bmatrix} \mathbf{f}_{\bar{\mathbf{x}}}(\hat{\mathbf{x}}_{k-1} + \hat{\mathbf{v}}_{\hat{\mathbf{x}}_{k-1}}, \ \boldsymbol{\upsilon} + \hat{\mathbf{v}}_\upsilon, \ \boldsymbol{\zeta} + \hat{\mathbf{v}}_\zeta) - \hat{\mathbf{x}} \\ \mathbf{f}_s^*(\hat{\mathbf{x}}, \ \hat{\mathbf{x}}_{k-1} + \hat{\mathbf{v}}_{\hat{\mathbf{x}}_{k-1}}, \ \boldsymbol{\upsilon} + \hat{\mathbf{v}}_\upsilon, \ \boldsymbol{\zeta} + \hat{\mathbf{v}}_\zeta) \\ \mathbf{f}_m(\hat{\mathbf{x}}, \mathbf{l}_m + \hat{\mathbf{v}}_{l_m}) \end{bmatrix} = \begin{bmatrix} \mathbf{f}_s(\hat{\mathbf{x}}_{k-1} + \hat{\mathbf{v}}_{\hat{\mathbf{x}}_{k-1}}, \boldsymbol{\upsilon} + \hat{\mathbf{v}}_\upsilon, \boldsymbol{\zeta} + \hat{\mathbf{v}}_\zeta, \hat{\mathbf{x}}) \\ \mathbf{f}_m(\hat{\mathbf{x}}, \mathbf{l}_m + \hat{\mathbf{v}}_{l_m}) \end{bmatrix}. \quad (21)$$

$\mathbf{f}_s^*$ implicitly contains the states of the previous and current epoch $\hat{\mathbf{x}}_{k-1}$ and $\hat{\mathbf{x}}$ as well as the system control $\boldsymbol{\upsilon}$ and system noise $\boldsymbol{\zeta}$ (note that the index k for the current epoch is again omitted). For

convenience, $\mathbf{f}_{\bar{\mathbf{x}}}$ and $\mathbf{f}_s^*$ are joined into one function vector $\mathbf{f}_s \in \mathbb{R}^{b_s \times 1}$ in (21), where $b_s = u + b_s^*$. The linearization of (21) leads to the same structure as in LSA based on the GHM

$$
\begin{aligned}
\mathbf{0} &\approx \begin{bmatrix} \mathbf{0} \\ \mathbf{w}_s^* \\ \mathbf{w}_m \end{bmatrix} + \begin{bmatrix} -\mathbf{I} \\ \mathbf{A}_s^* \\ \mathbf{A}_m \end{bmatrix} (\hat{\mathbf{x}} - \bar{\mathbf{x}}) + \begin{bmatrix} \mathbf{T} & \mathbf{Y} & \mathbf{Z} & \mathbf{0} \\ \mathbf{T}^* & \mathbf{Y}^* & \mathbf{Z}^* & \mathbf{0} \\ \mathbf{0} & \mathbf{0} & \mathbf{0} & \mathbf{B}_m \end{bmatrix} \begin{bmatrix} \hat{\mathbf{v}}_{\hat{\mathbf{x}}_{k-1}} \\ \hat{\mathbf{v}}_\upsilon \\ \hat{\mathbf{v}}_\zeta \\ \hat{\mathbf{v}}_{l_m} \end{bmatrix} \\
&\approx \begin{bmatrix} \mathbf{w}_s \\ \mathbf{w}_m \end{bmatrix} + \begin{bmatrix} \mathbf{A}_s \\ \mathbf{A}_m \end{bmatrix} d\hat{\mathbf{x}} + \begin{bmatrix} \mathbf{B}_s & \mathbf{0} \\ \mathbf{0} & \mathbf{B}_m \end{bmatrix} \begin{bmatrix} \hat{\mathbf{v}}_{l_s} \\ \hat{\mathbf{v}}_{l_m} \end{bmatrix} \\
&\approx \mathbf{w} + \mathbf{A} d\hat{\mathbf{x}} + \mathbf{B}\hat{\mathbf{v}} \\
\mathbf{A}_s^* &= \frac{\partial \mathbf{f}_s^*}{\partial \hat{\mathbf{x}}}|_{\bar{\mathbf{x}}, \hat{\mathbf{x}}_{k-1}, \boldsymbol{\upsilon}, \boldsymbol{\zeta}} \\
\mathbf{T}^* &= \frac{\partial \mathbf{f}_s^*}{\partial \hat{\mathbf{v}}_{\hat{\mathbf{x}}_{k-1}}}|_{\bar{\mathbf{x}}, \hat{\mathbf{x}}_{k-1}, \boldsymbol{\upsilon}, \boldsymbol{\zeta}} \\
\mathbf{Y}^* &= \frac{\partial \mathbf{f}_s^*}{\partial \hat{\mathbf{v}}_\upsilon}|_{\bar{\mathbf{x}}, \hat{\mathbf{x}}_{k-1}, \boldsymbol{\upsilon}, \boldsymbol{\zeta}} \\
\mathbf{Z}^* &= \frac{\partial \mathbf{f}_s^*}{\partial \hat{\mathbf{v}}_\zeta}|_{\bar{\mathbf{x}}, \hat{\mathbf{x}}_{k-1}, \boldsymbol{\upsilon}, \boldsymbol{\zeta}}.
\end{aligned}
\tag{22}
$$

It can be seen in the first line of (22), that the overdetermined part of the system equation results in an additional misclosure vector $\mathbf{w}_s^* \in \mathbb{R}^{b_s^* \times 1}$. As $\hat{\mathbf{x}}$ is implicitly included in $\mathbf{f}_s^*$, the corresponding design matrix $\mathbf{A}_s^* \in \mathbb{R}^{b_s^* \times u}$ is not equal to the identity matrix anymore (compared to the common state propagation model $\mathbf{f}_{\bar{\mathbf{x}}}$). Therefore, the system equation as a whole, exhibits a more complex structure compared to the common EKF, because the quantities belonging to the overall system equation, i.e. misclosure vector $\mathbf{w}_s \in \mathbb{R}^{b_s \times 1}$ and design matrix $\mathbf{A}_s \in \mathbb{R}^{b_s \times u}$, differ from the zero vector and identity matrix. $\hat{\mathbf{v}}_{l_s} = [\hat{\mathbf{v}}_{\hat{\mathbf{x}}_{k-1}}, \hat{\mathbf{v}}_\upsilon, \hat{\mathbf{v}}_\zeta]^T \in \mathbb{R}^{n_s \times 1}$ contains the residuals of the observation groups belonging to the system equation, where $n_s = u + n_\upsilon + n_\zeta$. The quantities in (22) are inserted into (3) to derive the update equations for $\hat{\mathbf{x}}$ and its VCM $\boldsymbol{\Sigma}_{\hat{\mathbf{x}}\hat{\mathbf{x}}}$

$$
\begin{aligned}
\boldsymbol{\Sigma}_{\hat{\mathbf{x}}\hat{\mathbf{x}}} &= (\mathbf{A}_s^T (\mathbf{B}_s \boldsymbol{\Sigma}_{\mathrm{ll}_s} \mathbf{B}_s^T)^{-1} \mathbf{A}_s + \mathbf{A}_m^T (\mathbf{B}_m \boldsymbol{\Sigma}_{\mathrm{ll}_m} \mathbf{B}_m^T)^{-1} \mathbf{A}_m)^{-1} \\
\hat{\mathbf{x}} &= \bar{\mathbf{x}} - \mathbf{K}_s \mathbf{w}_s - \mathbf{K}_m \mathbf{w}_m \\
\mathbf{K}_s &= \boldsymbol{\Sigma}_{\hat{\mathbf{x}}\hat{\mathbf{x}}} \mathbf{A}_s^T (\mathbf{B}_s \boldsymbol{\Sigma}_{\mathrm{ll}_s} \mathbf{B}_s^T)^{-1} \\
\mathbf{K}_m &= \boldsymbol{\Sigma}_{\hat{\mathbf{x}}\hat{\mathbf{x}}} \mathbf{A}_m^T (\mathbf{B}_m \boldsymbol{\Sigma}_{\mathrm{ll}_m} \mathbf{B}_m^T)^{-1}.
\end{aligned}
\tag{23}
$$

$\boldsymbol{\Sigma}_{\hat{\mathbf{x}}\hat{\mathbf{x}}}$ clearly differs from the common EKF (fourth line in (7)), because $\mathbf{A}_s \neq \mathbf{I}$ and the inversion of the whole term in the first line of (23) does not lead to a comparably simple structure. The state update (second line in (23)) exhibits an additional term due to the overdetermined system equation, where $\mathbf{K}_s \in \mathbb{R}^{u \times b_s}$ is the corresponding Kalman gain matrix.

In [A1], this novel EKF formulation is used in an attempt to improve inner reliability in orientation estimation for indoor positioning of pedestrians. The assumption is, that two ore more persons walk in the same direction, each carrying a MARG sensor array equipped smartphone. Thus, the yaw angle ψ is the same for all considered pedestrians but the roll φ and pitch θ angles still have to be determined individually. For two pedestrians, the linearized system equation has the following structure

$$\mathbf{f}_s(\bar{\mathbf{x}}, \hat{\mathbf{x}}_{k-1}, \boldsymbol{\omega}^B, \boldsymbol{\zeta}) = \mathbf{w}_s = \begin{bmatrix} 0 \\ 0 \\ 0 \\ 0 \\ 0 \\ \mathrm{w}_s^* \end{bmatrix} = \begin{bmatrix} \hat{\varphi}_{k-1,1} + dt \cdot \zeta_{\varphi,1} - \bar{\varphi}_1 \\ \hat{\theta}_{k-1,1} + dt \cdot \zeta_{\theta,1} - \bar{\theta}_1 \\ \hat{\varphi}_{k-1,2} + dt \cdot \zeta_{\varphi,2} - \bar{\varphi}_2 \\ \hat{\theta}_{k-1,2} + dt \cdot \zeta_{\theta,2} - \bar{\theta}_2 \\ \hat{\psi}_{k-1} + \frac{1}{\cos \hat{\theta}_{k-1,1}} \cdot (\omega_{y,1}^B \cdot \sin \hat{\varphi}_{k-1,1} + \omega_{z,1}^B \cdot \cos \hat{\varphi}_{k-1,1}) - \bar{\psi} \\ \hat{\psi}_{k-1} + \frac{1}{\cos \hat{\theta}_{k-1,2}} \cdot (\omega_{y,2}^B \cdot \sin \hat{\varphi}_{k-1,2} + \omega_{z,2}^B \cdot \cos \hat{\varphi}_{k-1,2}) - \bar{\psi} \end{bmatrix} \tag{24}$$

As already mentioned, φ and θ have to be estimated for both considered pedestrians which is indicated by the numbers 1 and 2 in the index. ψ does not exhibit this subscript as it is assumed to be the same for both pedestrians. Still, two condition equations can be set up, as both smartphones provide gyroscope observations (i.e. ω_y^B and ω_z^B with corresponding indices 1 and 2) which represent the system control quantities. From the fifth line in (24), the predicted yaw angle $\bar{\psi}$ is directly computed, leading to a zero entry at the fifth position of $\mathbf{w}_s$. The sixth line in (24) is redundant and therefore a discrepancy w_s^* appears at the sixth position of $\mathbf{w}_s$. The measurement equation consists of both equations in (16) as well as (17) for both pedestrians (i.e. in sum there are six condition equations). The observation vector $\mathbf{l}_m = [\mathbf{a}_1^B, \mathbf{a}_2^B, \mathbf{m}_1^B, \mathbf{m}_2^B]$ contains the accelerometer and magnetometer observations from both smartphones. The redundancy numbers are partially increased by using this approach (see appendix A.1). Still, there are observations, in which systematic deviations cannot be reasonably detected. That is the reason for the further analysis of inner reliability in [A2] in the following section. Additionally, the influence of adjustments in the stochastic model on the redundancy numbers is analyzed in [A1] (see appendix A.1).

In the application of pedestrian indoor navigation, there are some critical steps, in order to realize the approach of fusing the smartphone sensor observations from multiple pedestrians. Crowd-sourcing requires, that pedestrians share their smartphone data via a local network or the internet, such that a centralized algorithm can fuse these observations. It is also necessary to detect, if several pedestrians are heading in the same direction, which would be the case e.g. in corridors. In the case that the algorithm should provide the smartphone orientation in real-time, the pedestrians should be at the same time in such areas. Despite this implementation problems, the approach of fusing the observations from multiple pedestrians in one EKF is very promising with its ability to increase redundancy and therefore improve inner reliability (which is stated in section 5.2). This could be a possible field of future research, especially when considering other applications such as robotics or autonomous driving.

4.2 Publication A2

The results from [A1] show, that increasing the redundancy and adjusting the stochastic model, are not per se effective actions to improve the localization of biases. [A2] aims to provide the derivation of inner reliability in the GHM from scratch. Alternative hypothesis with one dimensional additional parameters are introduced in the GHM and the corresponding statistical tests (i.e. local tests) are derived. Beside assessing the detectability of systematic deviations with the MDB, also the separability of the alternative hypothesis (identifiability) is considered in [A2]. Therefore, the correlation coefficient ρ_{ij} of the local test values is used which equals its computation in the GMM.

For a better understanding of the inner reliability in the GHM, the equation of the residuals is analyzed

$$\hat{\mathbf{v}} = -\mathbf{B}^+(\mathbf{I} - \mathbf{A}\mathbf{A}^+)\mathbf{w}. \tag{25}$$

The difference to the GMM is the mapping from the observations space (with dimension n) into the condition space where the misclosures $\mathbf{w}$ are defined (i.e. the dimension is b) with the Jacobian matrix $\mathbf{B}$. The reverse mapping is done with the pseudo-inverse $\mathbf{B}^+$ given in (3). If one axis of the observation space is located in the null space of $\mathbf{B}$ (and therefore also $\mathbf{B}^+$), systematic deviations affecting it, cannot be detected. In this case, systematic deviations are not mapped into the condition space and the misclosures do not reflect their presence. A consequence could be, that in this case, systematic deviations can be neglected as they will have no effect on the estimated parameters either. Still, this is not a satisfying solution. On the one hand, one has to determine a threshold from which on it is necessary to control such observations and on the other hand, the influence of an observation on the misclosures is time-varying when using an EKF (in general). Thus, functional models exhibiting such a property should be avoided. Column vectors of $\mathbf{B}$ which are close to the zero vector, or with components being much smaller than the components of the other column vectors, are a rough indicator for such defects if the variances of the observations are very similar.

The second important mapping is the one from the condition space into the parameter space (and back again) which is the same situation as in the GMM. This mapping mainly defines the orthogonal decomposition of $\mathbf{w}$ into $\hat{\mathbf{w}} = \mathbf{A}\mathbf{A}^+\mathbf{w}$ and $\hat{\mathbf{v}}_{\mathrm{w}} = (\mathbf{I} - \mathbf{A}\mathbf{A}^+)\mathbf{w}$. Hence, misclosures which are located mainly (or even fully) in the parameters space do not contribute to the computation of $\hat{\mathbf{v}}_{\mathrm{w}}$ (i.e. they are located in the null space of the matrix $\mathbf{I} - \mathbf{A}\mathbf{A}^+$). Consequently, it is hardly possible to detect systematic deviations in such observations.

These findings are stated based on numeric examples of plane fitting and static yaw computation with a magnetometer in [A2] (see appendix A.2). Possibilities on introducing additional condition equations in the functional model to improve inner reliability are also outlined. The static yaw computation should be concisely recapitulated, as it is closely related to the evaluations in section 5.2 of this thesis. The idea is, using multiple, leveled and aligned magnetometers to estimate the yaw angle ψ with respect to magnetic north in a LSA. The functional model contains equation (17) for each magnetometer with standard deviation for both components being 0.1 μT and the known value of ψ is 0°. There is one alternative hypothesis containing a one dimensional bias for each observation (i.e. for all x- and y-components of the magnetometers). The MDBs of the x-components are unlimited in this case, as they have no effect on the misclosures as long as the y-components are zero. Thus, the corresponding column vectors in $\mathbf{B}$ equal approximately the zero vector. Additionally, it is not possible to correctly assign a detected bias as the local tests for the x- and y-component of one magnetometer are one-to-one correlated (figure 3 left). This means, that if only evaluating the global test and consecutive local tests, it is not possible to correctly assign a bias.
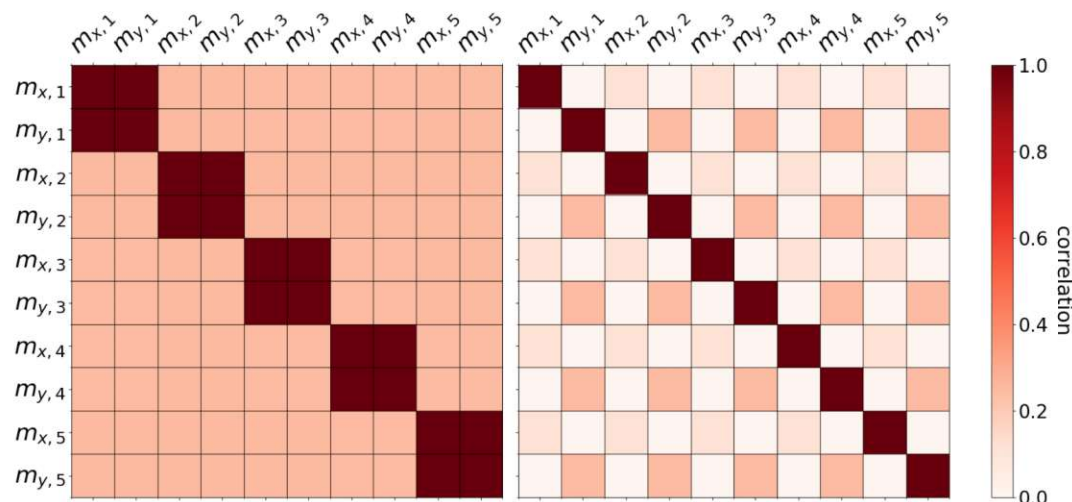
Figure 3: ρ_{ij} for the local tests of one dimensional biases in the static yaw computation. Left: only using the yaw condition equations (17). Right: additional condition equation on the magnitude of magnetometer observations.

In order to solve this issue, an additional condition equation is introduced for each magnetometer which controls the magnitude of the observed magnetic field by comparing it with the corresponding known value (see section 3.2). The MDBs are now equal for all x- and y-components (approximately four times the standard deviation) and also the alternative hypothesis or local tests are decorrelated (figure 3 right).

The analysis of inner reliability in the GHM in [A2] is based on one dimensional additional parameters in the alternative hypothesis. In the appendix of [A2], the estimation of any kind of systematic deviations in the observations is introduced. Still, this publication does not contain the test statistics and measures for inner reliability of multi dimensional additional parameter vectors. The intention of section 5.1 of this thesis is to close this gap and provide the MDB and correlation cefficient of local tests in the general, multi-dimensional case.

4.3 Publication A3

In publication [A3], an algorithm is developed, which provides the absolute smartphone orientation being robust to magnetic anomalies. Instead of fusing the observations from IMU and magnetometer in one estimation procedure (e.g. an EKF), the computation of inclination and heading as well as the magnetic anomaly detection are separated from each other. Pedestrian trajectories vary more or less only in the xy-plane of the N-frame (see section 3.2) as the user walks through the environment (i.e. rotations only appear around the vertical z-axis). Variations or rotations around the x- or y-axis of the N-frame occur only if the smartphone holding mode changes. Thus, pedestrian trajectories do not exhbit enough information to fully decorrelate the orientation states as well as parameterized sensor errors if they would be estimated within one EKF. Systematic deviations therefore would spread on all states and negatively influence all states.

Magnetic anomalies cause the highest magnitudes of systematic deviations in the computed orientation in indoor environments based on the coupling of IMU and magnetometer. Thus, the focus in [A3] is on the reliable detection of magnetic anomalies and use magnetometer observations for the heading computation

only in their absence. Magnetic anomaly detection is done with the global test values computed from the bias-EKF which is based on the magnetometer observation model

$$
\begin{aligned}
\mathbf{m}^B &= \mathbf{R}_N^B \mathbf{h}^N + \boldsymbol{\delta}_s^B + \boldsymbol{\delta}_f^B + \boldsymbol{\epsilon}_\mathrm{m} \\
\boldsymbol{\delta}_s^B &= (\mathbf{I} + \boldsymbol{\Delta}_{sn})\boldsymbol{\delta}_{hi}^B + \boldsymbol{\delta}_b^B \\
\boldsymbol{\delta}_f^B &= \mathbf{R}_N^B \boldsymbol{\delta}_a^N + (\boldsymbol{\Delta}_{sn}\boldsymbol{\Delta}_{si} + \boldsymbol{\Delta}_{sn} + \boldsymbol{\Delta}_{si})\mathbf{R}_N^B(\mathbf{h}^N + \boldsymbol{\delta}_a^N)
\end{aligned}
\tag{26}
$$

derived from (20). The state vector of the bias-EKF only contains the slow varying magnetometer bias $\boldsymbol{\delta}_s^B$. This quantity subsumes the sensor errors varying slowly in time in the B-frame. Contrary to this quantity, is the fast varying magnetometer bias $\boldsymbol{\delta}_f^B$ which exhibits a high variability in the B-frame. The assumption behind using the global test value from the bias EKF is, that if it is significant, $\boldsymbol{\delta}_f^B$ is present which cannot be represented by $\boldsymbol{\delta}_s^B$. In such time spans magnetometer observations should not be used to update the absolute heading. The heading is propagated with the gyroscope and is used as observation in the bias-EKF. Thus, undetected magnetometer errors cannot spread on the heading which would negatively affect the performance of the overall orientation estimation algorithm.

The developed algorithm requires an accurately known initial heading or the initial calibration of the magnetometer (e.g. with ellipsoid fitting) to provide an accurate heading. In order to relax this requirement, the magnetometer observations are monitored in an independent module with conditions derived from the known quantities of the EMF. With this additional procedure it is possible to detect discrepancies in the initial heading.

Beside the magnetic anomalies and other magnetometer related errors, systematic deviations have to be considerd for the the accelerometer and gyroscope too. As both sensors are sensitive to accelerations, the effects due to the user motion have to be considered, which is done in the inclination computation module according to [152, 65]. It is a challenging task to perfectly separate user motion from the remaining accelerometer signal. This is also the reason for not considering sensor biases for the accelerometer, because their magnitude is usually much lower than the user-motion-induced accelerations. The gyroscope bias only becomes apparent if the angular rates are integrated over a longer period of time. Thus, if regular updates for the inclination (from the accelerometer) and the heading (from the magnetometer) are available, the influence of the bias remains small or even negligible and it is not parameterized in the proposed approach.

The purposed orientation estimation algorithm is mainly heuristic as it neglects accelerometer and gyroscope biases and it requires a priori decisions of the developer (e.g. relying on the initial heading or on the additional conrol procedure of the magnetometer observations). Still, it exhibits a good performance as it is shown on the basis of numeric examples and a small scale experiment with a highly accurate ground truth of the smartphone orientation. Figure 4 shows the deviations of the estimated heading from the ground truth value for twelve trajectories (4 specific trajectories walked with three different smarthpones). The smartphones are carried in texting mode in all trajectories. In the trajectories 1 and 2 the user walked in the whole experiment area because the corresponding magnetometer observations are used to compute magnetic field maps by using spatial interpolation. That is the reason why they are much longer compared to trajectories 3 and 4, where the user walks straight through the experiment area and is closely passing a magnet which causes a heavy magnetic anomaly.

The developed algorithm (called "own" in figure 4) is compared to three other well established algorithms: the complementary filter "madgw" from [124], the EKF "magyq" from [145] and the EKF "han" from [53]. The overall root mean square error of the estimated heading from the developed algorithm is

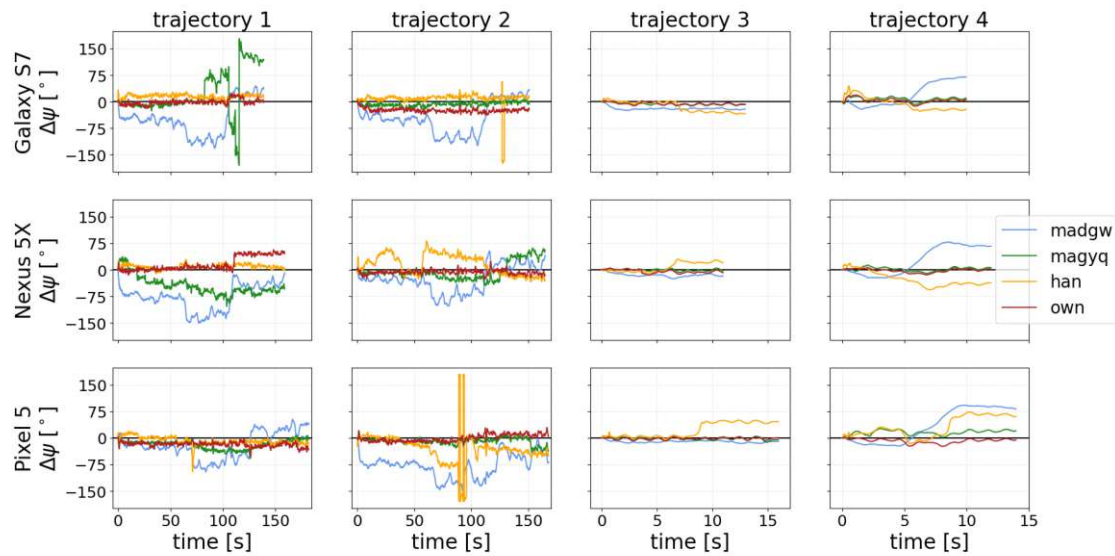$\approx 40~\%$ lower compared to the other algorithms.

Figure 4: Deviations $\Delta\psi$ of the estimated heading or yaw from the corresponding ground truth values. The developed algorihtm "own" is compared to three other algorithms from literature.

Due to the chosen measurement setup, larger scale experiments are not possible. Nevertheless, these experiments indicate the potential of the developed algorithm to be integrated into indoor positioning systems to further elaborate on the orientation performance.

5 Summarizing consideration and analysis

In this section, the insights from the publications for this thesis about inner reliability in the GHM are further elaborated. Section 5.1 provides the general equations to formulate alternative hypothesis in LSA and EKF in the GHM as well as the equations to compute the corresponding measures of inner reliability. In section 5.2, a simulation study is performed on the two newly developed algorithms for orientation determination in indoor positioning. Focus is on the analysis of inner reliability measures and their comparison to a baseline algorithm, to show, the potential of application of these algorithms. The whole chapter serves as a wrap-up to properly connect the publications and also raises further gaps and questions, which could be the topic of future research.

5.1 Inner reliability in the GHM

5.1.1 LSA

In this section, the statistical tests and corresponding measures of inner reliability for any non-linear systematic deviations in the observations are derived. The starting point is appendix A of [A2] with the generalized observation model

$$\mathbf{f}_l(\mathbf{l}, \tilde{\boldsymbol{\nabla}}) = E\{\mathbf{l}\} - \mathbf{v},\tag{27}$$

where $\mathbf{f}_l \in \mathbb{R}^{n \times 1}$ is a function vector which provides calibrated but still noisy observations. It is important, to have a numeric value $\boldsymbol{\nabla}^*$ for the additional parameters representing the systematic deviations, such that $\mathbf{f}_l(\mathbf{l}, \boldsymbol{\nabla}^*) = \mathbf{l}$. This enables major simplifications in the functional model

$$\begin{aligned}
\mathbf{0} &= \mathbf{f}(\hat{\mathbf{x}}_A, \mathbf{f}_l(\mathbf{l}, \hat{\boldsymbol{\nabla}}) + \hat{\mathbf{v}}_A) \\
&\approx \mathbf{f}(\hat{\mathbf{x}}^{(0)}, \mathbf{f}_l(\mathbf{l}, \hat{\boldsymbol{\nabla}}^{(0)}) + \hat{\mathbf{v}}^{(0)}) \\
&\quad + \frac{\partial \mathbf{f}}{\partial \hat{\mathbf{v}}_A}\big|_{\mathbf{f}_l(\mathbf{l}, \hat{\boldsymbol{\nabla}}^{(0)}) + \hat{\mathbf{v}}^{(0)}, \hat{\mathbf{x}}^{(0)}} (\hat{\mathbf{v}}_A - \hat{\mathbf{v}}^{(0)}) \\
&\quad + \frac{\partial \mathbf{f}}{\partial \hat{\mathbf{x}}_A}\big|_{\mathbf{f}_l(\mathbf{l}, \hat{\boldsymbol{\nabla}}^{(0)}) + \hat{\mathbf{v}}^{(0)}, \hat{\mathbf{x}}^{(0)}} (\hat{\mathbf{x}}_A - \hat{\mathbf{x}}^{(0)}) \\
&\quad + \frac{\partial \mathbf{f}}{\partial \mathbf{f}_l}\big|_{\mathbf{f}_l(\mathbf{l}, \hat{\boldsymbol{\nabla}}^{(0)}) + \hat{\mathbf{v}}^{(0)}, \hat{\mathbf{x}}^{(0)}} \cdot \frac{\partial \mathbf{f}_l}{\partial \hat{\boldsymbol{\nabla}}}\big|_{\mathbf{l}, \hat{\boldsymbol{\nabla}}^{(0)}} (\hat{\boldsymbol{\nabla}} - \hat{\boldsymbol{\nabla}}^{(0)})
\end{aligned}\tag{28}$$

of the alternative hypothesis. When setting $\hat{\boldsymbol{\nabla}}^{(0)} = \boldsymbol{\nabla}^*$, the importance of $\mathbf{f}_l(\mathbf{l}, \boldsymbol{\nabla}^*) = \mathbf{l}$ becomes apparent, because many quantities of (28) are equal to the quantities of H_0. Together with $\hat{\mathbf{v}}^{(0)} = \mathbf{0}$, $\frac{\partial \mathbf{f}}{\partial \hat{\mathbf{v}}_A} = \frac{\partial \mathbf{f}}{\partial \mathbf{f}_l} = \mathbf{B}$ and $\frac{\partial \mathbf{f}_l}{\partial \hat{\boldsymbol{\nabla}}} = \mathbf{C}$ the linearized functional model of H_A becomes

$$\mathbf{0} \approx \mathbf{w} + \mathbf{B}\hat{\mathbf{v}}_A + \mathbf{A}d\hat{\mathbf{x}}_A + \mathbf{BC}d\hat{\boldsymbol{\nabla}} = \mathbf{w} + \mathbf{B}\hat{\mathbf{v}}_A + \begin{bmatrix} \mathbf{A} & \mathbf{BC} \end{bmatrix} \begin{bmatrix} d\hat{\mathbf{x}}_A \\ d\hat{\boldsymbol{\nabla}} \end{bmatrix} = \mathbf{w} + \mathbf{B}\hat{\mathbf{v}}_A + \mathbf{A}_O d\hat{\mathbf{x}}_O,\tag{29}$$

which can be solved with (3). This is outlined in detail in appendix C.1. The overall parameter vector with corresponding cofactor matrix is

$$
\begin{aligned}
\mathbf{Q}_{\hat{x}\hat{x},O} &= \begin{bmatrix} \mathbf{Q}_{\hat{x}\hat{x},A} & \mathbf{Q}_{\hat{x}\hat{\nabla}} \\ \mathbf{Q}_{\hat{x}\hat{\nabla}}^T & \mathbf{Q}_{\hat{\nabla}\hat{\nabla}} \end{bmatrix} = \begin{bmatrix} \mathbf{Q}_{\hat{x}\hat{x}} + \mathbf{A}^+\mathbf{B}\mathbf{C}\mathbf{Q}_{\hat{\nabla}\hat{\nabla}}\mathbf{C}^T\mathbf{B}^T(\mathbf{A}^+)^T & -\mathbf{A}^+\mathbf{B}\mathbf{C}\mathbf{Q}_{\hat{\nabla}\hat{\nabla}} \\ -\mathbf{Q}_{\hat{\nabla}\hat{\nabla}}\mathbf{C}^T\mathbf{B}^T(\mathbf{A}^+)^T & (\mathbf{C}^T\mathbf{Q}_{ll}^{-1}\mathbf{Q}_{\hat{v}\hat{v}}\mathbf{Q}_{ll}^{-1}\mathbf{C})^{-1} \end{bmatrix} \\
d\hat{\mathbf{x}}_O &= \begin{bmatrix} d\hat{\mathbf{x}}_A \\ d\hat{\boldsymbol{\nabla}} \end{bmatrix} = \begin{bmatrix} d\hat{\mathbf{x}} - \mathbf{A}^+\mathbf{B}\mathbf{C}d\hat{\boldsymbol{\nabla}} \\ \mathbf{Q}_{\hat{\nabla}\hat{\nabla}}\mathbf{C}^T\mathbf{Q}_{ll}^{-1}\hat{\mathbf{v}} \end{bmatrix}.
\end{aligned}
\tag{30}
$$

Due to the inclusion of $\hat{\boldsymbol{\nabla}}$ in the overall parameter vector, the cofactor matrix $\mathbf{Q}_{\hat{x}\hat{x},A}$ of the original parameters in the H_A-model is increased compared to the H_0-model. This is reasonable, as each additional parameter reduces the redundancy by one. The incorporation of $\hat{\boldsymbol{\nabla}}$ also leads to a shift $\mathbf{A}^+\mathbf{B}\mathbf{C}d\hat{\boldsymbol{\nabla}}$ of the parameters of the H_0-model wich is the basic equation for the outer reliability (i.e. replacing $d\hat{\boldsymbol{\nabla}}$ with the corresponding MDB). In the same manner also the residuals with corresponding cofactor matrix are derived in the H_A-model

$$
\begin{aligned}
\mathbf{Q}_{\hat{v}\hat{v},A} &= \mathbf{Q}_{\hat{v}\hat{v}} - \mathbf{Q}_{\hat{v}\hat{v}}\mathbf{Q}_{ll}^{-1}\mathbf{C}\mathbf{Q}_{\hat{\nabla}\hat{\nabla}}\mathbf{C}^T\mathbf{Q}_{ll}^{-1}\mathbf{Q}_{\hat{v}\hat{v}} \\
\hat{\mathbf{v}}_A &= \hat{\mathbf{v}} - \mathbf{Q}_{\hat{v}\hat{v}}\mathbf{Q}_{ll}^{-1}\mathbf{C}d\hat{\boldsymbol{\nabla}}.
\end{aligned}
\tag{31}
$$

These are the same equations as in the GMM. As outlined in 4.2, the difference is in the computation of $\hat{\mathbf{v}}$ and $\mathbf{Q}_{\hat{v}\hat{v}}$, as here the additional mapping from the observation space into the condition space occurs. Because of the same structure of $\hat{\mathbf{v}}_A$ in the GHM and the GMM, the same statistical tests described in section 3.1.3 can be used for the assessment of inner reliability. Contrary to section 3.1.3, from here on, the restriction to the case of $u_\nabla = 1$ should be omitted. This leads to a more complex MDB, as it is not a scalar value anymore, but the equation

$$
\lambda_{A,\chi^2}(\alpha_A, \beta, u_\nabla) = d\hat{\boldsymbol{\nabla}}_0^T \boldsymbol{\Sigma}_{\hat{\nabla}\hat{\nabla}}^{-1} d\hat{\boldsymbol{\nabla}}_0
\tag{32}
$$

describes an u_∇-dimensional hyper-ellipsoid (in [71] pp. 301 it is also called threshold-ellipsoid). $d\hat{\boldsymbol{\nabla}}_0$ is not a unique vector but a set of vectors lying on the surface of the hyper-ellipsoid. It is possible to derive a condition on the euclidean norm $\|d\hat{\boldsymbol{\nabla}}_0\|_2$ (which is shown in detail in appendix C.2)

$$
\|d\hat{\boldsymbol{\nabla}}_0\|_2 \leq \sqrt{\lambda_{A,\chi^2}(\alpha_A, \beta, u_\nabla) \cdot \sqrt{e_{\max}}},
\tag{33}
$$

where $e_{\max}$ is the maximum eigenvalue of $\boldsymbol{\Sigma}_{\hat{\nabla}\hat{\nabla}}$. The square root of the maximum eigenvalue corresponds to the spectral norm. This is also a reasonable choice for inner reliability, as it represents the MDB with the maximum norm among all vectors described by (32). A vector quantity can be derived by using the eigenvector $\mathbf{u}_{\max}$ which corresponds to $e_{\max}$

$$
d\hat{\boldsymbol{\nabla}}_0 = \sqrt{\lambda_{A,\chi^2}(\alpha_A, \beta, u_\nabla) \cdot \sqrt{e_{\max}}} \cdot \mathbf{u}_{\max}.
\tag{34}
$$

The computation of $\lambda_{A,\chi^2}(\alpha_A, \beta, u_\nabla)$ is done iteratively by increasing λ_i until $(1-\phi_{\chi^2}(T_{A,c}(\alpha_A), u_\nabla, \lambda_i)) > (1-\beta)$ exceeds the preset power of the statistical test (where $\phi_{\chi^2}()$ is the cumulative distribution function of the non-central chi-square distribution with u_∇ degrees of freedom). The final λ_i equals the required $\lambda_{A,\chi^2}(\alpha_A, \beta, u_\nabla)$.

Until now, only one alternative hypothesis is considered in this section. In the case of multiple alternative hypothesis $H_{A,i}$, $i = 1, ..., n_A$, one has to consider the type III error, which is already introduced in section 3.1.3. [187] state that it is dependent on α_A, β and the correlation coefficients ρ_{ij} of the

test statistics (12) for each considered alternative hypothesis. As α, β and the number of considered alternative hypothesis n_A are preset values (and therefore α_A is also fixed), the correlation coefficients ρ_{ij} are the quantities of interest. If only one-dimensional alternative hypothesis are considered, the ρ_{ij} can be directly computed from the elements s_{ij}, $i, j = 1, ..., n_A$ of $\mathbf{Q}_{\hat{\nabla}\hat{\nabla}}^{-1}$ (for details see appendix C.3)

$$\rho_{ij} = \frac{s_{ij}}{\sqrt{s_{ii} \cdot s_{ij}}}. \tag{35}$$

If there are more than one additional parameter in the alternative hypothesis, it is necessary to extend the derivation of the correlation coefficient. [33] is the only publication, which could be found, describing this case and it states that ρ_{ij} corresponds to the minimum angle between all possible vector pairs from the two vector spaces $\mathcal{H}_i$ and $\mathcal{H}_j$ belonging to $H_{A,i}$ and $H_{A,j}$. Herein, ρ_{ij} is derived based on another reasoning, which leads to very similar results. The additional parameter vectors $d\hat{\boldsymbol{\nabla}}_i$ and $d\hat{\boldsymbol{\nabla}}_j$ from two alternative hypothesis are computed from the residuals $\hat{\mathbf{v}}$ of H_0

$$d\hat{\boldsymbol{\nabla}}_{\mathrm{O}} = \begin{bmatrix} d\hat{\boldsymbol{\nabla}}_i \\ d\hat{\boldsymbol{\nabla}}_j \end{bmatrix} = \begin{bmatrix} \boldsymbol{\Sigma}_{\hat{\nabla}_i \hat{\nabla}_i} \mathbf{C}_i^T \boldsymbol{\Sigma}_{\mathrm{ll}}^{-1} \\ \boldsymbol{\Sigma}_{\hat{\nabla}_j \hat{\nabla}_j} \mathbf{C}_j^T \boldsymbol{\Sigma}_{\mathrm{ll}}^{-1} \end{bmatrix} \hat{\mathbf{v}} = \mathbf{F}\hat{\mathbf{v}} \tag{36}$$

where the VCM of the overall additional parameter vector $d\hat{\boldsymbol{\nabla}}_{\mathrm{O}}$ is computed with variance propagation law

$$\boldsymbol{\Sigma}_{\hat{\nabla}_{\mathrm{O}} \hat{\nabla}_{\mathrm{O}}} = \mathbf{F} \boldsymbol{\Sigma}_{\hat{v}\hat{v}} \mathbf{F}^T = \begin{bmatrix} \boldsymbol{\Sigma}_{\hat{\nabla}_i \hat{\nabla}_i} & \boldsymbol{\Sigma}_{\hat{\nabla}_i \hat{\nabla}_j} \\ \boldsymbol{\Sigma}_{\hat{\nabla}_i \hat{\nabla}_j}^T & \boldsymbol{\Sigma}_{\hat{\nabla}_j \hat{\nabla}_j} \end{bmatrix}$$
$$\boldsymbol{\Sigma}_{\hat{\nabla}_i \hat{\nabla}_j} = \boldsymbol{\Sigma}_{\hat{\nabla}_i \hat{\nabla}_i} \mathbf{C}_i^T \boldsymbol{\Sigma}_{\mathrm{ll}}^{-1} \boldsymbol{\Sigma}_{\hat{v}\hat{v}} \boldsymbol{\Sigma}_{\mathrm{ll}}^{-1} \mathbf{C}_j \boldsymbol{\Sigma}_{\hat{\nabla}_j \hat{\nabla}_j}. \tag{37}$$

The covariance matrix $\boldsymbol{\Sigma}_{\hat{\nabla}_i \hat{\nabla}_j}$ describes the influence of the random variable $d\hat{\boldsymbol{\nabla}}_j$ on the distribution of the random variable $d\hat{\boldsymbol{\nabla}}_i$. This relation can be seen in the equation of the conditional expectation (e.g. in [89] pp. 131)

$$E\{d\hat{\boldsymbol{\nabla}}_i | d\hat{\boldsymbol{\nabla}}_j\} = E\{d\hat{\boldsymbol{\nabla}}_i\} + \boldsymbol{\Sigma}_{\hat{\nabla}_i \hat{\nabla}_j} \boldsymbol{\Sigma}_{\hat{\nabla}_j \hat{\nabla}_j}^{-1} (d\hat{\boldsymbol{\nabla}}_j - E\{d\hat{\boldsymbol{\nabla}}_j\}). \tag{38}$$

In the optimum case, $d\hat{\boldsymbol{\nabla}}_i$ and $d\hat{\boldsymbol{\nabla}}_j$ are independent (i.e. not correlated) which is the case if $\boldsymbol{\Sigma}_{\hat{\nabla}_i \hat{\nabla}_j} = \mathbf{0}$. One way to assess the correlation is, to compute the correlation matrix from $\boldsymbol{\Sigma}_{\hat{\nabla}_{\mathrm{O}}, \hat{\nabla}_{\mathrm{O}}}$ and analyze the corresponding correlation coefficients. Herein, the spectral norm (see also appendix C.2) of $\boldsymbol{\Sigma}_{\hat{\nabla}_i \hat{\nabla}_j}$ is used as scalar measure for the correlation, which corresponds to the maximum singular value (i.e. the square root of the maximum eigenvalue). The formulation of the eigenvalue problem of a rectangular matrix (e.g. [42] pp. 70 ff.)

$$\sqrt{e_{\max}} \cdot \mathbf{u}_{i,\max} = \boldsymbol{\Sigma}_{\hat{\nabla}_i \hat{\nabla}_j} \mathbf{u}_{j,\max} \tag{39}$$

indicates, that $\sqrt{e_{\max}}$ describes the correlation. $\sqrt{e_{\max}}$ is the length of the image of the eigenvector $\mathbf{u}_{j,\max}$ in the vector space $\mathcal{H}_i$. If it is zero, a change along the direction of $\mathbf{u}_{j,\max}$ has no influence in $\mathcal{H}_i$, i.e. there is no correlation. The bigger $\sqrt{e_{\max}}$, the bigger gets the influence of a change along the direction of $\mathbf{u}_{j,\max}$ in $\mathcal{H}_i$, i.e. the correlation increases. To ensure, that $\sqrt{e_{\max}}$ describes ρ_{ij} (i.e. it has to be in the range of $[-1, 1]$), the additional parameter vectors are standardized with ([71] pp. 99)

$$
\begin{aligned}
d\hat{\boldsymbol{\nabla}}'_i &= \boldsymbol{\Sigma}_{\hat{\nabla}_i\hat{\nabla}_i}^{-\frac{1}{2}} d\hat{\boldsymbol{\nabla}}_i \\
d\hat{\boldsymbol{\nabla}}'_j &= \boldsymbol{\Sigma}_{\hat{\nabla}_j\hat{\nabla}_j}^{-\frac{1}{2}} d\hat{\boldsymbol{\nabla}}_j.
\end{aligned}
\tag{40}
$$

Thus, $\sqrt{e_{\max}}$ is computed with singular value decomposition of the matrix $\boldsymbol{\Sigma}_{\hat{\nabla}_i\hat{\nabla}_i}^{-\frac{1}{2}} \boldsymbol{\Sigma}_{\hat{\nabla}_i\hat{\nabla}_j} \boldsymbol{\Sigma}_{\hat{\nabla}_j\hat{\nabla}_j}^{-\frac{1}{2}}$ and it is used as measure for the correlation of test statistic ρ_{ij} herein.

5.1.2 EKF

In section 4.1, the EKF is formulated as the linearized functional model of LSA. Thus, the equations from section 5.1.1 can be directly applied to the description of inner reliability in the EKF, considering that

$$
\begin{aligned}
\boldsymbol{\Sigma}_{\mathrm{ll}} &= \begin{bmatrix}
\boldsymbol{\Sigma}_{\hat{\mathbf{x}}\hat{\mathbf{x}},k-1} & \mathbf{0} & \mathbf{0} & \mathbf{0} \\
\mathbf{0} & \boldsymbol{\Sigma}_{vv} & \mathbf{0} & \mathbf{0} \\
\mathbf{0} & \mathbf{0} & \boldsymbol{\Sigma}_{\zeta\zeta} & \mathbf{0} \\
\mathbf{0} & \mathbf{0} & \mathbf{0} & \boldsymbol{\Sigma}_{\mathrm{ll},m}
\end{bmatrix} \\
\mathbf{A} &= \begin{bmatrix}
-\mathbf{I} \\
\mathbf{A}_s^* \\
\mathbf{A}_m
\end{bmatrix} \\
\mathbf{B} &= \begin{bmatrix}
\mathbf{T} & \mathbf{Y} & \mathbf{Z} & \mathbf{0} \\
\mathbf{T}^* & \mathbf{Y}^* & \mathbf{Z}^* & \mathbf{0} \\
\mathbf{0} & \mathbf{0} & \mathbf{0} & \mathbf{B}_m
\end{bmatrix}.
\end{aligned}
\tag{41}
$$

Inner reliability is analyzed for the system control $\boldsymbol{v}$ and the observations of the measurement equation $\mathbf{l}_m$, as these are the quantities possibly being affected by systematic deviations. Statistical tests (and therefore inner reliability) on the residuals of the previously estimated state $\hat{\mathbf{x}}_{k-1}$ are not considered herein, as this is the quantity which should be improved in the EKF update anyway. Another reason is, that the variance or VCM of the state should decrease with time in order to have a filter effect (i.e. stochastic observability - see section 2.1.1). Hence, it is very unlikely, that local tests (12) for systematic deviations in $\hat{\mathbf{x}}_{k-1}$ are the most significant ones when searching for the reason of discrepancy in the identification step. One can also consider H_A-models for the system noise $\boldsymbol{\zeta}$ as analysis tool to check if the propagation model of the system equation describes reality appropriately. Herein, inner reliability is only analyzed for $\boldsymbol{v}$ and $\mathbf{l}_m$.

The general form of the two considered obsevation models for $\boldsymbol{v}$ and $\mathbf{l}_m$ are

$$
\begin{aligned}
\mathbf{f}_l(\mathbf{l}, \boldsymbol{\nabla}_v) &= \begin{bmatrix} \hat{\mathbf{x}}_{k-1}^T & \mathbf{f}_v(\boldsymbol{v}, \boldsymbol{\nabla}_v)^T & \boldsymbol{\zeta}^T & \mathbf{l}_m^T \end{bmatrix}^T \\
\mathbf{f}_l(\mathbf{l}, \boldsymbol{\nabla}_{1,m}) &= \begin{bmatrix} \hat{\mathbf{x}}_{k-1}^T & \boldsymbol{v}^T & \boldsymbol{\zeta}^T & \mathbf{f}_{l,m}(\mathbf{l}_m, \boldsymbol{\nabla}_{1,m})^T \end{bmatrix}^T
\end{aligned}
\tag{42}
$$

with corresponding Jacobi matrices

$$\mathbf{C}_v = \begin{bmatrix} \mathbf{0}^T & (\frac{\partial \mathbf{f}_v}{\partial \hat{\boldsymbol{\nabla}}_v})^T & \mathbf{0}^T & \mathbf{0}^T \end{bmatrix}^T$$

$$\mathbf{C}_{\mathrm{l},m} = \begin{bmatrix} \mathbf{0}^T & \mathbf{0}^T & \mathbf{0}^T & (\frac{\partial \mathbf{f}_{\mathrm{l},m}}{\hat{\boldsymbol{\nabla}}_{\mathrm{l},m}})^T \end{bmatrix}^T \tag{43}$$

Thus, the analysis of inner reliability is in principle the same as in LSA.

In the field of assessing inner reliablity in the EKF exist approaches for further research. In EKF-applications, one has to consider the temporal extent of systematic deviations too as they are not restricted to one epoch in general. For example a sensor bias in smartphone observations is present from the first EKF epoch on or becomes apparent after a certain duration (change of battery charge or temperature). Another example are magnetic anomalies which are present in certain areas in a building (see section 4.3). Thus, the matrices in (43) can be extended to cover a certain time window with an arbitrary number of epochs. The strict way to compute the global test and local tests for multiple epochs is, to formulate the considered epochs in an LSA and compute the corresponding residuals with its VCM. This does not lead to an efficient computation because also intertemporal VCMs appear which is also stated in [150] on page 17. Especially for long trajectories and low-cost or edge devices with limited capablties on processing and battery performance, this approach becomes intractable. An alternative is, to neglect intertemporal correlations and stack the residuals from the considered epochs vertically and the corresponding VCMs diagonally as e.g. done in [175, 176]. Still, this approach fastly becomes complicated, as not all systematic deviations are constant with time. Sensor biases can be modeled as constant parameters in the B-frame and the stacking approach could help to detect its presence. Other deviations such as magnetic anomalies heavily vary with time (to be more precise: they vary with the change of the sensor position and attitude with respect to the source of anomaly). In such cases, the functional model of the alternative hypothesis considering multiple epochs becomes very complicated (if it is expressable at all) and the valuable property of a simple computation of inner reliability measures gets lost. A shaping filter (e.g. outlined in [113]) can be used in these scenarios to handle auto-correlated observations. Another approach could be, to use distributed EKFs (see section 2.1.1), i.e. process each hypothesis within a separate filter and use the results, where the global test is lowest. This approach can be also classified as a combinatorial method (see section 2.1.2). The risk here is, that the state vectors of the alternative hypothesis become unobservable. As these approaches are out of scope of this thesis, the inner reliability measures are only analyzed for each epoch in the next section. But these considerations represent aspects in further research.

5.2   EKF example for summary

In this section, the methodologic advancements from this thesis are combined with the developed algorithms for orientation estimation in indoor positioning. Based on a simulated indoor scenario, the outcomes and findings from [A1], [A2] and [A3] are connected to provide a concise summary.

The approach to create a simulated trajectory with corresponding smartphone sensor observations is basically the same as in [A3]. Figure 5 shows the trajectory and the indoor environment with magnetic anomalies. The only difference to the evaluations done in [A3] is, that only the 2D-case is considered which means, that the rotation from the B-frame into the L-frame is already solved. Thus, the only orientation parameter is the yaw angle ψ and the observations are $\mathbf{m}^L = [\mathrm{m}_x^L, \mathrm{m}_y^L]^T$ and $\dot{\psi}$. A baseline algorithm as well as the two algorithms developed in the course of this thesis are used to estimate ψ and the magnetometer bias $\boldsymbol{\delta}_s^L$ (the index s indicates, that the slow-varying systematic deviations are

subsumed within this quantity, for a detailed discussion see [A3]). Due to the focus of the thesis on inner reliability, the analysis of the results is restricted to the MDBs $d\hat{\boldsymbol{\nabla}}_{0,i}$ and the correlation coefficients ρ_{ij} with corresponding statistical tests (i.e. global test and local tests). This also means, that in the context of DIA, only the detection of sysyematic deviations in the observations and the corresponding identification (i.e. the correct allocation) are investigated. Adaptation strategies are not considered herein although the algorithm from [A3] implicitly contains measures for mitigating the systematic deviations induced by magnetic anomalies. In the first step, $d\hat{\boldsymbol{\nabla}}_{0,i}$ and ρ_{ij} are computed with unbiased observations, i.e. the magnetic anomalies (red spots in figure 5) are not considered in the computation of the observations. In the second step, the magnetic anomalies affect the computed observations and the global test T_G (8) as well as the local tests $T_{A,i}$ (12) are used to assess the detection and identification performance.
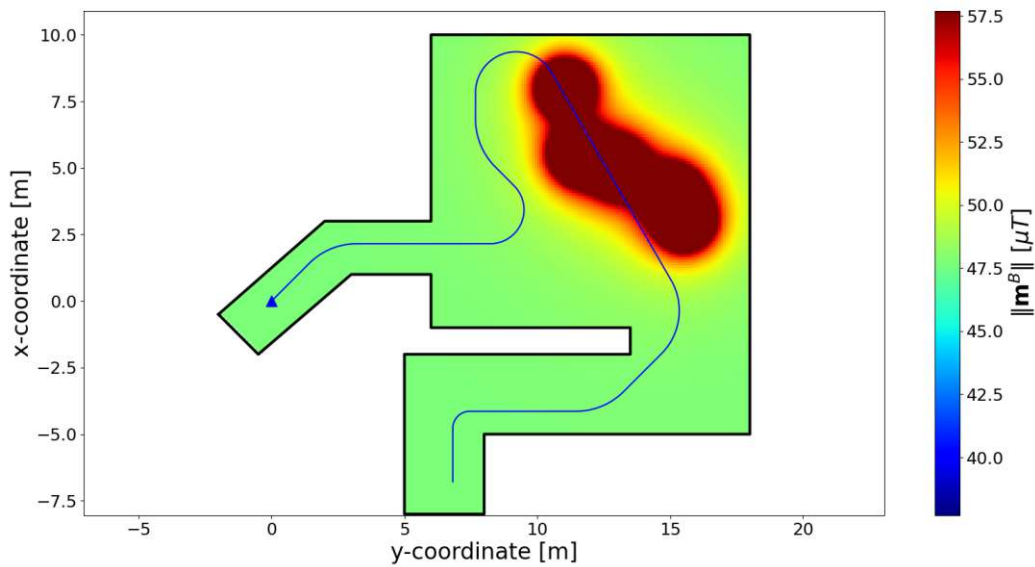
Figure 5: Simulated scenario with colormap showing the observed magentometer magnitude (green being areas where only the EMF is sensed, i.e. the unaffected case). The blue triangle marks the starting point of the trajectory (blue line).

The EKF acting as baseline algorithm (called "standard EKF"), exhibits the functional model

$$
\begin{aligned}
\text{system equation: } \mathbf{0} &= \begin{bmatrix} \hat{\bar{\psi}}_{k-1} + dt \cdot \dot{\psi} + 0.5 \cdot dt^2 \cdot \zeta_\psi - \bar{\psi} \\ \hat{\delta}^L_{s,x,k-1} + dt \cdot \zeta_x - \bar{\delta}^L_{s,x} \\ \hat{\delta}^L_{s,x,k-1} + dt \cdot \zeta_y - \bar{\delta}^L_{s,y} \end{bmatrix} \\
\text{measurement equation: } \mathbf{w}_m &= \begin{bmatrix} \mathrm{h}^N_x \cdot \cos\bar{\psi} + \bar{\delta}^L_{s,x} - \mathrm{m}^L_x \\ -\mathrm{h}^N_x \cdot \sin\bar{\psi} + \bar{\delta}^L_{s,y} - \mathrm{m}^L_y \end{bmatrix}
\end{aligned}
\tag{44}
$$

which can be evaluated with the common EKF update equations in the GMM. dt is the time interval and ζ_i are the system noise components for each state. h^N_x is the x-component of the earth magnetic field vector $\mathbf{h}^N$ and it is assumed, that the x-axis of the N-frame coincides with the magnetic north direction (i.e. $h^N_y = 0$). h^N_x is a deterministic quantity which value is derived from the magnetic field model already mentioned in section 3.2.1. The stochastic model equals a block diagonal matrix (see (41)) with

the sub-matrices for the EKF-observations in the system and measurement equation

$$
\boldsymbol{\Sigma}_{vv} = \begin{bmatrix} \sigma_{\dot\psi}^2 \end{bmatrix}
$$
$$
\boldsymbol{\Sigma}_{\zeta\zeta} = \begin{bmatrix} \sigma_{\zeta,\psi}^2 & 0 & 0 \\ 0 & \sigma_{\zeta,x}^2 & 0 \\ 0 & 0 & \sigma_{\zeta,y}^2 \end{bmatrix}
$$
$$
\boldsymbol{\Sigma}_{\mathrm{ll},m} = \begin{bmatrix} \sigma_{\mathrm{m},x}^2 & 0 \\ 0 & \sigma_{\mathrm{m},y}^2 \end{bmatrix}. \tag{45}
$$

The assumption is, that systematic deviations can be present in $\dot\psi$ or in $\mathbf{m}^L$. Thus, the alternative hypothesis with corresponding observation models are

$$
\begin{aligned}
H_{A,1} &: \ \mathrm{f}_v(\boldsymbol{v}, \nabla_{\dot\psi}) = \dot\psi + \nabla_{\dot\psi} \\
H_{A,2} &: \ \mathbf{f}_{l,m}(\mathbf{l}_m, \boldsymbol{\nabla}_{\mathrm{m}}) = \mathbf{m}^L + \boldsymbol{\nabla}_{\mathrm{m}}.
\end{aligned} \tag{46}
$$

Note the difference between the indexes. The italic m stands for "measurement equation" whereas the normal m indicates the additional parameter for the magnetometer bias (i.e. the systematic deviations which are not subsumed in $\boldsymbol{\delta}_s^L$). The algorithm from [A1] (called "multi-user EKF") requires, that multiple pedestrians walk in the same direction (which could be the case e.g. in corridors). Each pedestrian represents a sub-system which shares the same heading or yaw angle with the other pedestrians. $\boldsymbol{\delta}_s^L$ has to be estimated for each of the pedestrian's smartphone magnetometer independently. In this simulated scenario two pedestrians are considered and the functional model is

$$
\text{overdetermined system equation: } \mathbf{w}_s = \begin{bmatrix} 0 \\ 0 \\ 0 \\ 0 \\ 0 \\ \mathrm{w}_s^* \end{bmatrix} = \begin{bmatrix} \hat\delta_{s,x,1,k-1}^L + dt \cdot \zeta_{x,1} - \bar\delta_{s,x,1}^L \\ \hat\delta_{s,x,1,k-1}^L + dt \cdot \zeta_{y,1} - \bar\delta_{s,y,1}^L \\ \hat\delta_{s,x,2,k-1}^L + dt \cdot \zeta_{x,2} - \bar\delta_{s,x,2}^L \\ \hat\delta_{s,x,2,k-1}^L + dt \cdot \zeta_{y,2} - \bar\delta_{s,y,2}^L \\ \hat\psi_{k-1} + dt \cdot \dot\psi_1 + 0.5 \cdot dt^2 \cdot \zeta_{\psi,1} - \bar\psi \\ \hat\psi_{k-1} + dt \cdot \dot\psi_2 + 0.5 \cdot dt^2 \cdot \zeta_{\psi,2} - \bar\psi \end{bmatrix}
$$
$$
\text{measurement equation: } \mathbf{w}_m = \begin{bmatrix} \mathrm{h}_x^N \cdot \cos\bar\psi + \bar\delta_{s,x,1}^L - \mathrm{m}_{x,1}^L \\ -\mathrm{h}_x^N \cdot \sin\bar\psi + \bar\delta_{s,y,1}^L - \mathrm{m}_{y,1}^L \\ \mathrm{h}_x^N \cdot \cos\bar\psi + \bar\delta_{s,x,2}^L - \mathrm{m}_{x,2}^L \\ -\mathrm{h}_x^N \cdot \sin\bar\psi + \bar\delta_{s,y,2}^L - \mathrm{m}_{y,2}^L \end{bmatrix}, \tag{47}
$$

where the assumption is, that both pedestrians walked exactly the same trajectory. The stochastic model is derived by stacking the VCMs from (45) diagonally according to the number of considered pedestrians. For the sake of comparability with the other algorithms, systematic deviations are only considered for the first pedestrian

$$H_{A,1}: \; \mathbf{f}_v(\boldsymbol{v}, \nabla_{\dot{\psi}}) = \begin{bmatrix} \dot{\psi}_1 + \nabla_{\dot{\psi}} \\ \dot{\psi}_2 \end{bmatrix}$$

$$H_{A,2}: \; \mathbf{f}_{l,m}(\mathbf{l}_m, \boldsymbol{\nabla}_{\mathrm{m}}) = \begin{bmatrix} \mathbf{m}_1^L + \boldsymbol{\nabla}_{\mathrm{m}} \\ \mathbf{m}_2^L \end{bmatrix}. \tag{48}$$

The algorithm from [A3] (called "mag-bias EKF") consists of several submodules, which, in sum, provide ψ being robust or less sensitive to the influence of magnetic anomalies. Inner reliability is analyzed for the bias-EKF (a submodule of the mag-bias EKF) from [A3], whose state vector only contains $\boldsymbol{\delta}_s^L$

$$\text{system equation: } \mathbf{0} = \begin{bmatrix} \hat{\delta}_{s,x,k-1}^L + dt \cdot \zeta_x - \bar{\delta}_{s,x}^L \\ \hat{\delta}_{s,y,k-1}^L + dt \cdot \zeta_y - \bar{\delta}_{s,y}^L \end{bmatrix}$$

$$\text{measurement equation: } \mathbf{w}_m = \begin{bmatrix} \mathrm{h}_x^N \cdot \cos\psi + \bar{\delta}_{s,x}^L - \mathrm{m}_x^L \\ -\mathrm{h}_x^N \cdot \sin\psi + \bar{\delta}_{s,y}^L - \mathrm{m}_y^L \end{bmatrix} \tag{49}$$

and ψ is included in $\mathbf{l}_m$ (propagated with $\dot{\psi}$ outside of the EKF - see [A3]). As there is no control input, $\boldsymbol{\Sigma}_{vv}$ is not present in the stochastic model and σ_ψ^2 is computed with variance propagation (i.e. it is a time-variable quantity)

$$\boldsymbol{\Sigma}_{\zeta\zeta} = \begin{bmatrix} \sigma_{\zeta,x}^2 & 0 \\ 0 & \sigma_{\zeta,y}^2 \end{bmatrix}$$

$$\boldsymbol{\Sigma}_{\mathrm{ll},m} = \begin{bmatrix} \sigma_\psi^2 & 0 & 0 \\ 0 & \sigma_{\mathrm{m},x}^2 & 0 \\ 0 & 0 & \sigma_{\mathrm{m},y}^2 \end{bmatrix}. \tag{50}$$

The observation models for the two considered alternative hypothesis are

$$H_{A,1}: \; \mathbf{f}_{l,m}(\mathbf{l}_m, \nabla_\psi) = \begin{bmatrix} \psi + \nabla_\psi \\ \mathbf{m}^L \end{bmatrix}$$

$$H_{A,2}: \; \mathbf{f}_{l,m}(\mathbf{l}_m, \boldsymbol{\nabla}_{\mathrm{m}}) = \begin{bmatrix} \psi \\ \mathbf{m}^L + \boldsymbol{\nabla}_{\mathrm{m}} \end{bmatrix}. \tag{51}$$

∇_ψ is divided by dt in the following analyis in order to be comparable to $\nabla_{\dot{\psi}}$ from the standard and multi-user EKF.

The main difference of the multi-user EKF compared to the standard EKF is, that there are more equations in the system and measurement equation, i.e. the redundancy is increased. The mag-bias EKF stands out, because of the exclusion of ψ from the state vector, i.e. the number of states is decreased whilst redundancy stays the same as in the standard EKF.

The EKFs are all initialized by using the known heading at $k = 0$ and setting $\hat{\boldsymbol{\delta}}_{s,0}^L = \mathbf{0}$ (with corresponding variances $\sigma_{\hat{\psi},0}^2$, $\sigma_{\hat{\delta},x,0}^2$ and $\sigma_{\hat{\delta},y,0}^2$). Table 1 shows the values for all quantities which are set before the execution of the three considered algorithms.

Table 1: Preset values for the simulated scenario.

quantity	value
dt	$0.02\ s$
$\sigma_{\hat{\psi},0}$	$10.0\ °$
$\sigma_{\hat{\delta},x,0},\ \sigma_{\hat{\delta},y,0}$	$3.0\ \mu T$
$\sigma_{\zeta,\psi}$	$0.05\ °/s^2$
$\sigma_{\zeta,x},\ \sigma_{\zeta,y}$	$0.1\ \mu T/s$
$\sigma_{\dot{\psi}}$	$0.1\ °/s$
$\sigma_{\mathrm{m},x},\ \sigma_{\mathrm{m},y}$	$1.0\ \mu T$

Figure 6 shows the MDBs computed by applying the three previously described algorithms to the trajectory from figure 5 neglecting the magnetic anomalies.
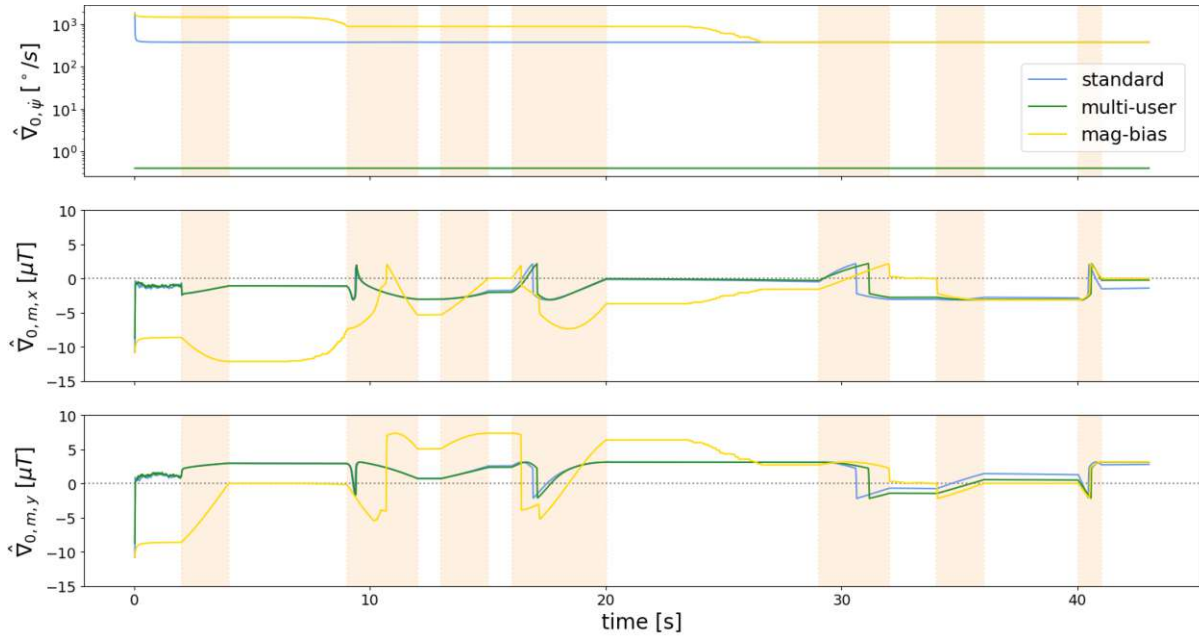
Figure 6: MDBs for the considered additional parameters. The y-axis of the top plot is logarithmically scaled. The orange vertical areas indicate the timespans where the pedestrian is turning.

For the standard EKF as well as for the mag-bias EKF, $\dot{\psi}$ is the problematic observation as the corresponding MDB is some hundred degree per second. Only with the multi-user EKF it is possible to reasonably detect gyroscope biases due to a MDB of approximately $0.4\ °/s$. The MDBs of the magnetometer observations are more or less the same for the standard EKF and the multi-user EKF. When using the mag-bias EKF, $\hat{\boldsymbol{\nabla}}_{0,\mathrm{m}}$ is considerably higher compared to the other two algorithms until approximately $25\ s$. From there on, the pattern of $\hat{\boldsymbol{\nabla}}_{0,\mathrm{m}}$ is very similar for all three algorithms. It is also apparent, that the magnitudes of $\hat{\nabla}_{0,\mathrm{m},x}$ and $\hat{\nabla}_{0,\mathrm{m},y}$ change when the user is turning (i.e. they are dependent upon the pedestrian heading). The mathematical reason for this behavior is the computation of ψ with the arctangent (17). Let us consider the last part of the trajectory, where the pedestrians

head towards south (figure 5). In this case, m_y^L solely determines the heading, whereas m_x^L can be any value as long m_y^L is zero. Thus, it is much harder to detect systematic deviations in m_y^L than in m_x^L, which can also be seen in figure 6 after the last turn (i.e. $\hat{\nabla}_{0,m,x}$ is smaller than $\hat{\nabla}_{0,m,y}$ and very close to zero). These conclusions differ from the ones in the analysis of the numerical example of multiple, static magnetometers in [A2] (section 4.2 or appendix A.2). The reason is, that the system equation acts as additional observation here, which is not present in the case of evaluating the multiple, static magnetometers with LSA. In the chosen setup the additional redundancy in the multi-user EKF by fusing the observations from multiple users only affects $\hat{\nabla}_{0,\dot{\psi}}$. The MDBs for the magnetometer observations are more or less the same as for the standard EKF. Figure 7 reveals, that the reason for this is the stochastic model which is determined by the preset standard deviations.
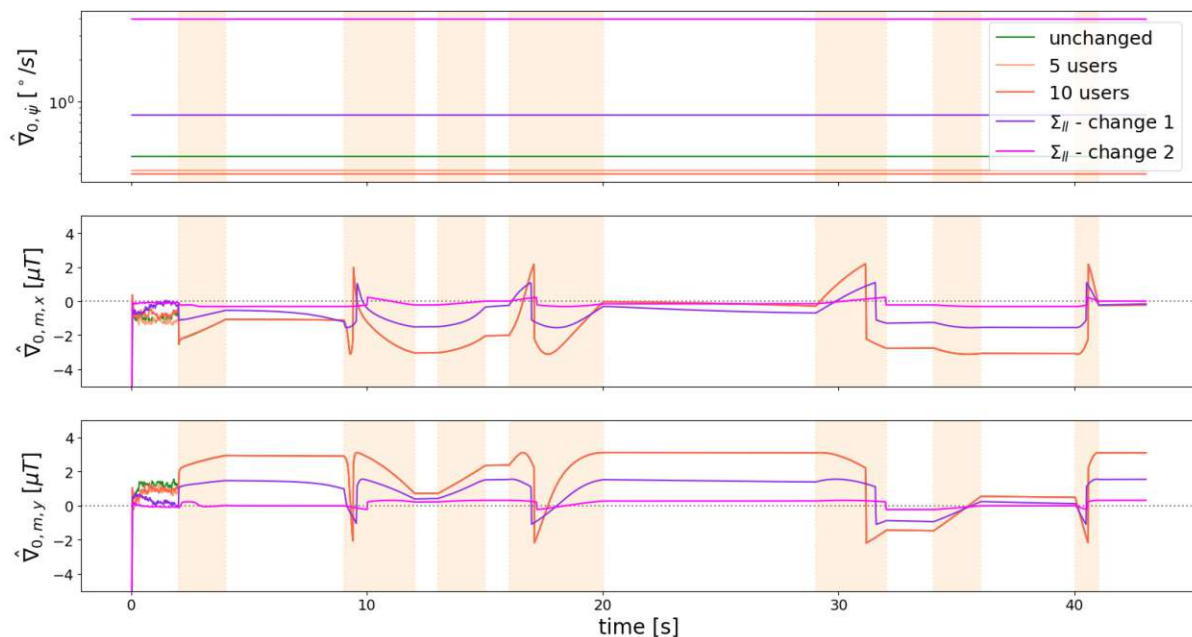
Figure 7: MDBs for the multi-user EKF when changing the number of pedestrians whose observations are fused to five and ten. In change 1 of $\boldsymbol{\Sigma}_{ll}$, $\sigma_{\dot{\psi}}$ and $\sigma_{\zeta,\psi}$ are doubled and $\sigma_{m,x}$, $\sigma_{m,y}$, $\sigma_{\zeta,x}$ and $\sigma_{\zeta,y}$ are halved. In change 2 of $\boldsymbol{\Sigma}_{ll}$, $\sigma_{\dot{\psi}}$ and $\sigma_{\zeta,\psi}$ are multiplied by ten and $\sigma_{m,x}$, $\sigma_{m,y}$, $\sigma_{\zeta,x}$ and $\sigma_{\zeta,y}$ are divided by ten.

The effect of increasing the redundancy by fusing the observations from more users is very small for all MDBs. Changing the stochastic model (i.e. varying the standard deviations of the observations, system control and system noise) leads to more intense changes in the MDBs. The problem with adjusting the stochastic model is, that ideally the standard deviations of the observation groups are carefully chosen to represent the sensor and system noise components appropriately. In the present case of orientation determination for indoor navigation, the need of a further reduction of $\hat{\nabla}_{0,m,x}$ and $\hat{\nabla}_{0,m,y}$ from figure 6 is questionable. As outlined in [A3], $\hat{\boldsymbol{\nabla}}_{0,m}$ represents the fast-varying systematic deviations (which more or less correspond to the magnetic anomalies). These systematic deviations can be much higher than the computed MDBs and therefore they can be detected anyway. Still, small and undetected deviations can bias the estimated heading which is hard to avoid without any other source of information or other kinds of observations.

The mag-bias EKF achieves a good performance in the sense of accuracy of the computed heading in [A3] as it contains (heuristic) measures to reduce the influence of magnetic anomalies. The idea of removing ψ from the state vector and include it as an observation obviously does not lead to an improved inner reliability (figure 6). In the beginning of the trajectory, the MDBs are significantly higher compared to the standard EKF and the multi-user EKF. The reason is, that the standard deviation of ψ only decreases when the absolute heading is updated (at approximately 9 s and 25 s). This is also shown in figure 8, where $\hat{\nabla}_{0,\dot{\psi}}$ and the magnitude of $\hat{\mathbf{\nabla}}_{0,\mathrm{m}}$ clearly decrease when σ_ψ decreases. This figure shows the normalized values in order to visualize these three quantities in one plot (i.e. each time series of data is divided by the corresponding first value). Additionally, the relative levels (i.e. the changes with respect to the first value) of $\hat{\nabla}_{0,\dot{\psi}}$ and $\|\hat{\mathbf{\nabla}}_{0,\mathrm{m}}\|$ behave exactly the same in this case.
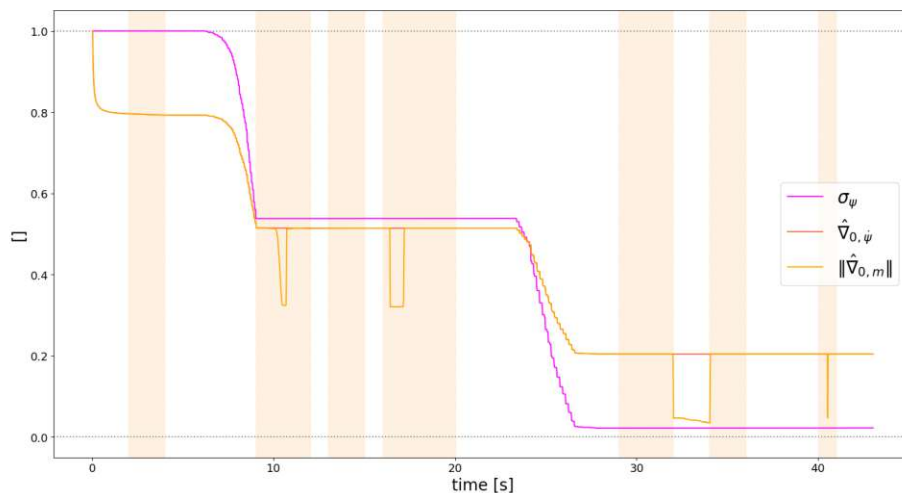
Figure 8: Relative changes of the yaw variance and MDBs compared to the value at time $k = 0$.

ρ_{1-2} is the measure to assess identifiablity (i.e. separability of $H_{A,1}$ and $H_{A,2}$). In the present scenario it is nearly constant for all three algorithms but its extent is different between the algorithms. Here, also the multi-user EKF stands out as ρ_{1-2} is approximately 0.0005 whereas it is 1.0 for the standard EKF and the mag-bias EKF. When considering the magnetic anomalies (figure 5) in the computation of the simulated magnetometer observations, the statistical tests in figure 9 state this finding. The local test for the gyroscope bias does not get significant in the presence of the magnetic anomalies and indicates, that the reason for the significant global test value is due to systematic deviations in the magnetometer observations. A desired property of the mag-bias EKF is, that even if $\hat{\boldsymbol{\delta}}_s^L$ gets distorted by magnetic anomalies, it converges back fast to the correct value after passing them. This is also the case in figure 9, as the test values of the mag-bias EKF are below the corresponding critcal values earlier compared to the other two algorithms.
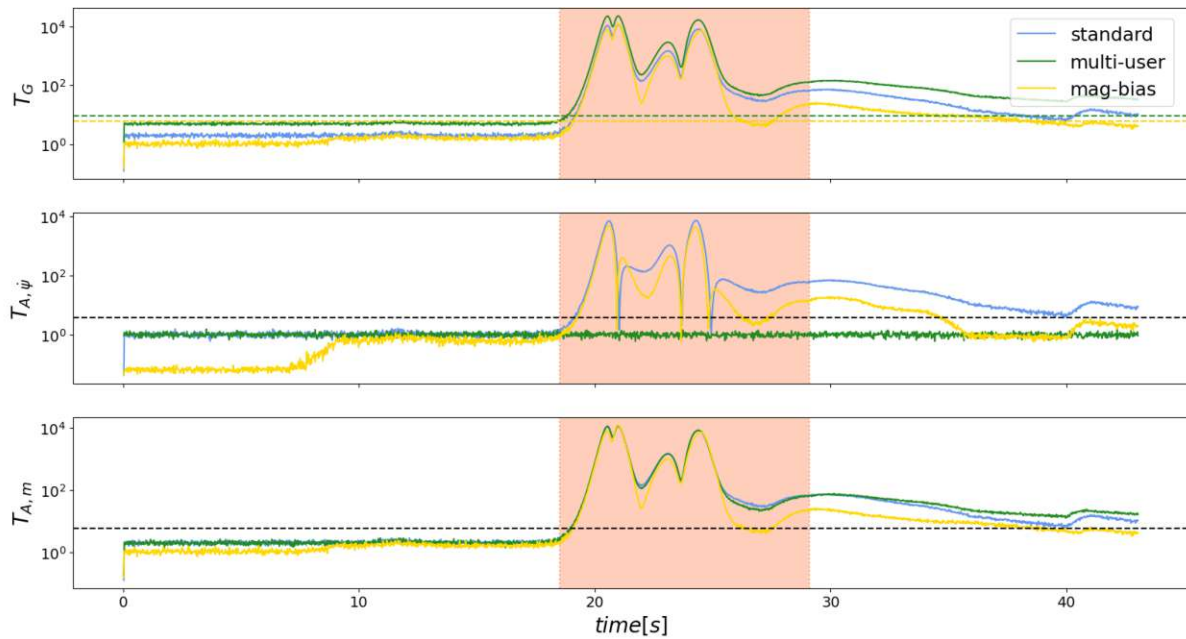
Figure 9: Global test and local tests of the considered alternative hypothesis. The light red area marks the timespan, where the magnitude of the magnetic anomalies exceed 1.0 μT. All y-axes are logarithmically scaled. The dashed line represent the critical values (top plot: the critical values for the standerd EKF and the mag-bias EKF are equal).

The analysis in this section reveal the high potential of the multi-user EKF respectively the approach of fusing systems sharing common states in one EKF. Clearly, this approach is more complicated to implement but e.g. in robotic applications or autonomous driving the circumstances are much more predictable than in pedestrian indoor navigation. Thus, further research on this approach in different applications or scenarios seems promising.

6   Conclusions and outlook

The advancements obtained in this thesis can be summarized as follows:

- The solution of the EKF update equations with an overdetermined system equation due to multiple sub-systems

- The derivation of inner reliability measures for the GHM based on a general formulation of systematic deviations in the observation model

- Fusing the smartphone sensor observations of multiple pedestrians in one EKF for orientation estimation

- Development of an orientation estimation algorithm being robust to magnetic anomalies.

The first two tasks are methodological advancements in the field of parameter estimation methods. The EKF update equations with overdetermined system equation are derived in [A1]. Another update term appears due to the redundant equations in the state propagation (beside the update term from the measurement equation). This framework or extended functional model is applicable to any kind of estimation problem and offers the flexibility to include system control quantities from multiple sub-systems in one state propagation step.

Inner reliability in the GHM is the main methodological topic of this thesis and it is subject of the three main publications [A1,A2,A3]. In [A1], the influence of adaptions in the functional and stochastic model of an EKF in the GHM on the redundancy numbers (as a measure for inner reliability) is analyzed. It turns out, that additional aspects have to be considered when using inner reliability measures in the GHM. Thus, [A2] focuses on a theoretical analysis of inner reliability in the GHM. Beside the orthogonal decomposition of the misclosures with regard to the parameter space, also the mapping between the observation and condition space plays an important role. The MDB together with the correlation coefficient of the local tests are the two measures to assess inner reliability regarding detectability and separability. These two measures are analyzed based on the numerical examples of plane fitting and magnetometer based yaw computation in [A2] and actions to improve inner reliability are outlined. Section 5.1 of this thesis contains a thorough summary on inner reliability in the GHM for LSA as well as the EKF. The local tests, the MDB and the correlation coefficients are derived for any kind of systematic deviation affecting the observations. Especially, the extension to multi-dimensional additional parameters in the alternative hypothesis describing systematic deviations is an important step forward in geodetic reliability analysis. [A3] does not directly include inner reliability considerations, but the global test used for magnetic anomaly detection also belongs to this field of research.

The latter two challenges are about the implementation of specific algorithms for orientation estimation in indoor positioning. The estimation of smartphone orienation based on the observations from multiple pedestrians is closely related to the first research question. An EKF model is developed which fuses the smartphone sensor observations such that the inclination is determined for each pedestrian, but the yaw angle is the same for all of them. This is simulated in [A1] by using the data from an experiment with one pedestrian and introducing the observations a second time with different smartphone inclination. Inner reliability could be improved, but only for observations with satisfactory redundancy numbers. In section 5.2 of this thesis, the EKF model from [A1] has been modified with respect to the yaw angle. It exhibits superior properties regarding inner reliability. The MDBs of the gyroscope bias can be greatly reduced and the local tests for gyroscope and magnetometer biases are decorrelated. Thus, it is possible

to reasonably detect and identify sensor biases in EKF models for smartphone orientation determination based on the data from multiple pedestrians.

In [A3] a heuristic orientation estimation algorithm for indoor positioning has been developed. The computation of inclination and heading as well as magnetic anomaly detection is separated in different modules. Thus, the influence of magnetic anomalies does not appear in the outcoming inclination and due to the bias-EKF model, they also do not spread on the heading. The residuals from the bias-EKF are used to compute the global test which is used for the detection of magnetic anomalies. Based on small-scale experiments with high-accuracy ground truth for the smartphone orientation, the performance is evaluated and compared to other algorithms from relevant publications on indoor positioning. The RMSE of the computed heading is $\approx 40\,\%$ lower compared to the comparison algorithms. Still, an accurate initial heading as well as temporarily error-free magnetometer observations are necessary conditions for the developed algorithm in order to provide reasonable results for the smartphone orientation. Additionally, the good performance has to be also stated in larger scale experiments with multiple users and different smartphone holding modes.

Concluding this thesis, challenges remain which have to be tackled in future research. From a methodological point of view, this thesis lacks the temporal modeling of systematic deviations in the alternative hypothesis EKF models. On the one hand, the observations can be subject to autocorrelated noise and on the other hand, systematic deviations usually do not appear in only one epoch. As it would be necessary to evaluate the alternative hypothesis model for different epochs at once, the real-time capability may get lost and also the computational burden increases. It seems worthwile to analyze the impact on inner reliability when using such extended and more complex models for the detection and identification of systematic deviations. On the example of magnetic anomalies, there is a clear dependency on the position and attitude of the smartphone with respect to the anomaly source. Modeling such influences is challenging but has the potential of enabling the creation of magnetic anomaly maps in postprocessing routines. Such maps can be used in turn for the real-time positioning of pedestrians within buildings, e.g. by using these maps for fingerprinting.

The other open question is the implementation of the multi-user approach in an indoor positioning system. Herein, only the EKF model has been developed but not used in multi-user experiments. A real-time application is only possible, if the smartphone sensor observations from the persons in a building are available to a central algorithm. Additionally, the question arises if users are indeed heading in the same direction. This is obviously the case in corridors and narrow parts of a building but it requires the detection of pedestrians being in such areas. Thus, a post-processing implementation of this algorithm seems more promising for pedestrian indoor positioning. Nevertheless, there are other fields of application which are more constrained or exhibit a more controlled pattern of motion, such as robotic/UAV navigation or autonomous driving. Here it is also easier to establish the connection between the sub-systems in order to share the observations. The application of EKFs with an overdetermined state propagation to process such systems seems promising and offers new research perspectives.

A   Main publications

[A1] Andreas Ettlinger, Hans Neuner and Thomas Burgess. Development of a Kalman filter in the Gauss-Helmert model for reliability analysis in orientation determination with smartphone sensors. *Sensors*, 18(2), 2018.

[A2] Andreas Ettlinger and Hans Neuner. Assessment of inner reliability in the Gauss-Helmert model. *Journal of Applied Geodesy*, 14(1), 2020.

[A3] Andreas Ettlinger, Andreas Wieser and Hans Neuner. Robust determination of smartphone heading by mitigation of magnetic anomalies. *NAVIGATION: Journal of the Institute of Navigation*, 71(1), 2024.

A.1   Development of a Kalman filter in the Gauss-Helmert model for reliability analysis in orientation determination with smartphone sensors

Development of a Kalman Filter in the Gauss-Helmert Model for Reliability Analysis in Orientation Determination with Smartphone Sensors

Andreas Ettlinger [1,*]**, Hans Neuner** [1] **and Thomas Burgess** [2]

[1] Department of Geodesy and Geoinformation, TU Wien, 1040 Wien, Austria; hans.neuner@geo.tuwien.ac.at
[2] indoo.rs GmbH, 1150 Wien, Austria; thomas@indoo.rs
* Correspondence: andreas.ettlinger@tuwien.ac.at; Tel.: +43-01-58801-12836

Abstract: The topic of indoor positioning and indoor navigation by using observations from smartphone sensors is very challenging as the determined trajectories can be subject to significant deviations compared to the route travelled in reality. Especially the calculation of the direction of movement is the critical part of pedestrian positioning approaches such as Pedestrian Dead Reckoning ("PDR"). Due to distinct systematic effects in filtered trajectories, it can be assumed that there are systematic deviations present in the observations from smartphone sensors. This article has two aims: one is to enable the estimation of partial redundancies for each observation as well as for observation groups. Partial redundancies are a measure for the reliability indicating how well systematic deviations can be detected in single observations used in PDR. The second aim is to analyze the behavior of partial redundancy by modifying the stochastic and functional model of the Kalman filter. The equations relating the observations to the orientation are condition equations, which do not exhibit the typical structure of the Gauss-Markov model ("GMM"), wherein the observations are linear and can be formulated as functions of the states. To calculate and analyze the partial redundancy of the observations from smartphone-sensors used in PDR, the system equation and the measurement equation of a Kalman filter as well as the redundancy matrix need to be derived in the Gauss-Helmert model ("GHM"). These derivations are introduced in this article and lead to a novel Kalman filter structure based on condition equations, enabling reliability assessment of each observation.

1. Introduction

Determining the orientation in pedestrian navigation with geometric-based approaches is an essential step for positioning. There are several possibilities to mathematically parameterize the orientation. In [1] three possibilities are given: the direction-cosine-matrix, Euler angles and quaternions. Discussion on the advantages and disadvantages of these concepts can be found in [2]. In this article the Euler angles—roll, pitch and yaw—are used as it is the yaw angle that is especially necessary for calculating the 2D-Position in pedestrian navigation approaches like Pedestrian Dead Reckoning ("PDR"). The orientation can be calculated directly by the use of an accelerometer and a magnetometer respectively a gyroscope, which are nowadays integrated in most of the available smartphones. Each of these sensors is subject to specific systematic effects [3], which have to be considered in detail when integrating low-cost sensors in smartphones. These systematic deviations clearly can have a noticeable impact on the resulting position of PDR, which makes determining the orientation the critical part.

Several approaches exist to fuse and improve the calculated orientation from the individual sensors. In [4] linear combinations are used, to calculate the yaw angle of the individual results from magnetometer and gyroscope. Using a Kalman filter to fuse accelerometer, magnetometer and gyroscope measurements [5–7] is the most common approach. Fusing these sensors offers the opportunity to detect and correct for systematic deviations in the observations. In [8] a Kalman filter is developed which uses the observed gravity and Earth magnetic field as well as the orientation quaternion which are propagated by means of the gyroscope. If static acceleration or magnetic flux is detected, systematic sensor deviations can be determined. In [9] or [10] the gyroscope is used to detect when the user is turning. If the user walks straight, systematic sensor deviations are derived. The same approach is used in [11] to smooth the resulting trajectory. A method to minimize systematic effects in acceleration measurements resulting from the steps of pedestrians by adapting the measurement noise can be found in [2]. Using additional data can improve the ability to detect systematic effects. One possibility to retrieve additional position and attitude information is to use pictures from the smartphone camera [12]. Also building plans can be used to support the calculation of the orientation [13]. The previously mentioned approaches only use observations from one device. Especially in pedestrian navigation, much data is produced from many different smartphones, which can be used for positioning in various ways. This crowd-sourced data is mainly used to support Wi-Fi fingerprinting [14,15] by extending and updating radio maps [16–18]. In the context of PDR, in [19] for example, trajectories from multiple users are used to minimize the influence of magnetic perturbations inside buildings.

Combining positions from signal strength observations with PDR is done, for example, in [20]—with an adaptive Kalman filter—or in [21]—with a particle filter–to improve positioning accuracy. Such signal strength observations or "Received Signal Strength" (RSS) can be used in geometric-based approaches or in feature-based approaches and require external infrastructure. Adding such positioning techniques—for example Wi-Fi [22,23], "radio-frequency identification" (RFID) [24] or artificial magnetic fields [25]—will increase the redundancy and minimize the influence of systematic effects. Geometric- and feature-based approaches are combined in [26], where also measures are derived to quantify accuracy independently from the distribution of the observations.

This paper focuses on determining the orientation for PDR with accelerometer, magnetometer and gyroscope in a Kalman filter. The focus is on analyzing the reliability of the observations from smartphone-sensors, which are non-linearly included in condition equations. The Kalman filter is commonly used to estimate states in a Gauss-Markov model ("GMM"—model with observation equations), wherein the observations of the measurement equation are linear and can be formulated as functions of the states [27,28]. However, the equations for the orientation determination in PDR are condition equations, containing implicit relations between states and observations. Thus, reliability analysis based on condition equations, necessitates a new derivation of the system equation and the measurement equation of a Kalman filter as well as the redundancy matrix in the Gauss-Helmert model ("GHM"—model with condition equations). The formulation of the system equation in the GHM can be found in [29,30], wherein the measurement equation and corresponding redundancy matrix are still assumed to satisfy the GMM. Hence, an important novelty of this article is the derivation of the whole Kalman filter structure in the GHM, enabling the possibility to calculate reliability measures for observations which are non-linearly included in the condition equations.

Section 2 contains the explanation of the existing approach and subsequent problem description of reliability, as well as the derivation of the update-equations and redundancy matrix of the reformulated Kalman filter. The data of a measured trajectory will be used to estimate the Euler angles as well as the reliability measures. These results are presented in Section 3 whereas Section 4 concludes this contribution.

2. Orientation Determination

2.1. Existing Approach

In the Kalman filter used for orientation determination in this article, the state parameters are the Euler angles roll φ, pitch θ and yaw ψ. Based on the assumption that roll and pitch are constant while the user is walking, they are predicted at actual epoch k with a random-walk model (1) and (2). The yaw angle is predicted with two different system equations, whereby (3) will be used if the user is walking straight and (4) will be used at detected turns. In the second case the observed turn rates from gyroscope $g_{y,k}$ and $g_{z,k}$ are included as control quantities summed in the vector $\boldsymbol{u}_k$. By doing this, the predicted yaw should immediately follow the user's turn. The noise components of the state parameters are $c_{k-1,\varphi}$, $c_{k-1,\theta}$, $c_{k-1,\psi}$ and Δt is the time interval between two consecutive Kalman updates:

$$f_1 : \varphi_k = \varphi_{k-1} + c_{k-1,\varphi} \tag{1}$$

$$f_2 : \theta_k = \theta_{k-1} + c_{k-1,\theta} \tag{2}$$

$$f_3 : \psi_k = \psi_{k-1} + c_{k-1,\psi} \tag{3}$$

$$f_3 : \psi_k = \psi_{k-1} + \frac{\Delta t}{\cos \theta_{k-1}} \left(g_{y,k} \sin \varphi_{k-1} + g_{z,k} \cos \varphi_{k-1} \right) + c_{k-1,\psi} \tag{4}$$

Turn detection is done by applying a statistical test on the filter innovations of the yaw angle $d_{\psi,i}$ [29,31]. The null hypothesis H_0 of this statistical test says that the vector $\boldsymbol{d}_\psi$ containing the filter innovations $d_{\psi,i}$ from the last n epochs is equal to the zero vector (5), whereas the alternate hypothesis H_A states that $\boldsymbol{d}_\psi$ is significantly different to the zero vector (6). If the test value exceeds the corresponding quantile of the chi-square distribution (7), (4) will be used to predict the yaw angle. $\boldsymbol{D}_\psi$ is the variance-covariance matrix (VCM) of the innovation vector $\boldsymbol{d}_\psi$ and only contains variances on the diagonal belonging to the corresponding $d_{\psi,i}$. This is a simplification, as auto-covariances may be present. The use of random-walk (3) results in smoother trajectories in sections when the user walks straight. By neglecting the observations from gyroscope in the random-walk model, the influence of systematic sensor deviations (gyro-drift) on the filter result is minimized:

$$H_0 : E(\boldsymbol{d}_\psi) = E\left(\begin{bmatrix} d_{\psi,1} & d_{\psi,2} & \cdots & d_{\psi,n} \end{bmatrix}^T \right) = \boldsymbol{0} \tag{5}$$

$$H_A : E(\boldsymbol{d}_\psi) \neq \boldsymbol{0} \tag{6}$$

$$P\{\boldsymbol{d}_\psi^T \boldsymbol{D}_\psi^{-1} \boldsymbol{d}_\psi \leq \chi^2_{n;1-\alpha} | H_0\} = 1 - \alpha \tag{7}$$

For the update equations also the VCM of the predicted state is needed (8):

$$\sum\nolimits_{\overline{xx},k} = \boldsymbol{T}_{k,k-1} \sum\nolimits_{\hat{x}\hat{x},k-1} \boldsymbol{T}_{k,k-1}^T + \boldsymbol{U}_{k,k-1} \sum\nolimits_{uu,k} \boldsymbol{U}_{k,k-1}^T + \boldsymbol{C}_{k,k-1} \sum\nolimits_{cc,k} \boldsymbol{C}_{k,k-1}^T \tag{8}$$

Therein, $\Sigma_{ii,k}$—with the index $i = \hat{x}_{k-1}$, u, c—are the VCMs of the corresponding observation groups in epoch k. $\boldsymbol{T}_{k,k-1}$ is the state transition matrix, $\boldsymbol{U}_{k,k-1}$ the control matrix and $\boldsymbol{C}_{k,k-1}$ is the noise matrix, each referred to epoch k. These system matrices are Jacobi matrices and in general contain the derivatives of the system equations with respect to the corresponding observation group [27–29]. Equations (9)–(11) show the system matrices for the approach presented in this section where $\boldsymbol{E}$ is the identity matrix.

$$\boldsymbol{T}_{k,k-1} = \begin{bmatrix} 1 & 0 & 0 \\ 0 & 1 & 0 \\ \frac{\partial f_3}{\partial \varphi_k} & \frac{\partial f_3}{\partial \theta_k} & 1 \end{bmatrix} \tag{9}$$

$$U_{k,k-1} = \begin{bmatrix} 0 & 0 & 0 \\ 0 & 0 & 0 \\ 0 & \frac{\partial f_3}{\partial g_{y,k}} & \frac{\partial f_3}{\partial g_{z,k}} \end{bmatrix} \tag{10}$$

$$C_{k,k-1} = \Delta t \cdot E_{3 \times 3} \tag{11}$$

The observations in the measurement equation are directly observed Euler angles, as also shown in [32]. Therefore, the design matrix $A_{m,k}$ of the Kalman filter equals the identity matrix. They are calculated outside of the Kalman filter ((12)–(14)) by using observed accelerations $a_{x,k}$, $a_{y,k}$, $a_{z,k}$ and magnetic flux densities $m_{x,k}$, $m_{y,k}$, $m_{z,k}$ [33]. The accelerations are filtered in a separate Kalman filter to remove high-frequency components due to the movement of the user [2]:

$$f_4 : \varphi_k = \tan^{-1}\left(\frac{a_{y,k}}{a_{z,k}} \right) \tag{12}$$

$$f_5 : \theta_k = \tan^{-1}\left(\frac{-a_{x,k}}{a_{y,k}\sin(\varphi_k) + a_{z,k}\cos(\varphi_k)} \right) \tag{13}$$

$$f_6 : \psi_k = \tan^{-1}\left(\frac{m_{z,k}\sin(\varphi_k) - m_{y,k}\cos(\varphi_k)}{m_{x,k}\cos(\theta_k) + m_{y,k}\sin(\theta_k)\sin(\varphi_k) + m_{z,k}\sin(\theta_k)\cos(\varphi_k)} \right) \tag{14}$$

The yaw angle calculated with (14) can be subject to magnetic perturbations, especially inside buildings. The redundant determination of the Euler angles in the Kalman filter by using the system equation and the measurement equation dampens the influence of magnetic perturbations. Additionally, the standard deviation of the magnetometer measurements σ_m will be increased if the magnitude of the measured magnetic field $\|m_k\|$ is not stable (15), leading to an adaptive standard deviation $\sigma_{m,k}$ for each Kalman filter epoch. As the geomagnetic field should be constant related to the dimensions of a building, it will be assumed that magnetic perturbations are present if the measured magnitude changes:

$$\sigma_{m,k} = \sigma_m + |\|m_k\| - \|m_{k-1}\|| \tag{15}$$

Using the covariance propagation law, the VCM belonging to the directly observed Euler angles $\Sigma_{\varphi\theta\psi,k}$ is derived (16), wherein H_k is a Jacobi matrix containing the derivatives of (12)–(14) with respect to the accelerometer and magnetometer measurements.

$$\Sigma_{\varphi\theta\psi,k} = H_k \begin{bmatrix} \Sigma_{aa,k} & \mathbf{0}_{3\times3} \\ \mathbf{0}_{3\times3} & \sigma_{m,k}E_{3\times3} \end{bmatrix} H_k^T$$

$$H_k = \begin{bmatrix} 0 & \frac{\partial f_4}{\partial a_{y,k}} & \frac{\partial f_4}{\partial a_{z,k}} & 0 & 0 & 0 \\ \frac{\partial f_5}{\partial a_{x,k}} & \frac{\partial f_5}{\partial a_{y,k}} & \frac{\partial f_5}{\partial a_{z,k}} & 0 & 0 & 0 \\ \frac{\partial f_5}{\partial a_{x,k}} & \frac{\partial f_5}{\partial a_{y,k}} & \frac{\partial f_5}{\partial a_{z,k}} & \frac{\partial f_5}{\partial m_{x,k}} & \frac{\partial f_5}{\partial m_{y,k}} & \frac{\partial f_5}{\partial m_{z,k}} \end{bmatrix} \tag{16}$$

2.2. Problem Description

To determine the user's position, the step length is also estimated and will be used with fixed variance in PDR. Figure 1 shows a trajectory calculated with PDR, whereby the yaw is estimated with the Kalman filter mentioned in Section 2.1. Additionally, the 95% confidence ellipses as well as the reference trajectory are part of Figure 1. This measured trajectory will also be used to analyze the partial redundancy in Section 3. During the measurements, the user held the smartphone in portrait mode (Figure 2 left, $\varphi_k \sim 0°$). The reference trajectory is calculated from the measurements of the TS16 total station (Leica Geosystems, Heerbrugg, Switzerland) which is tracking the user by the help of a 360°-mini-prism on a helmet (Figure 2 right).
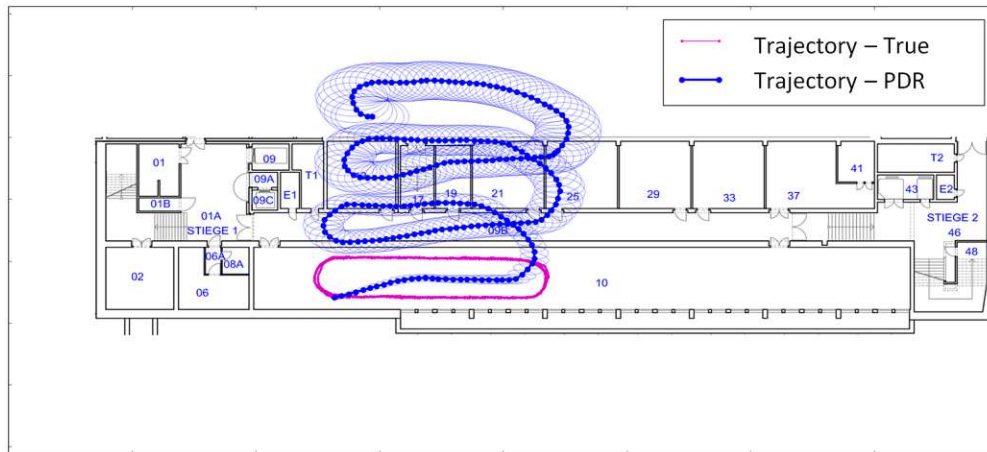
Figure 1. PDR Trajectory. Ground truth in magenta, estimated steps in blue with 95% confidence ellipses.

Figure 2. Used sensors and measurement setup: Samsung Galaxy S7 (Samsung, Seoul, Korea), smartphone running indoo.rs Mobile Toolkit^{TM} to collect sensor observations (**left**). Helmet with $360°$-mini-prism (**middle**) and Leica TS16 tracking the user (**right**).

In PDR, the yaw angle is responsible for the shape of the trajectory and the step length for the scale. Hence in Figure 1, the estimated orientation causes the deviations between the estimated and the reference trajectory. As these deviations are not captured by the confidence ellipses—which are a measure for the precision [34]—there are two possible reasons for their appearance: systematic deviations in the observed data or non-Gaussian distributed data. Because of the obvious systematics in the estimated trajectory, it is assumed that systematic deviations are present in the observed data.

Reliability theory deals with the detection of large systematic deviations (inner reliability) and their effect on the estimated quantities (outer reliability) [35,36]. To identify the measurements responsible for the systematic deviations of the orientation between estimated and reference trajectory, the inner reliability is used. Here the partial redundancies r_i play a key role. According to [29,37,38], all quantities with stochastic information can be treated as observations.

Observations related to the system equation are the estimated state from the previous epoch $\hat{x}_{k-1}$, the control variables $\boldsymbol{u}$ and the noise variables $\boldsymbol{c}$. The observations of the measurement equation are

summed in the vector l_m, where m labels quantities of the measurement equation. With (17)–(20) the partial redundancy can be calculated for the previously mentioned observations according to [29]:

$$\sum_{j=1}^{n_x} r_{\hat{x}_{k-1},k,j} = \sum_{j=1}^{n_x} e_j^T \sum_{\hat{x}\hat{x},k-1} T_{k,k-1}^T A_{m,k}^T D_k^{-1} A_{m,k} T_{k,k-1} e_j \tag{17}$$

$$\sum_{j=1}^{n_u} r_{u,k,j} = \sum_{j=1}^{n_u} e_j^T \sum_{uu,k} U_{k,k-1}^T A_{m,k}^T D_k^{-1} A_{m,k} U_{k,k-1} e_j \tag{18}$$

$$\sum_{j=1}^{n_w} r_{c,k,j} = \sum_{j=1}^{n_w} e_j^T \sum_{cc,k} C_{k,k-1}^T A_{m,k}^T D_k^{-1} A_{m,k} C_{k,k-1} e_j \tag{19}$$

$$\sum_{j=1}^{n_l} r_{l_m,k,j} = \sum_{j=1}^{n_l} e_j^T \sum_{ll,m,k} D_k^{-1} e_j \tag{20}$$

Therein, n_i is the number of observations in each observation group and D_k is the VCM of the filter innovation [27–29]. e_j is the unity vector to select the corresponding r_i respectively diagonal element. In the above formulation of the Kalman filter, the r_i can only be calculated for the directly observed angles in the measurement equation but not for the original observations from accelerometer and magnetometer due to the structure of (12)–(14).

2.3. Kalman Filter in the Gauss-Helmert Model

In the GMM, the true observations $\tilde{l}$ can be modeled as a function of the true parameters $\tilde{x}$—which also holds for the estimated observations $\hat{l}$ and estimated parameters $\hat{x}$ (21). As mentioned above, the measurement Equations (12)–(14) have another structure, which matches the GHM [39] shown in (22). Hence, the update equations of the Kalman filter have to be derived in the GHM, to directly use the observations from smartphone-sensors. Afterwards, the corresponding r_i need to be derived for this case. In [30] the GHM is also used to estimate variance components for the system noise. Though, there is still the assumption of using the GMM in the measurement equation and the results cannot be used in this article.

$$\tilde{l} - f(\tilde{x}) = \hat{l} - f(\hat{x}) = 0 \tag{21}$$

$$f\left(\tilde{l}, \tilde{x}\right) = f(\hat{l}, \hat{x}) = 0 \tag{22}$$

As the functional relations (22) are non-linear in general—and especially in this article—they have to be linearized. Neither the real observations and parameters, nor their estimated values are known a priori. Hence, to do Taylor linearization, approximate values l_0 and x_0 have to be used which also have to satisfy the non-linear relations [34]. In least-squares, especially x_0 is assumed to be non-stochastic. According to [40], l_0 can be replaced by the observed data l after linearization, which results in the linearized, functional model (23):

$$f(l, x_0) + A(\hat{x} - x_0) + B(\hat{l} - l) = 0 \tag{23}$$

The first term corresponds to the misclosure vector **w**, the bracketed expression in the second term equals the stochastic additions $\Delta\hat{x}$ to the approximate parameters x_0 and the bracketed expression in the third term equals the residuals **v**. Formula (23) is only valid for the first iteration of least-squares estimation, because linearization of the functional model necessitates an iterative approach. In the subsequent iterations, the functional model is always linearized at the previously estimated observations

and parameters [40]. Formulas (24)–(27) show, how the searched quantities with corresponding VCM are calculated in the GHM in the context of least-squares [41]:

$$\sum\nolimits_{\Delta\hat{x}\Delta\hat{x}} = \left(A^T\left(B\sum\nolimits_{ll}B^T\right)^{-1}A\right)^{-1} \tag{24}$$

$$\Delta\hat{x} = -\sum\nolimits_{\Delta\hat{x}\Delta\hat{x}}A^T\left(B\sum\nolimits_{ll}B^T\right)^{-1}w \tag{25}$$

$$v = -\sum\nolimits_{ll}B^T\left(B\sum\nolimits_{ll}B^T\right)^{-1}\left(E - A\sum\nolimits_{\Delta\hat{x}\Delta\hat{x}}A^T\left(B\sum\nolimits_{ll}B^T\right)^{-1}\right)w \tag{26}$$

$$\sum\nolimits_{vv} = \sum\nolimits_{ll}B^T\left(B\sum\nolimits_{ll}B^T\right)^{-1}\left(E - A\sum\nolimits_{\Delta\hat{x}\Delta\hat{x}}A^T\left(B\sum\nolimits_{ll}B^T\right)^{-1}\right)B\sum\nolimits_{ll} \tag{27}$$

B is the observation matrix, $\Sigma_{\Delta\hat{x}\Delta\hat{x}}$ is the VCM of the estimated additions, Σ_{ll} the VCM of the observations and Σ_{vv} is the VCM of the residuals. It is important that A and B are column-regular matrices. Otherwise the inverse matrices cannot be calculated. To avoid singular matrices, the functional relations have to be chosen, such that there will be no linearly dependent columns in these matrices.

The Kalman filter is based on sequential least-squares with an additional state transition model. The state transition model respectively system equation is described in general by non-linear, stochastic, vector-matrix differential equations. We assume, that such differential equations have the form shown in (28) after linearization, which is also basis for deriving the system equation in [27–29]:

$$\dot{x}(t) = Fx(t) + Lu(t) + Gc(t) \tag{28}$$

t is the continuous time variable. The system matrix F, control-input matrix L and noise-input matrix G are assumed to be time-invariant. Solving such differential equations in the state space—also shown in [27–29]—unambiguously defines the state parameters at time k and gives the approximate formulation (29):

$$x_k \approx T_{k,k-1}x_k + U_{k,k-1}u_k + C_{k,k-1}c_k \tag{29}$$

As mentioned in [27], the predicted parameter vector $\bar{x}_k$ should be calculated from the original set of functions (30) in the non-linear case to avoid linearization errors. Equation (29) is necessary for calculating the VCM of $\bar{x}_k$ with the covariance propagation law (8).

$$\bar{x}_k = f(\hat{x}_{k-1}, u_k, c_k) \tag{30}$$

The system can also be described by several sub-systems which yields in an over-determined system equation. This will be dealt with in the next section, where one yaw angle will be estimated from multiple trajectory data. Thus, the system equation decomposes into two sets of equations. The first set unambiguously defines the predicted parameters by using $\hat{x}_{k-1}$, u_k and c_k which is already shown in (29) respectively (30). This set of equations will be—analogue to [29]—formulated in the GHM, such that it contains the residuals belonging to $\hat{x}_{k-1}$, u_k and c_k (31). The derivation of (31) can be found in the Appendix A:

$$\bar{x}_k - \hat{x}_k + v_{\bar{x},k} = -E\Delta\hat{x}_k + \begin{bmatrix} T_{k,k-1} & U_{k,k-1} & C_{k,k-1} \end{bmatrix}\begin{bmatrix} v_{\hat{x}_{k-1},k} \\ v_{u,k} \\ v_{c,k} \end{bmatrix} = 0 \tag{31}$$

The second set consists of condition equations, having the same structure like (23). These condition equations contain the same quantities like the first set of equations and can therefore be formulated as shown in (32). $w^*_{s,k}$ are the misclosures, arising because of the overdetermined system equation

respectively condition equations. $A^*_{s,k}$ is the design matrix and $T^*_{k,k-1}$, $U^*_{k,k-1}$ and $C^*_{k,k-1}$ are the observation matrices which belong to the condition equations of the system equation:

$$w^*_{s,k} + A^*_{s,k} \Delta \hat{x}_k + \begin{bmatrix} T^*_{k,k-1} & U^*_{k,k-1} & C^*_{k,k-1} \end{bmatrix} \begin{bmatrix} v_{\hat{x}_{k-1},k} \\ v_{u,k} \\ v_{c,k} \end{bmatrix} = 0 \tag{32}$$

The functional model of the measurement equation has the structure (23). Fusing the system equation and the measurement equation leads to the functional model of a Kalman filter formulated in the GHM with additional condition equations in the system Equation (33):

$$\begin{bmatrix} 0 \\ w^*_{s,k} \\ w_{m,k} \end{bmatrix} + \begin{bmatrix} -E \\ A^*_{s,k} \\ A_{m,k} \end{bmatrix} \Delta \hat{x}_k + \begin{bmatrix} T_{k,k-1} & U_{k,k-1} & C_{k,k-1} & 0 \\ T^*_{k,k-1} & U^*_{k,k-1} & C^*_{k,k-1} & 0 \\ 0 & 0 & 0 & B_{m,k} \end{bmatrix} \begin{bmatrix} v_{\hat{x}_{k-1},k} \\ v_{u,k} \\ v_{c,k} \\ v_{l_m,k} \end{bmatrix} = \underbrace{\begin{bmatrix} w_{s,k} \\ w_{m,k} \end{bmatrix}}_{w} + \underbrace{\begin{bmatrix} A_{s,k} \\ A_{m,k} \end{bmatrix}}_{A} \Delta \hat{x}_k + \underbrace{\begin{bmatrix} B_{s,k,k-1} & 0 \\ 0 & B_{m,k} \end{bmatrix}}_{B} \underbrace{\begin{bmatrix} v_{l_s,k} \\ v_{l_m,k} \end{bmatrix}}_{v} = 0 \tag{33}$$

Now the formulas of the GHM in least-squares can be applied and the parameters with corresponding VCM can be calculated. Equation (34) shows the VCM of the estimated parameters, which is derived by inserting A and B into (24):

$$\Sigma_{\hat{x}\hat{x},k} = \left(A^T_{s,k} \left(B_{s,k,k-1} \Sigma_{ll,s,k} B^T_{s,k,k-1} \right)^{-1} A_{s,k} + A^T_{m,k} \left(B_{m,k} \Sigma_{ll,m,k} B^T_{m,k} \right)^{-1} A_{m,k} \right)^{-1} = \left(\Sigma^{-1}_{\hat{x}\hat{x},s,k} + \Sigma^{-1}_{\hat{x}\hat{x},m,k} \right)^{-1} \tag{34}$$

$\Sigma_{\hat{x}\hat{x},s,k}$ is the VCM of the parameters which would be the result of a Kalman filter only considering the system equation. Similarly, $\Sigma_{\hat{x}\hat{x},m,k}$ is the VCM of the parameters if only the measurement equation would be considered in the Kalman filter. $\Sigma_{\hat{x}\hat{x},k}$ is the inverse of the sum of these two matrices. To further process (34), the Woodbury formula for matrix inversion—according to [42]—is applied (35), where M, N, O and P are arbitrary matrices and not related to the derivations made in this section:

$$(M + NOP)^{-1} = M^{-1} - M^{-1}N \left(O^{-1} + PM^{-1}N \right)^{-1} PM^{-1} \tag{35}$$

Depending on which term of the sum in (34) is chosen to be the matrix M in the Woodbury formula (35), results will show two equivalent representations (36) and (37) of the VCM of the estimated parameters. It has to be mentioned, that this VCM corresponds to $\hat{x}_k$ and not to $\Delta \hat{x}_k$. The reason is that x_0 equals $\bar{x}_k$, which is stochastic and its stochastic information is implicitly integrated by adding its calculation to the functional model ((31) and (33)). Whereas in least-squares x_0 is non-stochastic and therefore $\Sigma_{\hat{x}\hat{x}}$ equals $\Sigma_{\Delta \hat{x} \Delta \hat{x}}$.

$$\Sigma_{\hat{x}\hat{x},k} = \left(E - \Sigma_{\hat{x}\hat{x},s,k} A^T_{m,k} \left(B_{m,k} \Sigma_{ll,m,k} B^T_{m,k} + A_{m,k} \Sigma_{\hat{x}\hat{x},s,k} A^T_{m,k} \right)^{-1} A_{m,k} \right) \Sigma_{\hat{x}\hat{x},s,k} \tag{36}$$

$$\Sigma_{\hat{x}\hat{x},k} = \left(E - \Sigma_{\hat{x}\hat{x},m,k} A^T_{s,k} \left(B_{s,k,k-1} \Sigma_{ll,s,k} B^T_{s,k,k-1} + A_{s,k} \Sigma_{\hat{x}\hat{x},m,k} A^T_{s,k} \right)^{-1} A_{s,k} \right) \Sigma_{\hat{x}\hat{x},m,k} \tag{37}$$

By comparing (36) with the update equation for the VCM of the estimated parameters in the GMM (see [29] or [27]), the VCM of the filter innovation $D_{m,k}$ and the gain matrix $K_{m,k}$—belonging to the measurement equation—can be found ((39) and (41)). In the same manner, the VCM of the filter innovation $D_{s,k}$ of and the gain matrix $K_{s,k}$ belonging to the system equation are derived ((38) and (40)):

$$D_{s,k} = B_{s,k,k-1} \Sigma_{ll,s,k} B^T_{s,k,k-1} + A_{s,k} \Sigma_{\hat{x}\hat{x},m,k} A^T_{s,k} \tag{38}$$

$$D_{m,k} = B_{m,k} \Sigma_{ll,m,k} B^T_{m,k} + A_{m,k} \Sigma_{\hat{x}\hat{x},s,k} A^T_{m,k} \tag{39}$$

$$K_{s,k} = \Sigma_{\hat{x}\hat{x},m,k} A^T_{s,k} D^{-1}_{s,k} \tag{40}$$

$$K_{m,k} = \sum_{\hat{x}\hat{x},s,k} A_{m,k}^T D_{m,k}^{-1} \tag{41}$$

The estimated additions to the approximate parameters are derived by using (25) and (33). Formula (42) shows these additions, where the results from the previous paragraph are already considered. Hence, it includes corrections respectively updates for the system equation as well as for the measurement equation:

$$\Delta\hat{x}_k = -K_{s,k} w_{s,k} - K_{m,k} w_{m,k} = -\begin{bmatrix} K_{s,k} & K_{m,k} \end{bmatrix} \begin{bmatrix} w_{s,k} \\ w_{m,k} \end{bmatrix} \tag{42}$$

If the system equation is not overdetermined, (32) will not be used in the functional model (33), which leads to simplifications in the update equations. The classical Kalman filter update equations as well as the two GHM variants are summarized in Table 1.

Table 1. Comparison of the Kalman filter update equations.

	Gauss-Markov	Gauss-Helmert (Simplification)	Gauss-Helmert
d	$l_m - f_m(\bar{x})$	$-w_m = -f_m(l_m, \bar{x})$	$\begin{bmatrix} -w_s \\ -w_m \end{bmatrix} = \begin{bmatrix} -f_s(l_s, \bar{x}) \\ -f_m(l_m, \bar{x}) \end{bmatrix}$
D	$A_m \sum_{\bar{x}\bar{x}} A_m^T$	$B_m \sum_{ll,m} B_m^T + A_m \sum_{\bar{x}\bar{x}} A_m^T$	$\begin{bmatrix} D_s & 0 \\ 0 & D_m \end{bmatrix} =$ $\begin{bmatrix} B_s \sum_{ll,s} B_s^T + A_s \sum_{\hat{x}\hat{x},m} A_s^T & 0 \\ 0 & B_m \sum_{ll,m} B_m^T + A_m \sum_{\hat{x}\hat{x},s} A_m^T \end{bmatrix}$
K		$\sum_{\bar{x}\bar{x}} A_m^T D^{-1}$	$\begin{bmatrix} K_s & K_m \end{bmatrix} = \begin{bmatrix} \sum_{\hat{x}\hat{x},m} A_s^T D_s^{-1} & \sum_{\hat{x}\hat{x},s} A_m^T D_m^{-1} \end{bmatrix}$
$\sum_{\hat{x}\hat{x}}$		$(E - KA_m)\sum_{\bar{x}\bar{x}}$	$(E - K_m A_m)\sum_{\hat{x}\hat{x},s} = (E - K_s A_s)\sum_{\hat{x}\hat{x},m}$
$\hat{x}$		$\bar{x} + Kd$	

Approaches whose aim is to detect systematic deviations in the observations respectively to quantify the inner reliability in the GMM, are often based on the disturbed residuals $\bar{v}$ [43]. The error-term $\nabla \mathbf{v}$ in (43) is caused by the systematic deviations in the observations, summed in the error-vector ∇l:

$$\bar{v} = v + \nabla v \tag{43}$$

r_i is the factor which specifies how an observation deviation ∇l_i influences the corresponding residual v_i (44). Hence, high r_i are desirable to detect systematic deviations [29]:

$$\nabla v_i = -r_i \nabla l_i \tag{44}$$

Transferring these thoughts to the GHM, (26) has to be used to derive R, containing the r_i on its diagonal. R is an idempotent matrix, whose trace equals the overall redundancy of the estimation problem [34]. Formula (26) only contains the misclosures $\mathbf{w}$, which can be linearized by Bl according to [34]. If ∇l is taken into account, results show the disturbed model (45):

$$\bar{v} = -\sum_{ll} B^T \left(B \sum_{ll} B^T \right)^{-1} \left(E - A \sum_{\Delta\hat{x}\Delta\hat{x}} A^T \left(B \sum_{ll} B^T \right)^{-1} \right) B(l + \nabla l) \tag{45}$$

Thus, there is a direct relation between observations and residuals and the redundancy matrix for the GHM is now available (46):

$$R = \sum_{ll} B^T \left(B \sum_{ll} B^T \right)^{-1} \left(E - A \sum_{\hat{x}\hat{x}} A^T \left(B \sum_{ll} B^T \right)^{-1} \right) B \tag{46}$$

By using (27), (46) equals the matrix product $\Sigma_{vv} \Sigma_{ll}^{-1}$, whereby the analogy to the GMM is stated again [34]. The proof that the trace of R equals the overall redundancy can be found in Appendix B.

3. Results

In this section the results of the trajectory shown in Section 2.2. will be analyzed by applying the simplified GHM (Table 1) on the approach described in Section 2.1. In a first step, the influence of the observation groups—accelerometer *a*, magnetometer *m*, estimated parameters of the previous epoch *x*, system noise *c* and gyroscope *g*—on the estimated orientation will be assessed by means of the r_i. Figure 3 shows a representative section of the calculated group redundancies for two different specifications of the sensor- and system noise standard deviations.
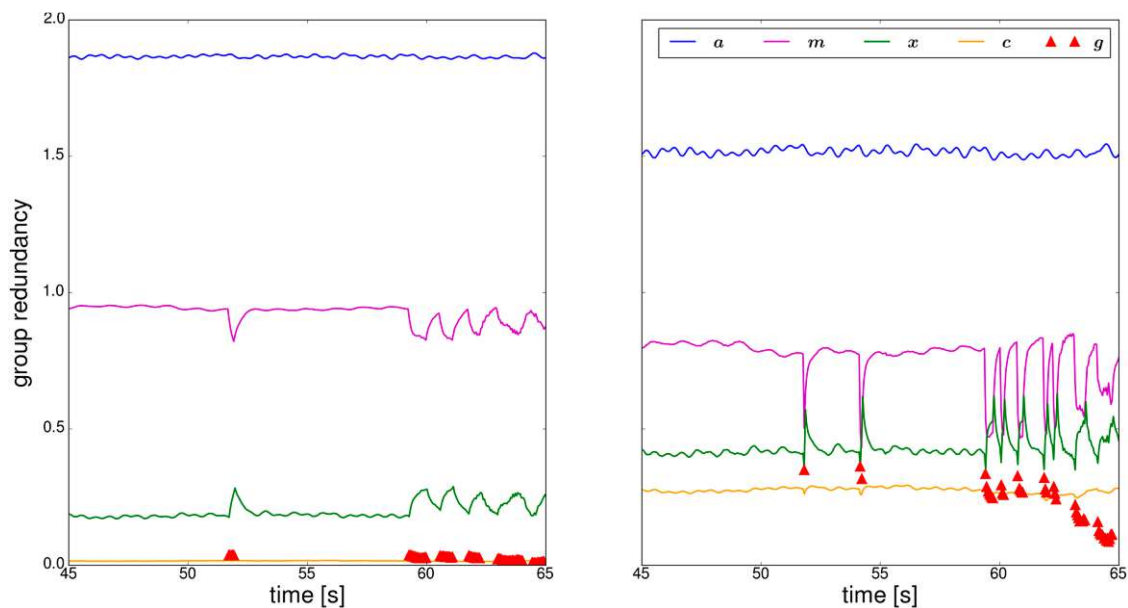
Figure 3. Redundancies of the observation groups used in the Kalman filter. (**Left**) Calculation with the original standard deviations; (**Right**) Calculation with adapted standard deviations.

For the beginning the focus lies on the left part of Figure 3, where the original standard deviations are used (Table 2). These are derived for each observation in the trajectory parts where the user walked straight. Using these standard deviations leads to a small partial redundancy of the observation groups (*x*, *c*, *g*) of the system equation in comparison to the ones of the measurement equation (*a*, *m*). This means that the estimated orientation mainly relies on the system equation. The reason for the high weight of the system equation is that the resulting trajectory should be smoothed [32]. The problem is that if the model assumptions made in the system equation do not capture the reality, the resulting deviations have high influence on the estimated orientation. There are mainly two possibilities to intervene in the partial redundancy respectively the inner reliability, which will be covered in the next two sections.

Table 2. Standard deviations used for the sensor measurements and system noise.

Standard Deviations	Gyroscope	System Noise	Accelerometer	Magnetometer
Original	$30°/s$	$10°/s$	1 m/s^2	5 µT
Adapted	$60°/s$	$20°/s$	0.5 m/s^2	2.5 µT

3.1. Adaption of the Stochastic Model

Adaption of the stochastic model means to change the standard deviations of the different observations. To align the group redundancies of the observation groups (Figure 3 left), the standard deviations of the sensors and system noise are changed until an improvement is visible. This leads to

the group redundancies in the right part of Figure 3, where the adapted standard deviations of Table 2 were used. The weight of the system equation in comparison to the measurement equation is now reduced, whereas the r_i of the gyroscope and the system noise are now clearly higher. The r_i of the magnetometer get close to the ones of the gyroscope if it is used when the user is turning, which yields in good mutual controllability.

To identify the critical observations, the r_i of the individual observations are analyzed. Figure 4 shows, that the r_i of the accelerometer are continuously higher than 0.2, which means that controllability is sufficient. Calculating the thresholds from which deviations can be—statistically justified—detected (according to [29]), gives ~1.4 m/s^2 for the y-component of the accelerometer and ~2 m/s^2 for the x- and z-component. The user's motion causes systematic deviations which exceeds these thresholds. Hence, accelerometer observations which should not be used for calculating pitch and roll can be detected.
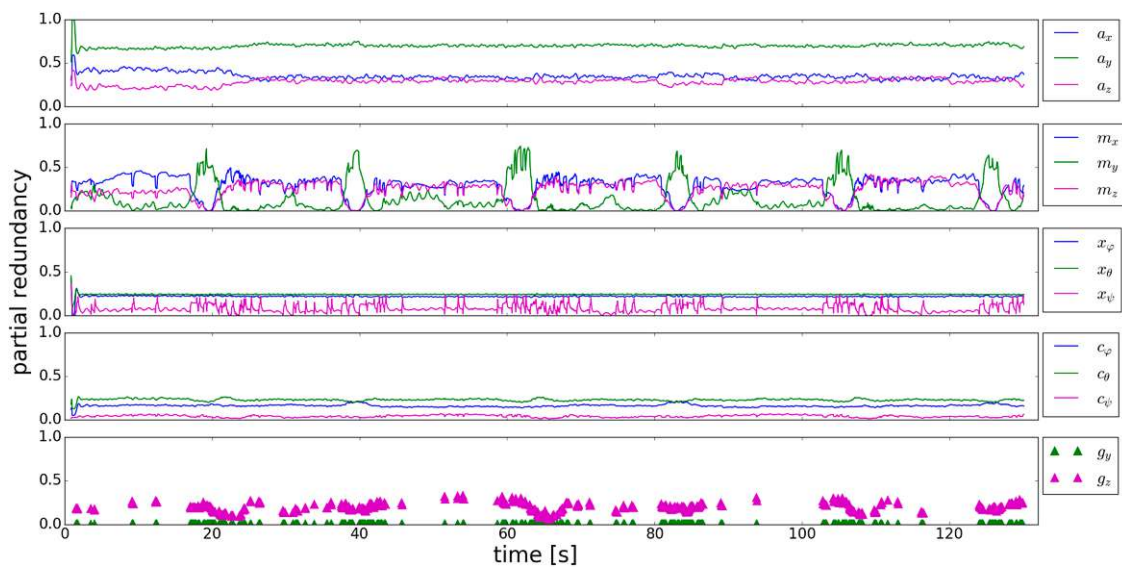
Figure 4. Partial redundancy of the accelerometer, magnetometer, previously estimated parameter, system noise and gyroscope (**top** to **bottom**).

The r_i of the magnetometer show a remarkable, alternating behavior. In the trajectory parts where the user walks straight, the r_i of m_y are close to zero. Whereas in parts where the user turns, controllability of m_x and m_z is bad. If there are systematic deviations in these observations, they cannot be detected and have a high influence on the estimated orientation angles. The r_i of x_φ and x_θ are again continuously higher than 0.2 and therefore sufficiently controlled. The same findings hold for c_φ and c_θ, whereas c_ψ is totally uncontrolled. Generally the r_i of the previously estimated parameters and the system noise behave in a similar manner. g_y is also uncontrolled as its r_i is very close to zero. The r_i of g_z are again higher than 0.2. The behavior of the r_i of the previously estimated yaw angle is interesting, as they go up to 0.25 if the gyroscope measurements are used in the system equation. If the gyroscope is not used in the following epochs the r_i decrease.

From the analysis of Figure 4 it can be concluded that there are uncontrollable observations in this approach, even if the standard deviations are adapted. To better understand the behavior of the r_i, the influence of the change of the standard deviation σ_i of one observation on the partial redundancy of the other observations is analyzed. This analysis should support an aimed change of the standard deviations to improve the r_i. Table 3 shows how the r_i change, if the standard deviation of one observation is multiplied with the factor 10 (left sign in Table 3) respectively 0.1 (right sign in Table 3). The standard deviation of all the observations was varied, except for the ones of the previously estimated parameters, as they are a direct result of the Kalman filter.

Table 3. Influence of the change of the standard deviation of one observation on the partial redundancy of the other observations. "+" indicates a raise and "−" a reduction of the partial redundancy. At the left sign, the standard deviation was increased by the factor 10 and at the right sign it was decreased by the factor 0.1. Grey shaded cells show the change in the corresponding observation and green means that the observations are functionally related.

	$\sigma_{g\text{-}y}$	$\sigma_{g\text{-}z}$	$\sigma_{c\text{-}\varphi}$	$\sigma_{c\text{-}\theta}$	$\sigma_{c\text{-}\psi}$	$\sigma_{a\text{-}x}$	$\sigma_{a\text{-}y}$	$\sigma_{a\text{-}z}$	$\sigma_{m\text{-}x}$	$\sigma_{m\text{-}y}$	$\sigma_{m\text{-}z}$
$r_{x\text{-}\varphi}$			− | −				− | +				
$r_{x\text{-}\theta}$				− | −		− | +		− | +			
$r_{x\text{-}\psi}$		+ | −			+ |				− | +	− | +	− | +
$r_{g\text{-}y}$	+ |										
$r_{g\text{-}z}$		+ | −							− | +	− | +	− | +
$r_{c\text{-}\varphi}$			+ | −				− | +			| +	
$r_{c\text{-}\theta}$				+ | −		− | +		− | +		| +	
$r_{c\text{-}\psi}$					+ | −						
$r_{a\text{-}x}$				− | +		+ | −		− | +			
$r_{a\text{-}y}$			− | +				+ | −				
$r_{a\text{-}z}$				− | +		− | +		+ | −		| +	
$r_{m\text{-}x}$		− | +							+ | −	− | +	− | +
$r_{m\text{-}y}$		− | +							− | +	+ | −	− | +
$r_{m\text{-}z}$		− | +							− | +	− | +	+ | −

The grey shaded cells show the influence of a change of σ_i of one observation on the corresponding r_i. If σ_i is increased, the weight of the observation will be less in state estimation. Hence the corresponding r_i should also be increased. A reduction of σ_i should cause a smaller r_i on the contrary. This is the case for most of the observations, except for g_y. The reason therefore is that its r_i are already close to zero and a reduction of σ_i has no effect.

Green shaded cells show a direct functional relation of the corresponding observations (see (1)–(4) and (12)–(14)). The change of σ_i of one observation influences also the partial redundancy of other observations. A raise of one σ_i should cause a reduction of partial redundancy of other observations, as they get more weight in the state estimation. A reduction of one σ_i should raise the partial redundancy of other observations on the contrary. Though, the change of σ_i of c_φ and c_θ, show another behavior. By increasing as well as decreasing $\sigma_{c\text{-}\varphi}$ and $\sigma_{c\text{-}\theta}$, the $r_{x\text{-}\varphi}$ and $r_{x\text{-}\theta}$ are reduced. A raise of σ_i of g_z respectively of c_ψ causes also a raise of the r_i of the previously estimated yaw angle.

A relation which is not expected from the system equations respectively the measurement equations, appears at the accelerometer measurements. a_y is only related to x_φ and c_φ, whereas a_x and a_z are related to x_θ and c_θ. The change of σ_i of one of the magnetometer measurements influences the r_i of x_ψ, g_z and the other two magnetometer components. m_y stands out, as a reduction of σ_i positively influences the r_i of c_φ and c_θ and the r_i of a_z. Hence, a reduction of σ_i of m_y would have the most positive influence on the r_i. As the controllability of this observation is bad, a further reduction is not advisable.

Changing the stochastic model clearly has an impact on the inner reliability but it also has limitations. As shown in Table 3, g_y as well as c_ψ are not controlled by any of the other observations (i.e., changing the standard deviation of any other observation does not influence $r_{g\text{-}y}$ and $r_{c\text{-}\psi}$). The only way left in the stochastic model is to increase the standard deviation of such observations. In this case it is very likely, that the raised standard deviations cover the systematic deviations which actually should be detected.

3.2. Adaption of the Functional Model

In general, the functional model can be adapted by changing respectively extending the system equations and the measurement equations. As seen in the previous section, the y-component of the gyroscope and the system noise of the yaw angle stay problematical observations, as their controllability cannot be improved by changing σ_i of other observations. Through the example of the r_i of the

gyroscope, the functional influences should be analyzed. (47) and (48) show the formulas to calculate the r_i of the gyroscope:

$$r_{g-y} = \sin^2 \varphi \cdot \frac{\sigma^2_{g-y} \cdot d^*_{33} \cdot \Delta t^2}{\cos^2 \theta} \tag{47}$$

$$r_{g-z} = \cos^2 \varphi \cdot \frac{\sigma^2_{g-z} \cdot d^*_{33} \cdot \Delta t^2}{\cos^2 \theta} \tag{48}$$

These equations are derived by evaluating (18), which is shown in Appendix C. d_{33}* corresponds to the third diagonal element of the inverse of **D**. The difference of (47) and (48) is the trigonometric function of the roll angle φ (σ^2_{g-y} and σ^2_{g-z} are assumed to be equal). As the roll angle is close to zero in the considered trajectory, also r_{g-y} will be close to zero even when changing σ_i of other observations (which influences d_{33}*). Hence, the smartphone orientation during the trajectory measurements has a huge impact on the calculated r_i—not only the ones from gyroscope, but also the ones from accelerometer and magnetometer ((12)–(14)). This seems reasonable if a closer look is taken on the quantities used to determine the smartphone orientation. The accelerometer should sense the gravity vector and the magnetometer the Earth magnetic field, which are both a vector quantity. The more sensor components sense these quantities, the better the mutual controllability should be. This should be the same for the gyroscope, which should sense the rotation of the user around the z-axis of the reference respectively navigation coordinate frame.

To check whether the assumptions made above are true, the recorded sensor data from the trajectory are rotated with the rotation matrix **R** given in (49):

$$\begin{aligned} &\boldsymbol{R} = \boldsymbol{R}_x \boldsymbol{R}_y \boldsymbol{R}_z \\ &\boldsymbol{R}_x = \begin{bmatrix} 1 & 0 & 0 \\ 0 & \cos\varphi & -\sin\varphi \\ 0 & \sin\varphi & \cos\varphi \end{bmatrix}, \ \boldsymbol{R}_y = \begin{bmatrix} \cos\theta & 0 & \sin\theta \\ 0 & 1 & 0 \\ -\sin\theta & 0 & \cos\theta \end{bmatrix}, \ \boldsymbol{R}_z = \begin{bmatrix} \cos\psi & -\sin\psi & 0 \\ \sin\psi & \cos\psi & 0 \\ 0 & 0 & 1 \end{bmatrix} \end{aligned} \tag{49}$$

φ is chosen to be 45° and θ and ψ are 0°. Evaluating the rotated sensor data in the same Kalman filter as used above, gives the partial redundancies shown in Figure 5. The r_i of the previously estimated parameters, the system noise as well as the x-components of the sensors are not affected by the rotated data, when comparing the results with Figure 4. The y- and z-components of the sensors are more balanced now, leading to a better mutual controllability. Especially the mean level of the r_i of the gyroscope y-component are now approximately 0.1, which is clearly higher compared to Figure 4.

The idea of the following approach is to use multiple trajectory data, to determine the actual smartphone's orientation. If one thinks of scenarios in crowded environments, it could be that multiple users have already taken the same path as the actual user does. If this data from the users who have taken the same path is stored, it could be used in a multiple trajectory data approach to determine the actual yaw angle, which equals the situation outlined in Section 2.3 where several sub-systems are used to determine the overall-system. Hence, the Gauss-Helmert Kalman filter which incorporates (32) in its functional model (33) has to be used now. In the case of orientation determination, the set of equations which unambiguously determine the state vector (31) are equal to (1), (2) and (3) respectively (4) for the actual trajectory. Now, for every additionally used trajectory, (1) and (2) have to be added to the unambiguous set of equations, as the smartphone's orientation could be different (the only assumption is that there is the same path, e.g., the same yaw angle). Thus—if N_{tr} is the number of used trajectories—N_{tr} roll angles, N_{tr} pitch angles and one yaw angle have to be estimated. If there is a turn detected in the actual trajectory, gyroscope measurements from multiple smartphones have to be processed. Hence, every additional trajectory contributes with a formula of type (4) to the system equation, which leads to $N_{tr}-1$ condition Equations (32) in the system equation. The measurement equation consists of N_{tr} triples of (12)–(14).
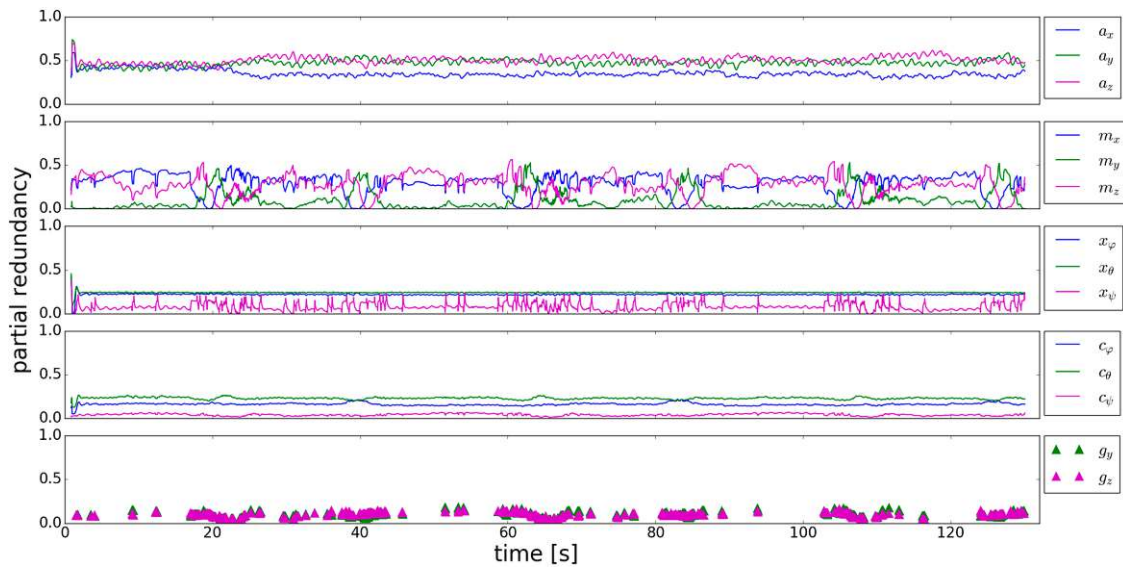
Figure 5. Partial redundancy of the rotated trajectory.

In this article additional trajectories are simulated, which means that they are retrieved from the trajectory considered in this section by performing rotations in the same manner as done in (49). This is a simplification respectively a synthetical example whose aim is to retrieve more insights into how additional observations affect the partial redundancy. Before using additional rotated trajectories, the effect of using the same trajectory data two times will be analyzed. The reason is that no additional roll and pitch angles have to be estimated and therefore the results for the partial redundancy can be directly compared to the results from Section 3.1 respectively Figure 4. The results of the partial redundancy of the observations from the actual trajectory are shown in Figure 6.
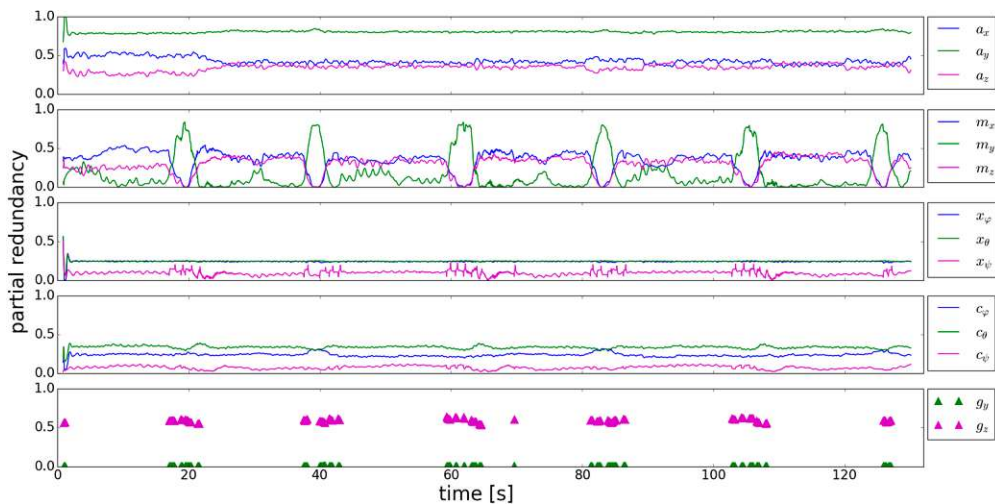
Figure 6. Partial redundancy of the actual trajectory when using two times the same trajectory data.

The most obvious effect can be seen in the turn detection. The gyroscope is used less in the straight trajectory parts, which leads to slightly different appearance of the r_i. Nevertheless, the height of the r_i can be compared. The r_i of the previously estimated roll and pitch angel has not changed. It can be seen, that the r_i of the accelerometer, the system noise components and the previously estimated yaw angle are raised by using additional observations, which is especially important for the system noise of the yaw angle. The controllability of this quantity is now slightly improved. The components of the

magnetometer and the gyroscope, which already had quite high r_i are now also raised, whereas an effect on the low r_i during turns is not visible.

This is not a surprise, as trajectory data is used two times where the controllability of these quantities is suboptimal. Figure 7 shows the partial redundancy of the observations from the actual trajectory by using one additional trajectory, where the smartphone's orientation is different. This additional trajectory comes from rotating the trajectory data as mentioned above (49), which is a simplification respectively simulation. In a real-life application some sort of search-algorithm would have to be performed on the stored trajectories, to find the ones where users took the same path as in the actual trajectory. The only thing that has changed, are the r_i of the previously estimated roll and pitch angles, as they are clearly reduced now. The reason could be that the overall redundancy has not changed from the scenario in Figure 6 to the scenario in Figure 7 but more parameters have to be estimated. The remaining r_i have not changed. Especially r_{g-y} is still close to zero, despite using an additional trajectory where the smartphone's orientation is different. The functional relation of the four gyroscope measurements—resulting from using the actual and the simulated trajectory (i.e., the two formulas of type (4))—doesn't lead to an improved mutual controllability. The same holds for the r_i of the magnetometer measurements which are close to zero.

Figure 8 shows the ground truth from total station (see Section 2.2), the raw result from the magnetometer and different variants of the estimated yaw angle. For better visibility, again a representative section of the trajectory is chosen. Estimation variant 1 clearly differs from the rest of the estimation variants as it is much smoother. In this variant the original standard deviations from Table 2 are used, whereas in the other variants the adapted ones are used. The differences between variant 2 and 3 are negligible. This is reasonable, as the additional trajectory data of variant 3 is just rotated in comparison to the original trajectory data. Thus, the additional trajectory data used in this article does not contribute to the state estimation process but to the improvement of the inner reliability. In future experiments, real multiple trajectory data has to be collected from different smartphones and users to further evaluate the approach presented in this section. In this article, variant 1 performs slightly better with the drawback of worse inner reliability. In the beginning of the trajectory section shown in Figure 8, the raw result from magnetometer as well as the estimated yaw angles are shifted due to undetected systematic deviations. The aim of future research will be to detect such systematic deviations based on improved inner reliability, enabling better performance of a Kalman filter used for orientation determination.
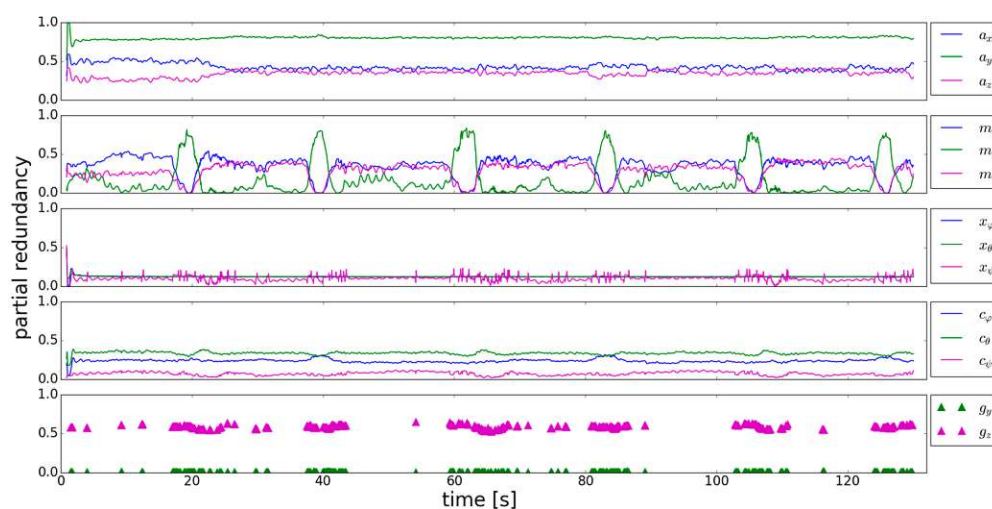
Figure 7. Partial redundancy of the actual trajectory when using additional data from one simulated, rotated trajectory.
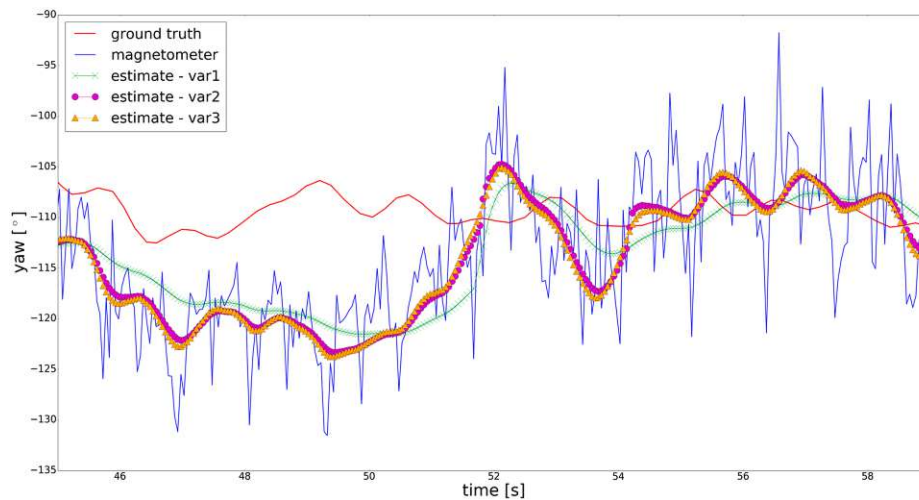
Figure 8. Different results for the yaw angle compared to ground truth from total station. In estimation variant 1 the original standard deviations from Table 2 are used. Variant 2 uses the adapted standard deviations. Variant 3 uses one simulated additional trajectory (equal to the one of Figure 7).

4. Discussion

The main novelty of this article is the formulation of the Kalman filter and the redundancy matrix in the GHM. Depending on the system description in the system equation two different sets of update equations are derived, which are both applied to orientation determination as well as to partial redundancy calculation. The results of these derivations are used to analyze the inner reliability based on the partial redundancy. Analyzing the partial redundancy shows that in the Kalman filter used in Section 2.1 the system equation contribute disproportionately highly to the estimation of the orientation compared the measurement equation. This means that the observations of the system equation are nearly uncontrolled. Two general ways are considered to intervene into the inner reliability respectively partial redundancy.

First, effects of changes in the stochastic model are analyzed. By adapting the standard deviations, the group redundancies can be improved. Analyzing the partial redundancy of the individual observations shows that observations which crucially determine the orientation are still badly controlled. Systematic deviations in such observations can cause huge disturbances in the estimated quantities. By increasing and decreasing the standard deviations, their influence on the partial redundancy was analyzed. It appears that reducing the standard deviation of the magnetometer's y-component, could increase many partial redundancies but its controllability is bad. The y-component of the gyroscope as well as the system noise of the yaw angle cannot be controlled by observations of the actual trajectory. It has to be mentioned that the resulting insights are in a way limited to the considered trajectory. Such adaptions in the stochastic model have to be also tested in other trajectories and different devices.

Furthermore, effects of changes in the functional model on the partial redundancy are considered. In a first step the influences of the smartphone's orientation on the partial redundancy were analyzed. Rotating the trajectory data shows that if more than one sensor axis is sensing the quantity of interest, the controllability will be improved. Using multiple trajectory data should take advantage of this behavior. The formulation of the Kalman filter update equations in the GHM enables processing multiple trajectory data in a Kalman filter. Partial redundancy is improved through this approach but still there are critical observations, such as the y-components of the gyroscope and magnetometer. Just using more data does not mandatory lead to better controllability in the GHM. Additionally, improving inner reliability does not lead to better accuracy of the estimated quantities. These questions respectively challenges will be addressed in future studies.

Appendix A

Formula (31) will be derived by rearranging (30):

$$\boldsymbol{0} = f(\hat{x}_{k-1}, u_k, c_k) - \bar{x}_k \tag{A1}$$

This is the approximate solution of the following least squares parameter estimation problem:

$$\boldsymbol{0} = f(\hat{\hat{x}}_{k-1}, \hat{u}_k, \hat{c}_k) - \hat{x}_k \tag{A2}$$

This is a special case of the GHM (22). Using the approximate solution for Taylor linearization—and neglecting second and higher order terms—yields:

$$\boldsymbol{0} = f(\hat{x}_{k-1}, u_k, c_k) - \bar{x}_k - E(\hat{x}_k - \bar{x}_k) + \frac{\partial f}{\partial \hat{x}_{k-1}}\left(\hat{\hat{x}}_{k-1} - \hat{x}_{k-1}\right) + \frac{\partial f}{\partial u_k}(\hat{u}_k - u_k) + \frac{\partial f}{\partial c_k}(\hat{c}_k - c_k) \tag{A3}$$

Taking (30) into account, the first two terms are equal to zero. The next step is to insert the following quantities in the linearized functional model above:

$$
\begin{aligned}
\frac{\partial f}{\partial \hat{x}_{k-1}} &= T_{k,k-1} \\
\frac{\partial f}{\partial u_k} &= U_{k,k-1} \\
\frac{\partial f}{\partial c_k} &= C_{k,k-1} \\
\hat{\hat{x}}_{k-1} - \hat{x}_{k-1} &= v_{\hat{x}_{k-1},k} \\
\hat{u}_k - u_k &= v_{u,k} \\
\hat{c}_k - c_k &= v_{c,k} \\
\Delta \hat{x}_k &= \hat{x}_k - \bar{x}_k
\end{aligned}
\tag{A4}
$$

Insertion gives:

$$\boldsymbol{0} = -E\Delta\hat{x}_k + T_{k,k-1}v_{\hat{x}_{k-1},k} + U_{k,k-1}v_{u,k} + C_{k,k-1}v_{c,k} \tag{A5}$$

The last step is to summarize $T_{k,k-1}$, $U_{k,k-1}$ and $C_{k,k-1}$ in one matrix and $v_{\hat{x},k-1,k}$, $v_{u,k}$ and $v_{c,k}$ in one vector:

$$-E\Delta\hat{x}_k + \begin{bmatrix} T_{k,k-1} & U_{k,k-1} & C_{k,k-1} \end{bmatrix} \begin{bmatrix} v_{\hat{x}_{k-1},k} \\ v_{u,k} \\ v_{c,k} \end{bmatrix} = \boldsymbol{0} \tag{A6}$$

Appendix B

The following calculation rules will be used to calculate the overall redundancy [42]:

$$
\begin{aligned}
tr(AB) &= tr(BA) \\
tr(A + B) &= tr(A) + tr(B)
\end{aligned}
\tag{A7}
$$

Calculation of the trace of R:

$$
\begin{aligned}
tr(R) &= tr\left(\sum_{ll} B^T \left(B\sum_{ll} B^T\right)^{-1}\left(E - A\sum_{\hat{x}\hat{x}} A^T\left(B\sum_{ll} B^T\right)^{-1}\right)B\right) = \\
&tr\left(\left(B\sum_{ll} B^T\right)^{-1}\left(E - A\sum_{\hat{x}\hat{x}} A^T\left(B\sum_{ll} B^T\right)^{-1}\right)B\sum_{ll} B^T\right) = \\
&tr\left(\left(B\sum_{ll} B^T\right)^{-1}\left(B\sum_{ll} B^T - A\sum_{\hat{x}\hat{x}} A^T\right)\right) = tr(E) - tr\left(\left(B\sum_{ll} B^T\right)^{-1}A\sum_{\hat{x}\hat{x}} A^T\right)
\end{aligned}
\tag{A8}
$$

The identity matrix comes from the matrix product $B\Sigma_{ll}B^T$ and its inverse. B contains the derivatives of the condition equations with respect to the observations. Therefore, its dimension is $b \times n$, where n equals the number of observations and b equals the number of condition equations. Hence, the identity matrix has dimension $b \times b$ and its trace corresponds to the number of condition equations:

$$
\begin{aligned}
tr(R) &= b - tr\left(\left(B\sum_{ll} B^T\right)^{-1}A\sum_{\hat{x}\hat{x}} A^T\right) = b - tr\left(A^T\left(B\sum_{ll} B^T\right)^{-1}A\sum_{\hat{x}\hat{x}}\right) = \\
&b - tr\left(A^T\left(B\sum_{ll} B^T\right)^{-1}A\left(A^T\left(B\sum_{ll} B^T\right)^{-1}A\right)^{-1}\right) = b - tr(E)
\end{aligned}
\tag{A9}
$$

As A contains the derivatives of the condition equations with respect to the parameters, the identity matrix has dimension $u \times u$, where u equals the number of parameters. Thus, the trace of R equals the number condition equations minus the number of parameters, which is the overall redundancy in the GHM [34].

$$
tr(R) = b - u = r
\tag{A10}
$$

Appendix C

To derive (47) and (48), the following quantities are used to evaluate (18):

$$
\begin{aligned}
\Sigma_{uu,k} &= \begin{bmatrix} \sigma_{g-x}^2 & 0 & 0 \\ 0 & \sigma_{g-y}^2 & 0 \\ 0 & 0 & \sigma_{g-z}^2 \end{bmatrix} = \sigma_g^2 E \\
U_{k,k-1} &= \begin{bmatrix} 0 & 0 & 0 \\ 0 & 0 & 0 \\ 0 & \sin\varphi\frac{\Delta t}{\cos\theta} & \cos\varphi\frac{\Delta t}{\cos\theta} \end{bmatrix} \\
A_{m,k} &= -E \\
D_k^{-1} &= \begin{bmatrix} d_{11}^* & d_{12}^* & d_{13}^* \\ d_{21}^* & d_{22}^* & d_{23}^* \\ d_{31}^* & d_{32}^* & d_{33}^* \end{bmatrix}
\end{aligned}
\tag{A11}
$$

$U_{k,k-1}$ contains the derivatives of (1), (2) and (4) with respect to the gyroscope measurements. $A_{m,k}$ contains the derivatives of (12)–(14) with respect to the parameters respectively the Euler angles and therefore equals the negative identity matrix The variances of the three gyroscope axes are assumed to be equal. Inserting these quantities into (12) gives:

$$
\sum_{j=1}^{n_u} r_{u,k,j} = \sigma_g^2 \cdot \sum_{j=1}^{n_u} e_j^T E \begin{bmatrix} 0 & 0 & 0 \\ 0 & 0 & \sin\varphi\frac{\Delta t}{\cos\theta} \\ 0 & 0 & \cos\varphi\frac{\Delta t}{\cos\theta} \end{bmatrix} (-E) \begin{bmatrix} d_{11}^* & d_{12}^* & d_{13}^* \\ d_{12}^* & d_{22}^* & d_{23}^* \\ d_{13}^* & d_{23}^* & d_{33}^* \end{bmatrix} (-E) \begin{bmatrix} 0 & 0 & 0 \\ 0 & 0 & 0 \\ 0 & \sin\varphi\frac{\Delta t}{\cos\theta} & \cos\varphi\frac{\Delta t}{\cos\theta} \end{bmatrix} e_j
\tag{A12}
$$

Evaluating the expression between the identity vectors e_j gives:

$$
\sum_{j=1}^{n_u} r_{u,k,j} = \frac{\sigma_g^2 \cdot d_{33}^* \cdot \Delta t^2}{\cos^2\theta} \cdot \sum_{j=1}^{n_u} e_j^T \begin{bmatrix} 0 & 0 & 0 \\ 0 & \sin^2\varphi & \sin\varphi\cdot\cos\varphi \\ 0 & \sin\varphi\cdot\cos\varphi & \cos^2\varphi \end{bmatrix} e_j
\tag{A13}
$$

References

1. Titterton, D.; Weston, J. *Strapdown Inertial Navigation Technology*, 2nd ed.; Institution of Engineering and Technology: Stevenage, UK, 2004; ISBN 978-0-86341-358-2.

2. Särkkä, S.; Tolvanen, V.; Kannala, J.; Rahtu, E. Adaptive Kalman filtering and smoothing for gravitation tracking in mobile systems. In Proceedings of the 2015 International Conference on Indoor Positioning and Indoor Navigation (IPIN), Banff, AB, Canada, 13–16 October 2015; IEEE: Piscataway, NJ, USA, 2015.

3. Groves, P.D. *Principles of GNSS, Inertial and Multisensor Integrated Navigation Systems*, 2nd ed.; Artech House: London, UK, 2013; ISBN 179-1-60807-005-3.

4. Kang, W.; Nam, S.; Han, Y.; Lee, S. Improved heading estimation for smartphone-based indoor positioning systems. In Proceedings of the 2012 IEEE 23rd International Symposium on Personal Indoor and Mobile Radio Communications (PIMRC), Sidney, NSW, Australia, 9–12 September 2012; IEEE: Piscataway, NJ, USA, 2012.

5. Crassidis, J.L.; Markley, F.L.; Cheng, Y. Survey of nonlinear attitude estimation methods. *J. Guid. Control Dyn.* **2007**, *30*, 12–28. [CrossRef]

6. Sabatini, A.M. Quaternion-based extended Kalman filter for determining orientation by inertial and magnetic sensing. *IEEE Trans. Biomed. Eng.* **2006**, *53*, 1346–1356. [CrossRef] [PubMed]

7. Tian, Z.; Zhang, Y.; Zhou, M.; Liu, Y. Pedestrian dead reckoning for MARG navigation using a smartphone. *EURASIP J. Adv. Signal Process.* **2014**, *2014*. [CrossRef]

8. Renaudin, V.; Combettes, C. Magnetic, Acceleration Fields and Gyroscope Quaternion (MAGYQ)-Based Attitude Estimation with Smartphone Sensors for Indoor Pedestrian Navigation. *Sensors* **2014**, *14*, 22864–22890. [CrossRef] [PubMed]

9. Zhu, X.; Li, Q.; Chen, G. APT: Accurate outdoor pedestrian tracking with smartphones. In Proceedings of the INFOCOM 2013, Turin, Italy, 14–19 April 2013; IEEE: Piscataway, NJ, USA, 2013.

10. Borenstein, J.; Ojeda, L.; Kwanmuang, S. Heuristic reduction of gyro drift in IMU-based personnel tracking systems. *J. Navig.* **2009**, *62*, 41–58. [CrossRef]

11. Jiménez, A.R.; Seco, F.; Prieto, J.C.; Guevara, J. Indoor pedestrian navigation using an INS/EKF framework for yaw drift reduction and a foot-mounted IMU. In Proceedings of the 7th Workshop on Positioning Navigation and Communication (WPNC), Dresden, Germany, 11–12 March 2010; IEEE: Piscataway, NJ, USA, 2010.

12. Blankenbach, J.; Sternberg, H.; Tilch, S. Indoor-Positionierung. In *Handbuch der Geodäsie*; Freeden, W., Rummel, R., Eds.; Springer: Berlin, Germany, 2015; pp. 1–36. ISBN 978-3-662-46900-2.

13. Sternberg, H.; Willemsen, T. Ein topologischer Ansatz zur Innenraumnavigation mit MEMS in Smartphones basierend auf dem Routing-Graph. In *Internationale Geodätische Woche Obergurgl 2017*; Hanke, K., Weinbold, T., Eds.; Wichmann: Berlin, Germany, 2017; pp. 51–60.

14. Bahl, P.; Padmanabhan, V. RADAR: An In-building RF-based User Location and Tracking System. In Proceedings of the INFOCOM 2000 19th Annual Joint Conference of the IEEE Computer and Communications Societies, Tel Aviv, Israel, 26–30 March 2000; IEEE: Piscataway, NJ, USA, 2000.

15. Honkavirta, V.; Perälä, T.; Ali-Löytty, S.; Piche, R. A Comparative Survey of WLAN Location Fingerprinting Methods. In Proceedings of the 6th Workshop on Positioning, Navigation and Communication (WPNC), Hannover, Germany, 19 March 2009; IEEE: Piscataway, NJ, USA, 2009.

16. Schmid, J.; Gädeke, T.; Curtis, D.; Ledlie, J. Improving sparse organic WiFi localization with inertial sensors. In Proceedings of the 9th Workshop on Positioning Navigation and Communication (WPNC), Dresden, Germany, 15–16 March 2012; IEEE: Piscataway, NJ, USA, 2012.

17. Zhu, J.; Sen, S.; Mohapatra, P.; Kim, K.H. Navigating in Signal Space: A Crowd-Sourced Sensing Map Construction for Navigation. In Proceedings of the 11th International Conference on Mobile Ad Hoc and Sensor Systems, Philadelphia, PA, USA, 28–30 October 2014; IEEE: Piscataway, NJ, USA, 2014.

18. Wang, Y.; Wong, A.K.S.; Cheng, R.S.K. Adaptive room-level localization system with crowd-sourced WiFi data. In Proceedings of the 2015 SAI Intelligent Systems Conference (IntelliSys), London, UK, 10–11 November 2015; IEEE: Piscataway, NJ, USA, 2015.

19. Abadi, M.J.; Luceri, L.; Hassan, M.; Chou, C.T.; Nicoli, M. A Collaborative Approach to Heading Estimation for Smartphone-based PDR Indoor Localisation. In Proceedings of the 2014 International Conference on Indoor Positioning and Indoor Navigation (IPIN), Busan, Korea, 27–30 October 2014; IEEE: Piscataway, NJ, USA, 2014.

20. Dong, B.; Burgess, T. Adaptive Kalman Filter for Indoor Navigation. In Proceedings of the 2016 International Conference on Indoor Positioning and Indoor Navigation (IPIN), Alcala de Henares, Madrid, Spain, 4–7 October 2016; IEEE: Piscataway, NJ, USA, 2016.

21. Guan, T.; Fang, L.; Dong, W.; Qiao, C. Robust Indoor Localization with Smartphones through Statistical Filtering. In Proceedings of the 2017 International Conference on Computing, Networking and Communications (ICNC), Santa Clara, CA, USA, 26–29 January 2017; IEEE: Piscataway, NJ, USA, 2017.

22. Retscher, G.; Tatschl, T. Indoor positioning using Wi-Fi lateration—Comparison of two common range conversion models with two novel differential approaches. In Proceedings of the 2016 Fourth International Conference on Ubiquitous Positioning, Indoor Navigation and Location Based Services (UPINLBS), Shanghai, China, 2–4 November 2016; IEEE: Piscataway, NJ, USA, 2016.

23. Kaemarungsi, K. Design of Indoor Positioning Systems Based on Location Fingerprinting Technique. Ph.D. Thesis, School of Information Science, University of Pittsburgh, Pittsburgh, PA, USA, 2005.

24. Gikas, V.; Dimitratos, A.; Perakis, H.; Retscher, G.; Ettlinger, A. Full-scale testing and performance evaluation of an active RFID system for positioning and personal mobility. In Proceedings of the 2016 International Conference on Indoor Positioning and Indoor Navigation (IPIN), Alcala de Henares, Madrid, Spain, 4–7 October 2016; IEEE: Piscataway, NJ, USA, 2016.

25. Hellmers, H.; Eichhorn, A.; Norrdine, A.; Blankenbach, J. IMU/magnetometer based 3D indoor positioning for wheeled platforms in NLoS scenarios. In Proceedings of the 2016 International Conference on Indoor Positioning and Indoor Navigation (IPIN), Alcala de Henares, Madrid, Spain, 4–7 October 2016; IEEE: Piscataway, NJ, USA, 2016.

26. Niedermayr, S. Positionsbestimmung durch Kombination geometrie- und merkmalsbasierter Verfahren unter Einbeziehung der Qualität. Ph.D. Thesis, Fakultät für Mathematik und Geoinformation, TU Wien, Vienna, Austria, 2015.

27. Gelb, A. *Applied Optimal Estimation*; MIT Press: Cambridge, MA, USA, 1974; ISBN 978-0-262-20027-1.

28. Simon, D. *Optimal State Estimation: Kalman, H infinity, and Nonlinear Approaches*; John Wiley & Sons: Hoboken, NJ, USA, 2006; ISBN 978-0-471-70858-2.

29. Heunecke, O.; Kuhlmann, H.; Welsch, W.; Eichhorn, A.; Neuner, H. *Auswertung Geodätischer Überwachungsmessungen*, 2nd ed.; Wichmann: Berlin, Germany, 2013; ISBN 978-3-87907-467-9.

30. Petersen, A.; Koch, R. Statistical Analysis of Kalman Filters by Conversion to Gauss-Helmert Models with Applications to Process Noise Estimation. In Proceedings of the 20th International Conference on Pattern Recognition, Istanbul, Turkey, 23–26 August 2010; IEEE: Piscataway, NJ, USA, 2010.

31. Wang, J.G. Filtermethoden zur Fehlertoleranten Kinematischen Positionsbestimmung. Ph.D. Thesis, Universität der Bundeswehr München, Neubiberg, Germany, 1997.

32. Ettlinger, A.; Neuner, H.; Burgess, T. Smartphone Sensor-Based Orientation Determination for Indoor-Navigation. In *Progress in Location-Based Services 2016*, 1st ed.; Gartner, G., Huang, H., Eds.; Springer: Berlin, Germany, 2017; pp. 49–68. ISBN 978-3-319-47288-1.

33. Ozyagcilar, T. *Implementing a Tilt-Compensated eCompass Using Accelerometer and Magnetometer Sensors; AN 2012, 4248*; Freescale Semiconductor: Austin, TX, USA, 2015.

34. Niemeier, W. *Ausgleichungsrechnung: Statistische Auswertemethoden*, 2nd ed.; Walter de Gruyter: Berlin, Germany, 2008; ISBN 978-3-11-019055-7.

35. Wieser, A.; Petovello, M.G.; Lachapelle, G. Failure scenarios to be considered with kinematic high precision relative GNSS positioning. In Proceedings of the 17th International Technical Meeting of the Satellite Division of The Institute of Navigation (ION GNSS), Long Beach, CA, USA, 21–24 September 2004; ION: Manassas, VA, USA, 2004.

36. Yang, L.; Li, B.; Shen, Y.; Rizos, C. Extension of Internal Reliability Analysis regarding Seperability Analysis. *J. Surv. Eng.* **2017**, *143*, 1–10. [CrossRef]

37. Wang, J.G. Reliability analysis in Kalman filtering. *J. Glob. Position. Syst.* **2009**, *8*, 101–111. [CrossRef]

38. Wang, J.G. Test Statistics in Kalman Filtering. *J. Glob. Position. Syst.* **2008**, *7*, 81–90. [CrossRef]

39. Koch, K.R. Outlier detection for the nonlinear Gauss Helmert model with variance components by the expectation maximization algorithm. *J. Appl. Geod.* **2014**, *8*, 185–194. [CrossRef]
40. Koch, K.R. Robust estimations for the nonlinear Gauss Helmert model by the expectation maximization algorithm. *J. Geod.* **2014**, *88*, 263–271. [CrossRef]
41. Jäger, R.; Müller, T.; Saler, H.; Schwäble, R. *Klassische und Robuste Ausgleichungsverfahren*; Wichmann: Berlin, Germany, 2005; ISBN 3-87907-370-8.
42. Voigt, C.; Adamy, J. *Formelsammlung der Matrizenrechnung*, 1st ed.; Oldenbourg Wissenschaftsverlag GmbH: München, Germany, 2007; ISBN 978-3-486-58350-2.
43. Kuusniemi, H.; Wieser, A.; Lachapelle, G.; Takala, J. User-level reliability monitoring in urban personal satellite-navigation. *IEEE Trans. Aerosp. Electron. Syst.* **2007**, *43*, 1305–1318. [CrossRef]

A.2   Assessment of inner reliability in the Gauss-Helmert model

Andreas Ettlinger* and Hans Neuner

Assessment of inner reliability in the Gauss-Helmert model

Abstract: In this contribution, the minimum detectable bias (MDB) as well as the statistical tests to identify disturbed observations are introduced for the Gauss-Helmert model. Especially, if the observations are uncorrelated, these quantities will have the same structure as in the Gauss-Markov model, where the redundancy numbers play a key role. All the derivations are based on one-dimensional and additive observation errors respectively offsets which are modeled as additional parameters to be estimated. The formulas to compute these additional parameters with the corresponding variances are also derived in this contribution. The numerical examples of plane fitting and yaw computation show, that the MDB is also in the GHM an appropriate measure to analyze the ability of an implemented least-squares algorithm to detect if outliers are present. Two sources negatively influencing detectability are identified: columns close to the zero vector in the observation matrix **B** and sub-optimal configuration in the design matrix **A**. Even if these issues can be excluded, it can be difficult to identify the correct observation as being erroneous. Therefore, the correlation coefficients between two test values are derived and analyzed. Together with the MDB these correlation coefficients are an useful tool to assess the inner reliability – and therefore the detection and identification of outliers – in the Gauss-Helmert model.

Keywords: Least-Squares Adjustment, Gauss-Helmert model, Inner Reliability

1 Introduction

The aim of many geodetic tasks is to determine unknown quantities (i. e. parameters) from redundant observations by using Least-Squares (LS). Most of the functional models in use equal the Gauss-Markov model (GMM) (e. g. [30] p. 129 ff.), explicitly relating the observations to functions

*Corresponding author: Andreas Ettlinger, Department of Geodesy and Geoinformation, TU Wien, Vienna, Austria, e-mail: andreas.ettlinger@geo.tuwien.ac.at
Hans Neuner, Department of Geodesy and Geoinformation, TU Wien, Vienna, Austria, e-mail: hans.neuner@geo.tuwien.ac.at

of parameters. Possible variants of the GMM are to use additional condition equations only containing the parameters ([14] pp. 184–185) or transferring it to an adjustment model with condition equations only containing the observations ([33] p. 61 ff.). Nevertheless, there are also tasks where the functional model can't be formulated just using observation equations, e. g. surface fitting based on point clouds [20]. Such applications necessitate using condition equations implicitly containing the unkonwn parameters as well as the observations, which leads to the most general adjustment model, the Gauss-Helmert model (GHM), originally proposed in [13]. Kinematic applications (e. g. different navigation tasks) require the use of sequential estimation algorithms. When additionally using a state transition model, one arrives at the well known Kalman filter which is formulated in the GMM ([10] p. 103 ff.). [6] derived the equations for sequential estimation in the GHM (including a state transition model) to solve the task of orientation determination with inertial sensors and magnetometer. It is possible to solve the GHM by the help of the errors-in-variables model leading to the approach of total Least-Squares [29], which is an extension to the GMM [11]. This contribution focuses on the solution of the GHM using an optimization approach based on Lagrangian multipliers with previously linearized condition equations.

Observations are not only subject to random errors, but also to systematic errors respectively outliers [23]. There are two main approaches to deal with outliers in the observation data: one can locate the erroneous observations and eliminate them from the error-free observations or one can use estimation procedures which are less sensitive to erroneous observations by reducing their influence on the estimated parameters.

In the first approach, very often statistical hypothesis tests are used to decide whether an observation is erroneous or not. The most popular approach is data snooping, leading to the concept of reliability, introduced to geodesy by Baarda [1, 2]. The assumption in Baarda's data snooping is, that there is one outlier present in the set of observations. Therefore, a one dimensional local hypothesis test is performed on each observation to identify the outlier. From this procedure the well known measures for inner reliability (the minimum detectable bias (MDB) and redundancy number) as well as outer reliability (influence

of not detected outliers on estimated parameters) are derived [8]. DIA (Detection – Identification – Adaption) is a more general approach of using multiple statistical hypothesis tests for handling outliers [35]. In the detection step, a global test is performed by using the LS results, indicating if outliers are present. In the identification step, local tests are used to identify erroneous observations and in the adaption step, these observations are removed or additional parameters for compensating outliers are estimated. The concepts of data snooping, reliability and DIA are also used in sequential LS respectively Kalman filtering, where kinematic GNSS positioning is an important application [36, 26]. Combinatorial methods are another way of identifying erroneous observations by adjusting many different subsets of observations. The optimal set of observations can then be chosen by using the same statistical hypothesis test as in the detection step of DIA [3, 5]. Other variants are to use the maximum subsample method to find the subset in the data with maximum number of consistent observations for the adjustment of geodetic networks [28] or to use the information criteria for model selection to determine outliers as well as their number [24]. The Least-Median of Squares (LMS) method [32] – which actually belongs to the field of robust estimation – can also be seen as a combinatorial method.

The other approach of dealing with outliers is to use estimators which have a bounded influence function to reduce the impact of outliers on the parameters which is the key property in robust estimation [15, 12]. Especially the robust M-estimators are commonly used and the idea is to iteratively solve the adjustment where in each iteration, the weights of the observations are updated and therefore the influence of outliers is reduced. There are many different variants to compute the weights, see for example [17] pp. 281–284 or [16] pp. 117–129. In geodesy this is e. g. implemented in kinematic GNSS positioning [22] or similarity transformation based on total LS [27].

The prementioned methods for outlier handling are mainly developed in the GMM. However, they are not limited to be used only in the GMM but can also be transferred to the GHM. [18, 19] developed an approach reducing the influence of outliers in the GHM by iteratively down-weighting the corresponding observations, where the weights are computed with the Expectation-Maximization (EM) algorithm. This method is applied to laser scanning to detect outliers in the surface fitting process [20] but also in the external calibration together with digital cameras [31] which both require the GHM to solve the adjustment. In the latter one, also local tests (of observation groups) based on standardized residuals are considered. As it will be shown in section 2, these tests are

only valid, if the observations (or observation groups) are not correlated. [21] already introduced hypothesis tests for additionally estimated parameters in the GHM but didn't extend this approach to the context of reliability and identification of outliers. Hence, the aim of this article is to derive the measures for inner reliability as well as to assess an implemented LS approach regarding the detection and identification of outliers. This will be done by analyzing the results of two numerical examples. The paper is organized as follows: in section 2 we derive inner reliability measures and test statistics for the GHM. Section 3 shows the application of the derived body of equations to plane fitting. Section 4 starts with a theoretical discussion of detecting and identifying outliers in the GHM and afterwards extends the numerical example of plane fitting by analyzing the previously introduced matrices and measures. Additionally, a second numerical example, namely the computation of the yaw angle using magnetometers, will be investigated.

2 Inner reliability in the Gauss-Helmert model

The main condition in LS is to minimize the weighted sum of squared residuals

$$f(\hat{\mathbf{v}}) = \hat{\mathbf{v}}^T \mathbf{Q}_{ll}^{-1} \hat{\mathbf{v}}, \tag{1}$$

with $\hat{\mathbf{v}} \in R^{n \times 1}$ being the residuals and $\mathbf{Q}_{ll}$ being a positive-definite cofactor matrix. This matrix results when extracting the variance of unit weight σ_0^2 from the variance-covariance matrix (VCM) $\mathbf{\Sigma}_{ll}$ of the observations $\mathbf{l} \in R^{n \times 1}$

$$\mathbf{\Sigma}_{ll} = \sigma_0^2 \mathbf{Q}_{ll}. \tag{2}$$

The secondary condition equals the functional model of the GHM

$$\mathbf{h}(\hat{\mathbf{x}}, \mathbf{l} + \hat{\mathbf{v}}) = \mathbf{h}(\hat{\mathbf{x}}, \hat{\mathbf{l}}) = \mathbf{0}, \tag{3}$$

where $\hat{\mathbf{x}} \in R^{u \times 1}$ are the parameters to be estimated. As the functional model (3) is non-linear in general, it has to be linearized with Taylor series expansion

$$\mathbf{h}(\hat{\mathbf{x}}, \hat{\mathbf{l}}) \approx \mathbf{h}(\mathbf{x}^{(0)}, \mathbf{l}^{(0)}) + \frac{\partial \mathbf{h}(\hat{\mathbf{x}}, \hat{\mathbf{l}})}{\partial \hat{\mathbf{x}}}|_{\mathbf{x}^{(0)}, \mathbf{l}^{(0)}} (\hat{\mathbf{x}} - \mathbf{x}^{(0)})$$
$$+ \frac{\partial \mathbf{h}(\hat{\mathbf{x}}, \hat{\mathbf{l}})}{\partial \hat{\mathbf{l}}}|_{\mathbf{x}^{(0)}, \mathbf{l}^{(0)}} (\hat{\mathbf{l}} - \mathbf{l}^{(0)}), \tag{4}$$

using approximate values $\mathbf{l}^{(0)}$ and $\mathbf{x}^{(0)}$ for the observations and the parameters. This linearization necessitates

to solve the adjustment iteratively, where the functional model is always linearized at the previously estimated parameters and observations [25]. The partial derivatives with respect to $\hat{\mathbf{x}}$ form the entries of the design matrix $\mathbf{A} \in R^{b \times u}$, the partial derivatives with respect to $\hat{\mathbf{l}}$ form the entries of the observation matrix $\mathbf{B} \in R^{b \times n}$ and $\hat{\mathbf{x}} - \mathbf{x}^{(0)}$ corresponds to $d\hat{\mathbf{x}}$, the estimated additions to the approximate values of the parameters. According to [18], the last bracketed term is expanded

$$\mathbf{h}(\hat{\mathbf{x}}, \hat{\mathbf{l}}) \approx \mathbf{h}(\mathbf{x}^{(0)}, \mathbf{l}^{(0)}) + \mathbf{A}d\hat{\mathbf{x}} + \mathbf{B}(\hat{\mathbf{l}} - \mathbf{l}) + \mathbf{B}(\mathbf{l} - \mathbf{l}^{(0)}), \quad (5)$$

where $\hat{\mathbf{l}} - \mathbf{l}$ equals the estimated residuals $\hat{\mathbf{v}}$. By introducing the misclosure vector $\mathbf{w} \in R^{b \times 1}$ and neglecting higher order terms, one arrives at the final formulation of the linearized functional model

$$\mathbf{h}(\hat{\mathbf{x}}, \hat{\mathbf{l}}) \approx \mathbf{w} + \mathbf{A}d\hat{\mathbf{x}} + \mathbf{B}\hat{\mathbf{v}}$$
$$\text{with } \mathbf{w} = \mathbf{h}(\mathbf{x}^{(0)}, \mathbf{l}^{(0)}) + \mathbf{B}(\mathbf{l} - \mathbf{l}^{(0)}). \quad (6)$$

As mentioned above, the adjustment has to be solved iteratively, where in the first iteration step, $\mathbf{l}^{(0)}$ is set to $\mathbf{l}$. The minimization of (1) under consideration of (6), can now be formulated as an optimization problem (see e. g. [4] p. 66 ff.)

$$L(d\hat{\mathbf{x}}, \hat{\mathbf{v}}, \hat{\mathbf{k}}) = \hat{\mathbf{v}}^T \mathbf{Q}_{ll}^{-1} \hat{\mathbf{v}} - 2\hat{\mathbf{k}}^T (\mathbf{w} + \mathbf{A}d\hat{\mathbf{x}} + \mathbf{B}\hat{\mathbf{v}}). \quad (7)$$

Solving this optimization problem, gives the results for $d\hat{\mathbf{x}}$, $\hat{\mathbf{k}}$ and $\hat{\mathbf{v}}$ and their corresponding cofactor matrices

$$\mathbf{Q}_{\hat{x}\hat{x}} = (\mathbf{A}^T \mathbf{N}^{-1} \mathbf{A})^{-1} \quad (8)$$

$$d\hat{\mathbf{x}} = -\mathbf{Q}_{\hat{x}\hat{x}} \mathbf{A}^T \mathbf{N}^{-1} \mathbf{w} \quad (9)$$

$$\mathbf{Q}_{\hat{k}\hat{k}} = \mathbf{N}^{-1}(\mathbf{I} - \mathbf{A}\mathbf{Q}_{\hat{x}\hat{x}} \mathbf{A}^T \mathbf{N}^{-1}) \quad (10)$$

$$\hat{\mathbf{k}} = -\mathbf{Q}_{\hat{k}\hat{k}} \mathbf{w} \quad (11)$$

$$\mathbf{Q}_{\hat{v}\hat{v}} = \mathbf{Q}_{ll} \mathbf{B}^T \mathbf{Q}_{\hat{k}\hat{k}} \mathbf{B} \mathbf{Q}_{ll} \quad (12)$$

$$\hat{\mathbf{v}} = \mathbf{Q}_{ll} \mathbf{B}^T \hat{\mathbf{k}}, \quad (13)$$

in which $\hat{\mathbf{k}} \in R^{b \times 1}$ are the Lagrangian multipliers, $\mathbf{I}$ is the identity matrix and $\mathbf{N} = \mathbf{B}\mathbf{Q}_{ll}\mathbf{B}^T$. It is important to mention, that rank$(\mathbf{A}) = u$ and rank$(\mathbf{B}) = b$. Otherwise, the matrices to be inverted get singular and the LS problem (respectively the normal equation system resulting from (7)) is not unambiguously solvable.

Reliability is based on Baardas' data snooping, which aim is to detect outliers in the observations with statistical hypothesis tests. It will be assumed that there is only one outlier ∇_i, $i = 1, ..., n$ which will be modeled as bias and treated as a deterministic parameter to be estimated. The vector $\mathbf{c}_i \in R^{n \times 1}$ specifies which observation is disturbed by

∇_i, containing a 1 on the i-th position and elsewhere zeroes. The observation model becomes

$$\mathbf{l} = E\{\mathbf{l}\} - \mathbf{c}_i \nabla_i - \mathbf{v}$$
$$\text{with } \mathbf{l} \sim N(E\{\mathbf{l}\}, \Sigma_{ll}) \text{ and } \mathbf{v} \sim N(\mathbf{0}, \Sigma_{ll}), \quad (14)$$

where $E\{\}$ is the expectation operator and $\mathbf{l}$ as well as $\mathbf{v}$ are random variables which are both normally distributed with the same variance (2). If $\nabla_i = 0$, one arrives at the observation model (3) used in the GHM. Using the linearized functional model (6), one can formulate two equivalent null hypothesis

$$H_0 : \nabla_i = 0 \quad \equiv \quad \mathbf{w} + \mathbf{A}d\hat{\mathbf{x}} + \mathbf{B}\hat{\mathbf{v}} = \mathbf{0}. \quad (15)$$

(14) is a special case of the more general observation model (43) shown in appendix A, where $\mathbf{g}_l(\mathbf{l}, \nabla) = \mathbf{l} + \mathbf{c}_i \nabla_i$. Thus, $\mathbf{A}_\nabla$ (the Jacobi matrix containing the partial derivatives of $\mathbf{g}_l(\mathbf{l}, \nabla)$ with respect to ∇) equals the vector $\mathbf{c}_i$ and the matrix product $\mathbf{B}\mathbf{A}_\nabla$ (appearing in (45)–(52)) can be replaced with $\mathbf{b}_i$, the i-th column of $\mathbf{B}$. Thus, the alternative hypothesis can be explicitly formulated if $\nabla_i \neq 0$ by adapting the linearized functional model (45) derived in appendix A

$$H_{A,i} : \nabla_i \neq 0 \quad \equiv \quad \mathbf{w} + \mathbf{A}d\hat{\mathbf{x}}' + \mathbf{B}\hat{\mathbf{v}}' + \mathbf{b}_i \hat{\nabla}_i = \mathbf{0}. \quad (16)$$

Due to the incorporation of $\hat{\nabla}_i$, the quantities $d\hat{\mathbf{x}}'$ and $\hat{\mathbf{v}}'$ are numerically different from the corresponding quantities in H_0, which can be seen in the equations (48) and (50) of appendix A. $\mathbf{w}$, $\mathbf{A}$ and $\mathbf{B}$ are unchanged, compared to the functional model of H_0, because $\nabla_i^{(0)}$ is set to zero. From now on it will be assumed, that the error due to the linearization is negligible compared to the systematic deviation caused by $\hat{\nabla}_i$. Hence, all following deductions regarding inner reliability will be done with respect to the first step of iteration.

The validity of H_0 has to be verified by using an appropriate statistical test. According to [16] pp. 187–197, there are several valid test values depending on the chosen variance of unit weight. In this article, the a priori variance of unit weight σ_0^2 from (2) will be used, leading to the test value

$$T_F(\nabla_i) = \frac{\hat{\nabla}_i^2}{\sigma_0^2 \cdot q_{\hat{\nabla}_i}} \sim F_{1,\infty} | H_0$$

$$T_F(\nabla_i) = \frac{\hat{\nabla}_i^2}{\sigma_0^2 \cdot q_{\hat{\nabla}_i}} \sim F_{1,\infty,\lambda_{F_i}} | H_{A,i}, \quad (17)$$

which follows the central F-distribution $F_{1,\infty}$ with the degrees of freedom 1 and ∞ in case of H_0 is true. Otherwise, this test value follows the non-central F-distribution

$F_{1,\infty,\lambda_{F_i}}$ with the non-centrality parameter λ_{F_i}. One can also use the square root of $\sqrt{T_F(\nabla_i)}$. This test value

$$T_N(\nabla_i) = \frac{\hat{\nabla}_i}{\sigma_0 \cdot \sqrt{q_{\hat{\nabla}_i}}} \sim N(0,1)|H_0$$

$$T_N(\nabla_i) = \frac{\hat{\nabla}_i}{\sigma_0 \cdot \sqrt{q_{\hat{\nabla}_i}}} \sim N(\lambda_{N,i},1)|H_{A_i} \qquad (18)$$

follows the central standardized normal distribution $N(0,1)$ in case of H_0 is true and otherwise it follows the non-central standardized normal distribution $N(\lambda_{N,i},1)$ with non-centrality parameter $\lambda_{N,i}$. Using the estimated variance of unit weight $\hat{\sigma}_0^2$ from (29) in (17), one would arrive at a test value following the F-distribution $F_{1,r-1}$ with degrees of freedom 1 and $r-1$ with $r = b-u$ being the redundancy of the adjustment. The square root of this test value is then t-distributed t_{r-1} with degree of freedom $r-1$ (see [16] p. 180). Using equation (52) and (51) of appendix A, one can compute the test values $T_F(\nabla_i)$ and $T_N(\nabla_i)$ for the i-th observation

$$T_F(\nabla_i) = \frac{\hat{\mathbf{k}}^T\mathbf{b}_i\mathbf{b}_i^T\hat{\mathbf{k}}}{\sigma_0^2 \cdot \mathbf{b}_i^T\mathbf{Q}_{\hat{k}\hat{k}}\mathbf{b}_i} = \frac{\hat{\mathbf{v}}^T\mathbf{B}^T\mathbf{N}^{-1}\mathbf{b}_i\mathbf{b}_i^T\mathbf{N}^{-1}\mathbf{B}\hat{\mathbf{v}}}{\sigma_0^2 \cdot \mathbf{b}_i^T\mathbf{N}^{-1}\mathbf{B}\mathbf{Q}_{\hat{v}\hat{v}}\mathbf{B}^T\mathbf{N}^{-1}\mathbf{b}_i} \qquad (19)$$

$$T_N(\nabla_i) = \frac{\mathbf{b}_i^T\hat{\mathbf{k}}}{\sigma_0 \cdot \sqrt{\mathbf{b}_i^T\mathbf{Q}_{\hat{k}\hat{k}}\mathbf{b}_i}} = \frac{\mathbf{b}_i^T\mathbf{N}^{-1}\mathbf{B}\hat{\mathbf{v}}}{\sigma_0 \cdot \sqrt{\mathbf{b}_i^T\mathbf{N}^{-1}\mathbf{B}\mathbf{Q}_{\hat{v}\hat{v}}\mathbf{B}^T\mathbf{N}^{-1}\mathbf{b}_i}}. \qquad (20)$$

For the derivation of the minimum detectable bias (MDB) $\hat{\nabla}_{0,i}$, $T_N(\nabla_i)$ will be used. It is an important measure of inner reliability and states how big an outlier in the i-th observation has to be, such that it can be detected by using a statistical test with preset significance number α_0 and power β_0. Setting α_0 and β_0, implies a fixed $\lambda_{0,N}$ as these three quantities are not independent of each other [14] p. 247. According to [2, 8], $\lambda_{0,N}$ can be calculated with

$$\lambda_{0,N} \approx \phi^{-1}(1 - \alpha_0/2) + \phi^{-1}(\beta_0), \qquad (21)$$

where ϕ^{-1} is the inverse of the density function of the standard normal distribution. If an outlier causes a noncentrality (i. e. a test value $T_N(\nabla_i)$) bigger than $\lambda_{0,N}$, it can be detected at the level of α_0 and β_0. This threshold equals the MDB

$$\hat{\nabla}_{0,i} = \lambda_{0,N} \cdot \sigma_0 \cdot \sqrt{q_{\hat{\nabla}_i}} = \frac{\lambda_{0,N} \cdot \sigma_0}{\sqrt{\mathbf{b}_i^T\mathbf{Q}_{\hat{k}\hat{k}}\mathbf{b}_i}} = \frac{\lambda_{0,N} \cdot \sigma_0}{\sqrt{\mathbf{b}_i^T\mathbf{N}^{-1}\mathbf{B}\mathbf{Q}_{\hat{v}\hat{v}}\mathbf{B}^T\mathbf{N}^{-1}\mathbf{b}_i}} \qquad (22)$$

which is derived by rearranging equation (18), using equation (52) of appendix A and setting $T_N(\nabla_i) = \lambda_{0,N}$.

The observations are often assumed to be uncorrelated. In this case $\mathbf{Q}_{ll}$ is a diagonal matrix and the formulas to calculate $\hat{\nabla}_i$, q_{∇_i}, $T_N(\hat{\nabla}_i)$ and $\hat{\nabla}_{0,i}$ can be further simplified

$$q_{\hat{\nabla}_i} = \frac{q_{l_i}}{r_{ii}} \qquad (23)$$

$$\hat{\nabla}_i = \frac{v_i}{r_{ii}} \qquad (24)$$

$$T_F(\nabla_i) = \frac{v_i^2}{\sigma_0^2 \cdot q_{l_i} \cdot r_{ii}} \qquad (25)$$

$$T_N(\nabla_i) = \frac{v_i}{\sigma_0 \cdot \sqrt{q_{l_i} \cdot r_{ii}}} \qquad (26)$$

$$\hat{\nabla}_{0,i} = \lambda_{0,N} \cdot \sigma_0 \sqrt{\frac{q_{l_i}}{r_{ii}}}, \qquad (27)$$

giving the same results as in the GMM (see e. g. [2, 8] or [16] pp. 193–194). Here, r_{ii} are the diagonal elements of the redundancy matrix

$$\mathbf{R} = \mathbf{Q}_{\hat{v}\hat{v}}\mathbf{Q}_{ll}^{-1} = \mathbf{Q}_{ll}\mathbf{B}^T\mathbf{N}^{-1}(\mathbf{I} - \mathbf{A}(\mathbf{A}^T\mathbf{N}^{-1}\mathbf{A})^{-1}\mathbf{A}^T\mathbf{N}^{-1})\mathbf{B} \qquad (28)$$

also called redundancy numbers [8]. $\mathbf{R}$ has the same importance as in the GMM, which can be illustrated by analyzing equation (50), as the matrix controlling the influence of $\hat{\nabla}_i$ on the residuals $\hat{\mathbf{v}}$ of H_0 equals $\mathbf{R}$ (e. g. shown in [6]).

Until now, it was assumed that there is only one outlier affecting one observation. In general it is not known which observation is disturbed. Thus, every observation has to be tested, leading to n local tests respectively alternative Hypothesis $H_{A,i}$. To transfer the previous thoughts into the context of DIA, the detection step has to be defined. Every adjustment task should be followed by a global test

$$T_F(\sigma_0^2) = \frac{\hat{\sigma}_0^2}{\sigma_0^2} = \frac{\hat{\mathbf{v}}^T\mathbf{Q}_{ll}^{-1}\hat{\mathbf{v}}}{(b-u) \cdot \sigma_0^2} \sim F_{b-u,\infty}|H_0$$

$$T_F(\sigma_0^2) = \frac{\hat{\sigma}_0^2}{\sigma_0^2} \sim F_{b-u,\infty,\lambda_{F,i}}|H_{A,i}, \qquad (29)$$

which states, whether the assumptions made in the functional and/or stochastic model are correct (see e. g. [16] p. 182). According to [34] pp. 182–183, the global test can also be seen as the detection step, indicating whether outliers are present in the observations or not. The significance number α of the global test $T_F(\sigma_0^2)$ as well as the significance numbers α_0 of the n local tests $T_N(\nabla_i)$ (or $T_F(\nabla_i)$) have to be matched by using the Bonferroni equation

$$\alpha_0 \approx \frac{\alpha}{n}, \qquad (30)$$

such that all the tests have similar sensitivity to an outlier [23].

3 Numerical example: plane fitting

In the following application the equations derived in section 2 will be applied. The focus will be on the analysis of the LS approach to detect if outliers are present (detection step of DIA) and to locate respectively identify the erroneous observation (identification step of DIA). Therefore, the MDB $\nabla_{0,i}$ and the local tests $T_N(\nabla_i)$ will be evaluated in this section.

Fitting a plane into a point cloud is a typical application of the GHM. If the points $\mathbf{p}_j \in R^{3 \times 1}$, $j = 1, ..., b$ are given in Cartesian coordinates, the plane can be parameterized by using the components of the (normalized) normal vector $\mathbf{n} \in R^{3 \times 1}$ and the distance to the origin d[1]

$$0 = \frac{n_x}{d} p_{x,j} + \frac{n_y}{d} p_{y,j} + \frac{n_z}{d} p_{z,j} - 1. \qquad (31)$$

By summarizing the coordinates of the points $\mathbf{p}_j$ in the observation vector $\mathbf{l}$ and setting the parameter vector $\mathbf{x} = \begin{bmatrix} \frac{n_x}{d} & \frac{n_y}{d} & \frac{n_z}{d} \end{bmatrix}^T$, one obtains the non-linear functional model of the GHM (3). Hence, there are b condition equations of the form (31) for each observed point, $n = 3b$ observations (i. e. the coordinates of the observed points) and $u = 3$ parameters. Introducing an approximate parameter vector $\mathbf{x}^{(0)}$, gives the misclosure vector $\mathbf{w}$. $\mathbf{x}^{(0)}$ can be calculated by first using three arbitrary (but not colinear) points, calculating a vector which is normal to these three points with the cross product and normalizing it. Choosing another arbitrary point and calculating the scalar product with the predetermined normal vector, yields the distance to the origin. $\mathbf{A}$ contains the point coordinates and $\mathbf{B}$ is a block-diagonal matrix, where the diagonal "elements" are equal to $(\mathbf{x}^{(0)})^T$.

The application of plane fitting will be simulated. It will be assumed, that the plane is represented by nine, equally spaced points ($2\,\text{m} \times 2\,\text{m}$) which serve as observations in the LS problem ($p_1 - p_9$ in figure 1). The distance of the plane to the origin d will always be set to $10\,\text{m}$. Random Gaussian noise with zero mean and standard deviation of $\sigma_p = 0.05\,\text{m}$ is added to the 3D coordinates of the observed points ($\mathbf{\Sigma}_{ll} = \sigma_p \cdot \mathbf{I}$). For better interpretation (i. e. not looking at results perturbed by the observation noise), this LS problem will be repeated 1000 times and the results will be visualized with boxplots (in which the box represents the values between the lower and upper quartile with a line at the median). The significance number of the global test is set to $\alpha = 0.05$ and the power to $\beta = 0.80$. The significance
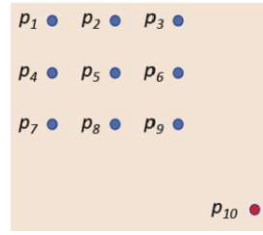
---

1 There are several methods to solve the plane adjustment, e. g. SVD. However, the GHM-approach is in our focus in this article.

**Figure 1:** Plane representation with observed points (including the leverage point p_{10}).

number of the n local tests α_0 is then computed with (30) and the power is also set to $\beta_0 = 0.80$.

In a first step the plane will be assumed to be parallel to the yz-plane of an arbitrary 3D Cartesian coordinate system. Figure 2a shows the results for the MDBs obtained with (22) or (27) respectively. It is obvious, that the y- and z-coordinates of the observed points are uncontrolled, as the corresponding MDBs are exorbitantly high. Also when adding an outlier to e. g. $p_{y,8}$ of $0.45\,\text{m}$, the global test does not indicate that an outlier is present as the mean value 0.948 of the 1000 repetitions is clearly below the critical value of 2.099. As the mean of the global tests is easily distorted by high test values, additionally the rejection rate of H_0 in the 1000 repetitions is computed, which is 4.7 % in the current case. The reason for not detecting the outlier is, that the condition equations (31) do not act as constraints on $p_{y,j}$ and $p_{z,j}$ if the plane is parallel to the yz-plane of the coordinate system. This can also be shown analytically: the normal vector of the considered plane has only a component in x-direction. Hence, the column vectors $\mathbf{b}_i$ belonging to the observations $p_{y,j}$ and $p_{z,j}$ are equal (or close) to the zero vector, which leads to a division by zero in (22).

The plane is now rotated such that the components of the normal vector are equal. By doing this, the inner reliability should be homogeneous for all observations. This can be seen in figure 2b. The median values of the MDBs of all coordinates are now approximately the same, whereas the dispersion differs between the coordinate axes. The MDBs of the x-coordinates are now clearly higher, as all observations contribute to the redundancy of 6 compared to the plane parallel to the yz-plane. Analyzing $\hat{\nabla}_{0,i}$ in the x-, y- and z-coordinates, leads to the conclusion that geometry is also an issue. The coordinates of p_5 in the middle of the plane are the best controlled ones, as its median MDB is the smallest with $\sim 0.37\,\text{m}$. On the contrary, p_1, p_3, p_7 and p_9 (the corners of the plane) have the highest median MDBs with $\sim 0.46\,\text{m}$. The question is, if there is an exposed point ("leverage point"), will the corresponding MDB be

(a) plane parallel to the yz-plane of the coordinate system.
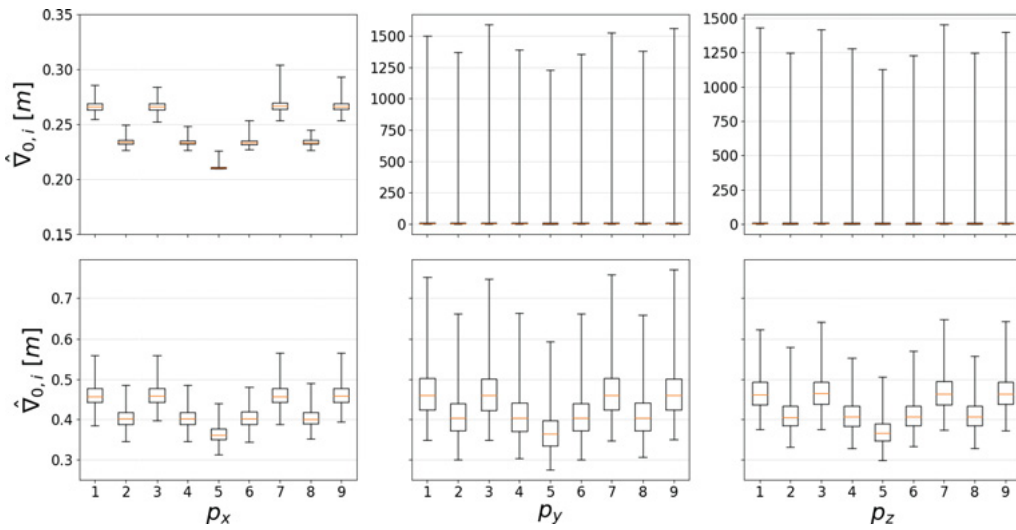
(b) rotated plane, such that the components of **n** are equal.

Figure 2: MDBs of observed point coordinates. Whiskers span the whole range of data.
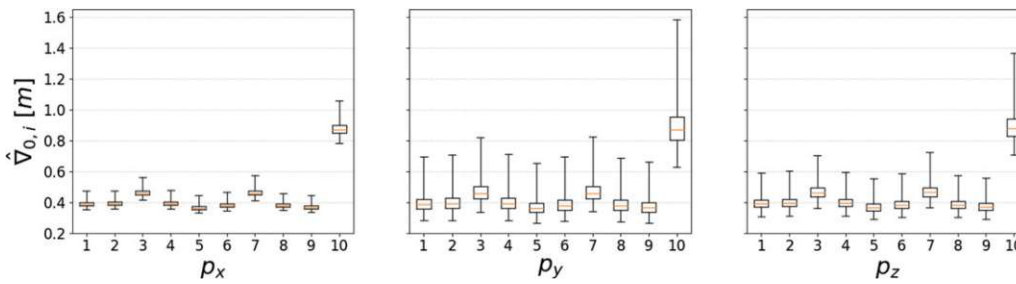

Figure 3: MDBs of observed point coordinates with one leverage point - plane is rotated.

higher than the other ones – what one would expect in the GMM. Therefore, the observation configuration will be changed according to figure 1. Now, there are ten observed points, where one point is clearly exposed from the others (2 m away from p_9). The corresponding MDBs are shown in figure 3. The MDBs of the coordinates of p_{10} are clearly higher at ∼ 0.88 m. As the redundancy is increased by one, it is also apparent that MDBs of the other points got lower or at least stayed at the same level. Especially the inner reliability of p_1 and p_9 has improved considerably (MDBs are now below 0.4 m).

Again an outlier of 0.45 m will be inserted to $p_{y,8}$ to test the ability of correctly detecting and identifying the erroneous observation (without the leverage point). The mean value of the global tests of the 1000 repetitions equals 4.535, which now clearly exceeds the corresponding critical value of 2.099 and also the rejection rate of H_0 is 95.1 %. Hence, the global test correctly detects, that an outlier is present in the observations. Figure 4 shows the test val-

ues $T_N(\nabla_i)$ of the n local tests for identifying the erroneous observations. It can be seen, that the erroneous point is correctly identified but not specifically the perturbed y-coordinate. All three coordinates are identified as being subject to an outlier. Hence, in this configuration it is not possible to correctly locate the outlier in $p_{y,8}$.

4 Discussion of the results

In the previous section it has been shown, that there are several factors negatively influencing inner reliability in general. Regarding detectability, there are two issues: on the one hand there is the impact of an observation on the misclosure vector **w** and on the other hand it is the geometry. Additionally, also identification respectively separability is an issue. Before making a proposal on how to assess an implemented LS approach regarding detectability and
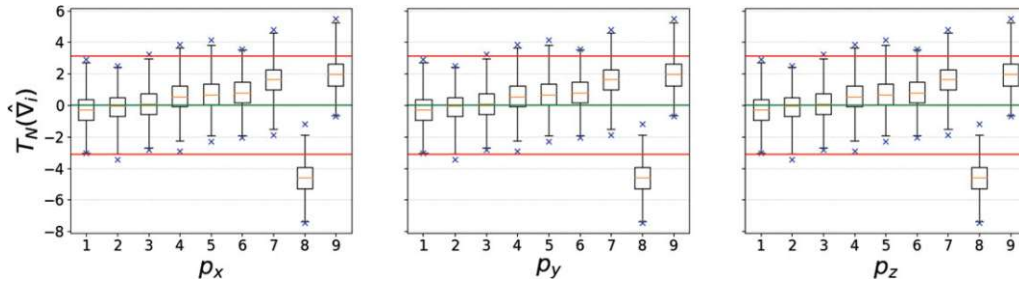
Figure 4: Local tests with corresponding critical values (red horizontal lines). The values exceeding $\alpha_0/2$ and $1 - \alpha_0/2$ are marked with blue crosses.
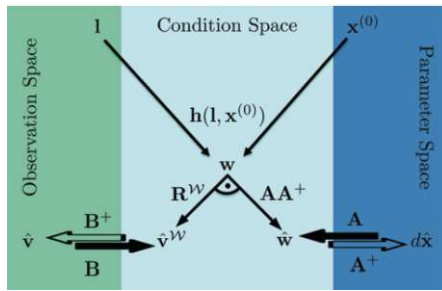
Figure 5: GHM overview: the three involved spaces (observation-, condition- and parameter space marked with different colors) and important matrices.

separability, the algebraic situation of the GHM will be analyzed to locate important matrices and measures.

4.1 Important matrices

There are three spaces involved in the GHM, namely the observation space $\mathcal{L}$, the condition space $\mathcal{W}$ and the parameter space $\mathcal{X}$. $\mathbf{B}$ and $\mathbf{A}$ describe the linear mapping from $\mathcal{L}$ and $\mathcal{X}$ to $\mathcal{W}$ respectively (see figure 5). The inverse linear mappings from $\mathcal{W}$ to $\mathcal{L}$ and $\mathcal{X}$ can be performed with the corresponding pseudo-inverses

$$\mathbf{A}^+ = (\mathbf{A}^T \mathbf{N}^{-1} \mathbf{A})^{-1} \mathbf{A}^T \mathbf{N}^{-1} \tag{32}$$

$$\mathbf{B}^+ = \mathbf{Q}_{ll} \mathbf{B}^T (\mathbf{B} \mathbf{Q}_{ll} \mathbf{B}^T)^{-1}. \tag{33}$$

The general structure of pseudo-inverses from rectangular matrices is shown in [9] p. 780 and an explanation of the special choice of weighting matrices $\mathbf{N}^{-1}$ and $\mathbf{Q}_{ll}$ can be found e. g. in [33] pp. 82–84. Using these matrices simplifies the further analysis.

As already explained in section 3, the matrix $\mathbf{B}$ is important for the ability to detect if outliers are present. As $\mathbf{B}$ is a Jacobian matrix, the columns are gradients describing how a change in one observation – more accurate: a

change along one axis of $\mathcal{L}$ – affects the basis vectors of $\mathcal{W}$ defined by the chosen conditions. Hence, if a column vector is close to the zero vector this means that the corresponding axis of $\mathcal{L}$ is orthogonal to $\mathcal{W}$. As mentioned in section 2, it will be assumed that the rank of $\mathbf{B}$ equals the number of conditions b (i. e. there are no linear dependent row vectors in $\mathbf{B}$).

Another issue regarding detectability in section 3 is the geometry determined by the observed points respectively the matrix $\mathbf{A}$ (as it contains the observed coordinates in the example of plane fitting). When only considering $\mathcal{W}$ and $\mathcal{X}$ and assuming $\mathbf{w}$ as being in the role of the observations (with corresponding cofactor matrix $\mathbf{N}$), equation (9) shows the same structure as in the GMM. Similarly, $\mathbf{w}$ is split by orthogonal projection (orthogonality with respect to the metric induced by $\mathbf{N}$) into a part lying in $\mathcal{X}$ specifying the adjusted misclosures

$$\hat{\mathbf{w}} = -\mathbf{A}\mathbf{A}^+ \mathbf{w} \tag{34}$$

and another part lying in the null space of $\mathbf{A}$ orthogonal to $\mathcal{X}$ specifying the residuals of the misclosures

$$\hat{\mathbf{v}}_w = -(\mathbf{I} - \mathbf{A}\mathbf{A}^+)\mathbf{w} = -\mathbf{R}_{\mathcal{W}}\mathbf{w}. \tag{35}$$

The orthogonal projector $\mathbf{I} - \mathbf{A}\mathbf{A}^+$ can be seen as the redundancy matrix $\mathbf{R}_{\mathcal{W}}$ of $\mathbf{w}$ with respect to the estimation of $d\hat{\mathbf{x}}$. As this contribution aims to detect and identify outliers in the observations $\mathbf{l}$, $\hat{\mathbf{v}}_w$ has to be transformed from $\mathcal{W}$ to $\mathcal{L}$ using $\mathbf{B}^+$ (36) in order to obtain $\hat{\mathbf{v}}$

$$\hat{\mathbf{v}} = \mathbf{B}^+ \hat{\mathbf{v}}_w = -\mathbf{B}^+ \mathbf{R}_{\mathcal{W}} \mathbf{w}. \tag{36}$$

This shows that the configuration reflected in $\mathbf{A}$ has to be considered when analyzing the inner reliability (based e. g. on the MDB). It has to be mentioned, that the main diagonal elements of $\mathbf{R}_{\mathcal{W}}$ must not be in the range from 0 to 1, because the components of $\mathbf{w}$ are correlated in general ($\mathbf{N} = \mathbf{B}\mathbf{Q}_{ll}\mathbf{B}^T$). In the correlated case, one has to analyze the whole structure of $\mathbf{R}_{\mathcal{W}}$: if the main diagonal element is the

one with the highest absolute value among the elements of the corresponding row (or column as $\mathbf{R}_{\mathcal{W}}$ is symmetric), this still indicates a good detectability, because the disturbed component of $\mathbf{w}$ has the biggest impact on the corresponding component of $\hat{\mathbf{v}}_w$.

The numerical example in section 3 shows that even if detectability is good, it can be difficult to exactly identify the erroneous observation. [37] extend the MDB in the GMM to the minimum separability bias (MSB). Therefore, they use the error of type 3 ("wrong exclusion"), which is the probability of identifying the wrong observation as being erroneous (i. e. selecting the wrong $H_{A,i}$). This probability is a function of α_0, β_0 and ρ_{ij}, the latter being the correlation coefficient between two test values $T_N(\nabla_i)$ and $T_N(\nabla_j)$. According to [7], ρ_{ij} can be calculated from the elements of the matrix $\mathbf{Q}_{ll}^{-1}\mathbf{Q}_{\hat{v}\hat{v}}\mathbf{Q}_{ll}^{-1}$. By using equation (12) and (28), this matrix can be reformulated

$$\mathbf{Q}_{ll}^{-1}\mathbf{Q}_{\hat{v}\hat{v}}\mathbf{Q}_{ll}^{-1} = \mathbf{B}^T\mathbf{Q}_{\hat{k}\hat{k}}\mathbf{B} = \mathbf{Q}_{ll}^{-1}\mathbf{R} = \mathbf{Q}_{ll}^{-1}\mathbf{B}^+\mathbf{R}_{\mathcal{W}}\mathbf{B} = (\mathbf{Q}_{\hat{\nabla}\hat{\nabla}}^{-1})_n,$$
(37)

where $(\mathbf{Q}_{\hat{\nabla}\hat{\nabla}}^{-1})_n$ is the resulting inverse of the cofactor matrix when estimating one bias (i. e. additional parameter) for each observation. In this case, the vector $\mathbf{c}_i$ in equation (14) becomes the $n \times n$ identity matrix. The correlation ρ_{ij} of every combination of estimated and afterwards tested offsets can be determined from this matrix

$$\rho_{ij} = \frac{(\mathbf{Q}_{\hat{\nabla}\hat{\nabla}}^{-1})_{ij}}{\sqrt{(\mathbf{Q}_{\hat{\nabla}\hat{\nabla}}^{-1})_{ii}(\mathbf{Q}_{\hat{\nabla}\hat{\nabla}}^{-1})_{jj}}}.$$
(38)

This only holds for additional parameters defined as shown in equation (14), as the full matrix $\mathbf{B}$ occurs in every alternative hypothesis. $\mathbf{c}_i$ and $\mathbf{c}_j$ select the corresponding covariance element of $(\mathbf{Q}_{\hat{\nabla}\hat{\nabla}}^{-1})_n$. This approach can also be extended to two different multi-dimensional $H_{A,i}$ and $H_{A,j}$, with m_i and m_j being the number of additional parameters in the corresponding alternative hypothesis. If the additional parameters in $H_{A,i}$ and $H_{A,j}$ are defined as shown in equation (14), $\mathbf{C}_i \in R^{n\times m_i}$ and $\mathbf{C}_j \in R^{n\times m_j}$ will select a sub-matrix $(\mathbf{Q}_{\hat{\nabla}\hat{\nabla}}^{-1})_{ij}$ from $(\mathbf{Q}_{\hat{\nabla}\hat{\nabla}}^{-1})_n$ with size $m_i \times m_j$

(see equation (39)). In this case, the correlation can be assessed by analyzing the eigenvalues of the similar matrix $[(\mathbf{Q}_{\hat{\nabla}\hat{\nabla}}^{-1})_{ji}(\mathbf{Q}_{\hat{\nabla}\hat{\nabla}}^{-1})_{ii}^{-1}(\mathbf{Q}_{\hat{\nabla}\hat{\nabla}}^{-1})_{ij}(\mathbf{Q}_{\hat{\nabla}\hat{\nabla}}^{-1})_{jj}^{-1}]$ [7]. Note that these four sub-matrices are computed with

$$(\mathbf{Q}_{\hat{\nabla}\hat{\nabla}}^{-1})_{ij} = \mathbf{C}_i^T(\mathbf{Q}_{\hat{\nabla}\hat{\nabla}}^{-1})_n\mathbf{C}_j.$$
(39)

In conclusion, there are three important matrices, which give insight into the structure of inner reliability of an implemented LS algorithm, namely the observation matrix $\mathbf{B}$, the redundancy matrix of the conditions $\mathbf{R}^{\mathcal{W}}$ and the inverse cofactor matrix of the additional parameters respectively biases to be estimated $(\mathbf{Q}_{\hat{\nabla}\hat{\nabla}}^{-1})_n$.

## 4.2 Plane fitting continued

In this section, the resulting matrices of the plane fitting example identified as being important for the assessment of inner reliability, will be analyzed. Figure 6a shows the observation matrix $\mathbf{B}$ for the plane parallel to the yz-plane of the coordinate system. In this case the columns belonging to the y- and z-coordinates are equal to the zero vector. As already mentioned in the previous sections, this means, that the corresponding observation has no influence on $\mathbf{w}$. This is somehow intuitive, as an outlier in $p_{y,j}$ or $p_{z,j}$ does not cause a deviation from zero in $\mathbf{w}$. The columns of $\mathbf{B}$ of the rotated plane (figure 6b) have all the same length, as the components of the normal vector are now nearly equal. This results in homogeneously distributed redundancy over all observations (and therefore homogeneous MDBs – see figure 2b).

$\mathbf{R}_{\mathcal{W}}$ will be analyzed to assess the geometry in the plane fitting example. As the components of $\mathbf{w}$ are uncorrelated (one can verify be evaluating $\sigma_p \cdot \mathbf{BB}^T$), the focus is on the main diagonal elements. Figure 7a shows $\mathbf{R}_{\mathcal{W}}$ for the rotated plane. The same conclusions can be drawn as in section 3: p_5 is the best controlled one (and therefore the corresponding x-, y- and z-coordinates) with a redundancy number of 0.89. The corner points are the ones
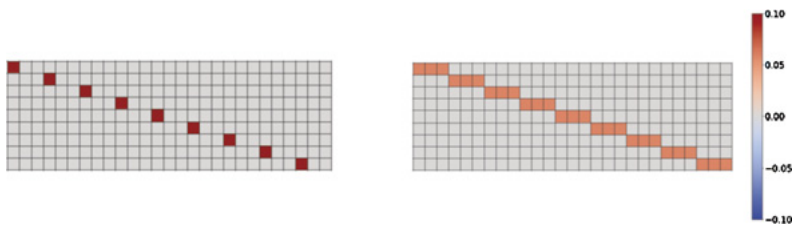
(a) plane parallel to the yz-plane of the coordinate system.

(b) rotated plane, such that the components of $\mathbf{n}$ are equal.

Figure 6: Observation matrix $\mathbf{B}$.
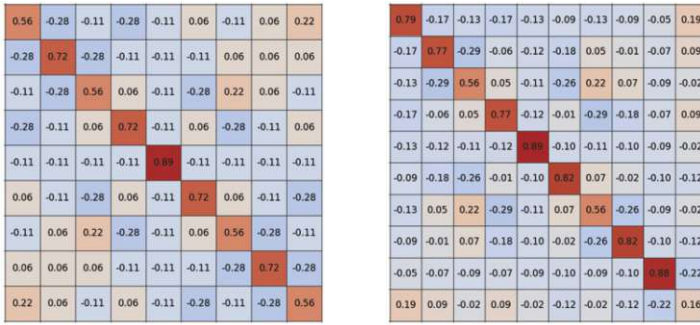
(a) rotated plane, such that the components of $\mathbf{n}$ are equal.

(b) rotated plane with leverage point.

Figure 7: Redundancy matrices of the conditions $\mathbf{R}_{\mathcal{W}}$.

with the lowest redundancy numbers being 0.56 – which still indicates good controllability of the corresponding observed coordinates. The redundancy number of the leverage point (lower right corner of figure 7b) is clearly lower at 0.16 which results in higher MDBs of the corresponding observed coordinates (see figure 3).

The analysis of separability will be based on the correlation coefficients ρ_{ij} (calculated with equation (38)) for all possible pairs of test values $T_N(\nabla_i)$ and $T_N(\nabla_j)$, where only one dimensional $H_{A,i}$ will be considered as specified by the observation model (14). Figure 8a shows the absolute values of the correlation coefficients of the rotated plane. In the 1000 repetitions of the LS algorithm, it happens, that the sign of ρ_{ij} is changing but the value itself stays the same. That is the reason for plotting the absolute values of ρ_{ij}. It can be seen, that the x-, y- and z-coordinates of one point are highly correlated, explaining the results of the local tests (figure 4). There are also correlations between the points due to geometry, which is – as previously mentioned – defined by $\mathbf{R}_{\mathcal{W}}$. The correlation structure of the different points (i. e. the correlation of the observed co-

ordinates of different points) in figure 8a is similar to the structure of the corresponding $\mathbf{R}_{\mathcal{W}}$ (figure 7a). The correlation coefficients of observations in one point respectively condition are 1, which means, that in the present configuration it is not possible to correctly locate an outlier.

One possibility to intervene, is to change the functional model (i. e. add linear independent conditions). Especially in plane fitting it could be, that the distance d_{i-j} between two points p_i and p_j is known (e. g. points signalized by reflective target marks) and conditions of the form

$$0 = \sqrt{(p_{x,i} - p_{x,j})^2 + (p_{y,i} - p_{y,j})^2 + (p_{z,i} - p_{z,j})^2} - d_{i-j} \quad (40)$$

can be added. In a first step, it will be assumed that the distance d_{4-8} is known (not as observation but deterministic). The resulting ρ_{ij} can be seen in figure 8b. The correlations between $p_{x,4}$ and $p_{y,4}$ respectively $p_{z,4}$ are now considerably lower, whereas the correlation between $p_{y,4}$ and $p_{z,4}$ is still high (the same holds for p_8). As the additional condition acts as constraint between p_4 and p_8, correlations between the corresponding coordinates arise. In
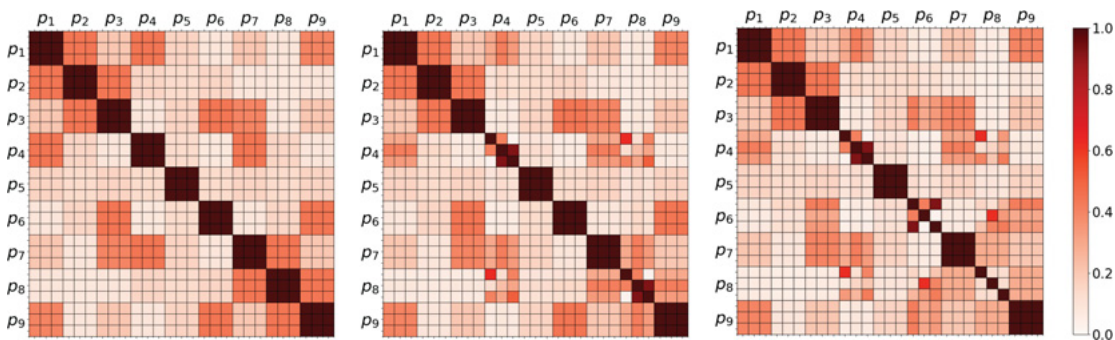
(a) rotated plane, such that the components of $\mathbf{n}$ are equal.

(b) rotated plane, with one additional condition.

(c) rotated plane, with two additional conditions.

Figure 8: Absolute values of correlation coefficients (without the outlier in $p_{y,8}$).
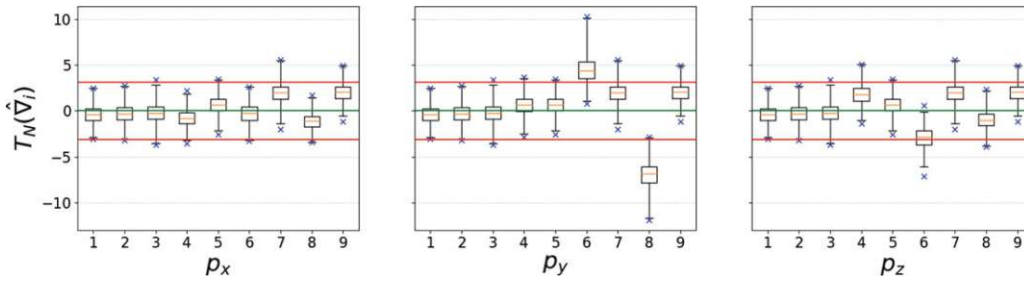
Figure 9: Local tests when using two additional conditions (d_{4-8} and d_{6-8}) with corresponding critical values (red horizontal lines). The values exceeding $\alpha_0/2$ and $1 - \alpha_0/2$ are marked with blue crosses.

particular, the correlation of the x-coordinates is clearly increased. Adding another condition – namely d_{6-8} – nearly decorrelates the coordinate observations of p_8 (figure 8c). The effect on the coordinates of p_6 is similar to the previous scenario: the correlations of $p_{y,6}$ to $p_{x,6}$ and $p_{z,6}$ are now considerably lower, whereas $p_{x,6}$ and $p_{z,6}$ are still highly correlated. Again, additional correlations arise between p_6 and p_8 (especially in the y-coordinates), due to the incorporation of the additional condition.

In the last scenario (two additional conditions d_{4-8} and d_{6-8}), $p_{y,8}$ will be again perturbed by an offset of 0.45 m and the test values for the local tests $T_N(\nabla_i)$ will be computed (figure 9). $p_{y,8}$ is now clearly indicated to be the erroneous observation. Also $p_{y,6}$ exceeds the critical value but as suggested in data snooping, one has to take care of the observation with the highest test value. After removing (or compensating by an additional parameter) the erroneous observation, the other test values should stay within the critical values.

It is theoretically possible to include many conditions of the form (40) to the plane fitting example and therefore improving inner reliability. One can mount reflective target marks on the plane of interest and measure them with an instrument having superior accuracy. However, such a procedure is possibly limited to special applications (e. g. calibration of terrestrial laser scanners). In practice, one has to consider the physical realization of such conditions and in general it can be a tricky task to find and formulate such additional conditions, improving inner reliability. The conclusion of this numerical example is, that the MDB (22) together with ρ_{ij} (38) are useful tools to assess the inner reliability respectively the detection and identification step of DIA in the GHM.

Another numerical example has been worked out and investigated, namely the 2D similarity transformation where the coordinates of the points in the two considered coordinate systems are introduced as the observations. The behavior of the MDB and the correlation coefficients

as well as the influence of the translation parameters and the rotation parameter on the inner reliability has been analyzed. The MDB is not dependent neither on a translation nor on a rotation and its structure is similar to the plane fitting example as points which are surrounded by others show lower MDBs than points in the border area. When just applying a translation, the two corresponding coordinates of one point in both systems are one-to-one correlated (i. e. outliers in these coordinates are not separable), whereas the rotation parameter causes a correlation of a coordinate in one system with both coordinates of the same point in the other system. The details on the numerical example as well as the results can be found in appendix B.

4.3 Numerical example: yaw computation

The derived body of equations can also be applied to the Kalman filter which is a sequential implementation of the LS estimator. In [6], the Euler angles roll φ, pitch θ and yaw ψ are estimated with a Kalman filter which is formulated in the GHM to directly introduce the smartphone-sensor readings as observations. As a preparatory step for analyzing the inner reliability of such Kalman filter implementations, a simplified numerical example will be considered in this chapter. The yaw angle ψ is assumed to be static and should be estimated from b consecutive magnetometer observations. As a further simplification it will be assumed that the originally 3D magnetometer readings sensing the earth magnetic field are already leveled. Hence, ψ can be computed with the two horizontal components $m_{x,j}$ and $m_{y,j}$ ($j = 1, ..., b$) and one can set up b condition equations

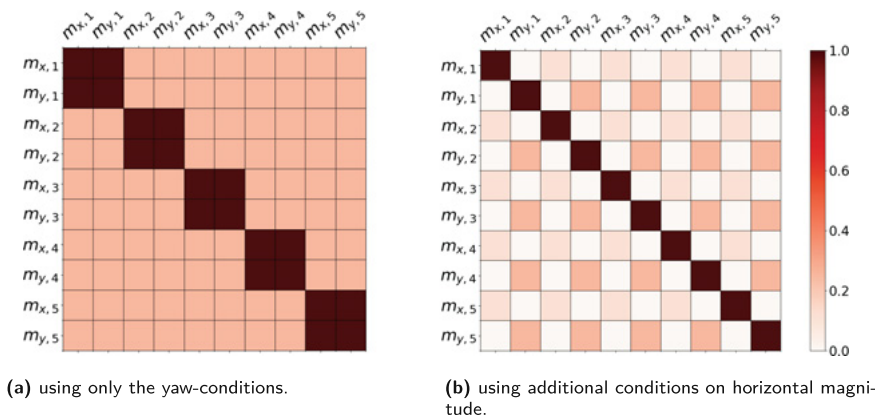$$0 = \arctan\left(\frac{-m_{y,j}}{m_{x,j}}\right) - \psi. \qquad (41)$$

For the numerical example, we will assume to have $b = 5$ such pairs of observations which should be adjusted,

(a) using only the yaw-conditions.
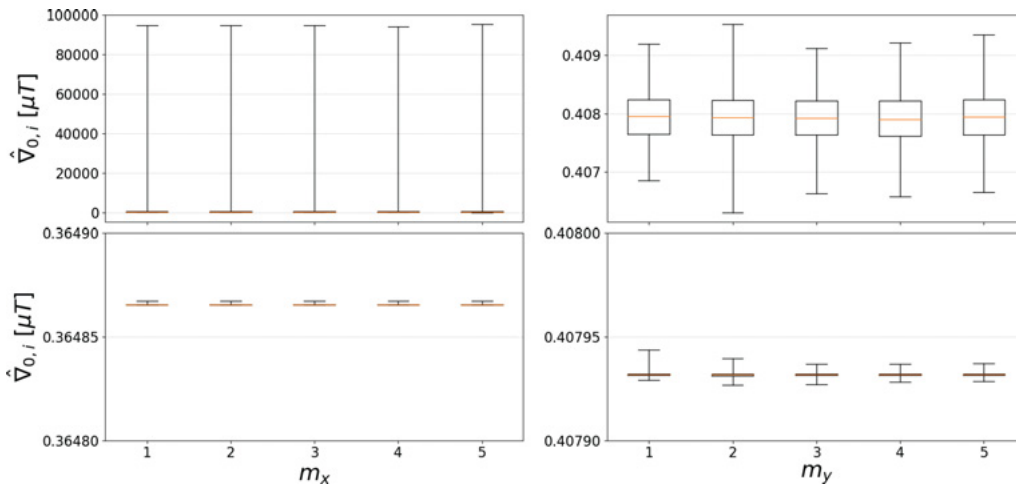
(b) using additional conditions on horizontal magnitude.

Figure 10: MDBs of magnetometer observations. Whiskers span the whole range of data.

(a) using only the yaw-conditions.

**(b)** using additional conditions on horizontal magnitude.

Figure 11: Absolute values of correlation coefficients.

where the magnetometers' x-axis points towards magnetic north (expected value of ψ is 0°). An approximate value $\psi^{(0)}$ for the yaw angle can be calculated from one of the five pairs of observations, yielding exactly zero in the corresponding condition equation. The procedure will be the same as in section 3: the LS algorithm will be repeated 1000 times and every time random Gaussian noise with zero mean and standard deviation $\sigma_m = 0.1\,\mu T$ will be added to the observations $m_{x,j}$ and $m_{y,j}$.

Figure 10a shows the resulting MDBs of the magnetometer observations. The $m_{x,j}$ are uncontrolled and the reason is the same as in the application of plane fitting: the corresponding columns of **B** are equal to the zero vector. Or analytically: changing $m_{x,j}$ in equation (41) does not influence the corresponding component of **w** as long as $m_{y,j}$ is zero (what should be the case if the magnetometer

points towards magnetic north). As suggested in the end of section 4.2, one should also analyze the correlation of the test statistics $T_N(\nabla_i)$ to assess the inner reliability. Figure 11a shows the corresponding correlation coefficients ρ_{ij}. Again, the situation is similar to the plane fitting example, as the observations appearing in the same condition equation are one to one correlated. In the case of yaw estimation, **A** equals the negative identity matrix. Therefore, the correlation between observations of different condition equations is now uniform (in contrast to plane fitting).

To improve this sub-optimal configuration, one can formulate conditions on the observations. If there are no magnetic perturbations present (neither instrumental nor environmental effects), the Euclidean distance of a pair of magnetometer observations should be equal to the hori-
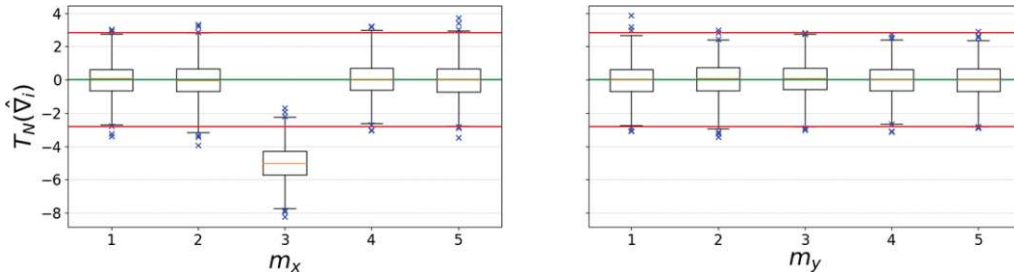
Figure 12: Local tests with corresponding critical values (red horizontal lines). The values exceeding $\alpha_0/2$ and $1 - \alpha_0/2$ are marked with blue crosses.

zontal component M_H of the earth magnetic field, which will be treated as a deterministic value. Thus, there will be one additional condition for every pair of leveled magnetometer observations

$$0 = \sqrt{m_{x,j}^2 + m_{y,j}^2} - M_H, \qquad (42)$$

increasing the overall redundancy as there are no additional parameters to be estimated. Solving the LS problem with these additional conditions, yields MDBs of the $m_{x,j}$ which are now considerably lower (figure 10b). The MDBs of $m_{y,j}$ stay approximately the same but the dispersion is much smaller. Also the ρ_{ij} are now clearly lower, especially the ones between the individual $m_{x,j}$ and $m_{y,j}$ (figure 11b). To test if outliers in observations are correctly detected and identified, a bias of $0.5\,\mu\text{T}$ is added to observation $m_{x,3}$. The global test indicates that an outlier is present, as its mean test value 3.7001 is considerably higher than the critical value 1.8799 and also the rejection rate of H_0 is 97 %. The erroneous observation is correctly identified by the local tests (figure 12).

The example of determining the yaw angle with magnetometer measurements confirmed that the MDB $\hat{\nabla}_{0,i}$ together with the correlation coefficients of the test statistics ρ_{ij} are appropriate tools to assess the inner reliability of an implemented LS algorithm. Additionally, it could be shown, that including condition equations solely between the observations in the functional model, considerably improves the ability to detect and identify outliers.

5 Conclusions

In this contribution, the theory of inner reliability is introduced for the Gauss-Helmert model (GHM). This includes the derivation of the minimum detectable bias (MDB) $\hat{\nabla}_{0,i}$ as well as the test values $T_F(\nabla_i)$ and $T_N(\nabla_i)$ for the local tests to identify disturbed observations. Especially, if the observations are uncorrelated, these measures for inner

reliability will have the same structure as in the Gauss-Markov model, where the redundancy numbers r_{ii} (main diagonal elements of redundancy matrix **R**) play a key role. All derivations for the inner reliability are based on one-dimensional and additive observation errors respectively offsets which are modeled as additional parameters ∇_i to be estimated. The formulas to compute these additional parameters with the corresponding variances $q_{\hat{\nabla}_i}$ are also derived in this contribution. Appendix A includes the results of the GHM for a more general observation model, containing multiple systematic observation errors non-linearly.

The numerical example of plane fitting showed that the MDB is also in the GHM an appropriate measure to analyze the ability of an implemented least-squares algorithm to detect if outliers are present in the observations. A high MDB value indicates, that an outlier in the corresponding observation cannot be detected. Two sources negatively influencing detectability are identified: columns close to the zero vector in the observation matrix **B** and suboptimal geometry in the design matrix **A** (which can be assessed by the redundancy matrix of the condition space $\mathbf{R}_\mathcal{W}$). Even if these issues can be excluded, it can be difficult to identify the correct observation as being erroneous. Therefore, the correlation coefficients ρ_{ij} of two test values $T_N(\nabla_i)$ and $T_N(\nabla_j)$ are calculated from the matrix $\mathbf{Q}_{ll}^{-1}\mathbf{R}$ and analyzed. High values for ρ_{ij} indicate, that the erroneous observation cannot be correctly identified. The numerical example of determining the yaw angle with magnetometer measurements confirmed these findings. As the MDB and the ρ_{ij} are convenient measures to illustrate detectability and separability, they should be used to assess the inner reliability of an implemented LS approach in the GHM. If there are problems one should further analyze **B** and $\mathbf{R}_\mathcal{W}$ to choose appropriate additional conditions which will fix (or at least improve) sub-optimal configurations. Finding such additional conditions is not a trivial task, as it highly depends on the desired application.

An obvious extension to the inner reliability in the GHM, is the outer reliability (influence of not detected outliers on the parameters), which is not considered in this contribution. However, one basic equation for outer reliability is already derived in appendix A, namely the influence of additional parameters on the parameters of the null hypothesis (48). As mentioned in section 4.3, the numerical example of yaw computation served as preparatory step to analyze the inner reliability of sequential GHM estimators. The measures introduced in this contribution, can support the implementation of algorithms used in navigation tasks (e. g. dead reckoning) being less sensitive to several systematic errors occurring in the used sensors.

Appendix A. General formulation of systematic observation errors

The observation model with non-linear systematic observation errors can be formulated as

$$\mathbf{g}_l(\boldsymbol{l}, \nabla) = E\{\boldsymbol{l}\} - \boldsymbol{v}. \tag{43}$$

$\mathbf{g}_l()$ is a function which gives calibrated observations depending on the – in general – non-linearly included systematic observation errors $\nabla \in R^{m \times 1}$, treated as deterministic additional parameters to be estimated. By setting $\nabla = \nabla^*$ such that $\mathbf{g}_l(\boldsymbol{l}, \nabla^*) = \boldsymbol{l}$, one arrives at the linearized functional model of the GHM (6). Hence, a GHM adjustment based on $\boldsymbol{l}$ can be solved with the equations (8)–(13) if the null hypothesis

$$H_0 : \ \nabla - \nabla^* = \mathbf{0} \tag{44}$$

is correct. To derive appropriate test values for checking the validity of H_0, the estimated additional parameters $\hat{\nabla}$ have to be computed. This is done with Lagrangian optimization (as also done in section 2), which corresponds to the procedure of deriving $\hat{\mathbf{v}}$ in the GMM (as shown in [16] p. 184 ff.). The linearization of the functional model with additional parameters is done with

$$\mathbf{0} = \mathbf{h}(\hat{\mathbf{x}}', \hat{\mathbf{l}}') = \mathbf{h}(\hat{\mathbf{x}}', \mathbf{g}_l(\boldsymbol{l}, \hat{\nabla}) + \hat{\mathbf{v}}')$$

$$\approx \mathbf{h}(\mathbf{x}^{(0)}, \mathbf{g}_l(\boldsymbol{l}, \nabla^{(0)}) + \mathbf{v}^{(0)}) + \frac{\partial \mathbf{h}(\hat{\mathbf{x}}', \hat{\mathbf{l}}')}{\partial \hat{\mathbf{x}}'}|_{\mathbf{x}^{(0)}, \mathbf{g}_l(\boldsymbol{l}, \nabla^{(0)}) + \mathbf{v}^{(0)}} \cdot d\hat{\mathbf{x}}'$$

$$+ \frac{\partial \mathbf{h}(\hat{\mathbf{x}}', \hat{\mathbf{l}}')}{\partial \hat{\mathbf{v}}'}|_{\mathbf{x}^{(0)}, \mathbf{g}_l(\boldsymbol{l}, \nabla^{(0)}) + \mathbf{v}^{(0)}} \cdot (\hat{\mathbf{v}}' - \mathbf{v}^{(0)})$$

$$+ \frac{\partial \mathbf{h}(\hat{\mathbf{x}}', \hat{\mathbf{l}}')}{\partial \hat{\nabla}}|_{\mathbf{x}^{(0)}, \mathbf{g}_l(\boldsymbol{l}, \nabla^{(0)}) + \mathbf{v}^{(0)}} \cdot (\hat{\nabla} - \nabla^{(0)})$$

$$\approx \mathbf{h}(\mathbf{x}^{(0)}, \mathbf{g}_l(\boldsymbol{l}, \nabla^{(0)}) + \mathbf{v}^{(0)}) + \frac{\partial \mathbf{h}(\hat{\mathbf{x}}', \hat{\mathbf{l}}')}{\partial \hat{\mathbf{x}}'}|_{\mathbf{x}^{(0)}, \mathbf{g}_l(\boldsymbol{l}, \nabla^{(0)}) + \mathbf{v}^{(0)}} \cdot d\hat{\mathbf{x}}'$$

$$+ \left[\frac{\partial \mathbf{h}(\hat{\mathbf{x}}', \hat{\mathbf{l}}')}{\partial \hat{\mathbf{l}}'} \cdot \frac{\partial \hat{\mathbf{l}}'}{\partial \hat{\mathbf{v}}'}\right]|_{\mathbf{x}^{(0)}, \mathbf{g}_l(\boldsymbol{l}, \nabla^{(0)}) + \mathbf{v}^{(0)}} \cdot (\hat{\mathbf{v}}' - \mathbf{v}^{(0)})$$

$$+ \left[\frac{\partial \mathbf{h}(\hat{\mathbf{x}}', \hat{\mathbf{l}}')}{\partial \hat{\mathbf{l}}'} \cdot \frac{\partial \hat{\mathbf{l}}'}{\partial \mathbf{g}_l(\boldsymbol{l}, \hat{\nabla})} \cdot \frac{\partial \mathbf{g}_l(\boldsymbol{l}, \hat{\nabla})}{\partial \hat{\nabla}}\right]|_{\mathbf{x}^{(0)}, \mathbf{g}_l(\boldsymbol{l}, \nabla^{(0)}) + \mathbf{v}^{(0)}} \cdot (\hat{\nabla} - \nabla^{(0)})$$

$$\approx \mathbf{h}(\mathbf{x}^{(0)}, \mathbf{g}_l(\boldsymbol{l}, \nabla^{(0)}) + \mathbf{v}^{(0)}) + \mathbf{A}' d\hat{\mathbf{x}}'$$

$$+ \mathbf{B}'\mathbf{I} \cdot (\hat{\mathbf{v}}' - \mathbf{v}^{(0)}) + \mathbf{B}'\mathbf{I}\mathbf{A}_\nabla d\hat{\nabla}$$

$$\approx \mathbf{w}' + \mathbf{A}' d\hat{\mathbf{x}}' + \mathbf{B}'\hat{\mathbf{v}}' + \mathbf{B}'\mathbf{A}_\nabla d\hat{\nabla}$$

$$\text{with } \mathbf{w}' = \mathbf{h}(\mathbf{x}^{(0)}, \mathbf{g}_l(\boldsymbol{l}, \nabla^{(0)}) + \mathbf{v}^{(0)}) - \mathbf{B}'\mathbf{v}^{(0)}. \tag{45}$$

In (45) $\mathbf{A}_\nabla \in R^{b \times m}$ is the Jacobi matrix, resulting from the partial derivatives of $\mathbf{g}_l(\boldsymbol{l}, \hat{\nabla})$ with respect to $\hat{\nabla}$ and having full column rank. By using quotation marks as superscripts, it should be clarified, that $\mathbf{w}'$, $\mathbf{A}'$ and $\mathbf{B}'$ are different to the corresponding quantities in section 2, as the partial derivatives are evaluated now additionally at the approximate, additional parameters $\nabla^{(0)}$. By setting $\nabla^{(0)} = \nabla^*$ (what will be assumed from here on), one can again set $\mathbf{w}' = \mathbf{w}$, $\mathbf{A}' = \mathbf{A}$ and $\mathbf{B}' = \mathbf{B}$. $\hat{\mathbf{x}}'$ and $\hat{\mathbf{v}}'$ (and therefore $d\hat{\mathbf{x}}'$ and $\hat{\mathbf{l}}'$) as well as $\hat{\mathbf{k}}'$ will differ from its corresponding quantities in section 2, due to the incorporation of $\hat{\nabla}$.

The extended normal equation system becomes:

$$\begin{bmatrix} \mathbf{N} & \mathbf{A} & \mathbf{B}\mathbf{A}_\nabla \\ \mathbf{A}^T & \mathbf{0} & \mathbf{0} \\ \mathbf{A}_\nabla^T\mathbf{B}^T & \mathbf{0} & \mathbf{0} \end{bmatrix} \begin{bmatrix} \hat{\mathbf{k}}' \\ d\hat{\mathbf{x}}' \\ d\hat{\nabla} \end{bmatrix} = \begin{bmatrix} -\mathbf{w} \\ \mathbf{0} \\ \mathbf{0} \end{bmatrix} \tag{46}$$

As stated e. g. in [16] p. 185, $d\hat{\nabla}$ is not unambiguously estimable if m exceeds the redundancy $r = b - u$, i. e. overall more parameters $(m + u)$ have to be estimated than conditions are given and the LS-problem gets underdetermined. The Lagrangian multipliers $\hat{\mathbf{k}}'$ are determined from the first row of (46)

$$\hat{\mathbf{k}}' = -\mathbf{N}^{-1}(\mathbf{w} + \mathbf{A}d\hat{\mathbf{x}}' + \mathbf{B}\mathbf{A}_\nabla d\hat{\nabla}). \tag{47}$$

Inserting (47) into the second row of (46) and rearranging this expression gives

$$d\hat{\mathbf{x}}' = -(\mathbf{A}^T\mathbf{N}^{-1}\mathbf{A})^{-1}\mathbf{A}^T\mathbf{N}^{-1}(\mathbf{w} + \mathbf{B}\mathbf{A}_\nabla d\hat{\nabla})$$

$$= d\hat{\mathbf{x}} - (\mathbf{A}^T\mathbf{N}^{-1}\mathbf{A})^{-1}\mathbf{A}^T\mathbf{N}^{-1}\mathbf{B}\mathbf{A}_\nabla d\hat{\nabla}. \tag{48}$$

Now one can insert this into (47), which equals

$$\hat{\mathbf{k}}' = -\mathbf{N}^{-1}(\mathbf{w} + \mathbf{A}d\hat{\mathbf{x}} + (\mathbf{I} - \mathbf{A}(\mathbf{A}^T\mathbf{N}^{-1}\mathbf{A})^{-1}\mathbf{A}^T\mathbf{N}^{-1})\mathbf{B}\mathbf{A}_\nabla d\hat{\nabla})$$

$$= \hat{\mathbf{k}} - \mathbf{N}^{-1}(\mathbf{I} - \mathbf{A}(\mathbf{A}^T\mathbf{N}^{-1}\mathbf{A})^{-1}\mathbf{A}^T\mathbf{N}^{-1})\mathbf{B}\mathbf{A}_\nabla d\hat{\nabla} \tag{49}$$

After setting $\mathbf{I} - \mathbf{A}(\mathbf{A}^T\mathbf{N}^{-1}\mathbf{A})^{-1}\mathbf{A}^T\mathbf{N}^{-1} = \mathbf{I} - \mathbf{A}\mathbf{A}^+ = \mathbf{R}_{\mathcal{W}}$ for convenience, the residuals are calculated with

$$\hat{\mathbf{v}}' = \mathbf{Q}_{ll}\mathbf{B}^T\hat{\mathbf{k}}'$$

$$= \mathbf{Q}_{ll}\mathbf{B}^T(\hat{\mathbf{k}} - \mathbf{N}^{-1}\mathbf{R}_{\mathcal{W}}\mathbf{B}\mathbf{A}_\nabla d\hat{\nabla})$$

$$= \hat{\mathbf{v}} - \mathbf{Q}_{ll}\mathbf{B}^T\mathbf{N}^{-1}\mathbf{R}_{\mathcal{W}}\mathbf{B}\mathbf{A}_\nabla d\hat{\nabla}. \tag{50}$$
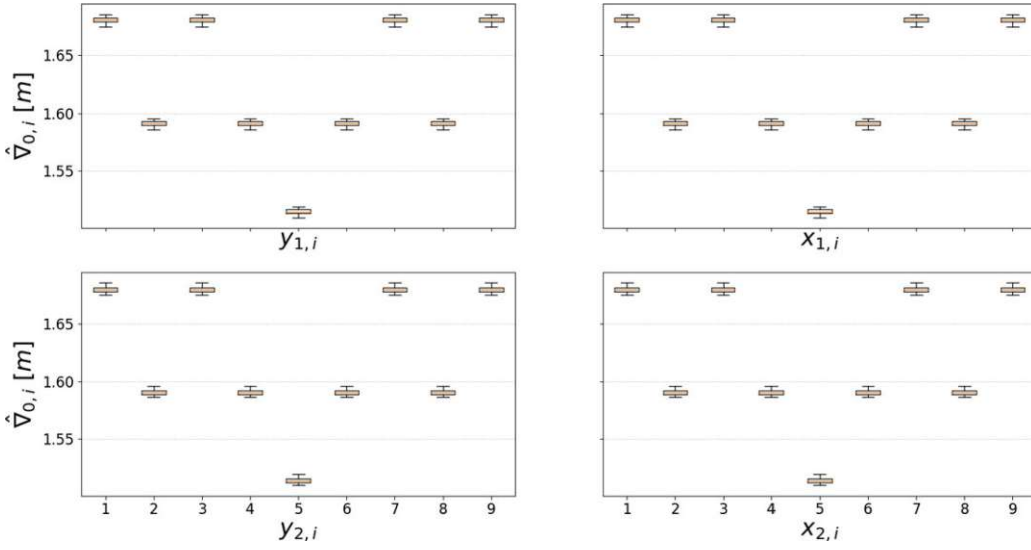
Figure 13: MDBs of point coordinates when applying translation of 200 m in x- and y-direction.

The result for $d\hat{\mathbf{V}}$ is obtained by inserting (49) into the third row of (46) and can be expressed in terms of $\mathbf{w}$, $\hat{\mathbf{k}}$ or $\hat{\mathbf{v}}$

$$
\begin{aligned}
d\hat{\mathbf{V}} &= -(\mathbf{A}_\nabla^T\mathbf{B}^T\mathbf{N}^{-1}\mathbf{R}_\mathcal{W}\mathbf{B}\mathbf{A}_\nabla)^{-1}\mathbf{A}_\nabla^T\mathbf{B}^T\mathbf{N}^{-1}\mathbf{R}_\mathcal{W}\mathbf{w} \\
&= (\mathbf{A}_\nabla^T\mathbf{B}^T\mathbf{N}^{-1}\mathbf{R}_\mathcal{W}\mathbf{B}\mathbf{A}_\nabla)^{-1}\mathbf{A}_\nabla^T\mathbf{B}^T\hat{\mathbf{k}} \\
&= (\mathbf{A}_\nabla^T\mathbf{B}^T\mathbf{N}^{-1}\mathbf{R}_\mathcal{W}\mathbf{B}\mathbf{A}_\nabla)^{-1}\mathbf{A}_\nabla^T\mathbf{B}^T\mathbf{N}^{-1}\mathbf{B}\hat{\mathbf{v}}.
\end{aligned} \tag{51}
$$

As $\mathbf{N}$ corresponds to the cofactor matrix of $\mathbf{w}$, $\mathbf{Q}_{\hat{\nabla}\hat{\nabla}}$ is derived by using error propagation, the fact that $\mathbf{R}_\mathcal{W}$ is idempotent and the identity $\mathbf{N}\mathbf{R}_\mathcal{W}^T\mathbf{N}^{-1} = \mathbf{R}_\mathcal{W}$. It can also be expressed in terms of $\mathbf{Q}_{\hat{k}\hat{k}}$ or $\mathbf{Q}_{\hat{v}\hat{v}}$

$$
\begin{aligned}
\mathbf{Q}_{\hat{\nabla}\hat{\nabla}} &= (\mathbf{A}_\nabla^T\mathbf{B}^T\mathbf{N}^{-1}\mathbf{R}_\mathcal{W}\mathbf{B}\mathbf{A}_\nabla)^{-1}\mathbf{A}_\nabla^T\mathbf{B}^T\mathbf{N}^{-1}\mathbf{R}_\mathcal{W}\mathbf{N}\mathbf{R}_\mathcal{W}^{'T}\mathbf{N}^{-1}\mathbf{B}\mathbf{A}_\nabla \\
&\quad \cdot (\mathbf{A}_\nabla^T\mathbf{B}^T\mathbf{N}^{-1}\mathbf{R}_\mathcal{W}\mathbf{B}\mathbf{A}_\nabla)^{-1} \\
&= (\mathbf{A}_\nabla^T\mathbf{B}^T\mathbf{N}^{-1}\mathbf{R}_\mathcal{W}\mathbf{B}\mathbf{A}_\nabla)^{-1} \\
&= (\mathbf{A}_\nabla^T\mathbf{B}^T\mathbf{Q}_{\hat{k}\hat{k}}\mathbf{B}\mathbf{A}_\nabla)^{-1} \\
&= (\mathbf{A}_\nabla^T\mathbf{B}^T\mathbf{N}^{-1}\mathbf{B}\mathbf{Q}_{\hat{v}\hat{v}}\mathbf{B}^T\mathbf{N}^{-1}\mathbf{B}\mathbf{A}_\nabla)^{-1}.
\end{aligned} \tag{52}
$$

Appendix B. Numerical example: 2D similarity transformation

In the numerical example of 2D similarity transformation, nine points $p_{s,j} = \begin{bmatrix} y_{s,j} & x_{s,j} \end{bmatrix}^T$ are considered which are arranged in the same way as in the plane fitting example. $s = 1, 2$ is the index for the coordinate system and $j = 1, \ldots, 9$ specifies the point-ID. In 2D similarity transformation, the transformation parameters are the translation vector components t_y and t_x, the rotation ψ and the scale

m. For each point, one can set up a pair of condition equations

$$
\begin{aligned}
0 &= y_{2,j} - t_y - (1 + m)(y_{1,j}\cos\psi + x_{1,j}\sin\psi) \\
0 &= x_{2,j} - t_x + (1 + m)(y_{1,j}\sin\psi - x_{1,j}\cos\psi)
\end{aligned} \tag{53}
$$

to estimate the transformation parameters in a GHM adjustment. For the numerical evaluations, the adjustment procedure is repeated again 1000 times, where in each repetition white Gaussian noise with zero mean and standard deviation of $\sigma_p = 0.25$ m is added to the point coordinates (i. e. the observations) in both systems.

In the first evaluation, only a translation of 200 m in both coordinate directions is applied. The resulting MDBs $\hat{\nabla}_{0,i}$ are shown in figure 13. The structure is the same in both coordinate systems as well as in the plane fitting example. The point in the middle is the best controlled one, whereas the MDBs of the corner points are considerably higher. The correlation coefficients ρ_{ij} of the test statistics $T_N(\nabla_i)$ in figure 14a show, that the corresponding coordinates in both coordinate systems are highly correlated. Hence, by only using the condition equations (53), one can't distinguish if the outlier influences the coordinate in system 1 or 2.

In another evaluation only a rotation of 45° is applied. The MDBs show the same structure as in the first evaluation (figure 13) but the behavior of the ρ_{ij} is slightly different (figure 14b). Because of the rotation of 45°, an outlier in one coordinate in system 1 appears to be an outlier with equal extent in both coordinate directions in system 2. Varying the scale parameter m from 1 ppm to 1000 ppm, shows no influence on the MDBS and the correlation coefficients.
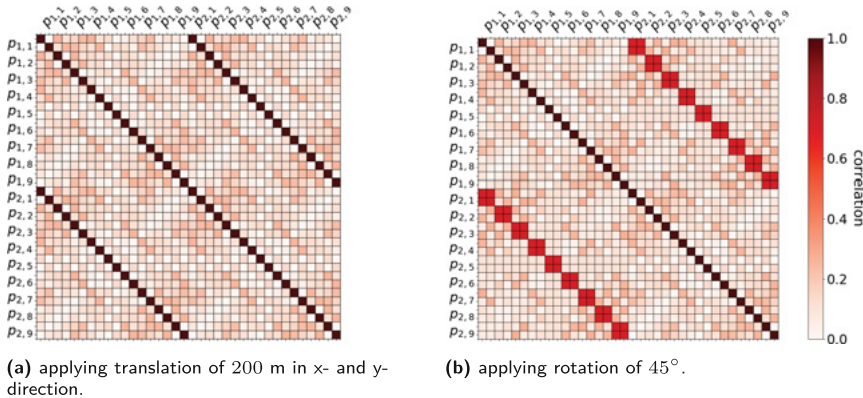
(a) applying translation of 200 m in x- and y-direction.

(b) applying rotation of $45°$.

Figure 14: Absolute values of correlation coefficients.

References

[1] Willem Baarda, *Statistical concepts in geodesy*, Publications on Geodesy 2, NCG, Delft, Netherlands, 1967.

[2] Willem Baarda, *A testing procedure for use in geodetic networks*, Publications on Geodesy 2, NCG, Delft, Netherlands, 1968.

[3] Sergio Baselga, Exhaustive search procedure for multiple outlier detection, *Acta Geodaetica et Geophysica Hungarica* 46 (2011), 401–416.

[4] Dimitri P. Bertsekas, *Constrained optimization and Lagrange multiplier methods*, Athena Scientific, Belmont, Massachusetts, USA, 1982.

[5] Ludovico Biagi and Stefano Caldera, An efficient leave one block out approach to identify outliers, *Journal of Applied Geodesy* 7 (2013), 11–19.

[6] Andreas Ettlinger, Hans Neuner and Thomas Burgess, Development of a Kalman filter in the Gauss-Helmert model for reliability analysis in orientation determination with smartphone sensors, *Sensors* 18 (2018).

[7] Wolfgang Förstner, *Reliability and discernability of extended Gauss-Markov models*, Seminar on Mathematical Models to Outliers and Systematic Errors, German Geodetic Commission (DGK), Vol. A No. 98, Munich, Germany, 1983, pp. 79–103.

[8] Wolfgang Förstner, Reliability analysis of parameter estimation in linear models with applications to mensuration problems in computer vision, *Computer Vision, Graphics and Image Processing* 40 (1987), 273–310.

[9] Wolfgang Förstner and Bernhard P. Wrobel, *Photogrammetric computer vision*, Geometry and Computing 11, Springer International Publishing, Basel, Switzerland, 2016.

[10] Arthur Gelb, *Applied optimal estimation*, MIT press, Cambridge, Massachusetts, USA, 1974.

[11] Gene H. Golub and Charles F. van Loan, *Matrix computations*, 3rd edition, The Johns Hopkins University Press, Baltimore, Maryland, USA, 1996.

[12] Frank R. Hampel, *Contributions to the theory of robust estimations*, Ph. D. thesis, University of California, Berkeley, 1968.

[13] Friedrich R. Helmert, *Die Ausgleichungsrechnung nach der Methode der kleinsten Quadrate*, 2nd edition, Teubner, Wiesbaden, Germany, 1907.

[14] Otto Heunecke, Heiner Kuhlmann, Walter Welsch, Andreas Eichhorn and Hans Neuner, *Auswertung geodätischer Überwachungsmessungen*, 2nd edition, Wichmann, Berlin, Germany, 2013.

[15] Peter J. Huber, Robust estimation of a location parameter, *The Annals of Mathematical Statistics* 35 (1964), 73–101.

[16] Reiner Jäger, Tilman Müller, Heinz Saler and Rainer Schwäble, *Klassische und Robuste Ausgleichungsverfahren*, Wichmann, Berlin, Germany, 2005.

[17] Karl-Rudolf Koch, *Parameterschätzung und Hypothesentests in linearen Modellen*, 4th edition, Dümmlers Verlag, Bonn, Germany, 2004.

[18] Karl-Rudolf Koch, Outlier detection for the nonlinear Gauss-Helmert model with variance components by the expectation maximization algorithm, *Journal of Applied Geodesy* 8 (2014), 185–194.

[19] Karl-Rudolf Koch, Robust estimations for the nonlinear Gauss-Helmert model by the expectation maximization algorithm, *Journal of Geodesy* 88 (2014), 263–271.

[20] Karl-Rudolf Koch and Boris Kargoll, Outlier detection by the EM algorithm for laser scanning in rectangular and polar coordinate systems, *Journal of Applied Geodesy* 9 (2015), 162–173.

[21] Stephan Kupferer, Mehrdimensionale Beobachtungstests bei Gauss-Helmert-Modellen, *AVN* 111 (2004), 264–269.

[22] Heidi Kuusniemi, Andreas Wieser, Gerard Lachapelle and Jarmo Takala, User-level reliability monitoring in urban personal satellite-navigation, *IEEE Transactions on Aerospace and Electronic Systems* 43 (2007), 1305–1318.

[23] Rüdiger Lehmann, On the formulation of the alternative hypothesis for geodetic outlier detection, *Journal of Geodesy* 87 (2013), 373–386.

[24] Rüdiger Lehmann and Michael Lösler, Multiple outlier detection: hypothesis tests versus model selection by information criteria, *Journal of Surveying Engineering* 142 (2016).

[25] Lothar Lenzmann and Enno Lenzmann, Strenge Auswertung des nichtlinearen Gauss-Helmert-Modells, *AVN* 111 (2004), 68–73.

[26] Helena Leppäkoski, Heidi Kuusniemi and Jarmo Takala, RAIM and complementary Kalman filtering for GNSS reliability enhancement, in: *Proceedings of the 2006 IEEE/ION Position,*

Location and Navigation Symposium, Institute of Navigation, IEEE, Coronado, California, USA, 2006.

[27] Jue Lu, Y. Chen, B.F. Li and X. Fang, Robust total least squares with reweighting iteration for three-dimensional similarity transformation, *Survey Review* 46 (2014), 28–36.

[28] Frank Neitzel, *Identifizierung konsistenter Datengruppen am Beispiel der Kongruenzuntersuchung geodätischer Netze*, German Geodetic Commission (DGK), Vol. C No. 565, Munich, Germany, 2004.

[29] Frank Neitzel, Generalization of total least-squares on example of unweighted and weighted 2D similarity transformation, *Journal of Geodesy* 84 (2010), 751–762.

[30] Wolfgang Niemeier, *Ausgleichungsrechnung: Statistische Auswertemethoden*, 2nd edition, Walter de Gruyter, Berlin, Germany, 2008.

[31] Mohammed Omidalizarandi, Boris Kargoll, Jens-Andre Pfaffenholz and Ingo Neumann, Robust external calibration of terrestrial lase scanner and digital camera for structural monitoring, *Journal of Applied Geodesy* 13 (2019).

[32] Peter J. Rousseeuw, Least median of squares regression, *Journal of the American Statistical Association* 79 (1984), 871–880.

[33] Peter J. G. Teunissen, *Adjustment theory*, Series on Mathematical Geodesy and Positioning, VSSD, Delft, Netherlands, 2002.

[34] Peter J. G. Teunissen, *Testing theory*, 2nd edition, Series on Mathematical Geodesy and Positioning, VSSD, Delft, Netherlands, 2006.

[35] Peter J. G. Teunissen, Distributional theory for the DIA method, *Journal of Geodesy* 92 (2018), 59–80.

[36] Andreas Wieser, Mark G. Petovello and Gerard Lachapelle, Failure scenarios to be considered with kinematic high precision relative GNSS positioning, in: *Proceedings of the 17th International Technical Meeting of the Satellite Division of the Institute of Navigation(ION GNSS)*, Institute of Navigation, pp. 1448–1459, Citeseer, Long Beach, California, USA, 2004.

[37] Ling Yang, Bofeng Li, Yunzhong Shen and Chris Rizos, Extension of internal reliability analysis regarding separability analysis, *Journal of Surveying Engineering* 143 (2017), 1–10.

A.3   Robust determination of smartphone heading by mitigation of magnetic anomalies

ORIGINAL ARTICLE

Robust Determination of Smartphone Heading by Mitigation of Magnetic Anomalies

Andreas Ettlinger*[1] | **Andreas Wieser[2]** | **Hans Neuner[1]**

[1] Department of Geodesy and Geoinformation, Technische Universität (TU) Wien, Vienna, Austria

[2] Institute of Geodesy and Photogrametry, Eidgenössische Technische Hochschule (ETH) Zürich, Zürich, Switzerland

Correspondence
Andreas Ettlinger
Wiedner Hauptstraße 8-10,
1040 Vienna, Austria.
Email: andreas.ettlinger@tuwien.ac.at

Present address
Wiedner Hauptstraße 8-10,
1040 Vienna, Austria

Abstract

We introduce an algorithm that provides robust three-dimensional orientation of a smartphone for pedestrian indoor localization. The algorithm focuses on integration of the magnetometer and a reformulated observation model such that the influence of magnetic anomalies is mitigated. The methodological novelty of this approach lies in the use of an extended Kalman filter (EKF), based on a state vector that contains only the slow-varying systematic deviation components of the magnetometer. We apply a statistical test to the EKF residuals to detect the presence of magnetic anomalies and update the absolute heading when beneficial conditions prevail. Otherwise, the heading is propagated based on gyroscope observations. We investigate the properties of the proposed algorithm by using simulated smartphone sensor observations with different scenarios of systematic deviations. In experiments with very accurate ground truth, the proposed algorithm achieves a root mean square error of 17.4° for the computed heading, outperforming state-of-the-art algorithms by at least 40%.

Keywords

extended Kalman filter, indoor navigation, magnetometer integration, orientation estimation

1 | INTRODUCTION

The computation of smartphone orientation is an important step in the process of pedestrian indoor localization, for example, when providing navigation to a certain location (Ehrlich & Blankenbach, 2018; Moder et al., 2018) or using the movement behavior of persons to gain insight into building utilization (Burgess et al., 2018; Kanda et al., 2007). We propose a new orientation-estimation algorithm (OEA) based on self-contained sensors, with a focus on magnetometer integration to provide robust absolute smartphone heading information.

The magnetometer observation model exhibits classical internal sensor errors such as those related to bias, scale factor, and misalignment (Renaudin et al., 2010) as well as platform- and environment-dependent errors such as hard-iron bias, soft-iron scaling, and magnetic anomaly bias (Groves, 2013). These latter errors are the primary reason that magnetometer integration in OEAs can cause large deviations in heading estimations. Routines for determining and mitigating these

systematic deviations are mandatory, and herein, we consider only procedures that are directly applied in the indoor localization process (i.e., on-site). There are two main approaches for on-site determination or mitigation of systematic deviations, namely, instruction-based procedures and in-run procedures (Martin et al., 2016). In instruction-based procedures, the smartphone must undergo special movements or trajectories prior to the localization process; in in-run procedures, sensor errors are determined during localization. The classic instruction-based approach for smartphones is the ellipsoid-fitting approach, in which the smartphone is rotated around its three main axes to determine sensor errors. With the constraint that magnetometer observations are ideally located on a sphere with known radius, i.e., the known value of the magnitude of the earth's magnetic field (EMF), it is possible to determine sensor and platform errors (Gebre-Egziabher et al., 2006; Klingbeil et al., 2014; Renaudin et al., 2010; Vasconcelos et al., 2011).

The obvious problem is that environment-dependent errors (i.e., magnetic anomalies) cannot be captured with the above-described approach. Thus, it is necessary to apply an in-run procedure in the OEA to determine the presence of magnetic anomalies in magnetometer observations. A common approach is to fuse the gyroscope, accelerometer, and magnetometer in an extended Kalman filter (EKF) to estimate the smartphone orientation (Gebre-Egziabher et al., 2004; Han & Wang, 2011). In these approaches, it is critical to note that magnetic anomalies also influence the inclination component of the orientation (roll φ and pitch θ in Euler angle parameterization). Madgwick et al. (2011) and Valenti et al. (2015) attempted to avoid this effect by using complementary filters, where the change in inclination is computed via the accelerometer sensor and the change in yaw (ψ in Euler angle parameterization) is computed via the magnetometer sensor. A possibility for mitigation is to use the known quantities of the EMF to determine whether magnetic anomalies are present. The literature contains many proposed solutions exploiting this information: Costanzi et al. (2016) used this knowledge to compute adaptive variances for magnetometer observations. Renaudin & Combettes (2014) and Lee et al. (2018) performed the EKF update only if conditions on the magnetometer observations were met, and Afzal et al. (2011) used statistical tests and fuzzy inference to determine the resulting heading error due to magnetic anomalies. Another approach is to parameterize the systematic deviations in an EKF (i.e., include them in the state vector). It is not common to estimate each type of systematic deviation separately in the EKF but to subsume them in a bias and an affine transformation parameterized with a symmetric matrix (Klingbeil et al., 2014; Renaudin et al., 2010). Crassidis et al. (2005) included this bias and the elements of a symmetric matrix in the state vector of an EKF and an unscented Kalman filter. Han et al. (2017) additionally integrated the EMF in the state vector and propagated it with the gyroscope observations.

Each of the previously mentioned approaches exhibits at least one of the following problems: On the one hand, systematic deviations in magnetometer observations cannot be sharply separated from the desired signal; rather, they can only be separated to a certain extent. When orientation parameters are included in the state vector of an EKF, small amounts of systematic deviations that cannot be detected influence the estimated states. On the other hand, trajectories from pedestrians do not usually contain sufficient information to decorrelate the state vector components, including orientation parameters and different types of systematic deviations.

Consequently, biased estimates arise in the presence of unmodeled effects such as magnetic anomalies. We propose an OEA that reduces these problems under some loose restrictions. The computation of the inclination, heading, and

systematic deviations is divided into separate modules to avoid undesired effects due to correlated parameters. Instead of absolutely computing the heading in every epoch, the algorithm propagates the heading with the gyroscope, and the absolute part is updated periodically when good conditions for EMF sensing prevail. The update of the absolute heading is triggered by an EKF, whose state vector consists only of the magnetometer bias subsuming the systematic deviations with low temporal variance (i.e., related to the sensor and its platform). This algorithm enables the reliable detection of rapidly varying systematic deviations (i.e., magnetic anomalies and their secondary effects); therefore, the update of the absolute heading can be suppressed in such phases. However, an OEA based solely on an inertial measurement unit and magnetometer is dependent on the condition that error-free magnetometer observations are available in at least some time windows (ideally in the initial phase of the algorithm). For edge cases in which magnetometer observations are faulty all the time, it is necessary to integrate additional observation types into the OEA.

In Section 2, we introduce the proposed OEA in detail. For convenience, a list of symbols used in the extensive equations is provided in Appendix B. We validate our OEA in Section 3.1 with simulated data to show that the OEA exhibits the proposed properties. In Section 3.2, we use measured smartphone sensor data and ground truth data from a laser tracker to compare our OEA with three of the OEAs mentioned above.

2 | PROPOSED ALGORITHM

The coordinate frames and smartphone sensor observations are shown in Figure 1. We assume that the observations from the gyroscope ω^B, accelerometer $\mathbf{a}^B$, and magnetometer $\mathbf{m}^B$ are available in the common smartphone body frame (B-frame). The aim of smartphone orientation determination is to link the B-frame with the navigation frame (N-frame), which corresponds to the coordinate system in which the pedestrian motion is described. To describe the rotations needed to link the B-frame with the N-frame, Euler angle parameterization is used herein. All frames are right-handed, and all angles are counted positive in the counter-clockwise direction. We use an intermediate frame, the local-level
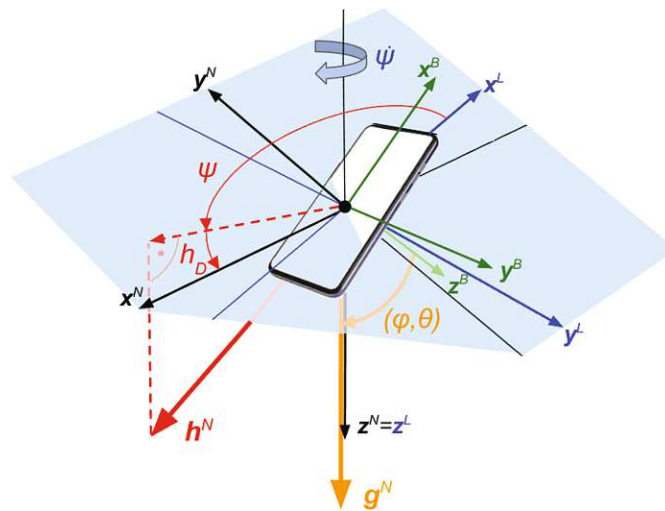

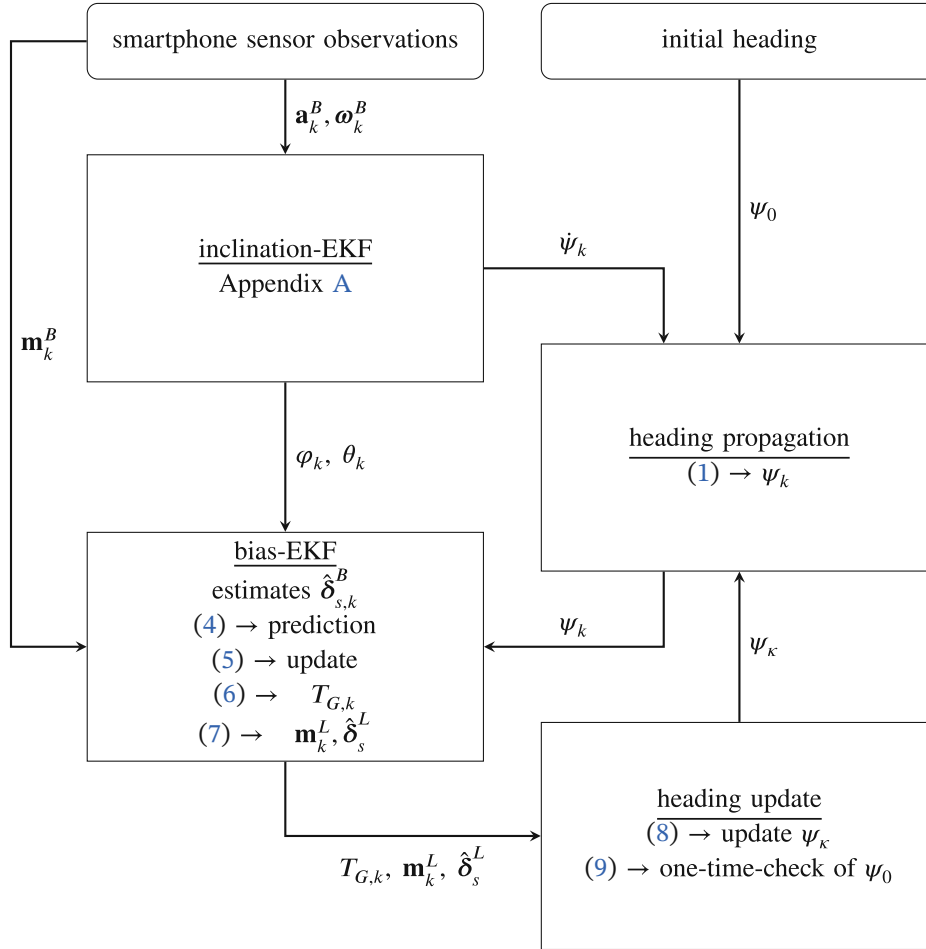**FIGURE 1** Visualization of the used coordinate frames

FIGURE 2 Overview of the proposed OEA

frame (L-frame), to separate the computation of the inclination from the computation of the heading.

The inclination computation (i.e., computing φ and θ) with $\boldsymbol{\omega}^B$ (angular velocity around the B-frame axes) and $\mathbf{a}^B$ (components of the gravity vector $\mathbf{g}^N$ in the B-frame) links the B-frame with the L-frame. The heading describes the rotation around the vertical z-axis and links the L-frame with the N-frame. The heading is computed by using $\mathbf{m}^B$ (components of the EMF vector $\mathbf{h}^N$ in the B-frame), the vertical angular velocity $\dot{\psi}$, and the magnetic declination h_D. Values for $\mathbf{h}^N$ and h_D are derived from an EMF model.[1]

Figure 2 shows an overview of the proposed OEA for determining smartphone orientation. The inputs are the sensor observations $\boldsymbol{\omega}_k^B$, $\mathbf{a}_k^B$, and $\mathbf{m}_k^B$ as well as an initial smartphone heading ψ_0 at time $k = 0$. The algorithm consists of four modules: The computation of the inclination follows the algorithms from Särkkä et al. (2015) and Hostettler & Särkkä (2016), as outlined in Appendix A. Heading propagation is conducted with $\dot{\psi}_k$ derived from the inclination-EKF (Section 2.1). The bias-EKF in Section 2.2 is based on a novel functional model. Its state vector contains the slow-varying systematic deviations in the magnetometer observations and uses $\varphi_k, \theta_k, \psi_k$ as well as $\mathbf{m}^B$ as observations. In the heading update module (Section 2.3), the results from the bias-EKF are collected in time windows. If these

---

[1]World Magnetic Model (WMM), online calculator: https://www.ngdc.noaa.bov/geomag/calculators/magcalc.shtml?model=wmm, accessed: 28.05.2022

data exhibit certain properties, the absolute heading is updated. Additionally, a one-time check of ψ_0 is performed in the heading update.

It is not necessary for the user to carry the smartphone in a certain mode. The smartphone can be carried in a pocket or bag but can also be held by the user in texting or calling mode. One of the following two conditions must be met for the proposed OEA to provide useful results: Either ψ_0 must be accurately known or the first couple of seconds of magnetometer observations must be free from systematic deviations (e.g., ensured by magnetometer calibration with ellipsoid fitting). We favor the second case, as it is common in several smartphone applications, requiring the user to perform certain rotations of the phone in order to trigger a built-in magnetometer calibration procedure. Still, the calibration with ellipsoid fitting must not result in an unbiased yaw angle. When ellipsoid fitting fails, there should be at least some time windows without magnetic anomalies in order to have an opportunity to improve an initial heading that is most likely erroneous. The proposed algorithm is dependent on this fact. If magnetic anomalies are present all the time, the smartphone heading can only be propagated with the relative changes derived from the gyroscope. In this case, drift effects due to the summation of gyroscpe bias must be considered, and additional observations are needed to stabilize the resulting smartphone heading. These limitations must be considered when the proposed algorithm is applied.

2.1 | Heading Propagation

The heading ψ for the current epoch k is derived by integrating $\dot{\psi}_k$ with the constant time interval between observations dt:

$$\psi_k = \psi_\kappa + d\psi_{\kappa|k} = \psi_\kappa + \sum_{i=\kappa+1}^{k} dt \cdot \dot{\psi}_i$$
$$\sigma_{\psi,k}^2 = \sigma_{\psi,\kappa}^2 + \sum_{i=\kappa+1}^{k} dt^2 \cdot \sigma_{\dot{\psi},i}^2 \tag{1}$$

This integration is performed from the epoch κ on, at which the absolute heading has been previously updated, where $d\psi_{\kappa|k}$ is the accumulated heading change. The computation of ψ_κ is outlined in Section 2.3. The variance σ_ψ^2 is derived with variance propagation, neglecting temporal correlations (i.e., autocorrelation). The propagated heading is the outcome of the proposed OEA but is also used as an observation in the bias-EKF, as described in the following section.

2.2 | Bias-EKF

We reformulate the magnetometer model (Groves, 2013) to develop a functional model of the bias-EKF:

$$\mathbf{m}^B = (\mathbf{I} + \mathbf{\Delta}_{sn})[(\mathbf{I} + \mathbf{\Delta}_{si})\mathbf{R}_N^B(\mathbf{h}^N + \boldsymbol{\delta}_a^N) + \boldsymbol{\delta}_{hi}^B] + \boldsymbol{\delta}_b^B + \boldsymbol{\epsilon}_m \tag{2}$$

$\mathbf{\Delta}_{sn}$ is a matrix that accounts for scaling and non-orthogonality of the magnetometer. $\boldsymbol{\delta}_b^B$ and $\boldsymbol{\delta}_{hi}^B$ are the sensor bias and hard-iron bias, and $\boldsymbol{\delta}_a^N$ accounts for magnetic anomalies in the sensor's environment. $\mathbf{\Delta}_{si}$ contains the soft-iron effects, which are dependent on smartphone position and orientation with respect to magnetic anomalies. $\boldsymbol{\epsilon}_m$ is the magnetometer white noise, and $\mathbf{I}$ is the identity matrix.

$\mathbf{R}_N^B$ is the rotation matrix linking the N-frame and B-frame; this term is computed from φ, θ, and ψ. We rearrange Equation (2) such that two new terms summarize the systematic deviations:

$$\begin{aligned}
\mathbf{m}^B &= \mathbf{R}_N^B \mathbf{h}^N + \boldsymbol{\delta}_s^B + \boldsymbol{\delta}_f^B + \boldsymbol{\epsilon}_m \\
\boldsymbol{\delta}_s^B &= (\mathbf{I} + \boldsymbol{\Delta}_{sn})\boldsymbol{\delta}_{hi}^B + \boldsymbol{\delta}_b^B \\
\boldsymbol{\delta}_f^B &= \mathbf{R}_N^B \boldsymbol{\delta}_a^N + (\boldsymbol{\Delta}_{sn}\boldsymbol{\Delta}_{si} + \boldsymbol{\Delta}_{sn} + \boldsymbol{\Delta}_{si})\mathbf{R}_N^B(\mathbf{h}^N + \boldsymbol{\delta}_a^N)
\end{aligned} \tag{3}$$

$\boldsymbol{\delta}_s^B$ subsumes the deviations that are related only to the magnetometer and its carrier platform (i.e., the smartphone). This term is treated as a slow-varying bias. $\boldsymbol{\delta}_f^B$ is the bias that exhibits rapid changes upon movement through the environment when magnetic anomalies are present.

As mentioned in Section 1, we choose a minimum parameterization of the state vector for the bias-EKF, which equals $\boldsymbol{\delta}_s^B$. The prediction is performed with a random walk model:

$$\bar{\boldsymbol{\delta}}_{s,k}^B = \hat{\boldsymbol{\delta}}_{s,k-1}^B + dt \cdot \boldsymbol{\zeta}_\delta \tag{4}$$

where $\bar{\boldsymbol{\delta}}_{s,k}^B$ is the predicted state, $\hat{\boldsymbol{\delta}}_{s,k-1}^B$ is the previously estimated state, and $\boldsymbol{\zeta}_\delta$ is the system noise. For better readability, we omit the index k from here on. Only the quantities related to the previously estimated state are indexed with $k-1$. The filter innovation $\mathbf{w}_m$ is computed by using $\mathbf{m}^B$ and the Euler angles as observations:

$$\mathbf{w}_m = \mathbf{m}^B - \bar{\boldsymbol{\delta}}_s^B - \mathbf{R}_N^B(\varphi, \theta, \psi)\mathbf{h}^N \tag{5}$$

Here, we use a slightly different formulation of the innovation computation that does not exhibit the common structure of "observed minus computed." Ettlinger et al. (2018) and Vogel et al. (2018) provided a detailed explanation of this EKF variant. In the presence of magnetic anomalies, $\mathbf{m}^B$ contains $\boldsymbol{\delta}_f^B$ (see Equation (3)), which is absorbed by $\hat{\boldsymbol{\delta}}_s^B$ only to a certain extent depending on the preset variances of $\mathbf{m}^B$ and $\boldsymbol{\zeta}_\delta$ (Table 1). Consequently, $\hat{\boldsymbol{\delta}}_s^B$ becomes biased, and the remaining influence of $\boldsymbol{\delta}_f^B$ affects the residuals $\hat{\mathbf{v}} = [\hat{\mathbf{v}}_{\hat{\boldsymbol{\delta}}_{s,k-1}}, \hat{\mathbf{v}}_{\boldsymbol{\zeta}_\delta}, \hat{\mathbf{v}}_m, \hat{\mathbf{v}}_{\varphi\theta\psi}]^T \in \mathbb{R}^{12 \times 1}$ of the bias-EKF. We use $\hat{\mathbf{v}}$ and the corresponding variance-covariance matrix (VCM) $\boldsymbol{\Sigma}_{\hat{\mathbf{v}}\hat{\mathbf{v}}}$ to formulate a statistical test (global model test):

$$\begin{aligned}
T_G = \hat{\mathbf{v}}^T \boldsymbol{\Sigma}_{\hat{\mathbf{v}}\hat{\mathbf{v}}}^{-1} \hat{\mathbf{v}} &\sim \chi_3^2 \mid H_0 \\
&\sim \chi_{3,\lambda}^2 \mid H_A
\end{aligned} \tag{6}$$

We use the above equation to verify the compliance between the observed data and the model assumptions of the bias-EKF. In the null hypothesis H_0, the expectation of the residuals is assumed to be zero $E\{\hat{\mathbf{v}}\} = \mathbf{0}$, and therefore, T_G follows a chi-square distribution with three degrees of freedom (DoFs) (i.e., the dimension of $\mathbf{w}_m$). In the presence of magnetic anomalies, $\boldsymbol{\delta}_f^B$ also affects $\hat{\mathbf{v}}$, leading to $E\{\hat{\mathbf{v}}\} \neq \mathbf{0}$; therefore, T_G should become significant (i.e., larger than the corresponding critical value $T_{G,c}(\alpha)$, where α is the type I error). In this case (i.e., under the alternative hypothesis H_A), T_G follows a non-central chi-square distribution $\chi_{3,\lambda}^2$ with non-centrality parameter λ.

Finally, we rotate $\mathbf{m}^B$ and $\hat{\boldsymbol{\delta}}_s^B$ into the L-frame:

$$\begin{aligned}
\mathbf{m}^L &= \mathbf{R}_B^L(\varphi, \theta)\mathbf{m}^B \\
\hat{\boldsymbol{\delta}}_s^L &= \mathbf{R}_B^L(\varphi, \theta)\hat{\boldsymbol{\delta}}_s^B
\end{aligned} \tag{7}$$

which we use in the following heading update step.

2.3 | Heading Update

The heading update step of the proposed OEA contains two actions: the update of ψ when certain conditions are met and the one-time check of ψ_0. The following equations describe the update:

$$\psi_\kappa = \frac{1}{n_{W,u}} \sum_{i=1}^{n_{W,u}} \arctan \frac{-(m_{y,i}^L - \hat{\delta}_{s,y,i}^L)}{(m_{x,i}^L - \hat{\delta}_{s,x,i}^L)} \quad \text{if} \quad (p_T \leq \alpha) \wedge (d\psi_{\kappa|k} \leq \gamma_{d\psi})$$

$$p_T = \frac{n_T}{n_{W,u}} \tag{8}$$

$$n_T = |\{T_{G,i} | T_{G,i} > T_{G,c}(\alpha)\}|$$

We collect $\mathbf{m}^L$, $\hat{\delta}_s^L$, and T_G in non-overlapping time windows with length $dt_{W,u}$. To update ψ_κ, two conditions must be fulfilled (first line in Equation (8)). The percentage p_T (second line in Equation (8)) is computed from the number of test values $T_{G,i}$ that exceed the corresponding critical value $T_{G,c}(\alpha)$ (third line in Equation (8)). If $p_T > \alpha$, we assume that magnetic anomalies are present, which cannot be absorbed by $\hat{\delta}_s^B$, leading to a bias in the computed heading. The second condition $d\psi_{\kappa|k} \leq \gamma_{d\psi}$ suppresses the update of ψ_κ if the user is turning within a time window because, in this case, the values in the time windows are not valid for the current epoch k. $\gamma_{d\psi}$ is a preset threshold, and the accumulated heading change $d\psi_{\kappa|k}$ from Equation (1) is used as an indicator for user turns.

Up to this point, the proposed OEA relies on the the unbiasedness of ψ_0, as it is used for the heading propagation and in the initialization of the bias-EKF. We use the following procedure only one time at the beginning of the trajectory to verify the compliance between ψ_0 and the magnetometer observations:

$$\psi_\kappa = \psi_m = \frac{1}{n_{W,0}} \sum_{i=1}^{n_{W,0}} \arctan \frac{-m_{y,i}^L}{m_{x,i}^L} \quad \text{if} \quad (|\psi_k - \psi_m| > \gamma_\psi) \wedge (d\psi_{0|k} \leq \gamma_{d\psi}) \wedge (p_m > \gamma_m)$$

$$p_m = \frac{n_m}{n_{W,0}}$$

$$n_m = |\{\mathbf{m}_i^L | c_1 \wedge c_2\}| \tag{9}$$

$$c_1 = |\|\mathbf{m}_i^L\| - \|\mathbf{h}^N\|| \leq \gamma_{\sigma m} \cdot \sigma_m$$

$$c_2 = |m_{z,i}^L - h_z^N| \leq \gamma_{\sigma m} \cdot \sigma_m$$

This value is independent from the results of the bias-EKF, and if the conditions are fulfilled, ψ_κ is updated accordingly and the bias-EKF is re-initialized. We collect only $\mathbf{m}^L$ in a time window with length $dt_{W,0}$ starting from k = 0. First, the difference $|\psi_k - \psi_m| > \gamma_\psi$ between the propagated heading ψ_k from Equation (1) and ψ_m must exceed the predefined threshold γ_ψ (otherwise, there is no reason for an update). The second condition is equivalent to the condition in Equation (8) and suppresses an update if the user turns within the time window. The third condition $p_m > \gamma_m$ requires that the percentage p_m (second line in Equation (9)) of $\mathbf{m}_i^L$, which fulfills two additional requirements c_1 and c_2 (third line in Equation (9)), is higher than the predefined threshold γ_m. Because we want to use the heading computed from raw magnetometer observations in this control procedure (i.e., $\hat{\delta}_s^B$ is not used in the first line of Equation (9)), the observations must be checked for systematic deviations. c_1 requires that the magnitude of $\mathbf{m}^L$ be equal to the magnitude of the EMF vector $\mathbf{h}^N$ (also derived from the EMF model in Section 2). This

condition is too sparse, as all accepted solutions theoretically lie on a sphere. Thus, c_2 requires that the z-component of $\mathbf{m}^L$ be equal to the z-component of $\mathbf{h}^N$. All acceptable solutions of c_2 lie on a plane, and the intersection with the sphere from c_1 results in a circle in the three-dimensional (3D) space of solutions that fulfill both conditions. Because of measurement noise, these conditions cannot be met exactly but must be fulfilled within the threshold $\gamma_{\sigma m} \cdot \sigma_m$, where σ_m is the standard deviation of ϵ_m and $\gamma_{\sigma m}$ is a predefined multiplier.

In the next section, we use simulated data and experiments performed with a high-accuracy 6-DoF reference measurement system to analyze the properties of the proposed OEA. Additionally, the results from the experiments are compared with the results of three other OEAs from the literature.

3 | EVALUATION

3.1 | Validation with Simulated Data

In this section, we use simulated data to validate the proposed OEA in different controlled conditions, where the influence of different systematic deviations affecting the magnetometer is exactly known. The smartphone sensor observations $\mathbf{a}^B$, ω^B, and $\mathbf{m}^B$ are determined from a straight trajectory, as shown in Figure 3, where the orientation of the coordinate frame equals the orientation of the N-frame. The trajectory also determines the heading or yaw angle $\tilde{\psi} = -61.0°$, and the inclination angles are constant $\tilde{\varphi} = 0.0°, \tilde{\theta} = -30.0°$. Thus, the rotation matrix $\tilde{\mathbf{R}}_N^B$ is available (˜ indicates known quantities), and $\mathbf{a}^B$ and $\mathbf{m}^B$ are computed as follows:

$$\mathbf{a}^B = \tilde{\mathbf{R}}_N^B \mathbf{g}^N + \epsilon_a$$
$$\mathbf{m}^B = \tilde{\mathbf{R}}_N^B \mathbf{h}^N + \epsilon_m \quad (10)$$
$$\omega^B = \epsilon_\omega$$

where ϵ_a, ϵ_m, and ϵ_ω are the noise vectors of the accelerometer, magnetometer, and gyroscope. The components of the noise vectors are modeled as zero-mean uncorrelated Gaussian noise with a corresponding standard deviation (see Table 1).
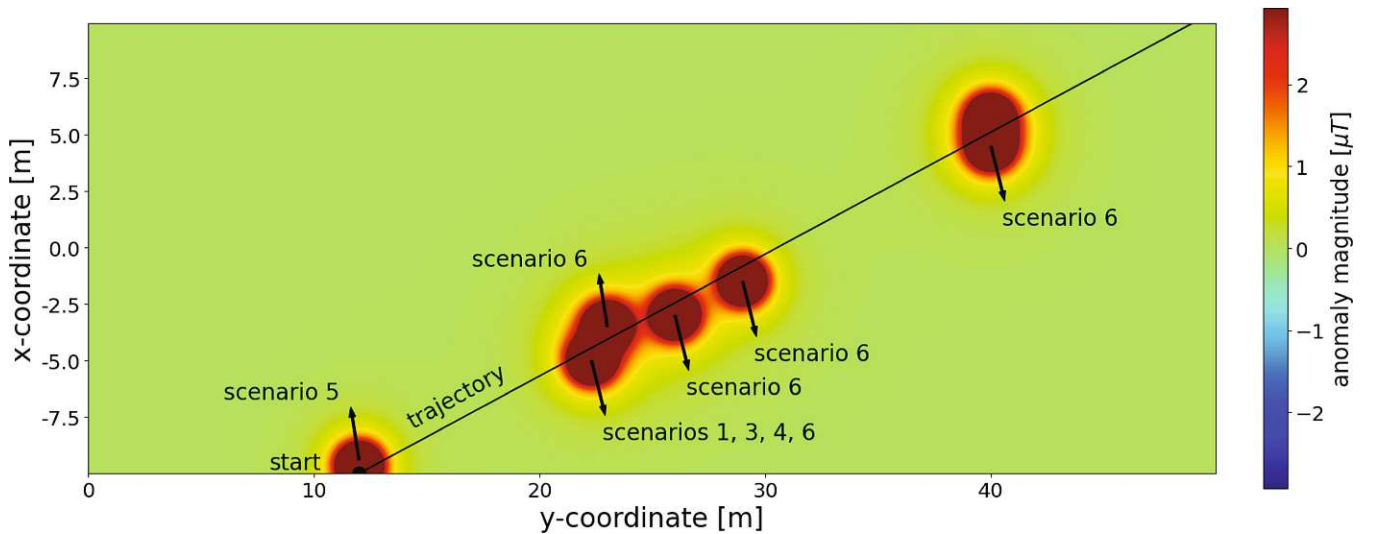

FIGURE 3 Map with trajectories and magnetic anomalies used in the simulation scenarios

The standard deviations are derived from the smartphones used in Section 3.2 when lying static for several minutes. As we do not model stride or step accelerations, the state of the inclination-EKF only consists of $\hat{\mathbf{g}}^B$. All settings of the proposed algorithm are summarized in Table 1.

We investigate six scenarios with different systematic deviations affecting the magnetometer observations. Additionally, a baseline scenario (scenario 0) is chosen, in which no systematic deviations are introduced. Magnetic anomalies are modeled in all scenarios (except scenario 2), representing $\boldsymbol{\delta}_f^B$. The anomalies are shown in Figure 3, modeled as a magnetic dipole according to previous work (Afzal, 2011). In scenarios 1, 3, and 4, there is only one magnetic anomaly, which occurs in the middle of the trajectory, and in scenario 5, there is one anomaly at the beginning of the trajectory. Scenario 6 contains six magnetic anomalies to imitate a more realistic indoor scenario. A slow-varying bias is modeled in scenarios 2 and 3, representing $\boldsymbol{\delta}_s^B$. The bias $\boldsymbol{\delta}_s^B = [2.0, 0.0, 0.0]^T \, [\mu T]$ is added to $\mathbf{m}^B$ from $15.0 \, s$ on (see Figure 4(a)). A linear increase starting from $0.0 \, \mu T$ in the x-component is modeled from $10.0 \, s$ to $15.0 \, s$, at which point $2.0 \, \mu T$ is reached. Both deviations are deterministic quantities, i.e., no noise is added. ψ_0 is drawn from a Gaussian distribution with zero mean and standard deviation $\sigma_{\psi,0}$, according to Table 2. To analyze the influence of the accuracy of ψ_0, $\sigma_{\psi,0}$ is increased in scenario 4. All scenarios are evaluated 3000 times. We investigate the results of the proposed algorithm from these six scenarios and compare them with the results for scenario 0.

Figure 4 shows the deviations $\Delta\hat{\boldsymbol{\delta}}_s^B$ of the estimated slow-varying bias from the corresponding known values for scenarios 1, 2, and 6. The results of scenario 4 do not differ from those shown in Figure 4(a), except during the first 3 s before the

TABLE 1
Settings of the Proposed Algorithm
$\sigma_{\zeta a,i,j}$ and $\sigma_{\zeta \dot{a},i,j}$ are only relevant for the measured data containing user motion in Section 3.2.

inclination-EKF		bias-EKF		heading update	
σ_a	$0.1 \, m/s^2$	σ_m	$2.0 \, \mu T$	$\gamma_{d\psi}$	$10.0°$
σ_ω	$0.1°/s$	$\sigma_{\zeta\delta}$	$0.5 \, \mu T/s$	γ_ψ	$5.0°$
$\sigma_{\zeta g,i}$	$0.02 \, m/s^2$	α	0.1	γ_m	0.95
$\sigma_{\zeta a,i,j}$	$0.02 \, m/s^2$			$\gamma_{\sigma m}$	3.0
$\sigma_{\zeta \dot{a},i,j}$	$0.02 \, m/s^3$			$dt_{W,u}$	$5.0 \, s$
				$dt_{W,0}$	$3.0 \, s$

TABLE 2
Mean and Standard Deviation of $\Delta\hat{\psi}$ (Deviation of Estimated $\hat{\psi}$ from Reference Value) from 3000 Evaluations
The bias column indicates whether a sensor bias is added to the simulated observations, and $\sigma_{\psi,0}$ is the standard deviation of the distribution from which ψ_0 is drawn.

scenario	anomaly	bias	$\sigma_{\psi,0}$ [°]	$\Delta\hat{\psi}$ [°]	$\sigma_{\Delta\hat{\psi}}$ [°]
0	no	no	10.0	−0.02	3.72
1	yes (one)	no	10.0	0.02	3.76
2	no	yes	10.0	0.15	3.80
3	yes (one)	yes	10.0	0.03	3.77
4	yes (one)	no	20.0	0.20	5.37
5	yes (start)	no	10.0	−0.12	4.55
6	yes (multiple)	no	10.0	−0.06	3.81
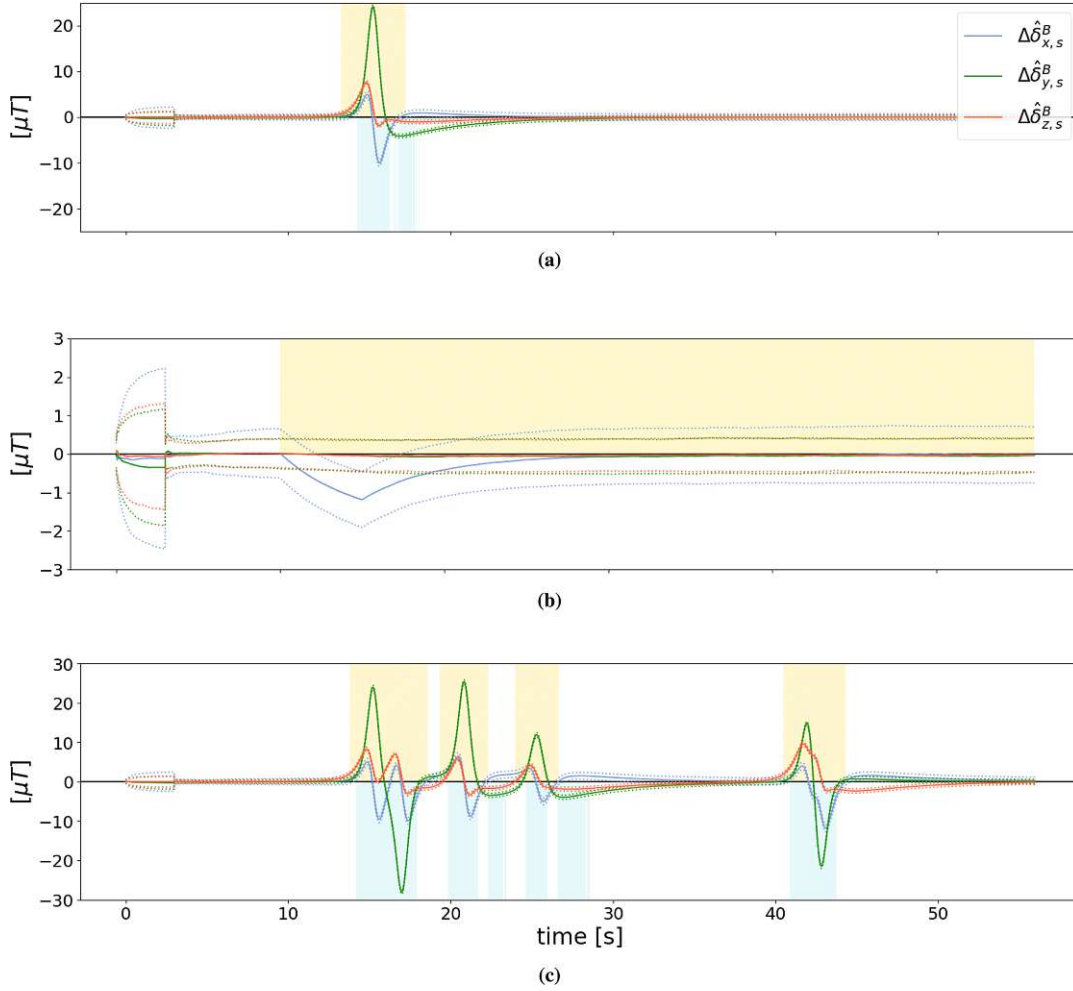
FIGURE 4 Mean deviations $\Delta\hat{\boldsymbol{\delta}}_s^B$ for three systematic deviation scenarios with the corresponding standard deviation (dotted line) (a) Scenario 1 (b) Scenario 2 (c) Scenario 6
The orange areas in scenarios 1 and 6 indicate the influence of magnetic anomalies, the yellow area in scenario 2 indicates the influence of the constant bias, and the blue areas indicate significant global tests according to Equation (6).

one-time check (Equation (9)) of ψ_0 is performed. The bias-EKF exhibits the proposed behavior. $\hat{\boldsymbol{\delta}}_s^B$ does not absorb the magnetic anomaly, which spreads on the residuals; therefore, T_G becomes significant (Figure 4(a)). An update of ψ_κ is not performed near the magnetic anomaly, as the heading angle would be biased and $\hat{\boldsymbol{\delta}}_s^B$ takes on the correct value only a couple of seconds after the magnetic anomaly is passed. In scenario 2 with the sensor bias, $\hat{\boldsymbol{\delta}}_s^B$ requires several seconds to follow the bias. Even if T_G never becomes significant (i.e., ψ_κ is updated with slightly biased values in Equation (8)), $\Delta\hat{\boldsymbol{\delta}}_s^B$ approaches zero again after the appearance of the bias. Moreover, in the case of multiple anomalies (Figure 4(c)), the bias-EKF exhibits the desired behavior. The global test values are significant in the vicinity of magnetic anomalies and converge back to zero after approximately 5 s.

The mean deviations of the resulting heading and their standard deviations are summarized in Table 2 for all scenarios. The mean deviation is slightly increased in scenarios 2, 4, and 5 compared with the other scenarios, which provide mean deviations similar to that of scenario 0. The issue with the sensor bias in scenario 2 was discussed in the previous paragraph. Scenarios 4 and 5 represent problematic conditions at the beginning of the trajectory (i.e., poor accuracy of ψ_0 or systematic

deviations in $\mathbf{m}^B$). These two scenarios also exhibit considerably higher values of $\sigma_{\delta\tilde{\psi}}$. This result indicates that problematic conditions in the initialization phase of the proposed OEA have the greatest impact on the achievable heading accuracy.

This simulation study is not all-encompassing, and real conditions have only been partially modeled. Yet, the results in this section indicate that the proposed OEA exhibits the desired properties. The OEA provides reasonable results for smartphone orientation when strong magnetic perturbations are present in the environment. In the next section, we analyze results from a small-scale experiment with high-accuracy ground truth values for smartphone orientation to further demonstrate the potential of the proposed OEA.

3.2 | Comparison with Measured Data

We performed experiments in the measurement laboratory of the Department of Geodesy and Geoinformation, TU Wien with three smartphones (Samsung Galaxy S10, LGE Nexus 5X, and Google Pixel 5) to evaluate the achievable orientation accuracy of the proposed algorithm. The reference values of the Euler angles $\tilde{\varphi}, \tilde{\theta}, \tilde{\psi}$ are determined with a Leica LTD800 laser tracker. The laser tracker provides observations in its local coordinate frame, which we denote as the Lt-frame. Pillars in the laboratory have known coordinates in a local north–east–up coordinate system, which is used to visualize the trajectories in Figure 6. The N-frame is oriented in the same way as the local north–east–up coordinate system. The coordinates of these pillars in the Lt-frame are derived from laser tracker observations to a corner cube reflector placed on the pillars. The rotation matrix $\mathbf{R}_{Lt}^{N}$ linking the Lt-frame to the N-frame is computed with an overdetermined similarity transformation. We assembled a platform with a 3D printer that can be carried by the

FIGURE 5 Experimental setup
The top row of images shows the measurement area with the laser tracker and magnet. The bottom row of images shows the 3D-printed platform with the rigidly mounted T-probe and smartphone and how the platform was held during the measurements.

user and that holds the smartphone as well as the T-probe (see Figure 5). With this device, the laser tracker provides the six DoF parameters linking the T-probe coordinate frame (Tp-frame) with the Lt-frame. The T-probe is mounted with known angular offsets from the smartphone body coordinate frame (B-frame) such that the rotation matrix $\mathbf{R}_B^{Tp}$ is available. The overall rotation matrix is composed from the previously described rotation steps:

$$\tilde{\mathbf{R}}_N^B = (\mathbf{R}_{Lt}^N \mathbf{R}_{Tp}^{Lt} \mathbf{R}_B^{Tp})^T \tag{11}$$

The standard deviation of the angles linking the N-frame with the Lt-frame from the overdetermined similarity transformation is $\sigma_{\varphi\theta\psi,N-Lt} = [0.001, 0.02, 0.001]^T$ [°]. The standard deviation of the angles linking the Lt-frame with the Tp-frame is $\sigma_{\varphi\theta\psi,Lt-Tp} = [0.002, 0.002, 0.002]^T$ [°], which is determined with the T-probe being static. Because these angles are measured kinematically, we assume that $\sigma_{\varphi\theta\psi,Lt-Tp}$ is increased by a factor of 10. Still, the uncertainty is clearly beyond a tenth of a degree for the "cumulated" angles linking the N-frame with the Tp-frame. The largest source of uncertainty is the mounting of the smartphone on the 3D-printed platform ($\sigma_{\varphi\theta\psi,Tp-B}$) and the realization of the B-frame in/on the smartphone. By carefully aligning the longitudinal side and back side of the smartphone with plastic screws (see Figure 5) to the 3D-printed platform, we ensure a precise alignment. From the numeric simulations in Section 3.1, we know that the accuracy of the resulting heading from the proposed algorithm is $4-5°$ under ideal conditions. We assume that this value increases by a factor of at least 2 under real conditions (platform and sensor imperfections, user motion, etc.). Thus, the chosen reference measurement system should be sufficient to provide reference values for the experiments and the following analysis.

The smartphone sensor observations $\mathbf{a}^B$, ω^B, and $\mathbf{m}^B$ as well as the rotation matrix $\mathbf{R}_{Tp}^{Lt}$ are collected kinematically. Time synchronization between the smartphone and tracker data is conducted by using cross-correlation. The two signals for cross-correlation are ω^B and $\tilde{\omega}^B$, which is derived according to previous work (Titterton & Weston, 2004):

$$\tilde{\omega}^B = \begin{bmatrix} \tilde{\dot{\varphi}} \\ 0 \\ 0 \end{bmatrix} + \mathbf{R}_x(\tilde{\varphi}) \begin{bmatrix} 0 \\ \tilde{\dot{\theta}} \\ 0 \end{bmatrix} + \mathbf{R}_x(\tilde{\varphi})\mathbf{R}_y(\tilde{\theta}) \begin{bmatrix} 0 \\ 0 \\ \tilde{\dot{\psi}} \end{bmatrix}$$

$$\begin{bmatrix} \tilde{\dot{\varphi}} \\ \tilde{\dot{\theta}} \\ \tilde{\dot{\psi}} \end{bmatrix} = \frac{1}{dt} \begin{bmatrix} \tilde{\varphi}_{i+1} - \tilde{\varphi}_i \\ \tilde{\theta}_{i+1} - \tilde{\theta}_i \\ \tilde{\psi}_{i+1} - \tilde{\psi}_i \end{bmatrix}, i = 0,...,n \tag{12}$$

Figure 6 shows trajectories 2, 3, and 4 (trajectory 1 is the same as trajectory 2) as well as the magnet (blue square), which was positioned in the experiment area. The colormap represents the magnitude of the deviation vector $\Delta\mathbf{m}^B = \mathbf{m}^B - \tilde{\mathbf{R}}_N^B \mathbf{h}^N$, computed from trajectory 2 by two-dimensional interpolation. Trajectory 1 was obtained in the same manner as trajectory 2 but without the magnet. Each phone is rotated around its three main axes to trigger the hard-iron bias calibration before trajectory 1 begins. We use a magnet with a known position to have at least one magnetic anomaly influencing the magnetometer observations. As shown in Figure 6, there is another magnetic anomaly present in the upper right region of the experiment area. This pattern could be reproduced with each phone for trajectories 1, 2, and 4 (at the beginning of the trajectory).
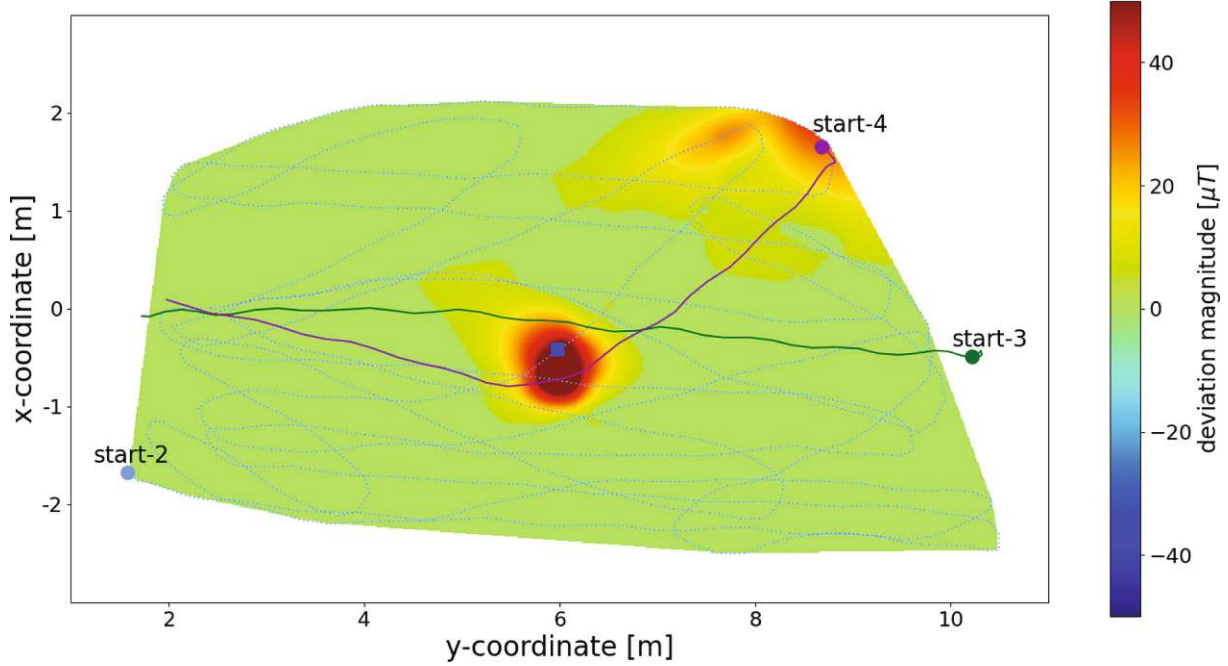
FIGURE 6 Trajectories 2, 3, and 4 plotted on a colormap representing the magnitude of the deviation vector $\Delta\mathbf{m}^B$
Trajectory 1 is not plotted, as it is nearly the same as trajectory 2. The blue square represents the magnet, which is positioned in the experiment area.

We compute the Euler angles for all 12 trajectories with the proposed OEA. To initialize the Euler angles, we compute φ and θ with $\mathbf{a}^B$ at time $k = 0$ (Appendix A), and $\psi_0 = \tilde{\psi}_0$ is derived from Equation (11) via the laser tracker measurements. Figure 7 (top) shows the deviations of the computed EMF in the B-frame with respect to the known values for the LGE Nexus 5X and trajectory 2. Figure 7 (bottom) presents the deviations of the computed Euler angles from the corresponding known quantities. The influence of the magnet and the anomaly in the upper right region of the experiment area on the components of $\mathbf{h}^B$ (and therefore on ψ) is very weak. Noticeable deviations of up to $25°$ occur in a few cases (e.g., after the initial check with Equation (9) and approximately $110\,s$), but they rapidly decrease to zero. The deviations of φ and θ basically have a zero mean, with a maximum of $\pm 7°$.

We use three algorithms for comparison: the complementary filter from Madgwick et al. (2011) (called Madgwick or "madgw" in some plots), the EKF from Renaudin & Combettes (2014) (called Magyq), and the EKF from Han et al. (2017) (called Han). Madgwick and Magyq fuse $\mathbf{a}^B, \mathbf{m}^B$, and $\boldsymbol{\omega}^B$ in one algorithm and deliver the quaternion, which describes the 3D rotation from the N-frame into the B-frame. Thus, in contrast to the algorithm proposed herein, the computations of the inclination and heading component are not totally separated in these two approaches. Han does not estimate orientation parameters; instead, it estimates the EMF in the B-frame $\mathbf{h}^B$ together with a magnetometer bias and symmetric matrix elements subsuming $\boldsymbol{\Delta}_{sn}$ and $\boldsymbol{\Delta}_{si}$. The estimation of the EMF (implicitly containing the heading information) and two categories of systematic deviations is the main difference of the proposed algorithm, which has minimal parameterization in the bias-EKF. The inclination angles are computed in the same way for the Han algorithm as in the proposed algorithm. We use these three algorithms to compute φ, θ, and ψ for all trajectories.
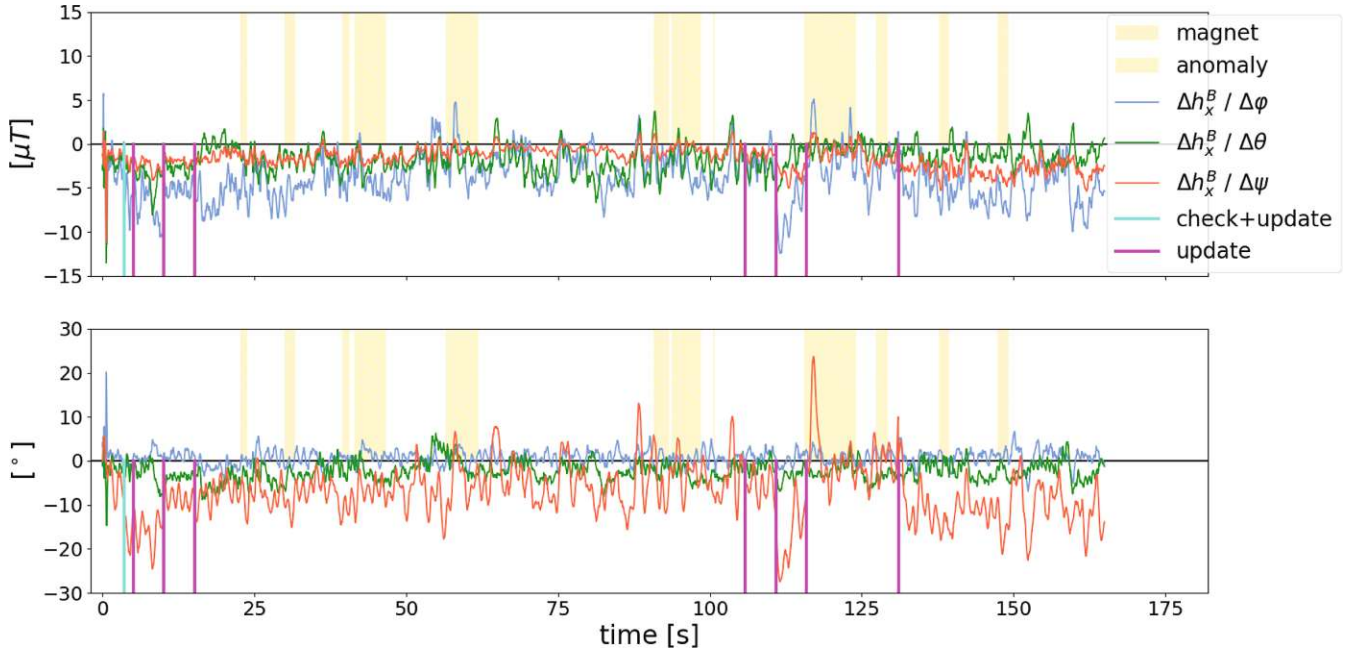
FIGURE 7 Deviations of $\mathbf{h}^B$ (top) and φ, θ, ψ (bottom) for trajectory 2 and LGE Nexus 5X The durations for which the phone is closer than $1.0\,m$ to the magnet are marked in orange (denoted "magnet" in the legend), and those for which the phone is closer than $2.0\,m$ to the anomaly in the upper right region of the experiment area are marked in yellow (denoted "anomaly" in the legend). The turquoise line marks the initial check with Equation (9), and the purple lines mark the updates of ψ_κ with Equation (8).

Each algorithm has at least one variable that can be used for tuning. We attempted to optimize the algorithms on the basis of the root mean square error (RMSE) of the computed heading. In the Madgwick algorithm, the maximum gyroscope measurement error can be adjusted; we set this term to $0.01°/s$. Renaudin & Combettes (2014) estimated the accelerometer bias (beside the orientation quaternion $\mathbf{q}$ and the gyroscope quaternion bias $\mathbf{q}_{b,\omega}$), which we omit herein. Thus, there are two system noise components for $\mathbf{q}$ and $\mathbf{q}_{b,\omega}$, whose standard deviations are set to $\sigma_q = 0.001$ and $\sigma_{q,\omega} = 0.001\,s^{-1}$. Additionally, Magyq performs static period detection and outlier rejection of $\mathbf{a}^B$ and $\mathbf{m}^B$ by comparing their magnitudes with the nominal values. The number of observations ($\mathbf{a}^B$ and $\mathbf{m}^B$) used for static period detection is set to 20, and the corresponding thresholds are set to $\gamma_{1,a} = 0.3\,m/s^2$ and $\gamma_{1,m} = 1.0\,\mu T$. The thresholds for outlier rejection are set to $\gamma_{2,a} = 1.0\,m/s^2$ and $\gamma_{2,m} = 3.0\,\mu T$. Han provides one tuning variable, which is a dimensionless multiplier for controlling the influence of the system noise; this term is set to 100.0.

The resulting deviations $\Delta\psi$ are shown in Figure 8, and the respective RMSE values are given in Appendix B (Table B1). Madgwick performs best in trajectory 3, which exhibits the most preferable properties (no anomaly in the beginning and short duration of only $12\,s$). The results from the other trajectories are significantly worse. For Han, the results from trajectory 1 (without the magnet) are clearly better than those for the other three trajectories. In the provided experimental setup, heavy magnetic anomalies cannot be reasonably estimated by using functional models containing several parameters for systematic deviations (i.e., bias and symmetric matrix). Due to the very low standard deviations of the system noise obtained when using Magyq, this algorithm performs better in the short trajectories 3 and 4. Trajectory 1 contains only two very high RMSE values for the Samsung Galaxy S7 and LGE Nexus 5X. If one neglected these two values, the
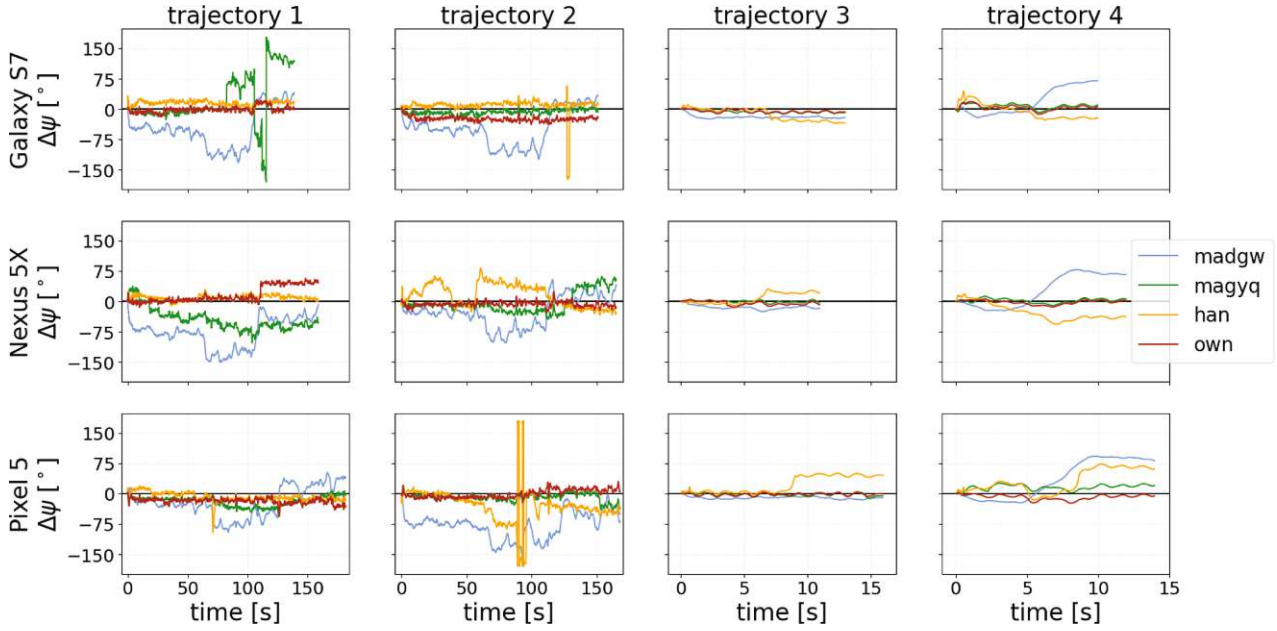
FIGURE 8 Deviation of the smartphone heading computed from the known quantities $\Delta\psi$ for all trajectories, phones, and algorithms

TABLE 3
RMSE Values of Euler Angles Over All Trajectories and Phones in [°]
Han and the proposed OEA use the same inclination computation procedure. Thus, these algorithms have the same RMSE values for φ and θ.

	Madgwick	Magyq	Han	Proposed OEA
RMSE φ	7.0	31.4	1.7	1.7
RMSE θ	9.7	13.6	2.6	2.6
RMSE ψ	65.8	36.5	29.2	17.4

overall RMSE would be very close to that of the proposed OEA. The drawback of Magyq (and therefore of all algorithms that compute the 3D orientation within one EKF) is that the magnetic anomalies also influence the inclination angles (see Table 3). Because Madgwick is based on a complementary filter, the RMSE values of the inclination angles are considerably smaller, even if all smartphone observations are fused in one algorithm. The proposed OEA delivers the lowest RMSE for the computed heading given an unbiased value of ψ_0 (Table 3).

We perform the evaluations again for biased values of ψ_0, as shown in Figure 9, where $\Delta\psi_0$ is the deviation from the correct value. The RMSE values are computed for each value $\Delta\psi_0$ in the same way as in Table 3. Over the whole range of $\Delta\psi_0$, the proposed OEA delivers the lowest RMSE values of the computed heading on average (with worse performance toward $\Delta\psi_0 = -90°$ compared with the other algorithms). It is counterintuitive that the minima of the graphs are not exactly at the correct value of ψ_0 (i.e., $\Delta\psi_0 = 0°$). Our explanation is that the shift in ψ_0 partially compensates for systematic deviations contained in the magnetometer observations. The low variation in headings when the magnet is passed leads to additional experiment-specific effects because the summation of the magnetic anomaly and sensor-related biases is similar for all trajectories. Still, this experiment with high-accuracy ground truth values for 3D orientation reveals the potential of the proposed OEA within smartphone or pedestrian localization systems.
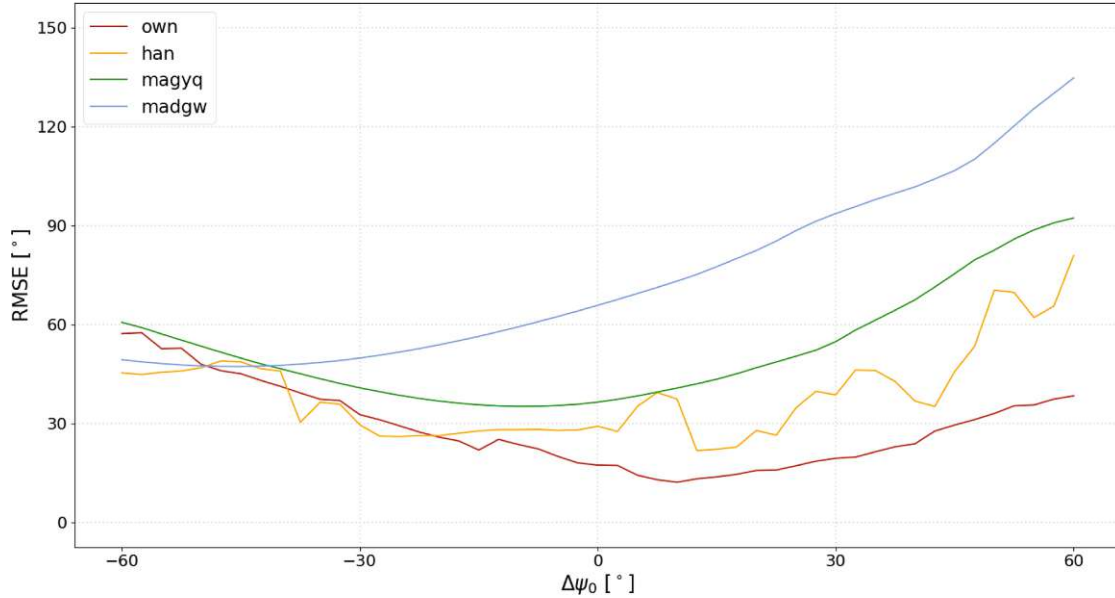
FIGURE 9 RMSE values of the computed heading for a biased initial heading

4 | CONCLUSION

We developed an OEA that provides the absolute 3D orientation of a consumer-grade device such as a smartphone. The proposed OEA exhibits the following properties:

- reliable detection of magnetic anomalies,
- fast convergence of the estimated bias back to the correct value after a magnetic anomaly is passed, and
- minimal/reduced influence of magnetic anomalies on the computed heading.

The limiting condition is that magnetometer observations that are free from systematic deviations must be available for at least certain time spans of the trajectory. Otherwise, the heading determination can only be performed in a relative manner by using the gyroscope or additional information from other sensors. We validated and analyzed the proposed OEA by using numerical simulations. We modeled magnetic anomalies, sensor biases, and two levels of accuracy of the initial heading in different scenarios. The scenarios with problematic conditions in the initialization phase of the proposed OEA led to slightly worse results. Nevertheless, the proposed OEA provides an estimated smartphone orientation with low deviation from the correct value.

We evaluated the performance of the proposed OEA based on experiments with high-accuracy ground truth values for 3D smartphone orientation. The proposed OEA was compared with three other algorithms from the literature that also use a magnetometer. If the initial heading is unbiased, the RMSE of the computed heading is 40% lower for the proposed OEA compared with the "second-best" algorithm over all trajectories (Tables 3 and B1). For a wide range of biased initial headings, the proposed OEA also delivers the lowest RMSE values for the computed heading (Figure 9). Although these small-scale experiments with laboratory conditions exhibit some limitations, the results indicate that the proposed OEA has potential to be included in positioning systems. In future work, the performance must be

evaluated in large-scale experiments with diverse data (more DoFs in the trajectories, multiple users, more smartphone holding modes, etc.). A by-product of the proposed OEA with a potentially high benefit is a global test for magnetic anomaly detection. This approach can be used to detect and locate magnetic anomalies, which can be used as features to aid in indoor positioning, e.g., with fingerprinting.

REFERENCES

Afzal, M. H. (2011). *Use of earth's magnetic field for pedestrian navigation* [Unpublished doctoral dissertation]. Department of Geomatics Engineering, University of Calgary.

Afzal, M. H., Renaudin, V., & Lachapelle, G. (2011). Magnetic field based heading estimation for pedestrian navigation environments. *Proc. of the 2011 International Conference on Indoor Positioning and Indoor Navigation (IPIN),* Guimaraes, Portugal, 1–10. https://www.doi.org/10.1109/IPIN.2011.6071947

Burgess, T., Metzler, B., Ettlinger, A., & Neuner, H. (2018). Geometric constraint model and mobility graphs for building utilization intelligence. *Proc. of the 2018 International Conference on Indoor Positioning and Indoor Navigation (IPIN),* Nantes, France, 1–7. https://www.doi.org/10.1109/IPIN.2018.8533726

Costanzi, R., Fanelli, F., Monni, N., Ridolfi, A., & Allotta, B. (2016). An attitude estimation algorithm for mobile robots under unknown magnetic disturbances. *IEEE/ASME Transactions on Mechatronics*, *21*(4), 1900–1911. https://www.doi.org/10.1109/TMECH.2016.2559941

Crassidis, J., Lai, K.-L., & Harman, R. R. (2005). Real-time attitude-independent three-axis magnetometer calibration. *Journal of Guidance, Control and Dynamics*, *28*(1), 115–120. https://www.doi.org/10.2514/1.6278

Ehrlich, C. R., & Blankenbach, J. (2018). Pedestrian localisation inside buildings based on multi-sensor smartphones. *Proc. of the2018 Ubiquitous Positioning, Indoor Navigation and Location-Based Services (UPINLBS),* Wuhan, China, 1–10. https://www.doi.org/10.1109/UPINLBS.2018.8559699

Ettlinger, A., Neuner, H., & Burgess, T. (2018). Development of a Kalman filter in the Gauss-Helmert model for reliability analysis in orientation determination with smartphone sensors. *Sensors*, *18*(2), 414. https://www.doi.org/10.3390/s18020414

Gebre-Egziabher, D., Elkaim, G. H., Powell, D. J., & Parkinson, B. W. (2006). Calibration of strapdown magnetometers in magnetic field domain. *Journal of Aerospace Engineering*, *19*(2), 1–16. https://www.doi.org/10.1061/(ASCE)0893-1321(2006)19:2(87)

Gebre-Egziabher, D., Hayward, R. C., & Powell, D. J. (2004). Design of multi-sensor attitude determination systems. *IEEE Transactions on Aerospace and Electronic Systems*, *40*(2), 627–649. https://www.doi.org/10.1109/TAES.2004.1310010

Groves, P. D. (2013). *Principles of GNSS, Inertial and Multisensor Integrated Navigation Systems* (2nd ed.). Artech House.

Han, K., Han, H., Wang, Z., & Xu, F. (2017). Extended Kalman filter-based gyroscope-aided magnetomter calibration for consumer electronics. *IEEE Sensors Journal*, *17*(1), 63–71. https://www.doi.org/10.1109/JSEN.2016.2624821

Han, S., & Wang, J. (2011). A novel method to integrate IMU and magnetometers in attitude and heading reference systems. *The Journal of Navigation*, *64*(4), 727–738. https://www.doi.org/10.1017/S0373463311000233

Hostettler, R., & Särkkä, S. (2016). IMU and magnetometer modeling for smartphone-based PDR. *Proc. of the 2016 International Conference on Indoor Positioning and Indoor Navigation (IPIN),* Alcala de Henares, Spain, 1–8. https://www.doi.org/10.1109/IPIN.2016.7743695

Kanda, T., Shiomi, M., Perrin, L., Nomura, T., Ishiguro, H., & Hagita, N. (2007). Analysis of people trajectories with ubiquitous sensors in a science museum. *Proc. of the 2007 IEEE Conference on Robotics and Automation,* Rome, Italy, 4846–4853. https://www.doi.org/10.1109/ROBOT.2007.364226

Klingbeil, L., Eling, C., Zimmermann, F., & Kuhlmann, H. (2014). Magnetic field sensor calibration for attitude determination. *Journal of Applied Geodesy*, *8*(2), 97–108. https://www.doi.org/10.1515/jag-2014-0003

Lee, J., Lim, J., & Lee, J. (2018). Compensated heading angles for outdoor mobile robots in magnetically disturbed environment. *IEEE Transactions on Industrial Electronics*, *65*(2), 1408–1419. https://www.doi.org/10.1109/TIE.2017.2726958

Madgwick, S. O., Harrison, A. J., & Vaidyanathan, R. (2011). Estimation of IMU and MARG orientation using a gradient descent algorithm. *Proc. of the 2011 IEEE International Conference on Rehabilitation Robotics*, Zurich, Switzerland, 1–7. https://www.doi.org/10.1109/ICORR.2011.5975346

Martin, H., Groves, P., & Newman, M. (2016). The limits of in-run calibration of MEMS inertial sensors and sensor arrays. *NAVIGATION*, *63*(2), 127–143. https://www.doi.org/10.1002/navi.135

Moder, T., Reitbauer, C., Wisiol, K. M., Wilfinger, R., & Wieser, M. (2018). An indoor positioning and navigation application for visually impaired people using public transport. *Proc. of the 2018 International Conference on Indoor Positioning and Indoor Navigation (IPIN),* Nantes, France, 1–7. https://www.doi.org/10.1109/IPIN.2018.8533747

Renaudin, V., Afzal, M. H., & Lachapelle, G. (2010). Complete triaxis magnetometer calibration in the magnetic domain. *Journal of Sensors*, *2010*. https://www.doi.org/10.1155/2010/967245

Renaudin, V., & Combettes, C. (2014). Magnetic, acceleration fields and gyroscope quaternion (MAGYQ)-based attitude estimation with smartphone sensors for indoor pedestrian navigation. *Sensors*, *14*(12), 22864–22890. https://www.doi.org/10.3390/s141222864

Särkkä, S., Tolvanen, V., Kannala, J., & Rahtu, E. (2015). Adaptive Kalman filtering and smoothing for gravitation tracking in mobile systems. *Proc. of the 2015 International Conference on Indoor Positioning and Indoor Navigation (IPIN),* Banff, AB, Canada, 1–7. https://www.doi.org/10.1109/IPIN.2015.7346762

Titterton, D., & Weston, J. (2004). *Strapdown inertial navigation technology* (2nd ed., Vol. 17). Institution of Engineering and Technology.

Valenti, R. G., Dryanovski, I., & Xiao, J. (2015). Keeping a good attitude: a quaternion-based orientation filter for IMUs and MARGs. *Sensors*, *15*(15), 19302–19330. https://www.doi.org/10.3390/s150819302

Vasconcelos, J. F., Elkaim, G. H., Silvestre, C., Oliveira, P., & Cardeira, B. (2011). Geometric approach to strapdown magnetometer calibration in sensor frame. *IEEE Transactions on Aerospace and Electronic Systems*, *47*(2), 1293–1306. https://www.doi.org/10.1109/TAES.2011.5751259

Vogel, S., Alkhatib, H., & Neumann, I. (2018). Iterated extended Kalman filter with implicit measurement equation and nonlinear constraints for information-based georeferencing. *Proc. of the 2018 21st International Conference on Information Fusion (FUSION),* Cambridge, UK, 1209–1216. https://www.doi.org/10.23919/ICIF.2018.8455258

APPENDIX

A | INCLINATION-EKF

In the inclination-EKF, the gravity vector in the B-frame $\hat{\mathbf{g}}^B$ is estimated; this vector is used later to compute φ and θ. $\mathbf{a}^B$ and $\boldsymbol{\omega}^B$ are smartphone sensor observations utilized as input in the inclination-EKF, in which the calibrated values delivered by the smartphone are used. $\boldsymbol{\omega}^B$ is the control input in the prediction of $\overline{\mathbf{g}}^B$:

$$\overline{\mathbf{g}}^B = (\mathbf{I} + \sin(dt\,\|\boldsymbol{\omega}^B\|) \cdot \boldsymbol{\Omega} + (1 - \cos(dt\,\|\boldsymbol{\omega}^B\|)) \cdot \boldsymbol{\Omega}^2) \cdot \hat{\mathbf{g}}_{k-1}^B + \boldsymbol{\zeta}_g$$

$$\text{with } \boldsymbol{\Omega} = \frac{1}{\|\boldsymbol{\omega}^B\|} \begin{bmatrix} 0 & \omega_y^B & -\omega_y^B \\ -\omega_z^B & 0 & \omega_x^B \\ \omega_y^B & -\omega_x^B & 0 \end{bmatrix}$$

and $\boldsymbol{\zeta}_g$ is the system noise of $\overline{\mathbf{g}}^B$.

The state vector of the inclination-EKF also contains stochastic resonators (Hostettler & Särkkä, 2016; Särkkä et al., 2015), which compensate for accelerations due to user motion. We include resonators for stride $a_{i,str}^B$, $\dot{a}_{i,str}^B$, $i = x, y, z$ and

step acceleration $a_{i,stp}^B, \dot{a}_{i,stp}^B, i = x, y, z$ for each coordinate axis (where $\dot{a}_{i,j}^B$ are the corresponding derivatives). These terms are propagated as follows:

$$\begin{bmatrix} \bar{a}_{i,str}^B \\ \bar{\dot{a}}_{i,str}^B \end{bmatrix} = \begin{bmatrix} \cos(f_0 \cdot dt) & \sin(f_0 \cdot dt) \\ -\sin(f_0 \cdot dt) & \cos(f_0 \cdot dt) \end{bmatrix} \begin{bmatrix} \hat{a}_{i,str,k-1}^B \\ \hat{a}_{i,str,k-1}^B \end{bmatrix} + \begin{bmatrix} \zeta_{a,i,str} \\ \zeta_{\dot{a},i,str} \end{bmatrix}$$

$$\begin{bmatrix} \bar{a}_{i,stp}^B \\ \bar{\dot{a}}_{i,stp}^B \end{bmatrix} = \begin{bmatrix} \cos(2f_0 \cdot dt) & \sin(2f_0 \cdot dt) \\ -\sin(2f_0 \cdot dt) & \cos(2f_0 \cdot dt) \end{bmatrix} \begin{bmatrix} \hat{a}_{i,stp,k-1}^B \\ \hat{a}_{i,stp,k-1}^B \end{bmatrix} + \begin{bmatrix} \zeta_{a,i,stp} \\ \zeta_{\dot{a},i,stp} \end{bmatrix}$$

$$i = x, y, z$$

where f_0 is the base frequency, which we set to the stride frequency, and the ζ terms are the system noise components of the stochastic resonators.

$\mathbf{a}^B$ equals the observation vector in the filter update (i.e., measurement equation) for computing the filter innovations:

$$\mathbf{w}_I = \mathbf{a}^B - \bar{\mathbf{g}}^B - \bar{\mathbf{a}}_{str}^B - \bar{\mathbf{a}}_{stp}^B$$

In the Euler angle representation, the roll angle φ and pitch angle θ describe the inclination; these terms are computed from $\hat{\mathbf{g}}^B$ as follows:

$$\varphi = \arctan(\frac{\hat{g}_y^B}{\hat{g}_z^B})$$

$$\theta = \arctan(\frac{-\hat{g}_x^B}{\hat{g}_y^B \cdot \sin\varphi + \hat{g}_z^B \cdot \cos\varphi})$$

The angular velocity around the z-axis of the L-frame or N-frame is computed as follows:

$$\dot{\psi} = \frac{1}{\cos\theta}(\omega_y^B \cdot \sin\varphi + \omega_z^B \cdot \cos\varphi)$$

To avoid the gimbal-lock problem $(\theta = \pm\frac{\pi}{2})$, one can also derive the orientation quaternion from $\hat{\mathbf{g}}^B$ (Valenti et al., 2015), which describes the same rotation as φ and θ. The gimbal-lock problem does not appear in the simulation study in Section 3.1 or in the experiments in Section 3.2; thus, we utilized only the Euler angle representation.

B | ADDITIONAL MATERIAL

TABLE B1
RMSE Values of Computed Heading in [°]
The RMSE per trajectory was computed by using the deviations of all phones and one trajectory, and the RMSE per phone was computed by using the deviations of all trajectories and one phone. The bold RMSE numbers were computed from the deviations over all phones and trajectories.

	Samsung Galaxy S7	LGE Nexus 5X	Google Pixel 5	RMSE per trajectory
		Madgwick		
trj-1	68.5	86.5	43.6	67.5
trj-2	64.6	45.9	85.9	67.7
trj-3	20.1	15.7	10.9	15.7
trj-4	38.5	47.7	58.2	49.9
RMSE per phone	64.5	67.2	65.6	**65.8** (overall RMSE)

(Continued)

TABLE B1 (*Continued*)

	Samsung Galaxy S7	LGE Nexus 5X	Google Pixel 5	RMSE per trajectory
Magyq				
trj-1	70.6	52.5	22.8	50.5
trj-2	9.2	25.8	13.4	17.8
trj-3	7.5	2.7	4.4	5.3
trj-4	9.4	5.5	16.8	12.0
RMSE per phone	47.5	39.8	18.4	**36.5** (overall RMSE)
Han				
trj-1	16.1	11.0	14.3	13.8
trj-2	25.0	32.2	52.5	38.8
trj-3	20.1	15.2	30.4	23.8
trj-4	19.4	33.4	42.1	34.1
RMSE per phone	21.1	24.4	37.7	**29.2** (overall RMSE)
Proposed OEA				
trj-1	7.8	25.7	19.8	19.6
trj-2	25.0	9.4	10.2	16.2
trj-3	6.7	6.8	3.6	5.7
trj-4	7.8	5.8	10.7	8.5
RMSE per phone	18.3	18.7	15.4	**17.4** (overall RMSE)

TABLE B2
Symbols Introduced in Sections 2 and 3

	sensor observations and rotations
$\boldsymbol{\omega}^B$	gyroscope observations in the B-frame
$\mathbf{a}^B$	accelerometer observations in the B-frame
$\mathbf{m}^B$	magnetometer observations in the B-frame
$\dot{\psi}$	angular rate around the z-axis of the N- or L-frame
$\mathbf{g}^N$	gravity vector in the N-frame
$\mathbf{h}^N$	EMF vector in the N-frame
h_D	magnetic declination
φ, θ, ψ	Euler angles roll, pitch, and yaw describing rotation from N- into the B-frame
$\mathbf{R}_N^B$	rotation matrix describing rotation from N- into the B-frame
ϵ	sensor white noise (index marks sensor)
σ	standard deviation of white noise component (index marks quantity)
	heading propagation
ψ_0	initial heading
ψ_κ	last updated absolute heading
$d\psi_{\kappa|k}$	accumulated heading change
k or κ	time indices indicating epochs or timestamps
dt	time interval
	bias-EKF
$\boldsymbol{\Delta}_{sn}$	matrix representing sensor scale and non-orthogonality of magnetometer
$\boldsymbol{\Delta}_{si}$	matrix representing soft-iron effects of platform in the magnetometer
$\boldsymbol{\delta}_a^N$	vector representing magnetic anomalies
$\boldsymbol{\delta}_{hi}^B$	vector representing hard-iron effects of platform in the magnetometer

(*Continued*)

TABLE B2 (*Continued*)

$\boldsymbol{\delta}_b^B$	vector representing sensor bias of the magnetometer
$\boldsymbol{\delta}_s^B$	vector subsuming slow-varying systematic deviations of the magnetometer
$\boldsymbol{\delta}_f^B$	vector subsuming fast-varying systematic deviations of the magnetometer
$\bar{\boldsymbol{\delta}}_s^B, \hat{\boldsymbol{\delta}}_s^B$	predicted and estimated $\boldsymbol{\delta}_s^B$ (EKF)
$\boldsymbol{\zeta}_\delta$	system noise of $\bar{\boldsymbol{\delta}}_s^B$ (EKF)
$\mathbf{w}_m$	filter innovation of bias-EKF
$\hat{\mathbf{v}}, \Sigma_{\hat{\mathbf{v}}}$	EKF residuals (index marks quantity) with VCM
$T_G,\ T_{G,c}(\alpha)$	global test value and its critical value
α	type I error of global test
χ_3^2	chi-square distribution (index indicates three DoFs)
λ	non-centrality parameter of chi-square distribution
$H_0,\ H_A$	null and alternative hypothesis
$E\{\}$	expectation of random variable
heading update	
$dt_{W,u},\ n_{W,u}$	length of time window for updating ψ and number of values contained
$dt_{W,0},\ n_{W,0}$	length of time window for controlling ψ_0 and number of values contained
$n_T,\ p_T$	number of $T_{G,i}$ values exceeding $T_{G,c}(\alpha)$ and corresponding percentage
$n_m,\ p_m$	number of $\mathbf{m}_i^L$ fulfilling conditions c_1 and c_2 and corresponding percentage
c_1	condition that the magnitudes of $\mathbf{m}_i^L$ and $\mathbf{h}^N$ must be the same
c_2	condition that the vertical components of $\mathbf{m}_i^L$ and $\mathbf{h}^N$ must be the same
$\gamma_{d\psi}$	preset threshold of maximum heading change in time window
γ_ψ	preset threshold for difference in propagated and magnetometer heading
γ_m	preset threshold of $\mathbf{m}_i^L$ values that must fulfill c_1 and c_2
$\gamma_{\sigma m}$	preset multiplier for σ_m acting as a threshold for c_1 and c_2

B   List of other publications

[B1] Andreas Ettlinger and Günther Retscher. Positioning using ambient magnetic fields in combination with Wi-Fi and RFID. IN *2016 International Conference on Indoor Positioning and Indoor Navigation*, Alcala de Henares, Madrid, Spain, 2016. IEEE, Piscataway, New Jersey, USA.

[B2] Vasillis Gikas, Andreas Dimitratos, Harris Perakis, Günther Retscher and Andreas Ettlinger. Full-scale testing and performance evaluation of an active RFID system for positioning and personal mobility. IN *2016 International Conference on Indoor Positioning and Indoor Navigation*, Alcala de Henares, Madrid, Spain, 2016. IEEE, Piscataway, New Jersey, USA.

[B3] Andreas Ettlinger, Hans Neuner and Thomas Burgess. Smartphone sensor-based orientation determination for indoor-navigation. In Georg Gartner and Haosheng Huag, editors, *Progress in Location-Based Services 2016*. Springer, Berlin, Germany, 2017.

[B4] Andreas Ettlinger, Hans Neuner and Thomas Burgess. Orientierungsberechnung mit Smartphone-Sensoren. *AVN - Allgemeine Vermessungs Nachrichten*, 2018(4):91-104, 2018.

[B5] Thomas Burgess, Barbara Metzler, Andreas Ettlinger and Hans Nuner. Geometric constraint model and mobility graphs for building utilization intelligence. In *2018 International Conference on Indoor Positioning and Indoor Navigation*, Nantes, France, 2018. IEEE, Piscataway, New Jersey, USA.

[B6] David Rejchrt, Tomas Thalmann, Andreas Ettlinger and Hans Neuner. Robot operating system - a modular and flexible framework for geodetic multi-sensor systems. *AVN - Allgemeine Vermessungs Nachrichten*, 2019(6):173-180, 2019.

C Supplementary material

C.1 Solution of the alternative hypothesis model in the GHM

First, the solutions for the overall parameter vector $d\hat{\mathbf{x}}_O$ and its cofactor matrix $\mathbf{Q}_{\hat{x}\hat{x},O}$ are derived in the model of H_A

$$\mathbf{Q}_{\hat{x}\hat{x},O} = (\mathbf{A}_O^T \mathbf{Q}_{ww}^{-1} \mathbf{A}_O)^{-1} = (\begin{bmatrix} \mathbf{A}^T \\ \mathbf{C}^T\mathbf{B}^T \end{bmatrix} \mathbf{Q}_{ww}^{-1} \begin{bmatrix} \mathbf{A} & \mathbf{BC} \end{bmatrix})^{-1}$$

$$= \begin{bmatrix} \mathbf{A}^T\mathbf{Q}_{ww}^{-1}\mathbf{A} & \mathbf{A}^T\mathbf{Q}_{ww}^{-1}\mathbf{BC} \\ \mathbf{C}^T\mathbf{B}^T\mathbf{Q}_{ww}^{-1}\mathbf{A} & \mathbf{C}^T\mathbf{B}^T\mathbf{Q}_{ww}^{-1}\mathbf{BC} \end{bmatrix}^{-1}$$

$$= \begin{bmatrix} \mathbf{Q}_{\hat{x}\hat{x}} + \mathbf{Q}_{\hat{x}\hat{x}}\mathbf{A}^T\mathbf{Q}_{ww}^{-1}\mathbf{BC}\mathbf{Q}_{\hat{\nabla}\hat{\nabla}}\mathbf{C}^T\mathbf{B}^T\mathbf{Q}_{ww}^{-1}\mathbf{A}\mathbf{Q}_{\hat{x}\hat{x}} & -\mathbf{Q}_{\hat{x}\hat{x}}\mathbf{A}^T\mathbf{Q}_{ww}^{-1}\mathbf{BC}\mathbf{Q}_{\hat{\nabla}\hat{\nabla}} \\ -\mathbf{Q}_{\hat{\nabla}\hat{\nabla}}\mathbf{C}^T\mathbf{B}^T\mathbf{Q}_{ww}^{-1}\mathbf{A}\mathbf{Q}_{\hat{x}\hat{x}} & (\mathbf{C}^T\mathbf{B}^T\mathbf{Q}_{ww}^{-1}\mathbf{BC} - \mathbf{C}^T\mathbf{B}^T\mathbf{Q}_{ww}^{-1}\mathbf{A}\mathbf{Q}_{\hat{x}\hat{x}}\mathbf{A}^T\mathbf{Q}_{ww}^{-1}\mathbf{BC})^{-1} \end{bmatrix}$$

$$= \begin{bmatrix} \mathbf{Q}_{\hat{x}\hat{x}} + \mathbf{A}^+\mathbf{BC}\mathbf{Q}_{\hat{\nabla}\hat{\nabla}}\mathbf{C}^T\mathbf{B}^T(\mathbf{A}^+)^T & -\mathbf{A}^+\mathbf{BC}\mathbf{Q}_{\hat{\nabla}\hat{\nabla}} \\ -\mathbf{Q}_{\hat{\nabla}\hat{\nabla}}\mathbf{C}^T\mathbf{B}^T(\mathbf{A}^+)^T & (\mathbf{C}^T\mathbf{Q}_{ll}^{-1}\mathbf{B}^+(\mathbf{Q}_{ww} - \mathbf{A}\mathbf{Q}_{\hat{x}\hat{x}}\mathbf{A}^T)(\mathbf{B}^+)^T\mathbf{Q}_{ll}^{-1}\mathbf{C})^{-1} \end{bmatrix}$$

$$= \begin{bmatrix} \mathbf{Q}_{\hat{x}\hat{x}} + \mathbf{A}^+\mathbf{BC}\mathbf{Q}_{\hat{\nabla}\hat{\nabla}}\mathbf{C}^T\mathbf{B}^T(\mathbf{A}^+)^T & -\mathbf{A}^+\mathbf{BC}\mathbf{Q}_{\hat{\nabla}\hat{\nabla}} \\ -\mathbf{Q}_{\hat{\nabla}\hat{\nabla}}\mathbf{C}^T\mathbf{B}^T(\mathbf{A}^+)^T & (\mathbf{C}^T\mathbf{Q}_{ll}^{-1}\mathbf{Q}_{\hat{v}\hat{v}}\mathbf{Q}_{ll}^{-1}\mathbf{C})^{-1} \end{bmatrix}$$

$$= \begin{bmatrix} \mathbf{Q}_{\hat{x}\hat{x},A} & \mathbf{Q}_{\hat{x}\hat{\nabla}} \\ \mathbf{Q}_{\hat{x}\hat{\nabla}}^T & \mathbf{Q}_{\hat{\nabla}\hat{\nabla}} \end{bmatrix}$$

$$d\hat{\mathbf{x}}_O = -\mathbf{Q}_{\hat{x}\hat{x},O} \begin{bmatrix} \mathbf{A}^T \\ \mathbf{C}^T\mathbf{B}^T \end{bmatrix} \mathbf{Q}_{ww}^{-1}\mathbf{w}$$

$$= \begin{bmatrix} d\hat{\mathbf{x}} - \mathbf{A}^+\mathbf{BC}\mathbf{Q}_{\hat{\nabla}\hat{\nabla}}\mathbf{C}^T\mathbf{B}^T(\mathbf{A}^+)^T\mathbf{A}^T\mathbf{Q}_{ww}^{-1} + \mathbf{A}^+\mathbf{BC}\mathbf{Q}_{\hat{\nabla}\hat{\nabla}}\mathbf{C}^T\mathbf{B}^T\mathbf{Q}_{ww}^{-1})\mathbf{w} \\ -(\mathbf{Q}_{\hat{\nabla}\hat{\nabla}}\mathbf{C}^T\mathbf{B}^T\mathbf{Q}_{ww}^{-1} - \mathbf{Q}_{\hat{\nabla}\hat{\nabla}}\mathbf{C}^T\mathbf{B}^T(\mathbf{A}^+)^T\mathbf{A}^T\mathbf{Q}_{ww}^{-1})\mathbf{w} \end{bmatrix}$$

$$= \begin{bmatrix} d\hat{\mathbf{x}} + \mathbf{A}^+\mathbf{BC}\mathbf{Q}_{\hat{\nabla}\hat{\nabla}}\mathbf{C}^T\mathbf{B}^T\mathbf{Q}_{ww}^{-1}(\mathbf{I} - \mathbf{A}\mathbf{A}^+)\mathbf{w} \\ -\mathbf{Q}_{\hat{\nabla}\hat{\nabla}}\mathbf{C}^T\mathbf{Q}_{ll}^{-1}\mathbf{B}^+(\mathbf{I} - \mathbf{A}\mathbf{A}^+)\mathbf{w} \end{bmatrix} = \begin{bmatrix} d\hat{\mathbf{x}} - \mathbf{A}^+\mathbf{BC}\mathbf{Q}_{\hat{\nabla}\hat{\nabla}}\mathbf{C}^T\mathbf{Q}_{ll}^{-1}\hat{\mathbf{v}} \\ \mathbf{Q}_{\hat{\nabla}\hat{\nabla}}\mathbf{C}^T\mathbf{Q}_{ll}^{-1}\hat{\mathbf{v}} \end{bmatrix}$$

$$= \begin{bmatrix} d\hat{\mathbf{x}} - \mathbf{A}^+\mathbf{BC}d\hat{\mathbf{\nabla}} \\ d\hat{\mathbf{\nabla}} \end{bmatrix} = \begin{bmatrix} d\hat{\mathbf{x}}_A \\ d\hat{\mathbf{\nabla}} \end{bmatrix}$$

where the identities $\begin{bmatrix} \mathbf{D} & \mathbf{E} \\ \mathbf{F} & \mathbf{G} \end{bmatrix}^{-1} = \begin{bmatrix} \mathbf{D}^{-1} + \mathbf{D}^{-1}\mathbf{E}(\mathbf{G} - \mathbf{F}\mathbf{D}^{-1}\mathbf{E})^{-1}\mathbf{F}\mathbf{D}^{-1} & -\mathbf{D}^{-1}\mathbf{E}(\mathbf{G} - \mathbf{F}\mathbf{D}^{-1}\mathbf{E})^{-1} \\ -(\mathbf{G} - \mathbf{F}\mathbf{D}^{-1}\mathbf{E})^{-1}\mathbf{F}\mathbf{D}^{-1} & (\mathbf{G} - \mathbf{F}\mathbf{D}^{-1}\mathbf{E})^{-1} \end{bmatrix}$

and $(\mathbf{A}^+)^T\mathbf{A}^T\mathbf{Q}_{ww}^{-1} = \mathbf{Q}_{ww}^{-1}\mathbf{A}\mathbf{A}^+$ are used. Before the derivation of the residuals $\hat{\mathbf{v}}_A$ and its cofactor matrix $\mathbf{Q}_{\hat{v}\hat{v},A}$, the term $\mathbf{A}_O\mathbf{Q}_{\hat{x}\hat{x},O}\mathbf{A}_O^T$ is evaluated

$$\mathbf{A}_O\mathbf{Q}_{\hat{x}\hat{x},O}\mathbf{A}_O^T = \begin{bmatrix} \mathbf{A} & \mathbf{BC} \end{bmatrix} \begin{bmatrix} \mathbf{Q}_{\hat{x}\hat{x}} + \mathbf{A}^+\mathbf{BC}\mathbf{Q}_{\hat{\nabla}\hat{\nabla}}\mathbf{C}^T\mathbf{B}^T(\mathbf{A}^+)^T & -\mathbf{A}^+\mathbf{BC}\mathbf{Q}_{\hat{\nabla}\hat{\nabla}} \\ -\mathbf{Q}_{\hat{\nabla}\hat{\nabla}}\mathbf{C}^T\mathbf{B}^T(\mathbf{A}^+)^T & \mathbf{Q}_{\hat{\nabla}\hat{\nabla}} \end{bmatrix} \begin{bmatrix} \mathbf{A}^T \\ \mathbf{C}^T\mathbf{B}^T \end{bmatrix}$$

$$= \mathbf{A}\mathbf{Q}_{\hat{x}\hat{x}}\mathbf{A}^T + \mathbf{BC}\mathbf{Q}_{\hat{\nabla}\hat{\nabla}}\mathbf{C}^T\mathbf{B}^T - \mathbf{A}\mathbf{A}^+\mathbf{BC}\mathbf{Q}_{\hat{\nabla}\hat{\nabla}}\mathbf{C}^T\mathbf{B}^T$$

$$- \mathbf{BC}\mathbf{Q}_{\hat{\nabla}\hat{\nabla}}\mathbf{C}^T\mathbf{B}^T(\mathbf{A}\mathbf{A}^+)^T + \mathbf{A}\mathbf{A}^+\mathbf{BC}\mathbf{Q}_{\hat{\nabla}\hat{\nabla}}\mathbf{C}^T\mathbf{B}^T(\mathbf{A}\mathbf{A}^+)^T$$

$$= \mathbf{A}\mathbf{Q}_{\hat{x}\hat{x}}\mathbf{A}^T + (\mathbf{I} - \mathbf{A}\mathbf{A}^+)\mathbf{BC}\mathbf{Q}_{\hat{\nabla}\hat{\nabla}}\mathbf{C}^T\mathbf{B}^T(\mathbf{I} - \mathbf{A}\mathbf{A}^+)^T$$

With the identity $(\mathbf{I}-\mathbf{A}\mathbf{A}^+)\mathbf{B} = (\mathbf{Q}_{ww}\mathbf{Q}_{ww}^{-1}-\mathbf{A}\mathbf{Q}_{\hat{x}\hat{x}}\mathbf{A}^T\mathbf{Q}_{ww}^{-1})\mathbf{B}\mathbf{Q}_{ll}\mathbf{Q}_{ll}^{-1} = (\mathbf{Q}_{ww}-\mathbf{A}\mathbf{Q}_{\hat{x}\hat{x}}\mathbf{A}^T)(\mathbf{B}^+)^T\mathbf{Q}_{ll}^{-1}$, the residuals and its cofactor matrix become

$$
\begin{aligned}
\mathbf{Q}_{\hat{v}\hat{v},A} &= \mathbf{B}^+(\mathbf{Q}_{ww} - \mathbf{A}_O\mathbf{Q}_{\hat{x}\hat{x},O}\mathbf{A}_O^T)(\mathbf{B}^+)^T \\
&= \mathbf{B}^+(\mathbf{Q}_{ww} - \mathbf{A}\mathbf{Q}_{\hat{x}\hat{x}}\mathbf{A}^T)(\mathbf{B}^+)^T - \mathbf{B}^+(\mathbf{I} - \mathbf{A}\mathbf{A}^+)\mathbf{B}\mathbf{C}\mathbf{Q}_{\hat{\nabla}\hat{\nabla}}\mathbf{C}^T\mathbf{B}^T(\mathbf{I} - \mathbf{A}\mathbf{A}^+)^T(\mathbf{B}^+)^T \\
&= \mathbf{Q}_{\hat{v}\hat{v}} - \mathbf{Q}_{\hat{v}\hat{v}}\mathbf{Q}_{ll}^{-1}\mathbf{C}\mathbf{Q}_{\hat{\nabla}\hat{\nabla}}\mathbf{C}^T\mathbf{Q}_{ll}^{-1}\mathbf{Q}_{\hat{v}\hat{v}} \\
\hat{\mathbf{v}}_A &= -\mathbf{B}^+(\mathbf{I} - \mathbf{A}_O\mathbf{A}_O^+)\mathbf{w} = -\mathbf{B}^+(\mathbf{I} - \mathbf{A}_O\mathbf{Q}_{\hat{x}\hat{x},O}\mathbf{A}_O^T\mathbf{Q}_{ww}^{-1})\mathbf{w} \\
&= -\mathbf{B}^+(\mathbf{I} - \mathbf{A}\mathbf{Q}_{\hat{x}\hat{x}}\mathbf{A}^T\mathbf{Q}_{ww}^{-1})\mathbf{w} + \mathbf{B}^+(\mathbf{I} - \mathbf{A}\mathbf{A}^+)\mathbf{B}\mathbf{C}\mathbf{Q}_{\hat{\nabla}\hat{\nabla}}\mathbf{C}^T\mathbf{B}^T(\mathbf{I} - \mathbf{A}\mathbf{A}^+)^T\mathbf{Q}_{ww}^{-1}\mathbf{w} \\
&= -\mathbf{B}^+(\mathbf{I} - \mathbf{A}\mathbf{A}^+)\mathbf{w} + \mathbf{Q}_{\hat{v}\hat{v}}\mathbf{Q}_{ll}^{-1}\mathbf{C}\mathbf{Q}_{\hat{\nabla}\hat{\nabla}}\mathbf{C}^T\mathbf{B}^T(\mathbf{I} - \mathbf{Q}_{ww}^{-1}\mathbf{A}\mathbf{Q}_{\hat{x}\hat{x}}\mathbf{A}^T)\mathbf{Q}_{ww}^{-1}\mathbf{w} \\
&= \hat{\mathbf{v}} + \mathbf{Q}_{\hat{v}\hat{v}}\mathbf{Q}_{ll}^{-1}\mathbf{C}\mathbf{Q}_{\hat{\nabla}\hat{\nabla}}\mathbf{C}^T\mathbf{Q}_{ll}^{-1}\mathbf{Q}_{ll}\mathbf{B}^T\mathbf{Q}_{ww}^{-1}(\mathbf{I} - \mathbf{A}\mathbf{A}^+)\mathbf{w} \\
&= \hat{\mathbf{v}} - \mathbf{Q}_{\hat{v}\hat{v}}\mathbf{Q}_{ll}^{-1}\mathbf{C}\mathbf{Q}_{\hat{\nabla}\hat{\nabla}}\mathbf{C}^T\mathbf{Q}_{ll}^{-1}\hat{\mathbf{v}} = \hat{\mathbf{v}} - \mathbf{Q}_{\hat{v}\hat{v}}\mathbf{Q}_{ll}^{-1}\mathbf{C}d\hat{\boldsymbol{\nabla}}
\end{aligned}
$$

C.2   n-dimensional MDB

The aim is to derive the equation of the u_∇-dimensional MDB $d\hat{\boldsymbol{\nabla}}_0$. The necessary condition for these derivations is, that $\boldsymbol{\Sigma}_{\hat{\nabla}\hat{\nabla}}$ (and therefore also $\boldsymbol{\Sigma}_{\hat{\nabla}\hat{\nabla}}^{-1}$) is positive definite, so eigenvalue decomposition can be done $\boldsymbol{\Sigma}_{\hat{\nabla}\hat{\nabla}} = \mathbf{U}^T\boldsymbol{\Lambda}\mathbf{U}$. The column vectors $\mathbf{u}$ of $\mathbf{U}$ represent the eigenvectors and the diagonal of $\boldsymbol{\Lambda}$ contains the sorted eigenvalues $e_{\max}, ..., e_{\min}$. The first step is to compute the square root of (32)

$$
\begin{aligned}
\sqrt{\lambda_{A,\chi^2}(\alpha_A, \beta_A, u_\nabla)} &= \sqrt{d\hat{\boldsymbol{\nabla}}_0^T\boldsymbol{\Sigma}_{\hat{\nabla}\hat{\nabla}}^{-1}d\hat{\boldsymbol{\nabla}}_0} = \sqrt{d\hat{\boldsymbol{\nabla}}_0^T\mathbf{U}\boldsymbol{\Lambda}^{-1}\mathbf{U}^T d\hat{\boldsymbol{\nabla}}_0} \\
&= \sqrt{d\hat{\boldsymbol{\nabla}}_0^T\mathbf{U}\boldsymbol{\Lambda}^{-\frac{1}{2}}\mathbf{U}^T\mathbf{U}\boldsymbol{\Lambda}^{-\frac{1}{2}}\mathbf{U}^T d\hat{\boldsymbol{\nabla}}_0} = \sqrt{d\hat{\boldsymbol{\nabla}}_0^T\boldsymbol{\Sigma}_{\hat{\nabla}\hat{\nabla}}^{-\frac{1}{2}}\boldsymbol{\Sigma}_{\hat{\nabla}\hat{\nabla}}^{-\frac{1}{2}}d\hat{\boldsymbol{\nabla}}_0}.
\end{aligned}
$$

where the identity $\mathbf{U}^T\mathbf{U} = \mathbf{I}$ is used, which holds, because $\mathbf{U}$ from eigenvalue decomposition is an orthogonal matrix.

The last expression is the vector norm

$$
\|\boldsymbol{\Sigma}_{\hat{\nabla}\hat{\nabla}}^{-\frac{1}{2}}d\hat{\boldsymbol{\nabla}}_0\|_2 = \sqrt{d\hat{\boldsymbol{\nabla}}_0^T\boldsymbol{\Sigma}_{\hat{\nabla}\hat{\nabla}}^{-\frac{1}{2}}\boldsymbol{\Sigma}_{\hat{\nabla}\hat{\nabla}}^{-\frac{1}{2}}d\hat{\boldsymbol{\nabla}}_0},
$$

where the index 2 means the euclidean norm, which is necessary later on for the defintion of the matrix norm. Further developing this expression gives

$$
\begin{aligned}
\sqrt{\lambda_{A,\chi^2}(\alpha_A, \beta_A, u_\nabla)} &= \|\boldsymbol{\Sigma}_{\hat{\nabla}\hat{\nabla}}^{-\frac{1}{2}}d\hat{\boldsymbol{\nabla}}_0\|_2 \\
\|\boldsymbol{\Sigma}_{\hat{\nabla}\hat{\nabla}}^{\frac{1}{2}}\|_2 \cdot \sqrt{\lambda_{A,\chi^2}(\alpha_A, \beta_A, u_\nabla)} &= \|\boldsymbol{\Sigma}_{\hat{\nabla}\hat{\nabla}}^{\frac{1}{2}}\|_2 \cdot \|\boldsymbol{\Sigma}_{\hat{\nabla}\hat{\nabla}}^{-\frac{1}{2}}d\hat{\boldsymbol{\nabla}}_0\|_2 \\
\|\boldsymbol{\Sigma}_{\hat{\nabla}\hat{\nabla}}^{\frac{1}{2}}\|_2 \cdot \sqrt{\lambda_{A,\chi^2}(\alpha_A, \beta_A, u_\nabla)} &\geq \|\boldsymbol{\Sigma}_{\hat{\nabla}\hat{\nabla}}^{\frac{1}{2}}\boldsymbol{\Sigma}_{\hat{\nabla}\hat{\nabla}}^{-\frac{1}{2}}d\hat{\boldsymbol{\nabla}}_0\|_2 \\
\|\mathbf{U}^T\boldsymbol{\Lambda}^{\frac{1}{2}}\mathbf{U}\|_2 \cdot \sqrt{\lambda_{A,\chi^2}(\alpha_A, \beta_A, u_\nabla)} &\geq \|d\hat{\boldsymbol{\nabla}}_0\|_2.
\end{aligned}
$$

The norm $\|...\|_2$ of a matrix is called the spectral norm and it equals the square root of the maximum eigenvalue of the matrix [59] pp. 37-4. Thus, an upper bound for the magnitude of the MDB is available

$$\|d\hat{\mathbf{V}}_0\|_2 \leq \sqrt{\lambda_{A,\chi^2}(\alpha_A, \beta_A, u_\nabla) \cdot \sqrt{e_{\max}}}$$

The inequality appears because of the submultiplicative property

$$\|\mathbf{\Sigma}_{\hat{\nabla}\hat{\nabla}}^{\frac{1}{2}}\|_2 \cdot \|\mathbf{\Sigma}_{\hat{\nabla}\hat{\nabla}}^{-\frac{1}{2}}d\hat{\mathbf{V}}_0\|_2 \geq \|\mathbf{\Sigma}_{\hat{\nabla}\hat{\nabla}}^{\frac{1}{2}}\mathbf{\Sigma}_{\hat{\nabla}\hat{\nabla}}^{-\frac{1}{2}}d\hat{\mathbf{V}}_0\|_2$$

of the spectral norm [59] pp. 18-6.

C.3 VCM of n_A one-dimensional test statistics

The square root of the Fisher-distributed test statistic

$$T_A = \frac{d\hat{\mathbf{V}}^T \mathbf{\Sigma}_{\hat{\nabla}\hat{\nabla}}^{-1} d\hat{\mathbf{V}}}{r} \begin{cases} H_0: & T_A \leq T_{A,c}(\alpha) \to T_A \sim F_{u_\nabla, \infty} \\ H_A: & T_A > T_{A,c}(\alpha) \to T_A \sim F_{u_\nabla, \infty, \lambda_A} \end{cases}$$

follows a normal distribution considering that there is only one additional parameter $d\hat{\mathbf{V}} = d\hat{\nabla} \in \mathbb{R}^{1\times1}$ in the alternative hypothesis. The test statistic becomes

$$T_A = \frac{1}{\sqrt{r}} \cdot \frac{d\hat{\nabla}}{\sigma_{\hat{\nabla}}} = \frac{1}{\sqrt{r}} \cdot \frac{\sigma_{\hat{\nabla}}^2 \mathbf{c}^T \mathbf{Q}_{ll}^{-1}\hat{\mathbf{v}}}{\sigma_{\hat{\nabla}}} = \frac{\sigma_{\hat{\nabla}}}{\sqrt{r}} \cdot \mathbf{c}^T \mathbf{Q}_{ll}^{-1}\hat{\mathbf{v}}$$

in which the results from (30) are used for $d\hat{\nabla}$. The test statistics $T_{A,i}, \ i = 1, ..., n_A$ for all considered alternative hypothesis are collected in a vector

$$\mathbf{t}_A = \begin{bmatrix} T_{A,1} \\ T_{A,2} \\ \vdots \\ T_{A,n_A} \end{bmatrix} = \frac{1}{\sqrt{r}} \begin{bmatrix} \sigma_{\hat{\nabla}_1} \cdot \mathbf{c}_1^T \\ \sigma_{\hat{\nabla}_2} \cdot \mathbf{c}_2^T \\ \vdots \\ \sigma_{\hat{\nabla}_{n_A}} \cdot \mathbf{c}_{n_A}^T \end{bmatrix} \mathbf{\Sigma}_{ll}^{-1}\hat{\mathbf{v}} = \frac{1}{\sqrt{r}} \cdot diag(\sigma_{\hat{\nabla}_i}) \mathbf{C}^T \mathbf{\Sigma}_{ll}^{-1}\hat{\mathbf{v}} = \mathbf{F}\hat{\mathbf{v}}.$$

$$diag(\sigma_{\hat{\nabla}_i}) = \begin{bmatrix} \sigma_{\hat{\nabla}_1} & 0 & \dots & 0 \\ 0 & \sigma_{\hat{\nabla}_2} & \dots & 0 \\ \vdots & \vdots & \ddots & \vdots \\ 0 & 0 & \dots & \sigma_{\hat{\nabla}_{n_A}} \end{bmatrix}$$

This shows, that the test statistics for all considered one-dimensional alternative hypothesis are a linear imaging of the estimated residuals from H_0. Thus, the VCM of all test statistics is derived by using variance propagation

$$\mathbf{\Sigma_{tt},A} = \mathbf{F}\mathbf{\Sigma}_{\hat{v}\hat{v}}\mathbf{F}^T = \frac{1}{r} \cdot diag(\sigma_{\hat{\nabla}_i})\mathbf{C}^T\mathbf{\Sigma}_{\mathrm{ll}}^{-1}\mathbf{\Sigma}_{\hat{v}\hat{v}}\mathbf{\Sigma}_{\mathrm{ll}}^{-1}\mathbf{C} \; diag(\sigma_{\hat{\nabla}_i})$$

$$= \frac{1}{r} \cdot diag(\sigma_{\hat{\nabla}_i})\mathbf{\Sigma}_{\hat{\nabla}\hat{\nabla}}^{-1} \; diag(\sigma_{\hat{\nabla}_i})$$

$$= \frac{1}{r} \cdot diag(\sigma_{\hat{\nabla}_i}) \begin{bmatrix} s_{11} & s_{12} & \cdots & s_{1n_A} \\ s_{21} & s_{22} & \cdots & s_{2n_A} \\ \vdots & \vdots & \ddots & \vdots \\ s_{n_A1} & s_{n_A2} & \cdots & s_{n_An_A} \end{bmatrix} diag(\sigma_{\hat{\nabla}_i}).$$

The main- and off-diagonal elements of $\mathbf{\Sigma_{tt},A}$ can be written in the following form

$$\sigma_{ii}^2 = \frac{s_{ii} \cdot \sigma_{\hat{\nabla}_i}^2}{r}$$

$$\sigma_{ij} = \frac{s_{ij} \cdot \sigma_{\hat{\nabla}_i} \cdot \sigma_{\hat{\nabla}_j}}{r}.$$

When computing the correlation coefficients for the different test statistics from $\mathbf{\Sigma_{tt},A}$

$$\rho_{ij} = \frac{\sigma_{ij}}{\sqrt{\sigma_{ii}^2 \cdot \sigma_{jj}^2}} = \frac{s_{ij}}{\sqrt{s_{ii} \cdot s_{jj}}}$$

only the elements from $\mathbf{\Sigma}_{\hat{\nabla}\hat{\nabla}}^{-1}$ remain.

Bibliography

[1] Muhammed Harris Afzal, Valerie Renaudin, and Gerard Lachapelle. Magnetic field based heading estimation for pedestrian navigation environments. In *2011 International Conference on Indoor Positioning and Indoor Navigation (IPIN)*, Guimaraes, Portugal, 2011. IEEE, Piscataway, New Jersey, USA.

[2] Mohamed-Hedi Amri, Didier Aubry, Yasmina Becis, and Nacim Ramdani. Robuts fault detection and isolation applied to indoor localization. *IFAC-PapersOnLine*, 48(21):440–445, 2015.

[3] Hameed Anum and Anisa Ahmed Hafiza. Survey on indoor positioning applications based on different technologies. In *2018 12th International Conference on Mathematics, Actuarial Science, Computer Science and Statistics (MACS)*, Karachi, Pakistan, 2018. IEEE, Piscataway, New Jersey, USA.

[4] Akin Ayanoglu, Daniel M. Schneider, and Ben Eitel. Crowdsourcing-based magnetic map generation for indoor localization. In *2018 IEEE International Conference on Communications (ICC)*, Nantes, France, 2018. IEEE, Piscataway, New Jersey, USA.

[5] Willem Baarda. *Statistical concepts in geodesy*. Number 4 in Publications on Geodesy. NCG, Delft, Netherlands, 1967.

[6] Willem Baarda. *A testing procedure for use in geodetic networks*. Number 5 in Publications on Geodesy. NCG, Delft, Netherlands, 1968.

[7] Yoram Baram and Thomas Kailath. Estimability and regulability of linear systems. *IEEE Transactions on automatic control*, 33(12):1116–1121, 1988.

[8] Sergio Baselga. Exhaustive search procedure for multiple outlier detection. *Acta Geodaetice et Geophysica Hungarica*, 46:401–416, 2011.

[9] Yoaf Benjamini and Yosef Hochberg. Controlling the false discovery rate: a practical and powerful approach to multiple testing. *Journal of the Royal Statistical Society, Series B*, 57(1):289–300, 1995.

[10] Dimitri P. Bertsekas. *Constrained Optimization and Lagrange Multiplier Methods*. Athena Scientific, Belmont, Massachusetts, USA, 1982.

[11] David M. Bevly and Bradford Parkinson. Cascaded kalman filters for accurate estimation of multiple biases, dead-reckoning navigation and full state feedback control of ground vehicles. *IEEE Transactions on Control Systems Technology*, 15(2):199–208, 2007.

[12] Ludovico Biagi and Stefano Calder. An efficient leave one block out approach to identify outliers. *Journal of Applied Geodesy*, 7:11–19, 2013.

[13] Johannes Bureick, Sören Vogel, Ingo Neumann, Jakob Unger, and Hamza Alkhatib. Georeferencing of an unmanned aerial system by means of an iterated extended kalman filter using a 3d city model. *Journal of Photogrammetry, Remote Sensing and Geoinformation Science*, online(online), 2019.

[14] Aaron Canciani and Christopher J. Brennan. An analysis of the benefits and difficulties of aerial magnetic vector navigation. *IEEE Transactions on Aerospace and Electronic Systems*, 56(6):4161–4176, 2020.

[15] Aaron Canciani and John Raquet. Airborne magnetic anomaly navigation. *IEEE Transactions on Aerospace and Electronic Systems*, 53(1):67–80, 2017.

[16] Yanjun Cao and Giovanni Beltrame. Vir-slam: visual, inertial and ranging slam for single and multi-robot systems. *Autonomous Robots*, 45:905–917, 2021.

[17] Ching-Han Chen, Pi-Wei Chen, Pi-Jhong Chen, and Tzung-Hsin Liu. Indoor positioning using magnetic fingerprint map captured by magnetic sensor array. *Sensors*, 21(5707), 2021.

[18] Weijie Chen, Xingfa Shen, Quanbo Ge, and Yongcai Wang. Unsupervised learning of radio map from imbalanced crowd-sourced trajectories. In *2020 Chinese Automation Congress (CAC)*. IEEE, Piscataway, New Jersey, USA, 2020.

[19] Domenica Costantino, Gabriele Vozza, Massimiliano Pepe, and Vincenzo Saverio Alfio. Smartphone lidar technologies for surveing and reality modelling in urban scenarios: evaluation methods, performance and challanges. *Applied System Innovation*, 5(63), 2022.

[20] Riccardo Costanzi, Francesco Fanelli, Niccolo Monni, Alessandro Ridolfi, and Benedetto Allotta. An attitude estimation algorithm for mobile robots under unknown magnetic disturbances. *IEEE/ASME Transactions on Mechatronics*, 21(4):1900–1911, 2016.

[21] Jackson Cothren. Reliability in constrained gauss-markov models: an analytical and differential approach with applications to photogrammetry. Technical report, Department of Civil and Environmental Engineering and Geodetic Science, Ohio State University, 2005.

[22] John Crassidis, Kok-Laim Lai, and Richard R. Harman. Real-time attitude-independent three-axis magnetometer calibration. *Journal of Guidance, Control and Dynamics*, 28(1), 2005.

[23] Thao Dang. *Kontinuierliche Selbstkalibrierung von Stereokameras*. PhD thesis, Institut für Mess- und Regelungstechnik, KIT, Karlsruhe, Germany, 2007.

[24] Thao Dang. An iterative parameter estimation method for observation models with nonlinear constraints. *Metrology and Measurement Systems*, 15(4):421–432, 2008.

[25] Hani Dbouk. *Alternative integrity measures based on interval analysis and set theory*. PhD thesis, Fakultät für Bauingenieurwesen und Geodäsie, Gottfried Wilhelm Leibniz Universität Hannover, Hannover, Germany, 2021.

[26] Boxian Dong and Thomas Burgess. Adaptive kalman filter for indoor navigation. In *Proceedings of the 2016 International Conference on Indoor Positioning and Indoor Navigation (IPIN)*, Alcala de Henares, Madrid, Spain, 2016. IEEE, Piscataway, New Jersey, USA.

[27] Liping Du, Longji Chen, Xiaotian Hou, and Yueyun Chen. Cooperative vehicle localization base on extended kalman filter in intelligent transportation system. In *28th Wireless and Optical Communications Conference (WOCC)*, Beijing, China, 2019. IEEE, Piscataway, New Jersey, USA.

[28] Utkan Mustafa Durdag, Serif Hekimoglu, and Bahattin Erdogan. Outlier detection by using fault detection and isolation techniques in geodetic networks. *Survey Review*, 48(351):400–408, 2015.

[29] Catia R. Ehrlich and Jörg Blankenbach. Pedestrian localisation inside buildings based on multi-sensor smartphones. In *2018 Ubiquitous Positioning, Indoor Navigation and Location-Based Services (UPINLBS)*, Wuhan, China, 2018. IEEE, Piscataway, New Jersey, USA.

[30] Catia Real Ehrlich and Jörg Blankenbach. Indoor localization for pedestrians with real-time capability using multi-sensor smarphones. *Geo-spatial Information Science*, 22(2):73–88, 2019.

[31] Jay A. Farrell. *Aided Navigation. GPS with high rate sensors*. McGraw-Hill, New York City, New York, USA, 2008.

[32] Jianxin Feng, Zidong Wang, and Ming Zeng. Distributed weigthed robust kalman filter fusion for uncertain systems with autocorrelated and cross-correlated noises. *Information Fusion*, 14(2013), 2013.

[33] Wolfgang Förstner. Reliability and discernability of extended Gauss-Markov models. In *Seminar on Mathematical Models to Outliers and Systematic Errors*, number 98 in Series A, pages 79–103. Deutsche Geodätische Kommission, Munich, Germany, 1983.

[34] Wolfgang Förstner. Reliability analysis of parameter estimation in linear models with applications to mensuration problems in computer vision. *Computer Vision, Graphics and Image Processing*, 40:273–310, 1987.

[35] Wolfgang Förstner and Bernhard P. Wrobel. *Photogrammetric Computer Vision*. Number 11 in Geometry and Computing. Springer International Publishing, Basel, Switzerland, 2016.

[36] Enrique Garcia, Pablo Poudereux, Alvaro Hernandez, Jesus Urena, and David Gualda. A robuts uwb indoor positioning system for highly complex environments. In *2015 IEEE International Conference on Industrial Technology (ICIT)*, Seville, Spain, 2015. IEEE, Piscataway, New Jersey, USA.

[37] Demoz Gebre-Egziabher, Gabriel H. Elkaim, David J. Powell, and Bradford W. Parkinson. Calibration of strapdown magnetometers in magnetic field domain. *Journal of Aerospace Engineering*, 19(2):1–16, 2006.

[38] Demoz Gebre-Egziabher, Roger C. Hayward, and David J. Powell. Design of multi-sensor attitude determination systems. *IEEE Transactions on Aerospace and Electronic Systems*, 40(2):627–649, 2004.

[39] Arthur Gelb. *Applied optimal estimation*. MIT press, Cambridge, Massachusetts, USA, 1974.

[40] I. Gillisen and I.A. Elema. Test results of dia: a real-time adaptive integrity monitoring procedure, used in an integrated navigation system. *International Hydrographic Review*, 37(1):75–103, 1996.

[41] Yoshinao Goi and Chul-Woo Kim. Bayesian outlier detection for health monitoring of bridges. *Procedia Engineering*, 199(2017):2120–2125, 2017.

[42] Gene H. Golub and Charles F. van Loan. *Matrix Computations*. The Johns Hopkins University Press, Baltimore, Maryland, USA, 3 edition, 1996.

[43] Drora Goshen-Meskin and Itzhack Y. Bar-Itzhack. On the connection between estimability and observability. *IEEE Transactions on Automatic Control*, 37(8):1225–1226, 1992.

[44] Mohinder S. Grewal and Angus P. Andrews. *Kalman filtering. Theory and practice using matlab*. John Wiley & Sons, Hoboken, New Jersey, USA, 3 edition, 2008.

[45] Paul D. Groves. *Principles of GNSS, Inertial and Multisensor Integrated Navigation Systems*. GNSS Technology and Application Series. Artech House, London, United Kingdom, 2 edition, 2013.

[46] Yang Gu, Caifa Zhou, Andreas Wieser, and Zhimin Zhou. Wifi based trajectory alignment, claibration and crowdsourced site survey using smart phones and foot-mounted imus. In *2017 Internation Conferencen on Indoor Positioning and Indoor Navigation (IPIN)*, Sapporo, Japan, 2017. IEEE, Piscataway, New Jersey, USA.

[47] Ran Guan and Robert Harle. Crowdsourcing mobile data for a passive indoor positioning system - the maa case study. In *2022 18th International Conference on Mobility, Sensing and Networking (MSN)*, Guangzhou, China, 2022. IEEE, Piscataway, New Jersey, USA.

[48] Q Gui, Y Gong, G Li, and B Li. A bayesian approach to the detection of gross errors based on posterior probability. *Journal of Geodesy*, 81:651–659, 2007.

[49] Roberto Guidorzi, Roberto Diversi, and Umberto Soverini. Optimal errors-in-variables filtering. *Automatica*, 39(2):281–289, 2003.

[50] Jianfeng Guo, Jikun Ou, and Haitao Wang. Robust estimation for correlated observations: two local sensitivity-based downweighting strategies. *Journal of Geodesy*, 84(4):243–250, 2010.

[51] Frank R. Hampel. *Contributions to the theory of robust estimations*. PhD thesis, University of California, Berkeley, Berkeley, California, USA, 1968.

[52] Frank R. Hampel, Elvezio M. Ronchetti, Peter J. Rousseeuw, and Werner A. Stahel. *Robust Statistics. The approach based on influence functions.* John Wiley & Sons, Hoboken, New Jersey, USA, 1986.

[53] Ke Han, He Han, Zhifeng Wang, and Feng Xu. Extended kalman filter-based gyroscope-aided magnetomter calibration for consumer electronics. *IEEE Sensors Journal*, 17(1):63–71, 2017.

[54] Songlai Han and Jinling Wang. A novel method to integrate imu and magnetometers in attitude and heading reference systems. *The Journal of Navigation*, 64:727–738, 2011.

[55] Joachim Hartung, Bärbel Elpelt, and Karl-Heinz Klösener. *Statistik, Lehr- und Handbuch der angewandten Statistik.* Oldenbourg Verlag GmbH, Munich, Germany, 10 edition, 1995.

[56] Douglas M. Hawkins. *Identification of outliers.* Monographs on Statistical and Applied Probability. Springer Netherlands, Dordrecht, Netherlands, 1980.

[57] Chengyeng He, Chao Tang, and Chengpu Yu. A federated derivative cubature kalman filter for imu-uwb indoor positioning. *Sensors*, 20(12), 2020.

[58] Otto Heunecke, Heiner Kuhlmann, Walter Welsch, Andreas Eichhorn, and Hans Neuner. *Auswertung geodätischer Überwachungsmessungen.* Wichmann, Berlin, Germany, 2 edition, 2013.

[59] Leslie Hogben. *Handbook of linear algebra.* Discrete mathematics and its applications. Taylor & Francis Group, London, UK, 2007.

[60] Sture Holm. A simple sequentially rejective multiple test procedure. *Scandinavian Journal of Statistics*, 6(2):65–70, 1979.

[61] Christoph Holst, Christian Eling, and Heiner Kuhlmann. Automatic optimization of height network configurations for detection of surface deformations. *Journal of Applied Geodesy*, 7(2), 2013.

[62] Fabian Hölzke, Johann-P. Wolff, Frank Golatowski, and Christian Haubelt. Low-complexity online correction and calibration of pedestrian dead reckoning using map matching and gps. *Geo-spatial Information Science*, 22(2):114–127, 2019.

[63] Sinpyo Hong, Man Hyung Lee, Ho-Hwan Chun, Sun-Hong Kwon, and Jason L. Speyer. Observability of error states in gps/ins integration. *IEEE Transactions on Vehicular Technology*, 54(2):731–743, 2005.

[64] Ville Honkavirta, Tommi Perälä, Simo Ali-löytty, and Robert Piche. A comparative survey of wlan location fingerprinting methods. In *6th Workshop on Positioning, Navigation and Communication (WPNC)*, Hannover, Germany, 2009. IEEE, Piscataway, New Jersey, USA.

[65] Roland Hostettler and Simo Särkkä. Imu and magnetometer modeling for smartphone-based pdr. In *2016 International Conference on Indoor Positioning and Indoor Navigation (IPIN)*, Alcala de Henares, Spain, 2016. IEEE, Piscataway, New Jersey, USA.

[66] Baichuan Huang, Jingbin Liu, Wei Sun, and Fan Yang. A robust indoor positioning method based on bluetooth low energy with separate channel information. *Sensors*, 19(3487), 2019.

[67] Peter J. Huber. Robust estimation of a location parameter. *The Annals of Mathematical Statistics*, 35(1):73–101, 1964.

[68] D. Imparato, Peter J.G. Teunissen, and C.C.J.M. Tiberius. Minimal detectable and identifiable biases for quality control. *Survey Review*, 51(367):289–300, 2019.

[69] Lucian Ioan Iozan, Martti Kirkko-Jaakkola, Jussi Collin, Jarmo Takala, and Cornelius Rusu. Using a mems gyroscope to measure the earth's rotation for gyrocompassing applications. *Measurement Science and Technology*, 46(6), 2012.

[70] Robert Jackermeier and Bernd Ludwig. Exploring the limits of pdr-based indoor localisation systems under realistic conditions. *Journal of Location Based Services*, 12(3-4):231–272, 2018.

[71] Reiner Jäger, Tilman Müller, Heinz Saler, and Rainer Schwäble. *Klassische und robuste Ausgleichungsverfahren*. Wichmann, Berlin, Germany, 2005.

[72] Jannik Janß en, Heiner Kuhlmann, and Christoph Holst. Target-based terrestrial laser scan registration extended by target orientation. *Journal of Applied Geodesy*, 16(2), 2021.

[73] Chen Jiang, Shu-Bi Zhang, and Qiu-Zhao Zhang. A new adaptive h-infinity filtering algorithm for the gps/ins integrated navigation. *Sensors*, 16(12), 2016.

[74] Wei Jiang, Dan Liu, Baigen Cai, Chris Rizon, Jian Wang, and Wei Shangguan. A fault-tolerant tightly coupled gnss/ins/ovs integration vehicle navigation system based on an fdp algorithm. *IEEE Transactions on Vehicular Technology*, 68(7):6365–6378, 2019.

[75] Yeon Fuh Jiang and Yu Ping Lini. Error estimation of ins ground alignment through observability analysis. *IEEE Transactions on Aerospace and Electronic Systems*, 28(1):92–97, 1992.

[76] Antonio R. Jimenez, Fernando Seco, Pekka Peltola, and Maccarena Espinilla. Location of persons using binary sensors and ble beacons for ambient assistive living. In *2018 International Conference on Indoor Positinoing and Indoor Navigation (IPIN)*, Nantes, France, 2018. IEEE, Piscataway, New Jersey, USA.

[77] Myungin Jin, Bonhyun Koo, Sangwoo Lee, Chansik Park, Min Joon Lee, and Sunwoo Kim. Imu-assisted nearest neghbor selection for real-time wifi fingerprinting positioning. In *2018 International Conference on Indoor Positinoing and Indoor Navigation (IPIN)*, Busan, South Korea, 2014. IEEE, Piscataway, New Jersey, USA.

[78] Mathieu Joerger and Boris Pervan. Solution separation and chi-squared araim for fault detection and exclusion. In *2014 IEEE/ION Position, Location and Navigation Symposium - PLANS 2014*, Monterey, California, USA, 2014. IEEE, Piscataway, New Jersey, USA.

[79] Mathieu Joerger and Boris Pervan. Fault detection and exclusion using solution separation and chi-squared araim. *IEEE Transaction on Aerospace and Electronic Systems*, 52(2):726–742, 2016.

[80] Kamol Kaemarungsi. *Design of indoor positioning systems based on location fingerprinting technique*. PhD thesis, School of Information Science, University of Pittsburgh, Pittsburgh, Pennsylvania, USA, 2005.

[81] Rudolf E. Kalman. A new approach to linear filtering and prediction problems. *Transactions of the ASME-Journal of Basic Engineering*, 82:35–45, 1960.

[82] Takayuki Kanda, Masahiro Shiomi, Laurent Perrin, Tatsuya Nomura, Hiroshi Ishiguro, and Norihiro Hagita. Analysis of people trajectories with ubiquitous sensors in a science museum. In *2007 IEEE Conference on Robotics and Automation*, Rome, Italy, 2007. IEEE, Piscataway, New Jersey, USA.

[83] Alexander A. Kaufmann, Richard O. Hansen, and Robert L.K. Kleinberg. *Principles of magnetic methods in geophysics*. Methods in Geochemistry and Geophysics. Elsevier, Amsterdam, Netherlands, 2008.

[84] Samer Khanafseh, Naeem Roshan, Steven Langel, Fang-Cheng Chan, Mathieu Joerger, and Boris Pervan. Gps spoofing detection using raim with ins coupling. In *2014 IEEE/ION Position, Location and Navigation Symposium - PLANS 2014*, Monterey, California, USA, 2014. IEEE, Piscataway, New Jersey, USA.

[85] Jung-Hyang Kim, Chol-Jin Kim, and Ryong-Jin Li. Study on detection of gross error in geodetic network adjustment. *Geodesy and Cartography*, 67(1):57–69, 2018.

[86] Lasse Klingbeil, Christian Eling, Florian Zimmermann, and Heiner Kuhlmann. Magnetic Field Sensor Calibration for Attitude Determination. *Journal of Applied Geodesy*, 8(2):97–108, 2014.

[87] Nathan L. Knight, Jingling Wang, and Chris Rizos. Generalised measures of reliability for multiple outliers. *Journal of Geodesy*, 84:625–635, 2010.

[88] Karl R. Koch and Y. Yang. Robust kalman filter for rank deficient observation models. *Journal of Geodesy*, 72:436–441, 1998.

[89] Karl-Rudolf Koch. *Parameterschätzung und Hypothesentests in linearen Modellen*. Dümmlers Verlag, Bonn, Germany, 4 edition, 2004.

[90] Karl-Rudolf Koch. *Introduction to Bayesian statistics*. Springer, Berlin, Germany, 2 edition, 2007.

[91] Karl-Rudolf Koch. Robust estimation for the nonlinear gauss-helmert model by the expectation maximization algorithm. *Journal of Geodesy*, 88(3):263–271, 2014.

[92] Karl-Rudolf Koch. Robust estimations for the nonlinear gauss helmert model by the expectation maximization algorithm. *Journal of Geodesy*, 88(3):263–271, 2014.

[93] Karl-Rudolf Koch. Minimal detectable outliers as measures of reliability. *Journal of Geodesy*, 89(2015):483–490, 2015.

[94] Karl-Rudolf Koch and Boris Kargoll. Expectation maximization algorithm for the variance-inflation model by applying the t-distribution. *Journal of Applied Geodesy*, 7(3):217–225, 2013.

[95] Karl-Rudolf Koch and Boris Kargoll. Outlier detection by the em algorithm for laser scanning in recatngular and polar coordinate systems. *Journal of Applied Geodesy*, 9(3):162–173, 2015.

[96] Johan J. Kok. On data snooping and multiple outlier testing. Technical report, U.S. Department of Commerce, National Oceanic and Atmospheric Administration, 1984.

[97] Jack B. Kuipers. *Quaternions and rotation sequences: A primer with applications to orbits, aerospace and virtual reality*. Princeton University Press, Princeton, New Jersey, USA, 1999.

[98] Stephan Kupferer. Mehrdimensionale beobachtungstests bei gauss-helmert modellen. *AVN*, 111(7):264–269, 2004.

[99] Heidi Kuusniemi, Mohammad Zahidul H. Bhuiyan, Marten Ström, Stefan Söderholm, Timo Jokitalo, Liang Chen, and Ruizhi Chen. Utilizing pulsed pseudolites and high-sensitivity gnss for ubiquitous outdoor/indoor satellite navigation. In *2012 International Conference on Indoor Positioning and Indoor Navigation*, Sydney, New South Wales, Australia, 2012.

[100] Heidi Kuusniemi and Gerard Lachapelle. Gnss signal reliability testing in urban and indoor environments. In *Proceedings of the 2004 National Meeting of the Institute of Navigation*, San Diego, California, USA, 2004. Institute of Navigation, Manassas, Virginia, USA.

[101] Heidi Kuusniemi, Andreas Wieser, Gerard Lachapelle, and Jarmo Takala. User-level reliability monitoring in urban personal satellite-navigation. *IEEE Transactions on Aerospace and Electronic Systems*, 43(3):1305–1318, 2007.

[102] Sylvie Lamy-Perbal, Nicolas Guenard, Mehdi Boukallel, and Anne Landragin-Frassati. A hmm map-matching approach enhancing indoor positioning performances of an inertial measurement system. In *2018 International Conference on Indoor Positinoing and Indoor Navigation (IPIN)*, Banff, Alberta, Canada, 2015. IEEE, Piscataway, New Jersey, USA.

[103] Christos Laoudias, Michalis P. Michaelides, and Christos G. Panayiotou. Fault detection and mitigation in wlan rss fingerprint-based positioning. *Journal of Location Based Services*, 6(2):101–116, 2012.

[104] Jehong Lee, Jeonggeun Lim, and Jongho Lee. Compensated heading angles for outdoor mobile robots in magnetically disturbed environment. *IEEE Transactions on Industrial Electronics*, 65(2):1408–1419, 2018.

[105] Rüdiger Lehmann and VoßBöhme. On the statistical power of baarda's outlier test and some alternative. *Journal of Geodetic Science*, 7(1), 2017.

[106] Rüdiger Lehmann, Micahel Lösler, and Frank Neitzel. Mean shift versus variance inflation approach for outlier detection - a comparative study. *Mathematics*, 8(6), 2020.

[107] Rüdiger Lehmann and Michael Lösler. Multiple outlier detection: hypothesis tests versus model selection by information criteria. *Journal of Surveying Engineering*, 142(4), 2016.

[108] Zs. Lendek, R. Babuska, and B. De Schutter. Distributed kalman filtering for multiagent systems. In *2007 European Control Conference*, Kos, Greece, 2007. IEEE, Piscataway, New Jersey, USA.

[109] Helena Leppäkoski, Heidi Kuusniemi, and Jarmo Takala. Raim and complementary kalman filtering for gnss reliability enhancement. In *2006 IEEE/ION Position, Location and Navigation Symposium*, Coronado, California, USA, 2006. IEEE, Piscataway, New Jersey, USA.

[110] Otto Lerke and Volker Schwieger. Analysis of a kinematic real-time robotic total station network for robot control. *Journal of Applied Geodesy*, 15(3), 2021.

[111] Binghao Li, Thomas Gallagher, Andrew G. Dempster, and Chris Rizos. How feasible is the use of magnetic field alone for indoor positioning. In *2012 International Conference on Indoor Positioning and Indoor Navigation*, Sydney, Australia, 2012. IEEE, Piscataway, New Jersey, USA.

[112] Chao Li, Wennan Chai, Xiaohui Yang, and Qingdang Li. Crowdsourcing-based indoor semantic map construction and localization using graph optimization. *Sensors*, 2022(22), 2022.

[113] L. Li and Heiner Kuhlmann. Real-time deformation measurements using time series of gps coordinates processed by kalman filter with shaping filter. *Survey Review*, 44(326):189–197, 2012.

[114] Wei Li and Jinling Wang. Effective adaptive kalman filter for mems-imu/magnetometers integrated attitude and heading reference systems. *The Journal of Navigation*, 66:99–113, 2013.

[115] Wei Li and Jinling Wang. Magnetic sensors for navigation applications: an overview. *The Journal of Navigation*, 67:263–275, 2014.

[116] Wen Li, Dongyan Wei, Qifeng Lai, Xianghong Li, and Hong Yuan. Geomagnetism-aided indoor wi-fi radio-map construction via smartphone crowdsourcing. *Sensors*, 2018(18), 2018.

[117] Zan Li, Xiaohui Zhao, and Hui Liang. Automatic construction of radio maps by crodsourcing pdr traces for indoor positioning. In *2018 IEEE International Conference on Communications (ICC)*, Kansas City, Missouri, USA, 2018. IEEE, Piscataway, New Jersey, USA.

[118] Jihao Liu, Xihai Li, Aimin Du, Xiaoniu Zeng, and Yong Yang. A gyro-aided strapdown triaxial magnetometer calibration method robust to gyro bias. *IEEE Transactions on Instrumentation and Measurement*, 70, 2021.

[119] Tiantian Liu, Huan Li, Hua Lu, Muhammad Aamir Cheema, and Lidan Shou. Towards crowd-aware indoor path planning. *Proceedings of the VLDB Endowment*, 14(8):1365–1377, 2021.

[120] Weng Liu, Jing Li, Zhongliang Deng, Xiao Fu, and Qianqian Cheng. A calibrated-rssi/pdr/map integrated system based on a novel particle filter. In *2019 International Conference on Indoor Positioning and Indoor Navigation (IPIN)*, Pisa, Italy, 2019. IEEE, Piscataway, New Jersey, USA.

[121] Yiran Luo, Chunyang Yu, Bing Xu, Jian Li, Guang-Je Tsai, You Li, and Naser El-Sheimy. Assessment of ultra-tightly coupled gnss/ins integration system towards autonomous ground vehicle navigation using smartphone imu. In *2019 IEEE International Conference on Signal, Infomration and Data Processing (ICSIDP)*, Chongqing, China, 2019. IEEE, Piscataway, New Jersey, USA.

[122] Weiwei Lyu, Xianghong Cheng, and Jinling Wang. Adaptive federated imm filter for auv integrated navigation systems. *Sensors*, 20(20), 2020.

[123] Wenyuan Ma, Xinning Zhu, Junfei Huang, and Guochu Shou. Detecting pedestrians behavior in building based on wi-fi signals. In *2015 IEEE International Conference on Smart City/SocialCom/SustainCom (SmartCity)*, Chengdu, China, 2015. IEEE, Piscataway, New Jersey, USA.

[124] Sebastian O.H. Madgwick, Andrew J.L. Harrison, and Ravi Vaidyanathan. Estimation of imu and marg orientation using a gradient descent algorithm. In *2011 IEEE International Conference on Rehabilitation Robotics*, Zurich, Switzerland, 2011. IEEE, Piscataway, New Jersey, USA.

[125] Vahid Mahboub, Somayeh Ebrahimzadeh, Mohammed Saadatseresht, and Mehran Faramarzi. On robust constrained kalman filter for dynamic errors-in-variables model. *Survey Review*, 52(372):253–260, 2020.

[126] Vahid Mahboub, Mohammed Saadatseresht, and Alireza A. Ardalan. A general weighted total kalman filter algorithm with numerical evaluation. *Studia Geophysica et Geodaetica*, 61:19–34, 2017.

[127] Vahid Mahboub, Mohammed Saadatseresht, and Alireza A. Ardalan. A solution to dynamic errors-in-variables within system equations. *Acta Geodaetica et Geophysica*, 53:31–44, 2018.

[128] Magdi S. Mahmoud and Haris M. Khalid. Distributed kalman filtering: a bibliographic review. *IET Control Theory applications*, 7(4):483–501, 2013.

[129] Henry Martin, Paul Groves, and Mark Newman. The limits of in-run calibration of MEMS inertial sensors and sensor arrays. *Navigation*, 63(2):127–143, 2016.

[130] Andrea Masiero, Francesca Fissore, Francesca Pirotti, Alberto Guarnieri, and Antonio Vettore. Toward the use of smartphones for mobile mapping. *Geo-spatial Information Science*, 19(3):210–221, 2016.

[131] Thomas Moder, Petra Hafner, Karin Wisiol, and Manfred Wieser. 3d indoor positioning with pedestrian dead reckoning and activity recognition based on bayes filtering. In *2018 International Conference on Indoor Positinoing and Indoor Navigation (IPIN)*, Busan, South Korea, 2014. IEEE, Piscataway, New Jersey, USA.

[132] Thomas Moder, Clemens Reitbauer, Karin M.D. Wisiol, Roman Wilfinger, and Manfred Wieser. An indoor positioning and navigation application for visually impaired people using public transport. In *2018 International Conference on Indoor Positioning and Indoor Navigation (IPIN)*, Nantes, France, 2018. IEEE, Piscataway, New Jersey, USA.

[133] Jeong Hyun Moon, Sinpyo Hong, Ho-Hwan Chun, and Man Hyung Lee. Estimability measures and their application to gps/ins. *Journal of Mechanical Science and Technology*, 22:905–913, 2008.

[134] Frank Neitzel. Identifizierung konsistenter datengruppen am beispiel der kongruenzuntersuchung geodätischer netze. In *German Geodetic Commission (DGK)*, volume No. 565 of *Vol. C*. Munich, Germany, 2004.

[135] Frank Neitzel. Generalization of total least-squares on example of unweighted and weighted 2d similarity transformation. *Journal of Geodesy*, 84(12):751–762, 2010.

[136] Xin Hui Ng and Woan Ning Lim. Design of a mobile augmented reality-based indoor navigation system. In *2020 4th International Symposium on Multidisciplinary Studies and Innovative Technologies (ISMSIT)*, Istanbul, Turkey, 2020. IEEE, Piscataway, New Jersey, USA.

[137] Xiaoji Niu, Sameh Nassar, and Naser El-Sheimy. An accurate land-vehicle mems imu/gps navigation system using 3d auxiliary velocity updates. *Navigation*, 54(3):177–188, 2007.

[138] Talat Ozyagcilar. Implementing a tilt-compensated ecompass using accelerometer and magnetometer sensors. Technical report, Freescale Semiconductor, Austin, Texas, USA, 2012.

[139] Allen J. Pope. The statistics of residuals and the detection of outliers. Technical report, United States Department of Commerce, National Oceanic and Atmospheric Administration, National Ocean Survey, 1976.

[140] Alwin Poulose and Dong Seog Han. Indoor localization using pdr with wi-fi weighted path loss algorithm. In *2019 International Conference on Information and Communication Technology Convergence (ICTC)*, Jeju, South Korea, 2019. IEEE, Piscataway, New Jersey, USA.

[141] Witold Proszynski. Another approach to reliability measures for systems with correlated observations. *Journal of Geodesy*, 84(2010):547–556, 2010.

[142] Witold Proszynski. Revisiting baarda's concept of minimal detectable bias with regard to outlier identifiability. *Journal of Geodesy*, 89(10):993–1003, 2015.

[143] Jesperi Rantanen, Maija Mäkelä, Laura Ruotsalainen, and Martti Kirkko-Jaakkola. Motion context adaptive fusion of inertial and visual pedestrian navigation. In *2018 International Conference on Indoor Positinoing and Indoor Navigation (IPIN)*, Nantes, France, 2018. IEEE, Piscataway, New Jersey, USA.

[144] Valerie Renaudin, Muhammad Haris Afzal, and Gerard Lachapelle. Complete triaxis magnetometer calibration in the magnetic domain. *Journal of Sensors*, 2010, 2010.

[145] Valerie Renaudin and Christophe Combettes. Magnetic, acceleration fields and gyroscope quaternion (magyq)-based attitude estimation with smartphone sensors for indoor pedestrian navigation. *Sensors*, 14(12):22864–22890, 2014.

[146] Günther Retscher and Thomas Tatschl. Indoor positioning using differential wi-fi lateration. *Journal of Applied Geodesy*, 11(4):249–269, 2017.

[147] Peter J. Rousseeuw. Least median of squares regression. *Journal of the American Statistical Association*, 79(388):871–880, 1984.

[148] Laura Ruotsalainen, Heidi Kuusniemi, Mohammad Zahidul H. Bhuiyan, Liang Chen, and Ruizhi Chen. A two-dimensional pedestrian navigation solution aided with a visual gyroscope and a visual odometer. *GPS Solutions*, 17:575–586, 2013.

[149] Vinod Kumar Saini and Arnab Maity. Random sample consensus in decentralized kalman filter. *European Journal of Control*, 65(2022), 2022.

[150] Martin Salzmann. *Least squares filtering and testing for geodetic navigation applications*. Number 37 in Publications on Geodesy. NCG, Delft, Netherlands, 1993.

[151] Simo Särkkä, Arno Solin, Aapo Nummenmaa, Aki Vehtari, Toni Auranen, Simo Vanni, and Fa-Husan Lin. Dynamic retrospective filtering of physiological noise in bold fmri: Drifter. *NeuroImage*, 60(2):1517–1525, 2012.

[152] Simo Särkkä, Ville Tolvanen, Juho Kannala, and Esa Rahtu. Adaptive kalman filtering and smoothing for gravitation tracking in mobile systems. In *2015 International Conference on Indoor Positioning and Indoor Navigation (IPIN)*, Banff, Alberta, Canada, 2015. IEEE, Piscataway, New Jersey, USA.

[153] Burkhard Schaffrin. Towards total kalman filtering for mobile mapping. *International Archives in Photogrammetry, Remote Sensing and Spatial Information Sciences*, 36:270–274, 2008.

[154] Burkhard Schaffrin and Sibel Uzun. Errors-in-variables for mobile mapping algorithms in the presence of outliers. *Archives of Photogrammetry, Cartography and Remote Sensing*, 22:377–389, 2011.

[155] Steffen Schön and Olaf Bielenberg. On the capability of high sensitivity gps for precise indoor positioning. In *2008 5th Workshop on Positioning, Navigation and Communication (WPNC)*, Hannover, Germany, 2008. IEEE, Piscataway, New Jersey, USA.

[156] Xingfa Shen, Chuang Li, Weijie Chen, and Yongcai Wang. Mapict: Unsupervised radio-map learning from imbalanced crowd-sourced trajectories. *IEEE Sensors Journal*, 22(3):2399–2408, 2022.

[157] Rathin Chandra Shit, Suraj Sharam, and Kumar and Yelamarthi. Ai-enabled fingerprinting and crowdsource-based vehicle localization for resilient and safe transportation systems. *IEEE Transactions on Intelligent Transportation Systems*, 22(7):4660–4669, 2021.

[158] Felipe O. Silva, Elder M. Hemerly, and Waldemar C. Leite Filho. On the error state selection for stationary sins alignment and calibration kalman filters - part ii: Observability/estimability analysis. *Sensors*, 17(439), 2017.

[159] Dan Simon. *Optimal state estimation: Kalman, H infinity, and nonlinear approaches*. John Wiley & Sons, Hoboken, New Jersey, USA, 2006.

[160] Richard Steffen and Christian Beder. Recursive estimation with implicit constraints. In Fred A. Hamprecht, Christoph Schnörr, and Bernd Jähne, editors, *Pattern Recognition. 29th DAGM Symposium, Heidelberg, Germany, September 12-14, 2007, Proceedings*, Image Processing, Computer Vision, Pattern Recognition and Graphics. Springer-Verlag, Berlin, Germany, 2007.

[161] Stefano Tavani, Andrea Billi, Amerigo Corradetti, Marco Mercuri, Alessandro Bosman, Marco Cuffaro, Thomas Seers, and Eugenio Carminati. Smartphone assisted fieldwork: towards the digital transition of geoscience fieldwork using lidar-equipped iphones. *Earth-Science Reviews*, 227(103969), 2022.

[162] Peter J.G. Teunissen. Minimal detectable biases of gps data. *Journal of Geodesy*, 72:236–244, 1998.

[163] Peter .J.G. Teunissen. *Dynamic Data Processing*. Series on Mathematical Geodesy and Positioning. VSSD, Delft, Netherlands, 2001.

[164] Peter J.G. Teunissen. *Network quality control*. Series on Mathematical Geodesy and Positioning. VSSD, Delft, Netherlands, 2006.

[165] Peter J.G. Teunissen. *Testing theory: an introduction*. Series on Mathematical Geodesy and Positioning. VSSD, Delft, Netherlands, 2 edition, 2006.

[166] Peter J.G. Teunissen and M.A. Salzmann. A recursive slippage test for use in state-space filtering. *Manuscripta Geodaetica*, 14(6):383–390, 1989.

[167] Yulun Tian, Yun Chang, Fernando Herrera Arias, Carlos Nieto-Granda, Jonathan P. How, and Luca Carlone. Kimera-multi: Robust, distributed, dense metric-semantic slam for multi-robot system. *IEEE Transactions on Robotics*, 38(4), 2022.

[168] David Titterton and John Weston. *Strapdown inertial navigation technology*, volume 17 of *IET Radar, Sonar, Navigation and Avionics*. Institution of Engineering and Technology, Stevenage, United Kingdom, 2 edition, 2004.

[169] Ishak Hilton Pujantoro Tnunay. *Distributed coordination and estimation of multi-agent systems*. PhD thesis, Department of Electrical and Electronic Engineering, University of Manchester, Manchester, UK, 2020.

[170] Giancoarlo Troni and Ryan M. Eustice. Magnetometer bias calibration based on relative angular position: Theory and experimental comparative evaluation. In *2014 IEEE/RSJ International Conference on Intelligent Robots and Systems*, Chicago, Illinois, USA, 2014. IEEE, Piscataway, New Jersey, USA.

[171] Roberto G. Valenti, Ivan Dryanovski, and Jizhong Xiao. Keeping a good attitude: a quaternion-based orientation filter for imus and margs. *Sensors*, 15(15):19302–19330, 2015.

[172] Jose F. Vasconcelos, Gabriel H. Elkaim, Carlos Silvestre, Paulo Oliveira, and Bruno Cardeira. Geometric approach to strapdown magnetometer calibration in sensor frame. *IEEE Transactions on Aerospace and Electronic Systems*, 47(2):1293–1306, 2011.

[173] Sören Vogel, Hamza Alkhatib, and Ingo Neumann. Iterated extended kalman filter with implicit measurement equation and nonlinear constraints for information-based georeferencing. In *2018 21st International Conference on Information Fusion (FUSION)*, Cambridge, UK, 2018. IEEE, Piscataway, New Jersey, USA.

[174] Sören Vogel, Hamza Alkhatib, Johannes Bureick, Rozhin Moftizadeh, and Ingo Neumann. Georeferencing of Laser Scanner-Based Kinematic Multi-Sensor Systems in the Context of Iterated Extended Kalman Filters Using Geometrical Constraints. *Sensors*, 19(10), 2019.

[175] Jian-Guo Wang. Test statistics in kalman filtering. *Journal of Global Positioning Systems*, 7(1):81–90, 2008.

[176] Jian-Guo Wang. Reliability analysis in kalman filtering. *Journal of Global Positioning Systems*, 8(1):101–111, 2009.

[177] Jingling Wang, Yongqi Cheng, and Benzao Tao. Outlier detection and reliability of adjustment models with singular covariance matrices. *Geo-spatial Information Science*, 1(1):55–59, 1998.

[178] Shizhuang Wang, Xingqun Zhan, Yawei Zhai, Jiawen Shen, and Hanyu Wang. Performance estimation for kalman filter based multi-agent cooperative navigation by employing graph theory. *Aerospace Science and Technology*, 112, 2021.

[179] Xinxin Wang, Danyang Qin, Ruolin Guo, Min Zhao, Lin Ma, and Teklu Merhawit Berhane. The technology of crowd-sourcing landmarks-assisted smartphone in indoor localization. *IEEE Access*, 8, 2020.

[180] Andreas Wieser. Reliability checking for gnss baseline and network processing. *GPS Solutions*, 8(2):55–66, 2004.

[181] Andreas Wieser, Mark G. Petovello, and Gerard Lachapelle. Failure scenarios to be considered with kinematic highh precision relative gnss positiioning. In *17th International Technical Meeting of the Satellite Division of the Institute of Navigation (ION GNSS)*, Long Beach, California, USA, 2004. Institute of Navigation, Manassas, Virginia, USA.

[182] Yuanxin Wu, Hongliang Zhang, Meiping Wu, Xiaoping Hu, and Dewen Hu. Observability of strapdown ins alignment: a global perspective. *IEEE Transactions on Aerospace and Electronic Systems*, 48(1), 2012.

[183] Zhuoling Xiao, Hongkai Wen, Andrew Markham, and Niki Trigoni. Robust pedestrian dead reckoning (r-pdr) for arbitrary mobile device placement. In *2014 Internation Conference on Indoor Positioning and Indoor Navigation*, Busan, South Korea, 2014. IEEE, Piscataway, New Jersey, USA.

[184] Zhuoling Xiao, Hongkai Wen, Andrew Markham, and Niki Trigoni. Robust indoor positioning with lifelong learning. *IEEE Journal on Selected Areas in Communications*, 33(11):2287–2301, 2015.

[185] Jun Xiong, Yuan Zhuang, Joon Wayn Cheong, and Andrew G. Dempster. Message passing enhanced distributed kalman filter for cooperative localization. *IEEE Signal Processing Letters*, 29:2652–2656, 2022.

[186] Xiaobin Xu, Fenglin Pang, Yingying Ran, Yonghua Bai, Lei Zhang, Zhiying Tan, Changyun Wei, and Minzhou Luo. An indoor mobile robot positioning algorithm based on adaptive federated kalman filter. *IEEE Sensors Journal*, 21(20):23098–23107, 2021.

[187] Ling Yang, Bofeng Li, Yunzhong Shen, and Chris Rizos. Extension of Internal Reliability Analysis Regarding Separability Analysis. *Journal of Surveying Engineering*, 143(3):1–10, 2017.

[188] Ling Yang, Jingling Wang, Nathan L. Knight, and Yunzhong Shen. Outlier separability analysis with a multiple alternative hypothesis test. *Journal of Geodesy*, 87(6):591–604, 2013.

[189] Haiyun Yao, Hong Shu, Xinlian Liang, Hongji Yan, and Hongxing Sun. Integrity monitoring for bluetooth low energy beacons rssi based indoor positioning. *IEEE Access*, 8:215173–215191, 2020.

[190] Haiyun Yao, Hong Shu, Hongxing Sun, B.G. Mousa, Zhenghang Jiao, and Yingbo Suo. An integrity monitoring algorithm for wifi/pdr/smartphone-integrated indoor positioning system based on unscented kalman filter. *EURASIP Journal on Wireless Communications and Networking*, 2020(246), 2020.

[191] Leehter Yao, Yeong-Wei Andy Wu, Lei Yao, and Zhe Zheng Liao. An integrated imu and uwb sensor based indoor positioning system. In *2017 International Conference on Indoor Positioning and Indoor Navigation (IPIN)*, Sapporo, Japan, 2017. IEEE, Piscataway, New Jersey, USA.

[192] Mevlut Yetkin and Mustafa Berber. Robustness analysis using the measure of external reliability for multiple outliers. *Survey Review*, 45(330):215–219, 2013.

[193] H Yu, Y Shen, L Yang, and Y Nie. Robust m-estimation using the equivalent weights constructed by removing the influence of an outlier on the residuals. *Survey Review*, 51(364):60–69, 2019.

[194] Yue Yu, Ruizhi Chen, Liang Chen, Wei Li, Yuan Wu, and Haitao Zhou. Autonomous 3d indoor localization based on crowdsourced wi-fi fingerprinting and mems sensors. *IEEE Sensors Journal*, 22(6), 2022.

[195] Yonghao Zhao, Wai-Choong Wong, Hari Krishna Garg, and Tianyi Feng. Pedestrian dead reckoning with turn-based correction. In *2018 International Conference on Indoor Positioning and Indoor Navigation (IPIN)*, Nantes, France, 2018. IEEE, Piscataway, New Jersey, USA.

[196] Yonghao Zhao, Zhixiang Zhang, Tianyi Feng, Wai-Choong Wong, and Hari Krishna Garg. Graphips: Calibration-free and map-free indoor positioning using smartphone crowdsourced data. *IEEE Internet of Things Journal*, 8(1):393–406, 2021.

[197] Biao Zhou, Changqiang Jing, Chao Sun, and Youngok Kim. A joint indoor positioning scheme exploiting pedestrian dead reckoning and radio frequency tomography. *Journal of Electromagnetic Waves and Applications*, 32(18):2386–2403, 2018.

[198] Ni Zhu, Miguel Ortiz, and Valerie Renaudin. Seamless indoor-outdoor infrastructure-free navigation for pedestrians and vehicles with gnss-aided foot-mounted imu. In *2019 International Conference on Indoor Positioning and Indoor Navigation*, Pisa, Italy, 2019. IEEE, Piscataway, New Jersey, USA.

[199] Enrico Zio. Reliability engineering: old problems and new challanges. *Reliability Engineering & System Safety*, 94(2):125–141, 2009.

[200] Enrico Zio. Some challanges and opportunities in reliability engineering. *IEEE Transactions on Reliability*, 65(4):1769–1782, 2016.